CONTROL PREDICTIVO DE CORRIENTE CON FRECUENCIA DE CONMUTACIÓN FIJA APLICADO A SISTEMAS MULTIFÁSICOS

UNIVERSIDAD NACIONAL
DE ASUNCIÓN
FACULTAD DE
INGENIERÍA

TESIS DOCTORAL

UNIVERSIDAD NACIONAL DE ASUNCIÓN
Facultad de Ingeniería
Laboratorio de Sistemas de Potencia y Control
Doctorado en Ingeniería Electrónica

CONTROL PREDICTIVO DE CORRIENTE CON FRECUENCIA DE CONMUTACIÓN FIJA APLICADO A SISTEMAS MULTIFÁSICOS

Osvaldo Julián González Barrios
Autor

Prof. Dr. Jorge Esteban Rodas Benítez
Prof. Dr. Raúl Igmar Gregor Recalde
Tutores

Mayo 2021
Campus Universitario, Luque, Paraguay

TRIBUNAL EXAMINADOR

PRESIDENTE

SILVIA ARRÚA, Universidad Nacional de Asunción, Paraguay

SECRETARIO

JORGE RODAS, Universidad Nacional de Asunción, Paraguay

VOCALES

JESÚS DOVAL-GANDOY, Universidad de Vigo, España

MARIO JAVIER DURAN, Universidad de Málaga, España

JOSÉ RODRÍGUEZ, Universidad Andres Bello, Chile

RAÚL GREGOR, Universidad Nacional de Asunción, Paraguay

Mayo 2021
Campus Universitario, San Lorenzo, Paraguay

RESUMEN

En las últimas décadas, los sistemas de accionamientos eléctricos, compuestos por máquinas multifásicas (número de fases mayor a tres en el estátor) y convertidores de potencia, han surgido como una alternativa confiable debido a la redundancia de fases para varias aplicaciones industriales, tales como la propulsión de barcos eléctricos, vehículos eléctricos y en aplicaciones relacionadas a energías renovables. Esto se debe a las inherentes ventajas que presenta las máquinas multifásicas sobre las máquinas convencionales trifásicas, como mejor distribución de potencia fase, menor contenido de armónicos en las corrientes del estátor y en el par electromagnético, además de una mejorada tolerancia a fallas, lo que implica que la máquina multifásica continuará operando en ausencia de una o más fases teniendo en cuenta que las fases restantes deben ser igual o mayor a tres.

Sin embargo, los accionamientos eléctricos multifásicos requieren del desarrollo de sofisticados algoritmos de control para regular la velocidad y la corriente de la máquina que resultan en un elevado costo computacional. En ese sentido, mediante el avance tecnológico y el desarrollo de nuevos controladores digitales de señales conocidos como DSP es posible la aplicación de controladores predictivos basados en el modelo (MPC) en este tipo de sistemas. Este es el caso del control predictivo basado en el modelo de estados finitos (FCS-MPC). Dentro de los controladores predictivos aplicados a sistemas multifásicos el más analizado y con características prometedoras es el control predictivo de corriente (MPCC), el cual presenta un buen desempeño dinámico y flexibilidad en la definición de objetivos de control. Esta técnica de control utiliza el modelo del sistema para realizar las predicciones de las variables de control teniendo en cuenta la posición de las referencias de corrientes mediante una función de costo el cual evalúa el error de seguimiento de las corrientes del estátor. No obstante, el MPCC presenta algunas limitaciones como frecuencia de conmutación variable lo que se traduce en mayores rizados en las variables de control, además de generar corrientes elevadas vinculadas a pérdidas produciendo deterioro en el sistema. Por lo tanto, en esta Tesis Doctoral, la investigación realizada se centra en paliar las limitaciones mencionadas anteriormente en el MPCC mediante novedosas estrategias de control basadas en el uso de moduladores.

El principal aporte de esta Tesis Doctoral se centra en el análisis teórico y la validación experimental en la implementación de estrategias de modulación en el control predictivo de corriente priorizando la reducción de las corrientes relacionadas a las pérdidas sin descuidar el correcto seguimiento de las corrientes principales involucradas en la conversión de energía.

Las validaciones de las estrategias de control propuestas se realizan mediante simulaciones y pruebas experimentales utilizando una máquina de inducción (IM) asimétrica de seis fases. Los resultados obtenidos mediante esta investigación fueron presentados en conferencias y en revistas internacionales de alto impacto, todas ellas arbitradas e indexadas los cuales se constituyen como una validación de las principales aportaciones de esta Tesis Doctoral.

OSVALDO GONZÁLEZ BARRIOS

Mayo, 2021. Luque, Paraguay.

SUMMARY

In recent decades, electric drive systems, composed of multiphase machines (number of phases greater than three in the stator) and power converters, have emerged as a reliable alternative due to phase redundancy for various industrial applications, such as electric ship propulsion, electric vehicles and applications related to renewable energy. This is due to the inherent advantages that multiphase machines have over conventional three-phase machines, such as better power distribution per phase, lower harmonic contents in the stator currents and in the electromagnetic torque, as well as improved fault tolerance, which implies that the multiphase machine can continue operating in the absence of one or more phases, taking into account that the remaining phases must be equal to or greater than three.

However, multiphase electric drives require the development of sophisticated control algorithms to regulate the speed and current of the machine that result in a high computational cost. In this sense, through technological advancement and the development of new digital signal processors known as DSP, it is possible to apply model-based predictive controllers (MPC) in these types of systems. This is the case of finite control set model predictive control (FCS-MPC). Among the predictive controllers applied to multiphase systems, the most analyzed and with promising characteristics is the predictive current control (MPCC), which presents good dynamic performance and flexibility in the definition of control objectives. This control technique uses the system model to perform the predictions of the control variables taking into account the position of the current references through a cost function that evaluates the stator currents tracking error. However, the MPCC presents some limitations such as the variable switching frequency, which translates into higher ripples in the control variables, in addition to generating high currents associated with losses that cause deterioration in the system. Therefore, in this Doctoral Thesis, the research carried out focuses on alleviating the limitations mentioned above in the MPCC by means of novel control strategies based on the use of modulators.

The main contribution of this Doctoral Thesis focuses on theoretical analysis and experimental validation of modulation strategies in the predictive current control prioritizing the reduction of currents related to losses without neglecting the correct tracking of the main currents involved in energy conversion.

The validations of the proposed control strategies are carried out through simulations and experimental tests using an asymmetric six-phase induction machine (IM). The results obtained through this research were presented at conferences and in high impact international journals, all of them refereed and indexed which which constitute a validation of the main contributions of this Doctoral Thesis.

OSVALDO GONZÁLEZ BARRIOS

May, 2021. Luque, Paraguay.

AGRADECIMIENTOS

En primer lugar, agradezco a Dios por permitirme llegar hasta aquí y por brindarme la fortaleza necesaria para continuar.

A mis tutores, Raúl Gregor y Jorge Rodas, quienes compartieron conmigo sus comentarios y conocimientos para hacer posible la conclusión de esta Tesis Doctoral. Valoro mucho las sugerencias recibidas. A mis compañeros del laboratorio LSPyC de la FIUNA, por sus ayudas y conocimientos durante el desarrollo de este trabajo de investigación. A los profesores, por sus aportes, enseñanzas y por encaminarnos hacia el área de la investigación durante el proceso del Doctorado.

En el ámbito personal, a mis padres Mario y María, por los valores que me inculcaron, por sus enseñanzas y por apoyarme incondicionalmente en todo momento. A mis hermanos y hermana quienes me brindan su apoyo para seguir adelante, además a todos mis familiares. A mi novia Carolina por su estímulo y cariño durante el desarrollo de este trabajo y por el apoyo de siempre. Por último, a todos mis amigos, quienes tuvieron una palabra de apoyo para mí durante los momentos de mucho empeño.

Osvaldo González Barrios

AGRADECIMIENTOS INSTITUCIONALES

Al Consejo Nacional de Ciencia y Tecnología (CONACYT) del Paraguay por el apoyo económico a través del programa de Doctorado POSG16-05.

Al Laboratorio de Sistemas de Potencia y Control (LSPyC) de la Facultad de Ingeniería y al grupo de investigación APET (Vigo, España) por el apoyo para la validación experimental de los trabajos de investigación propuestos.

Osvaldo González Barrios

Dedicado a
mis padres, hermanos,
abuelos y a mi novia
Carolina

ÍNDICE GENERAL

ÍNDICE DE FIGURAS

ÍNDICE DE TABLAS

ACRÓNIMOS

AC	Corriente alterna.
ALS	Autocovarianza de mínimos cuadrados.
DC	Corriente continua.
DRFOC	Control vectorial directo de campo orientado.
DTC	Control directo de par.
DSP	Procesador digital de señales.
FOC	Control de campo orientado.
FCS-MPC	Control predictivo basado el modelo de estados finitos.
IGBT	Transistor bipolar de puerta aislada.
IRFOC	Control vectorial indirecto de campo rotórico orientado.
KF	Filtro de Kalman.
LO	Observador de Luenberger.
MMF	Fuerza magnetomotriz.

MPC	Control predictivo basado en modelo.
MSE	Error cuadrático medio.
MPCC	Control predictivo de corriente.
MPCC-FSF	Control predictivo de corriente a frecuencia de conmutación fija.
MPCC-VV	Control predictivo de corriente basado en vectores virtuales.
PI	Proporcional integral.
PWM	Modulación por ancho de pulsos.
SVM	Modulación de vectores espaciales.
THD	Distorsión armónica total.
VSD	Descomposición en vectores espaciales.
2L-VSI	Inversor con fuente de tensión de dos niveles.

PARTE I

GENERALIDADES

CAPÍTULO 1

JUSTIFICACIÓN Y METODOLOGÍA

1.1 Introducción

Las máquinas de inducción (IM) rotativas con un número de fases mayor a tres en el estátor ($n > 3$) son conocidas en la literatura como IM multifásicas. La adopción de esta tecnología en la industria para aplicaciones de velocidad variable ha incrementado en las últimas décadas en comparación a las IM trifásicas debido a las ventajas que ofrece tales como mejor distribución espacial de la fuerza magnetomotriz (MMF) en el entrehierro de la máquina, disminuyendo las pérdidas de cobre en el rotor, menor contenido de armónico en las corrientes del estátor, tolerancia a fallos, además de menores rizados de par [1]. Por lo tanto, resulta claro las aplicaciones de las IM en accionamientos multifásicos de elevada fiabilidad y potencia, tales como la propulsión de barcos eléctricos, vehículos eléctricos así como también la generación de energía eólica [2].

Sin embargo, los accionamientos mencionados anteriormente requieren el desarrollo de sofisticados algoritmos de control que resultan en un elevado costo computacional, lo que limita su estudio e implementación. No obstante, mediante el avance tecnológico y el continuo desarrollo de procesadores digitales de señales (DSP) ya no resulta un inconveniente a la hora de la implementarlo. Esto ha permitido explotar las ventajas que ofrecen las máquinas multifásicas utilizando distintas configuraciones que mejore las prestaciones dinámicas del sistema. En ese sentido, las máquinas multifásicas se pueden clasificar de acuerdo a la distribución del devanado como máquinas de devanados distribuidos o de devanados concentrados, siendo una de las características mas relevante en esta última la presencia de un alto contenido de armónicos en la MMF que pueden emplearse para el aumento del par, mientras que para el caso de las máquinas con devanados distribuidos los armónicos pueden despreciarse mediante un buen diseño del devanado del estátor [3, 4]. Otra clasificación sería de acuerdo al desplazamiento espacial entre fases resultando en máquinas simétricas o asimétricas con uno o más neutros aislados [5]. Las máquinas simétricas están constituidos por devanados de fase consecutivos igualmente espaciados 360/n, mientras que las asimétricas están constituidas por conjuntos independientes de devanados espaciados 180/n. Desde el punto de vista del numero de fases, se diferencian máquinas con un número par o impar de fases, donde los devanados simétricos son mayormente empleados para un número impar de fases mientras que las asimétricas para un número par de fases, siendo las más estudiadas las IM de cinco y seis fases respaldadas por el uso de convertidores de potencia en los accionamientos multifásicos [1, 6, 7].

En cuanto a los convertidores de potencia utilizados en los accionamientos multifásicos, la topología más utilizada es la configuración back-to-back, donde la etapa de entrada normalmente se encuentra constituida por un rectificador trifásico conectado eléctricamente a la red con el mismo número de fases, mientras que la etapa de salida (etapa inversora), constituida por dispositivos semiconductores de alta frecuencia de conmutación, puede contar con más de tres fases, teniendo en cuenta que la conexión entre etapas se realiza mediante un enlace intermedio conocido como DC-link. Es decir, el convertidor de potencia desacopla la máquina de la red principal permitiendo el empleo de máquinas con cualquier número de fases en el devanado del estátor [8]. El inversor de fuente de tensión de dos niveles (2L-VSI) basado en transistores bipolares de puerta aislada (IGBT) es el inversor más utilizado en los accionamientos multifásicos. Además, en la literatura pueden encontrarse otras topologías de convertidores dependiendo de los requerimientos de la aplicación [9, 10].

Esto ha llevado a investigadores a proponer nuevas estrategias de control enfocados a los accionamientos multifásicos para aprovechar de manera óptima sus inherentes ventajas. En ese sentido, una de las estrategias que ha surgido recientemente como una alternativa prometedora en comparación a las estrategias convencionales como el control orientado de campo (FOC) o el control directo de par (DTC), es el control predictivo basado en el modelo (MPC), específicamente para el control de corriente conocido como (MPCC), debido a su rápida respuesta dinámica y a la capacidad que posee de incluir varios objetivos de control [11–15]. Sin embargo, el MPCC presenta algunas desventajas cuando se aplica a sistemas multifásicos, algunas de ellas son las elevadas corrientes relacionadas con las pérdidas de cobre que se encuentran proyectadas en un plano secundario denominado plano $x-y$, y un alto contenido de armónicos en la corriente debido a la ausencia de moduladores lo que resulta en una frecuencia de conmutación variable [14]. Investigaciones recientes han sido abordadas para hacer frente a estos inconvenientes, por ejemplo, en [16] se propuso un MPCC utilizando vectores virtuales para generar en promedio tensiones próximas a cero en el plano $(x-y)$ pero con un rango limitado de tensiones en el plano principal conocido como plano $(\alpha-\beta)$ aplicado a una IM asimétrica de seis fases. Además, se han propuestos otros enfoques basados en MPCC que utilizan estrategias de modulación para mitigar las elevadas corrientes en el plano $(x-y)$. En [17] se ha presentado un estudio comparativo del MPCC empleando dos técnicas de modulación para una IM de seis fases, mientras que en [18] se ha abordado un MPCC a frecuencia de conmutación fija mediante un patrón de conmutación aplicado al VSI de dos niveles. Sin embargo, un seguimiento mejorado de las corrientes del estátor en el plano $(\alpha-\beta)$ con corrientes reducidas en el plano $(x-y)$ mediante nuevas estrategias de modulación no se ha abordado aún.

En este contexto, la principal aportación de esta Tesis Doctoral se centra en el análisis y evaluación experimental de estrategias de modulación incorporados al MPCC aplicado a una IM asimétrica de seis fases que permita mejorar las prestaciones dinámicas del accionamiento multifásico así como las reducciones de las figuras de mérito tales como el error cuadrático medio (MSE) y la distorsión armónica total (THD).

1.2 Objetivos

El objetivo de esta Tesis es el estudio y análisis del comportamiento de los accionamientos eléctricos multifásicos, concretamente la IM asimétrica de seis fases, empleando estrategias de modulación en el MPCC. Los objetivos específicos se citan a continuación:

- Evaluar en términos comparativos el control predictivo de corriente basado en estrategias de modulación aplicado a los accionamientos multifásicos.
- Implementar una estrategia de control predictivo de corriente eficiente con una etapa de modulación para lograr una frecuencia de conmutación fija de los dispositivos de potencia en aplicaciones de IM asimétrica de seis fases.
- Implementar el control predictivo de corriente basado en una modulación con vectores virtuales para reducir las corrientes en el plano $x-y$ aplicado a la IM asimétrica de seis fases.

- Realizar aportaciones al estado del arte del control predictivo de corriente a frecuencia fija aplicado al accionamiento de seis fases.

1.3 Organización del documento

El documento se ha organizado en tres partes. En la Parte I, se describen las generalidades de la Tesis, abordando inicialmente la justificación y objetivos del mismo (Capítulo 1). Posteriormente se presenta el modelo matemático basado en espacio de estados de la IM asimétrica de seis fases así como el convertidor de potencia a ser utilizado para su control (Capítulo 2). En el mismo capítulo se introduce las estrategias de control más estudiadas para el caso de la IM de seis fases, haciendo especial énfasis en el MPCC con técnicas de modulación.

En la Parte II se analizan los resultados logrados mediante las técnicas de control propuestas en el marco de la presente Tesis Doctoral (Capítulo 3). En ese sentido, se ha realizado dos aportaciones siendo la primera el MPCC utilizando una estrategia de modulación basada en un patrón de conmutación para obtener una frecuencia fija de conmutación (Artículo 1). Mientras que la segunda aportación se enfoca en el MPCC basado en una estrategia de modulación incorporando vectores virtuales (Artículo 2). Finalmente, se formulan las principales conclusiones que se derivan del desarrollo de la Tesis y se plantean futuros trabajos en la línea de investigación propuesta en esta Tesis Doctoral (Capítulo 4).

La Parte III se compone de tres artículos, desarrollados y publicados durante la realización de la presente Tesis Doctoral aplicados a la IM asimétrica de seis fases.

Finaliza el documento anexando otras contribuciones realizadas durante el desarrollo de la presente Tesis, basadas en la aplicación de estrategias de MPCC en IM de seis fases.

CAPÍTULO 2

CONTROL PREDICTIVO DE UNA IM ASIMÉTRICA DE SEIS FASES

El presente capítulo está orientado a presentar el estado actual del desarrollo de la tecnología de los accionamientos multifásicos y las técnicas de control aplicados a éstos. Primeramente, se analizan detalladamente el modelo matemático de la IM asimétrica de seis fases y del convertidor de potencia utilizado, respectivamente, a fin de proporcionar un marco teórico y poner en manifiesto el interés de la Tesis Doctoral. Posteriormente, se analizan las estrategias de control aplicados al accionamiento multifásico.

2.1 Modelado Matemático

El esquema del accionamiento multifásico utilizado en la presente Tesis Doctoral se representa en la **Figura 2.1**, el mismo se encuentra constituido de un 2L-VSI, basado en dispositivos semiconductores IGBT, empleando dos IGBT por cada fase o rama del convertidor de potencia con sus correspondientes diodos antiparalelo. Estos dispositivos a su vez se encuentran conectados a una fuente de tensión de corriente continua de baja impedancia denominada DC-link o V_{dc}, además, se muestra la IM asimétrica de seis fases

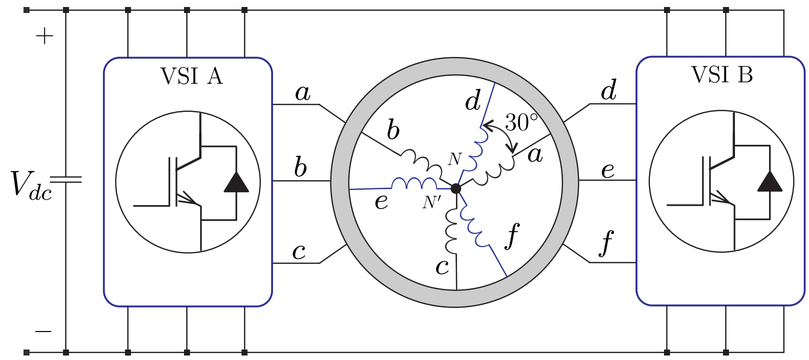

Figura 2.1 Esquema del accionamiento eléctrico de seis fases.

compuesta por dos devanados trifásicos independientes desplazados entre sí $\varphi = 30°$. Este accionamiento representa uno de los tópicos más estudiados y por consiguiente se ha abordado distintos modelos matemáticos con distintas topologías de convertidores de potencia multifásico siendo el más utilizado la dos niveles [19]. En este contexto, se desarrollan las ecuaciones del modelado para la IM asimétrica de seis fases y se examina el modelo físico de la máquina en variables de fase.

Con el propósito de reducir la complejidad del modelo y número de variables de estado necesarias para controlar la máquina, el modelo se analiza en el marco de referencia estacionario (plano $(\alpha - \beta)$) utilizando la transformación de Clarke. Además, mediante la transformación de Park, es posible analizar el modelo de la máquina en el marco de referencia dinámico (plano $(d - q)$) para fines de control. Asimismo, se aborda el modelado del convertidor de potencia y, posteriormente, se examinan las tensiones de fase y de línea que dependen del estado de conmutación del inversor y son representados los vectores espaciales de tensión disponibles en el marco de referencia estacionario.

Una técnica comúnmente utilizada para simplificar el modelo matemático de la IM asimétrica de seis fases es mediante el método de descomposición de espacio vectorial (VSD) [20, 21]. El método VSD considera las variables de la máquina en el plano $(\alpha - \beta)$ o en el plano $(d - q)$. Por lo tanto, para obtener el modelo de la máquina en el marco de referencia estacionario, se aplica el método VSD y se implementa la matriz de transformación de Clarke a las variables en cuestión.

En ese sentido, el modelo eléctrico de la IM asimétrica de seis fases es analizado en condiciones normales de operación [22]. A continuación son mencionadas las consideraciones preliminares para el desarrollo del modelo matemático de la IM de seis fases [19]:

- La máquina se encuentra compuesta por devanados idénticos uniformemente distribuidos alrededor del estátor y del rotor. El rotor posee una topología de jaula de ardilla.
- El flujo en el entrehierro de la máquina se considera constante.
- Se ignoran la saturación del campo magnético, las inductancias de fugas mutuas y las pérdidas del núcleo debidas a corrientes parásitas.
- Las resistencias del estátor y del rotor y las inductancias de fuga se consideran constantes. Se ignoran las variaciones debidas a factores de temperatura y frecuencia.
- El efecto de los armónicos no nulos en el flujo y el par es un efecto no modelado.

2.1.1 Modelo en Función de las Variables de Fase

La IM asimétrica multifásica, en este caso la de seis fases, se puede describir mediante un conjunto de ecuaciones de equilibrio de tensión de fase del estátor y rotor referidas a un marco de referencia fijo unido al estátor (**Figura 2.2**), el cual se describen como sigue:

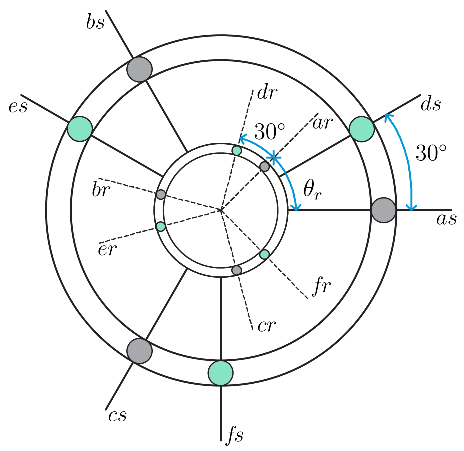

Figura 2.2 Esquema del bobinado de la IM asimétrica de seis fases.

$$\mathbf{v_s} = R_s\mathbf{i_s} + \frac{d\mathbf{\Psi_s}}{dt} = R_s\mathbf{i_s} + \mathbf{L_{ss}}\frac{d\mathbf{i_s}}{dt} + \frac{d\mathbf{L_{sr}}}{dt}\mathbf{i_r} \tag{2.1}$$

$$\mathbf{v_r} = R_r\mathbf{i_r} + \frac{d\mathbf{\Psi_r}}{dt} = R_r\mathbf{i_r} + \mathbf{L_{rr}}\frac{d\mathbf{i_r}}{dt} + \frac{d\mathbf{L_{rs}}}{dt}\mathbf{i_s} \tag{2.2}$$

$$\theta_r(t) = \int_0^t \omega_r dt \tag{2.3}$$

donde las variables $\mathbf{v}$, $\mathbf{i}$ y $\boldsymbol{\Psi}$ representan a las magnitudes eléctricas de tensión, corriente y flujo magnético, respectivamente, mientras que θ_r representa la posición angular eléctrica del rotor respecto al estátor, y gira a la velocidad eléctrica del rotor ω_r. Además, los subíndices s y r representan las variables eléctricas correspondientes a los circuitos de estátor y rotor, respectivamente.

Los vectores de tensión del estátor ($\mathbf{v_s}$) y rotor ($\mathbf{v_r}$), las corrientes del estátor ($\mathbf{i_s}$) y rotor ($\mathbf{i_r}$), los flujos del estátor ($\boldsymbol{\Psi}_\mathbf{s}$) y rotor ($\boldsymbol{\Psi}_\mathbf{s}$) se representan por medio de las siguientes ecuaciones:

$$\mathbf{v_s} = [v_{as},\, v_{ds},\, v_{bs},\, v_{es},\, v_{cs},\, v_{fs}]^T \tag{2.4}$$

$$\mathbf{v_r} = [v_{ar},\, v_{dr},\, v_{br},\, v_{er},\, v_{cr},\, v_{fr}]^T \tag{2.5}$$

$$\mathbf{i_s} = [i_{as},\, i_{ds},\, i_{bs},\, i_{es},\, i_{cs},\, i_{fs}]^T \tag{2.6}$$

$$\mathbf{i_r} = [i_{ar},\, i_{dr},\, i_{br},\, i_{er},\, i_{cr},\, i_{fr}]^T \tag{2.7}$$

$$\boldsymbol{\Psi}_\mathbf{s} = [\psi_{as},\, \psi_{ds},\, \psi_{bs},\, \psi_{es},\, \psi_{cs},\, \psi_{fs}]^T \tag{2.8}$$

$$\boldsymbol{\Psi}_\mathbf{r} = [\psi_{ar},\, \psi_{dr},\, \psi_{br},\, \psi_{er},\, \psi_{cr},\, \psi_{fr}]^T \tag{2.9}$$

donde las tensiones en el rotor son nulas debido a la topología de jaula de ardilla de la IM asimétrica de seis fases. Las matrices de resistencias del estátor ($\mathbf{R_s}$) y rotor ($\mathbf{R_r}$) e inductancias del estátor ($\mathbf{L_{ss}}$) y rotor ($\mathbf{L_{rr}}$) se encuentran definidas tal como se describe en las ecuaciones siguientes:

$$\begin{aligned} \mathbf{R_s} &= R_s \mathbf{I_6} \\ \mathbf{R_r} &= R_r \mathbf{I_6} \end{aligned} \tag{2.10}$$

$$\begin{aligned} \mathbf{L_{ss}} &= L_{ls} \mathbf{I_6} + M\boldsymbol{\Theta} \\ \mathbf{L_{rr}} &= L_{lr} \mathbf{I_6} + M\boldsymbol{\Theta} \end{aligned} \tag{2.11}$$

Así mismo las inductancias de fuga del estátor y del rotor se representan por L_{ls} y L_{lr}, respectivamente, $\mathbf{I_6}$ es la matriz identidad de orden 6, mientras que la inductancia de magnetización se representa por M, donde $\mathbf{R_s}$, $\mathbf{R_r}$ y $\mathbf{\Theta}$ se definen de la siguiente forma:

$$\mathbf{R_s} = \begin{bmatrix} R_s & 0 & 0 & 0 & 0 & 0 \\ 0 & R_s & 0 & 0 & 0 & 0 \\ 0 & 0 & R_s & 0 & 0 & 0 \\ 0 & 0 & 0 & R_s & 0 & 0 \\ 0 & 0 & 0 & 0 & R_s & 0 \\ 0 & 0 & 0 & 0 & 0 & R_s \end{bmatrix} R_r = \begin{bmatrix} R_r & 0 & 0 & 0 & 0 & 0 \\ 0 & R_r & 0 & 0 & 0 & 0 \\ 0 & 0 & R_r & 0 & 0 & 0 \\ 0 & 0 & 0 & R_r & 0 & 0 \\ 0 & 0 & 0 & 0 & R_r & 0 \\ 0 & 0 & 0 & 0 & 0 & R_r \end{bmatrix} \tag{2.12}$$

$$\mathbf{\Theta} = \begin{bmatrix} 1 & \cos(\varphi) & \cos(4\varphi) & \cos(5\varphi) & \cos(8\varphi) & \cos(9\varphi) \\ \cos(11\varphi) & 1 & \cos(3\varphi) & \cos(4\varphi) & \cos(7\varphi) & \cos(8\varphi) \\ \cos(8\varphi) & \cos(9\varphi) & 1 & \cos(\varphi) & \cos(4\varphi) & \cos(5\varphi) \\ \cos(7\varphi) & \cos(8\varphi) & \cos(11\varphi) & 1 & \cos(3\varphi) & \cos(4\varphi) \\ \cos(4\varphi) & \cos(5\varphi) & \cos(8\varphi) & \cos(9\varphi) & 1 & \cos(\varphi) \\ \cos(3\varphi) & \cos(4\varphi) & \cos(7\varphi) & \cos(8\varphi) & \cos(11\varphi) & 1 \end{bmatrix} \tag{2.13}$$

Cabe mencionar que los devanados de fase en el estátor se encuentran asimétricamente distribuidos y que se han considerado idénticos. Además, las inductancias mutuas entre el estátor y rotor son iguales, esto hace posible establecer la siguiente relación:

$$\mathbf{L_{sr}} = \mathbf{L_{rs}}^T = M\mathbf{\Gamma} \tag{2.14}$$

$$\mathbf{\Gamma} = \begin{bmatrix} \cos(\theta_r) & \Delta_1 & \Delta_3 & \Delta_4 & \Delta_6 & \Delta_7 \\ \Delta_8 & \cos(\theta_r) & \Delta_2 & \Delta_3 & \Delta_5 & \Delta_6 \\ \Delta_6 & \Delta_7 & \cos(\theta_r) & \Delta_1 & \Delta_3 & \Delta_4 \\ \Delta_5 & \Delta_6 & \Delta_8 & \cos(\theta_r) & \Delta_2 & \Delta_3 \\ \Delta_3 & \Delta_4 & \Delta_6 & \Delta_7 & \cos(\theta_r) & \Delta_1 \\ \Delta_2 & \Delta_3 & \Delta_5 & \Delta_6 & \Delta_8 & \cos(\theta_r) \end{bmatrix} \tag{2.15}$$

definiéndose Δ como los cosenos del ángulo del rotor respecto al estátor que para la IM asimétrica de seis fases se representa de la siguiente manera:

$$\begin{aligned} &\Delta_1 = \cos(\varphi + \theta_r) \quad \Delta_2 = \cos(3\varphi + \theta_r) \quad \Delta_3 = \cos(4\varphi + \theta_r) \quad \Delta_4 = \cos(5\varphi + \theta_r) \\ &\Delta_5 = \cos(7\varphi + \theta_r) \quad \Delta_6 = \cos(8\varphi + \theta_r) \quad \Delta_7 = \cos(9\varphi + \theta_r) \quad \Delta_8 = \cos(11\varphi + \theta_r) \end{aligned} \tag{2.16}$$

Así también, el par electromagnético (T_e) puede calcularse mediante la siguiente ecuación:

$$T_e = P \begin{bmatrix} \mathbf{i_s} \\ \mathbf{i_r} \end{bmatrix}^T \frac{d}{d\theta_r} \begin{bmatrix} \mathbf{L_{ss}} & \mathbf{L_{sr}} \\ \mathbf{L_{rs}} & \mathbf{L_{rr}} \end{bmatrix} \begin{bmatrix} \mathbf{i_s} \\ \mathbf{i_r} \end{bmatrix} \tag{2.17}$$

No obstante, utilizando la ecuación (2.17), donde P representa el número de pares de polos magnéticos de la IM asimétrica de seis fases y empleando las matrices de impedancia expresadas en las ecuaciones (2.10)-(2.15), se consigue una expresión alternativa mediante la siguiente ecuación:

$$T_e = P(\mathbf{i_s}^T \frac{d\mathbf{L_{sr}}}{d\theta_r} \mathbf{i_r}) \tag{2.18}$$

A su vez, la velocidad de la máquina, el cual depende del par electromagnético, se puede expresar mediante la siguiente ecuación:

$$J_m \frac{d\omega_m}{dt} = T_e - T_L - B_m \omega_m \tag{2.19}$$

donde ω_m es la velocidad mecánica del rotor, que a su vez se encuentra relacionada con la velocidad eléctrica ($\omega_r = P\omega_m$), T_L es el par mecánico de la carga aplicado al eje de la máquina, J_m es la inercia de rotación y B_m es el coeficiente de fricción mecánica.

2.1.2 Transformaciones aplicadas a la IM de seis fases

En la literatura se reportan dos transformaciones distintas aplicas a las IMs de seis fases que conducen a una significativa simplificación del modelo de la máquina, la transformación doble $d-q$ y la transformación VSD [21,23]. La transformación doble $d-q$ consiste en la aplicación de la transformada de Park a los dos conjuntos de devanados y fue ampliamente utilizada en las primeras estrategias FOC y DTC propuestas para IMs de seis fases [24]. Hoy en día la transformación VSD es ampliamente utilizada no solo en la estrategia FCS-MPC sino también en las estrategias FOC y DTC [4] ya que permite separar los componentes de corriente, flujo y tensión responsables de la conversión electromecánica de la energía, proyectados en el plano ($\alpha - \beta$), de los componentes restantes, proyectados en el plano ($x - y$), los cuales pueden utilizarse como grados de libertad adicionales [25]. Además, la transformación VSD elimina los términos de acoplamiento entre los diferentes planos en el modelado de máquinas de seis fases, el cual están presentes cuando se utiliza la transformación doble $d - q$ [23]. Cabe mencionar que, la transformación VSD proyecta los armónicos de corriente, flujo y tensión de orden $h = 12m \pm 1$ con $m = 1, 2, ...$ sobre el plano ($\alpha - \beta$), mientras que los armónicos de orden $h = 6m \pm 1$ con $m = 1, 3, ...$ son proyectados sobre el plano ($x - y$) [26].

2.1.3 Inversores de fuente de tensión de dos niveles

Considerando una IM asimétrica de seis fases con una configuración de neutros aislados, las tensiones de fase dependen del vector de estado de conmutación S del convertidor 2L-VSI expresado en (2.20) y son obtenidos mediante (2.21):

$$[S] = [S_a, S_d, S_b, S_e, S_c, S_f]^T \tag{2.20}$$

$$\begin{bmatrix} v_{as} \\ v_{ds} \\ v_{bs} \\ v_{es} \\ v_{cs} \\ v_{fs} \end{bmatrix} = \frac{V_{dc}}{3} \begin{bmatrix} 2 & 0 & -1 & 0 & -1 & 0 \\ 0 & 2 & 0 & -1 & 0 & -1 \\ -1 & 0 & 2 & 0 & -1 & 0 \\ 0 & -1 & 0 & 2 & 0 & -1 \\ -1 & 0 & -1 & 0 & 2 & 0 \\ 0 & -1 & 0 & -1 & 0 & 2 \end{bmatrix} S \tag{2.21}$$

donde $S_j = \{0, 1\}$ es el estado de conmutación de la fase j, con $j \in \{a, d, b, e, c, f\}$. Si $S_j = 1$, el IGBT superior de la fase j se encuentra encendido mientras que el IGBT inferior se encuentra apagado, y ocurre lo contrario cuando $S_j = 0$. Los componentes de tensión del estátor de la IM asimétrica de seis fases en los planos ($\alpha - \beta$), ($x - y$) y

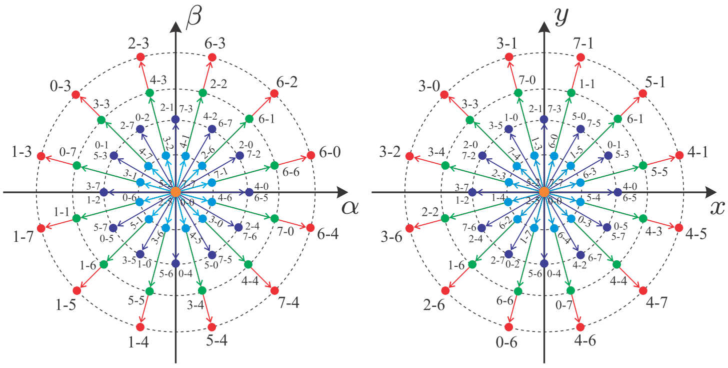

Figura 2.3 Vectores de tensión de la IM de seis fases en un marco de referencia estacionario, proyectados en los planos $(\alpha-\beta)$ y $(x-y)$.

$(z_1 - z_2)$ son calculados mediante (2.23) aplicando la transformación VSD definido en (2.22) a las tensiones de fase representado en (2.21) [26]:

$$C = \frac{1}{3}\begin{bmatrix} 1 & \frac{\sqrt{3}}{2} & -\frac{1}{2} & -\frac{\sqrt{3}}{2} & -\frac{1}{2} & 0 \\ 0 & \frac{1}{2} & \frac{\sqrt{3}}{2} & \frac{1}{2} & -\frac{\sqrt{3}}{2} & -1 \\ 1 & -\frac{\sqrt{3}}{2} & -\frac{1}{2} & \frac{\sqrt{3}}{2} & -\frac{1}{2} & 0 \\ 0 & \frac{1}{2} & -\frac{\sqrt{3}}{2} & \frac{1}{2} & \frac{\sqrt{3}}{2} & -1 \\ 1 & 0 & 1 & 0 & 1 & 0 \\ 0 & 1 & 0 & 1 & 0 & 1 \end{bmatrix} \tag{2.22}$$

$$[v_{\alpha s}, v_{\beta s}, v_{xs}, v_{ys}, v_{z1s}, v_{z2s}]^T = C\,[v_{as}, v_{ds}, v_{bs}, v_{es}, v_{cs}, v_{fs}]^T \tag{2.23}$$

Se debe tener en cuenta que, las 64 posibilidades diferentes para el vector de estado de conmutación S dan como resultado 49 vectores distintos de tensión proyectados en los planos $(\alpha-\beta)$ y $(x-y)$ simultáneamente, como se muestra en la **Figura 2.3**. Además, las proyecciones de los vectores de tensón en el plano $(z_1 - z_2)$ no se consideran en el modelado de la IM de seis fases con una configuración de neutros aislados ya que no hay circulación de corrientes de secuencia cero [27].

2.2 Técnicas de Control Aplicadas a las IM de Seis Fases

Con el creciente interés en accionamientos multifásicos para aplicaciones de velocidad variable de alta potencia y alta fiabilidad, la necesidad de controladores de alto rendimiento ha liderado la actividad de investigación en los últimos años. Los esquemas de control de accionamientos multifásicos se basan principalmente en la extensión de las técnicas de control tradicionales propuestas inicialmente para las máquinas trifásicas, cuyo objetivo es la rápida y precisa regulación de la velocidad y el par [28, 29]. Las técnicas de control propuestas aprovechan los grados de libertad adicionales inherentes a las máquinas multifásicas, que pueden ser utilizados para varios propósitos de control sin afectar la producción de flujo de par [30]. En ese sentido, entre las estrategias de control más utilizadas y aplicadas a las IM de seis fases se encuentra el control vectorial o FOC [31], otra estrategia de control propuesta que compite directamente con el FOC es la estrategia DTC [32]. Además, éstas estrategias han sido extendidas al caso post-falta [33–35].

En las unidades siguientes se presentan los fundamentos de las estrategias de control más aplicadas. Primeramente se describe el principio de funcionamiento del FOC acompañado con los fundamentos del control predictivo, el cual representa actualmente la estrategia de control más estudiada para el control de accionamientos de seis fases [15]. Seguidamente se describe el método de implementación de la estrategia MPC, para luego abordar al método MPCC que es el enfoque principal de esta Tesis. Finalmente, se describe al método MPCC con observadores de estado óptimos para mejorar el funcionamiento del MPCC.

2.2.1 Control Vectorial de Campo Orientado (FOC)

El FOC ha sido propuesta a inicios de los setenta y representa el método más empleado para el control independiente del flujo y del par de IMs y su desarrollo ha desplazado a las máquinas de corriente continua en aplicaciones donde son requeridas control de velocidad [36]. Para ello, es necesario una adecuada transformación de las variables controladas al plano $(d-q)$, donde el eje d es alineado con uno de los componentes del flujo (flujo del estátor o flujo del rotor) para lograr el desacoplamiento. En ese sentido, la corriente es relacionada respecto al plano $(d-q)$, que gira a una frecuencia eléctrica, donde el eje d es alineado al flujo del rotor (conocido como RFOC), con esto se obtiene un funcionamiento similar al de una máquina de corriente continua. Cabe mencionar que, el RFOC es el más utilizado entre las estrategias de FOC en aplicaciones industriales [24].

Existen dos estrategias de control RFOC, el control indirecto conocido como IRFOC y el control directo denominado DRFOC, siendo la principal diferencia entre ambos métodos, la manera en que se obtiene la posición angular del flujo del rotor. Al implementar el método RFOC, las corrientes del rotor en el plano $(d-q)$ pueden obtenerse mediante las ecuaciones de flujo del rotor, teniendo en cuenta que el flujo del rotor en el eje q es nulo.

$$\begin{aligned}\psi_{dr} &= (L_{lr}+L_m)i_{dr}+L_m i_{ds} \\ i_{dr} &= \frac{(\psi_{dr}-L_m i_{ds})}{L_r}\end{aligned} \tag{2.24}$$

$$\begin{aligned}0=\psi_{qr} &= (L_{lr}+L_m)i_{qr}+L_m i_{qs} \\ i_{qr} &= -\left(\frac{L_m}{L_r}\right)i_{qs}\end{aligned} \tag{2.25}$$

Además, mediante las ecuaciones (2.24) y (2.25) el modelado de la máquina en el plano $(d-q)$ puede expresarse de la siguiente manera:

$$\psi_{dr}+\tau_r\frac{d\psi_{dr}}{dt}=L_m i_{ds} \tag{2.26}$$

$$\omega_{sl}\psi_{dr}\tau_r=L_m i_{qs} \tag{2.27}$$

$$T_e=P\frac{L_m}{L_r}\psi_{dr}i_{qs} \tag{2.28}$$

siendo $\tau_r=\frac{L_r}{R_r}$ la constante de tiempo del rotor.

Una característica importante del método IRFOC es que para una adecuada orientación es necesario un buen conocimiento de algunos parámetros de las máquina. Asimismo, las estrategias FOC se pueden implementar utilizando controladores proporcionales integrales (PI).

A partir de las ecuaciones (2.26)-(2.28) se puede deducir que el flujo del rotor se controlará en la componente d de la corriente, mientras que la producción de par se controlará en la componente q de la corriente. El esquema de control IRFOC aplicado al accionamiento de seis fases se puede ver en la **Figura 2.4**. El esquema consta de bucles de control de velocidad, control de flujo y control de corriente en el plano $x-y$. La corriente del eje d es controlado mediante un regulador PI. Adicionalmente, el control de corriente del eje q se obtiene mediante un regulador PI de velocidad externo conectado a otro regulador PI de corriente interno. Por otra parte, los componentes de las corrientes en el plano $(x-y)$ se controlan mediante reguladores PI individuales.

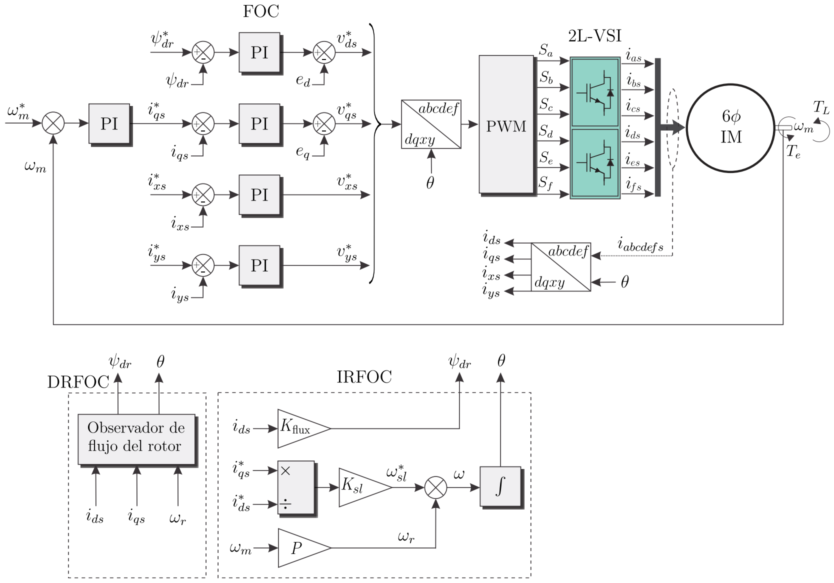

Figura 2.4 Esquema del control vectorial para la IM de seis fases.

A través del método VSD, las corrientes de la IM de seis fases en los planos $(\alpha - \beta)$ y $(x - y)$ se obtienen mediante la matriz de transformación de Clarke. Seguidamente, los componentes de las corrientes del plano $(\alpha - \beta)$ se giran al marco de referencia $(d - q)$ mediante la transformación de Park, mientras que la estimación de la posición (θ), ahora corresponde al ángulo del flujo del rotor y se obtiene por medio de la siguiente ecuación:

$$\theta = \int (\omega_r + \omega_{sl})dt = \int (\omega_r + \frac{R_r i_{qs}^*}{L_r i_{ds}^*})dt \tag{2.29}$$

La velocidad de deslizamiento (ω_{sl}) es estimada mediante la ecuación (2.27), teniendo en cuenta las corrientes de referencias productoras del flujo y par (i_{ds}^* y i_{qs}^*). Además, existen otras dos componentes más de corrientes disponibles para el control de la IM de seis fases. Ya que el accionamiento eléctrico se centra en una máquina con devanados distribuidos, los componentes de la corriente en el plano $(x - y)$ no generan par eléctrico, por lo cual deben reducirse para minimizar las pérdidas en el sistema. Por ello, las corrientes de referencias en dicho plano son establecidas al valor cero. Cabe mencionar que, esto no ocurre al emplear máquinas con devanados concentrados, ya que estos grados de libertad adicionales pueden utilizarse mejorar la producción de par mediante la inyección de armónicos de corriente [37].

Una vez determinada la acción de control para cada bucle, se establecen las referencias de tensión v_{ds}^*, v_{qs}^*, v_{xs}^*, y v_{ys}^* obtenidas por medio de los controladores PI, y estas son transformadas en variables de fase. Posteriormente, estas tensiones de fase son moduladas por medio de la estrategia PWM proporcionando el patrón de conmutación para ser aplicado al convertidor de potencia. La estrategia PWM consiste en controlar y establecer la duración de encendido de los pulsos aplicados en la puerta de los semiconductores de cada fase o rama del convertidor, y de esta manera controlar la magnitud y la frecuencia de la tensión de salida del inversor.

Es importante mencionar que, una alternativa prometedora en comparación a los controladores internos de corriente utilizados en la estrategia IRFOC, es el MPCC, el cual constituye la estrategia de control utilizada en el marco de la presente Tesis Doctoral. El principio de operación, fundamentos, ventajas y limitaciones en su uso para el control de las IM de seis fases se abordará a continuación.

2.2.2 Control Predictivo basado en el Modelo (MPC)

Una estrategia de control alternativa y prometedora a los métodos clásicos empleados en los accionamientos multifásicos, como lo son el DTC o FOC, es el MPC. El principio de funcionamiento del control predictivo se basa en la predicción del comportamiento futuro de la variables del sistema mediante el uso de un modelo matemático. Las predicciones son empleadas para seleccionar la acción de control óptima a ser aplicada de acuerdo a una función de costo predefinida, el cual contiene los objetivos de control [38]. En ese sentido, la formulación intuitiva del dilema de control, la posibilidad de realizar un control multivariable, así como la inclusión de restricciones o no linealidades en el proceso de control a través de una adecuada función de costo en la estrategia MPC, ha promovido el interés de los investigadores en el campo de los accionamientos eléctricos [39]. Las características mencionadas anteriormente permite la reducción de la complejidad del controlador ya que es posible eliminar la estructura en cascada utilizada en el método FOC, y esto produce una rápida respuesta dinámica.

Por otro lado, la implementación de la estrategia MPC requiere de un alto costo computacional debido al proceso de optimización teniendo en cuenta todas las acciones de control. Sin embargo, en las últimas décadas el aumento de la potencia computacional de las plataformas de control que incluyen microprocesadores ha permitido la implementación de estrategias MPC en los accionamientos eléctricos [14]. Las estrategias MPC generalmente se clasifican en dos categorías, el MPC de estado continuo (CCS-MPC) y el MPC de estado finito (FCS-MPC) [39]. Ambas estrategias de control se enfocan en el mismo principio de operación (se utiliza un modelo predictivo para determinar la acción de control óptima). Sin embargo, generalmente se prefiere la estrategia FCS-MPC en el control de accionamientos eléctricos, el cual se basa en un modelo discreto del sistema empleado para calcular las predicciones mediante una función de costo que permite la fácil inclusión de restricciones y por lo general se encuentra compuesta por los errores entre las referencias y las predicciones de las variables analizadas. Además, la estrategia FCS-MPC aprovecha la naturaleza discreta del convertidor de potencia que presenta un número limitado de estados de conmutación, donde el estado de conmutación óptimo que minimiza la función de costo es seleccionado a través de un proceso iterativo conocido como proceso de optimización. Finalmente, el estado de conmutación óptimo seleccionado es aplicado directamente sin la implementación de alguna técnica de modulación a diferencia de la estrategia CCS-MPC que sí implementa una etapa de modulación (usualmente basado en la estrategia PWM) para proporcionar el patrón de conmutación a ser aplicado al convertidor de potencia.

Por otro lado, es importante mencionar las diferencias que existen entre ambos esquemas de control tales como la frecuencia de conmutación fija para el caso de la estrategia CCS-MPC debido a la inclusión de una etapa de modulación, en cambio la estrategia FCS-MPC presenta una frecuencia de conmutación variable. Sin embargo, el esquema de control basado en la estrategia CCS-MPC es más complejo que la estrategia FCS-MPC ya que no tiene en cuenta la naturaleza discreta del convertidor de potencia. Por ello, las investigaciones relacionadas al control de accionamientos multifásicos se centran en la estrategia FCS-MPC debido a la flexibilidad que presenta [39, 40]. Entre las variantes de la estrategia FCS-MPC la aplicación más utilizada es la combinación con la estrategia FOC, empleada para el control de corriente de máquinas multifásicas. Esta estrategia es conocida como MPCC, y teniendo en cuenta que las corrientes del estátor son las variables controladas, el control del mismo se realiza por medio de un bucle interno de corriente mientras que el control de velocidad se realiza mediante un bucle externo empleando la estrategia FOC [41, 42].

Sin embargo, aparte de la gran cantidad de cálculos necesarios para resolver el problema de optimización en la estrategia MPCC, la implementación del mismo presenta algunas desventajas tales como el alto contenido de armónicos presentes en las corrientes controladas debido a la ausencia de técnicas de modulación en la implementación del control, donde un solo vector de conmutación es aplicado en un periodo de muestreo produciendo deterioro en el rendimiento en el sistema.

El diseño e implementación de la estrategia MPCC utilizada para el control de corriente de la IM de seis fases que es el enfoque principal del trabajo de investigación realizado en esta Tesis serán presentados en las secciones siguientes.

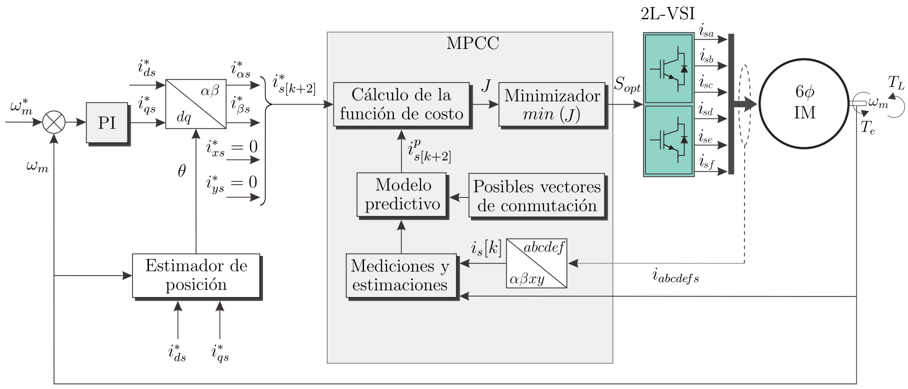

Figura 2.5 Esquema general de la estrategia MPCC para la IM de seis fases.

2.3 Control Predictivo de Corriente aplicado a la IM de Seis Fases

El esquema general de la estrategia MPCC utilizado en esta Tesis se representa en la **Figura 2.5**, compuesta por la IM asimétrica de seis fases el cual es alimentado por un convertidor de potencia del tipo 2L-VSI. Según lo descrito en la sección anterior, el esquema del MPCC está constituido por un bucle externo de control de velocidad basado en la estrategia FOC y un bucle interno de control de corriente. Por lo tanto, el objetivo de la estrategia MPCC es determinar el vector o estado óptimo de conmutación del 2L-VSI (S_{opt}) que debe ser aplicado para el seguimiento de las referencias de corriente del estátor ($i^*_{s[k+2]}$). Para ello, se emplea un modelo discreto del sistema para predecir el comportamiento futuro de las corrientes ($i^p_{s[k+2]}$) considerando un cierto horizonte de predicción. Las predicciones son calculadas para todos los vectores de conmutación, luego estas predicciones son comparadas con sus referencias mediante una función de costo donde se representa los objetivos de control. Luego, el estado de conmutación obtenido mediante la minimización de la función de costo debe aplicarse al convertidor 2L-VSI durante todo el periodo de muestreo siguiente.

El modelo predictivo del sistema se obtiene a partir de las ecuaciones eléctricas de la IM expresadas en variables VSD y del modelo del convertidor. Posteriormente, el modelo predictivo es representado en la forma de espacio de estado, como se muestra en la ecuación (2.30), donde el vector de estado ($X_{(t)}$) se encuentra constituido por las corrientes del estátor y del rotor expresados en los planos ($\alpha - \beta$) y ($x - y$) (ecuación (2.31)), mientras que el vector de entrada ($U_{(t)}$) está compuesto por las tensiones del estátor representado en la ecuación (2.32). Las matrices $A_{(t)}$ y $B_{(t)}$, expresados en las ecuaciones (2.33) y (2.34), respectivamente, dependen de los parámetros eléctricos de la IM de seis fases y del valor actual de la velocidad del rotor, cuyos coeficientes serán detallados en el modelo predictivo discreto [13].

$$\frac{dX_{(t)}}{dt} = A_{(t)}\, X_{(t)} + B_{(t)}\, U_{(t)} \tag{2.30}$$

$$X_{(t)} = [x_1, x_2, x_3, x_4, x_5, x_6]^T = [i_{\alpha s}, i_{\beta s}, i_{xs}, i_{ys}, i_{\alpha r}, i_{\beta r}]^T \tag{2.31}$$

$$U_{(t)} = [u_1, u_2, u_3, u_4]^T = [u_{\alpha s}, u_{\beta s}, u_{xs}, u_{ys}]^T \tag{2.32}$$

$$A_{(t)} = \begin{bmatrix} a_{11} & a_{12} & 0 & 0 & a_{15} & a_{16} \\ a_{21} & a_{22} & 0 & 0 & a_{25} & a_{26} \\ 0 & 0 & a_{33} & 0 & 0 & 0 \\ 0 & 0 & 0 & a_{44} & 0 & 0 \\ a_{51} & a_{52} & 0 & 0 & a_{55} & a_{56} \\ a_{61} & a_{62} & 0 & 0 & a_{65} & a_{66} \end{bmatrix} \tag{2.33}$$

$$B_{(t)} = \begin{bmatrix} b_{11} & 0 & 0 & 0 \\ 0 & b_{22} & 0 & 0 \\ 0 & 0 & b_{33} & 0 \\ 0 & 0 & 0 & b_{44} \\ b_{51} & 0 & 0 & 0 \\ 0 & b_{62} & 0 & 0 \end{bmatrix} \tag{2.34}$$

El modelo predictivo expresado en espacio de estado (ecuación 2.30) puede expandirse de la siguiente manera:

$$\begin{aligned} \frac{dx_1}{dt} &= a_{11}x_1 + a_{12}x_2 + a_{15}x_5 + a_{16}x_6 + b_{11}u_1 \\ \frac{dx_2}{dt} &= a_{21}x_1 + a_{22}x_2 + a_{25}x_5 + a_{26}x_6 + b_{22}u_2 \\ \frac{dx_3}{dt} &= a_{33}x_3 + b_{33}u_3 \\ \frac{dx_4}{dt} &= a_{44}x_4 + b_{44}u_4 \\ \frac{dx_5}{dt} &= a_{51}x_1 + a_{52}x_2 + a_{55}x_5 + a_{56}x_6 + b_{51}u_1 \\ \frac{dx_6}{dt} &= a_{61}x_1 + a_{62}x_2 + a_{65}x_5 + a_{66}x_6 + b_{62}u_2 \end{aligned} \tag{2.35}$$

Luego, el modelo en tiempo continuo deber ser discretizado a causa de la naturaleza discreta del controlador utilizando alguna estrategia de discretización adecuada. Para el caso de la estrategia MPCC, generalmente se emplea el método de Euler hacia adelante ya que permite obtener un modelo discreto preciso del sistema así como su facilidad de implementación. A continuación, se expresa la ecuación del modelo predictivo de la IM de seis fases en tiempo discreto:

$$\mathbf{X}^{p}_{[k+1|k]} = \mathbf{X}_{[k]} + \mathrm{f}\left(\mathbf{X}_{[k]},\ \mathbf{U}_{[k]},\ T_s,\ \omega_{r[k]}\right) \tag{2.36}$$

teniendo en cuenta que k representa la muestra actual, T_s es el periodo de muestreo y $\mathbf{X}^{p}_{[k+1|k]}$ corresponde a la predicción de la muestra futura.

2.3.1 Observadores de Orden Reducido Aplicado al MPCC

De acuerdo a la ecuación (2.36), solamente las corrientes del estátor y la velocidad mecánica del rotor son medibles, por ello es importante resaltar que para calcular las predicciones de las corrientes del estátor se deben conocer los valores de las variables del rotor. Las tensiones del estátor pueden ser fácilmente estimadas mediante los estados de conmutación enviados el convertidor 2L-VSI, sin embargo, las corrientes del rotor no son directamente medibles en las IMs por lo que deben ser estimadas. Esta limitación puede ser resuelta mediante la estimación de las corrientes del rotor utilizando el concepto de observadores de orden reducido. La característica de los observadores de orden reducido es que solo estima el valor de las partes no medibles del vector de estado. Este tema de interés ha sido resuelto mediante el uso de estrategias basadas en el observador de Luenberger (LO) y en el filtro de Kalman (KF), donde el observador basado en la estrategia KF es considerado como la mejor opción ya que las ganancias del observador son optimizadas teniendo en cuenta la entrada de ruido a los sensores de medición. Para el caso del observador basado en la estrategia LO, las ganancias no son optimizadas y el ajuste es determinístico [43, 44].

Por lo tanto, el observador basado en la estrategia KF es el que será diseñado e implementado en esta Tesis para mejorar el desempeño de la estrategia MPCC, además de incrementar la exactitud de las predicciones.

Básicamente, el observador KF es un algoritmo que se basa en el modelo de espacio de estado de un sistema para estimar el estado futuro y la salida futura realizando un filtrado óptimo a la señal de salida. De esta manera, el observador KF es un estimador tipo predictor-corrector el cual es óptimo ya que minimiza el error estimado de las covarianzas de los ruidos (ruidos de medida y ruidos de proceso). De esta forma la matriz de realimentación de los estados es recalculada de manera óptima en cada periodo de muestreo dado que emplea parámetros estadísticos. Esta particularidad resulta atractiva para la estrategia MPCC, primordialmente si no son conocidos los valores exactos de los parámetros internos de la IM y además las mediciones de las variables de estado se encuentran perturbados por ruido gaussiano. Como el observador KF se basa en un método recursivo enfocado en el concepto de espacio de estado, permitiendo un ahorro de memoria, esto lo hace apropiado a la hora de ser implementado en un sistema digital.

En ese sentido, teniendo en cuenta ruidos de medición gaussiano con media cero y procesos no correlacionados, las ecuaciones del modelo predictivo en tiempo discreto expresadas en la forma de espacio de estado, se definen como:

$$\mathbf{X}^{p}_{[k+1]|k} = \mathbf{A}_{[k]}\mathbf{X}_{[k]} + \mathbf{B}_{[k]}\mathbf{U}_{[k]} + \mathbf{H}\varpi_{[k]} \tag{2.37}$$

$$\mathbf{Y}_{[k+1]|k} = \begin{bmatrix} 1 & 0 & 0 & 0 & 0 & 0 \\ 0 & 1 & 0 & 0 & 0 & 0 \\ 0 & 0 & 1 & 0 & 0 & 0 \\ 0 & 0 & 0 & 1 & 0 & 0 \end{bmatrix} \mathbf{X}_{[k+1]} + \nu_{[k+1]} \tag{2.38}$$

donde las matrices en tiempo discreto $\mathbf{A}_{[k]}$ y $\mathbf{B}_{[k]}$ se representan mediante las ecuaciones (2.39) y (2.40), respectivamente. La matriz $\mathbf{H}$ representa la ponderación del ruido, la matriz $\varpi_{[k]}$ corresponde al ruido de proceso y $\nu_{[k+1]}$ es considerada la matriz de ruido de medición. La descripción detallada de la dinámica y de la convergencia del error del observador KF se analizan en [43, 44] y no fue incluida en esta sección ya que no representa el enfoque principal de la presente Tesis.

$$\mathbf{A}_{[k]} = \begin{bmatrix} a_{11[k]} & a_{12[k]} & 0 & 0 & a_{15[k]} & a_{16[k]} \\ a_{21[k]} & a_{22[k]} & 0 & 0 & a_{25[k]} & a_{26[k]} \\ 0 & 0 & a_{33[k]} & 0 & 0 & 0 \\ 0 & 0 & 0 & a_{44[k]} & 0 & 0 \\ a_{51[k]} & a_{52[k]} & 0 & 0 & a_{55[k]} & a_{56[k]} \\ a_{61[k]} & a_{62[k]} & 0 & 0 & a_{65[k]} & a_{66[k]} \end{bmatrix} \tag{2.39}$$

$$\mathbf{B}_{[k]} = \begin{bmatrix} b_{11[k]} & 0 & 0 & 0 \\ 0 & b_{22[k]} & 0 & 0 \\ 0 & 0 & b_{33[k]} & 0 \\ 0 & 0 & 0 & b_{44[k]} \\ b_{51[k]} & 0 & 0 & 0 \\ 0 & b_{62[k]} & 0 & 0 \end{bmatrix} \tag{2.40}$$

Posteriormente, los parámetros de las matrices $\mathbf{A}_{[k]}$ y $\mathbf{B}_{[k]}$, se definen a continuación:

$$\begin{aligned}
a_{11[k]} &= a_{22[k]} = 1 - \frac{R_s L_r T_s}{L_s L_r - L_m^2} & a_{12[k]} &= -a_{21[k]} = \frac{L_m^2 \omega_{r(k)} T_s}{L_s L_r - L_m^2} \\
a_{15[k]} &= a_{26[k]} = \frac{R_r L_m T_s}{L_s L_r - L_m^2} & a_{16[k]} &= -a_{25[k]} = \frac{L_m L_r \omega_{r(k)} T_s}{L_s L_r - L_m^2} \\
a_{33[k]} &= a_{44[k]} = 1 - \frac{R_s T_s}{L_{ls}} & a_{51[k]} &= a_{62[k]} = \frac{R_s L_m T_s}{L_s L_r - L_m^2} \\
a_{52[k]} &= -a_{61[k]} = -\frac{L_s L_m \omega_{r(k)} T_s}{L_s L_r - L_m^2} & a_{55[k]} &= a_{66[k]} = 1 - \frac{R_r L_s T_s}{L_s L_r - L_m^2} \\
a_{56[k]} &= -a_{65[k]} = -\frac{L_r L_s \omega_{r(k)} T_s}{L_s L_r - L_m^2} & b_{11[k]} &= b_{22[k]} = \frac{L_r T_s}{L_s L_r - L_m^2} \\
b_{33[k]} &= b_{44[k]} = \frac{T_s}{L_{ls}} & b_{51[k]} &= b_{62[k]} = -\frac{L_m T_s}{L_s L_r - L_m^2}
\end{aligned} \tag{2.41}$$

2.3.2 Función de Costo

El diseño de la función de costo permite la optimización de varias variables objetivos tales como minimización de rizado del par de la IM, pérdidas de conmutación en el convertidor y minimización del contenido de armónicos [40]. Sin embargo, en la estrategia MPCC el objetivo de control es el error de seguimiento de las variables controladas de acuerdo a sus referencias. Por lo tanto, la función de costo está compuesta por la diferencia entre los valores predichos de las corrientes del estátor y sus referencias, y por lo general esta figura de mérito constituye la selección habitual en los accionamientos multifásicos [14]. En ese sentido, los valores futuros de la corrientes del estátor son calculados mediante los valores medidos en el instante anterior para cada vector de conmutación y así obtener el vector de conmutación óptimo que minimice el objetivo de control. El tiempo requerido para las mediciones, cálculos de las predicciones y la selección del vector óptimo puede ser significativo en comparación a T_s dando como resultado un retardo entre el instante en que fue realizada las mediciones utilizadas para las predicciones y el momento en que la siguiente acción de control es realizada. Esta consecuencia puede ser corregida mediante la función de costo definida en la ecuación (2.42), donde se lleva a cabo una predicción de horizonte 2 ($[k+2|k)$ [45, 46].

$$J_{[k+2|k]} = (e_{\alpha s})^2 + (e_{\beta s})^2 + \lambda_{xy}[(e_{xs})^2 + (e_{ys})^2] \tag{2.42}$$

siendo:

$$\begin{aligned} e_{\alpha s} &= i^*_{\alpha s[k+2]} - i^p_{\alpha s[k+2|k]} \\ e_{\beta s} &= i^*_{\beta s[k+2]} - i^p_{\beta s[k+2|k]} \\ e_{xs} &= i^*_{xs[k+2]} - i^p_{xs[k+2|k]} \\ e_{ys} &= i^*_{ys[k+2]} - i^p_{ys[k+2|k]} \end{aligned} \tag{2.43}$$

$$\begin{aligned} i^p_{\alpha s[k+2|k]} &= a_{11[k]} i^p_{\alpha s[k+1|k]} + a_{12[k]} i^p_{\beta s[k+1|k]} + a_{15[k]} i^e_{\alpha r[k+1|k]} \\ &+ a_{16[k]} i^e_{\beta r[k+1|k]} + b_{11[k]} u_{\alpha s[k+1]} \\ i^p_{\beta s[k+2|k]} &= a_{21[k]} i^p_{\alpha s[k+1|k]} + a_{22[k]} i^p_{\beta s[k+1|k]} + a_{25[k]} i^e_{\alpha r[k+1|k]} \\ &+ a_{26[k]} i^e_{\beta r[k+1|k]} + b_{22[k]} u_{\beta s[k+1]} \\ i^p_{xs[k+2|k]} &= a_{33[k]} i^p_{xs[k+1|k]} + b_{33[k]} u_{xs[k+1]} \\ i^p_{ys[k+2|k]} &= a_{44[k]} i^p_{ys[k+1|k]} + b_{44[k]} u_{ys[k+1]} \end{aligned} \tag{2.44}$$

El parámetro o factor de peso (λ_{xy}) es un tema de investigación que ha sido abordado en trabajos recientes, el cual permite priorizar el seguimiento de las corrientes del estátor en el plano ($\alpha - \beta$) o reducir las corrientes del estátor en el plano ($x - y$), disminuyendo las pérdidas de cobre [47, 48]. Sin embargo, el desempeño del controlador puede verse afectado dependiendo del valor seleccionado para los factores de peso, por ello, es necesario realizar un correcto ajuste de estos parámetros. El ajuste del factor de peso suele realizarse mediante experimentos de prueba y error o utilizando algoritmos de optimización mas complejos [49]. Además, pueden ser definidas diferentes alternativas con el propósito de incluir varias restricciones de control y por lo tanto optimizar el desempeño del sistema. Esto resulta una ventaja para la estrategia MPCC en comparación con las estrategias de control clásicas. Usualmente, para el caso de las IMs multifásicas, λ_{xy} provee la importancia relativa del seguimiento de referencia de las corrientes en los planos ($\alpha - \beta$) y ($x - y$) [50].

2.4 Resumen

En este capítulo se ha realizado una descripción del estado del arte del control aplicado al accionamiento eléctrico de seis fases. Para ello, se desarrolló el modelo matemático de la IM de seis fases, además del modelo del convertidor 2L-VSI. En ese contexto, se describieron las estrategias de control aplicadas a la IM de seis fases, centrándose en el diseño e implementación de la estrategia MPCC detallando sus ventajas y limitaciones, siendo las más relevantes el gran contenido de armónicos, el alto costo computacional y elevadas corrientes en el plano $(x - y)$. Además, se ha abordado la teoría de observadores de estado de orden reducido para mejorar el desempeño del controlador. Uno de los objetivos de esta Tesis consiste en el desarrollo de técnicas de modulación enfocado al control de corriente para efectivamente mitigar las limitaciones mencionadas. El mismo será abordado en el capítulo posterior, donde se detallará el proceso de implementación de las técnicas propuestas validadas mediante pruebas experimentales y simulaciones.

PARTE II

ANÁLISIS DE CONTENIDO

CAPÍTULO 3

DISCUSIÓN DE LAS APORTACIONES

El trabajo de investigación llevado a cabo en esta Tesis Doctoral se enfoca en el desarrollo e implementación de técnicas de modulación aplicado al MPCC cuyo caso de estudio se basa en el accionamiento de la IM asimétrica de seis fases. Estas técnicas de modulación han sido propuestas como una alternativa al MPCC clásico debido a las desventajas que presenta, tales como frecuencia de conmutación variable que se traduce en un alto contenido de armónicos en las corrientes del estátor, el elevado costo computacional y una pobre reducción de las corrientes del estátor en el plano $(x-y)$ como se ha descrito en el capítulo anterior. La teoría de modulación ha sido aplicado satisfactoriamente a los accionamientos eléctricos para el control de corriente, tal como la modulación PWM basada en vectores espaciales, el cual se adapta a la implementación digital [51]. Sin embargo, existen algunos aspectos que deben tenerse en cuenta al momento de implementar técnicas de modulación enfocados a los accionamientos multifásicos, tales como la cantidad de vectores que deben ser seleccionados, qué vectores deben seleccionarse y el cálculo del tiempo de aplicación de los vectores seleccionados. De esta manera, será factible la regulación de las corrientes en los planos $(\alpha-\beta)$ y $(x-y)$, ya que actualmente resulta imposible reducir las corrientes del estátor en el plano $(x-y)$ utilizando un solo estado de conmutación.

En ese sentido, las descripciones y discusiones de los trabajos de investigación publicados serán abordados en este capítulo, resaltando los hallazgos y las principales contribuciones obtenidas, donde las discusiones se centran en las comparativas de las técnicas de modulación propuestas para el control de corriente con otras estrategias disponibles en la literatura como el método MPCC clásico.

3.1 Técnica de Modulación a Frecuencia de Conmutación Fija (MPCC-FSF)

Las aplicaciones para las cuales se utilizan accionamientos eléctricos multifásicos, requieren de estrategias de control que regulen de manera precisa las corrientes del estátor no solo en régimen permanente sino también en régimen transitorio. Este es el caso de la estrategia de control del tipo bucle cerrado MPCC, que exige una respuesta rápida con un rendimiento dinámico preciso. En ese sentido, la estrategia MPCC presenta desafíos adicionales como la aparición de grados extras de libertad o planos adicionales existentes en las máquinas multifásicas que deben considerarse para la regulación de las corrientes. Cabe mencionar que, estos planos adicionales son obtenidos luego de la transformación VSD. Este hecho requiere de un seguimiento de corriente simultáneo en los planos $(\alpha-\beta)$ y $(x-y)$. Por ello, además de las corrientes en el plano $(\alpha-\beta)$, también es necesario controlar o regular las corrientes en el plano $(x-y)$. Esto se debe a que los componentes de corriente del plano $(x-y)$ no afectan la producción de par en las máquinas con devanados distribuidos, pero permiten la circulación de armónicos de bajo orden que aumentan las pérdidas en el entrehierro.

Otra particularidad de la estrategia MPCC, es la aplicación de un solo estado de conmutación durante todo el periodo de muestreo. Además, cada estado de conmutación genera simultáneamente vectores de tensión en los planos $(\alpha-\beta)$ y $(x-y)$, y esto hace imposible suministrar una tensión óptima en el plano $(\alpha-\beta)$, lo cual conduce inevitablemente a la aparición de elevadas corrientes no nulas en el plano $(x-y)$ [13]. Las elevadas corrientes en el plano $(x-y)$ también se deben a la baja impedancia equivalente de las IM multifásicas.

Una alternativa para hacer frente a estos inconvenientes es mediante el incremento de la frecuencia de conmutación del convertidor y de la impedancia en el plano $(x-y)$, proporcionando un rendimiento favorable para accionamientos multifásicos de baja potencia. No obstante, la frecuencia de conmutación se ve limitada a medida que aumenta la potencia en los accionamientos multifásicos y la impedancia de las bobinas de la IM disminuye. Bajo estas condiciones, la implementación de técnicas de modulación surge como una

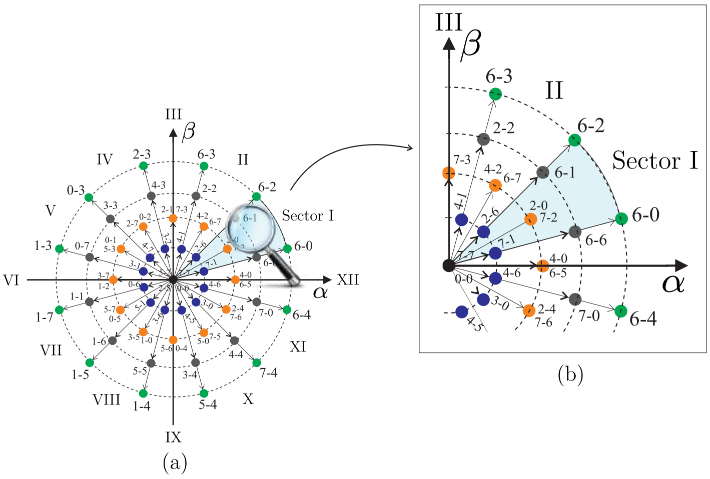

Figura 3.1 Sectores considerados para el convertidor 2L-VSI en plano ($\alpha - \beta$): (a) Vectores disponibles; (b) Sector específico seleccionado mostrado en vista ampliada.

opción atractiva para el control de corriente, ya que no resulta favorable el uso de un solo estado de conmutación en la estrategia MPCC para la regulación de las corrientes en el plano ($x - y$).

Con el objetivo de resolver las limitaciones del MPCC clásico, en el Artículo 1 se propone una estrategia MPCC modulada para una IM de seis fases alimentada a través de un convertidor de potencia del tipo 2L-VSI. La estrategia propuesta integra una técnica de modulación en el algoritmo de control para reducir los componentes de corrientes en el plano ($x - y$).

En ese sentido, esta estrategia consiste en determinar cada sector disponible para el convertidor 2L-VSI. Los mismos son obtenidos y proyectados en los planos ($\alpha - \beta$) y ($x - y$) mediante la transformación VSD, resultado en un total de 48 sectores. Estos sectores se componen de dos vectores activos adyacentes con la misma amplitud y un vector nulo, como se muestra en la **Figura 3.1**. La técnica propuesta estima la predicción de dos vectores activos que componen los 12 sectores exteriores y analiza sus respectivas funciones de costo independientemente en cada periodo muestreo [15, 17]. Las funciones de costo son definidas como J_0, J_1 y J_2 y son calculados mediante la ecuación (3.1). El principal objetivo de esta técnica de modulación es obtener cualquier vector de tensión en el plano ($\alpha - \beta$) utilizando los vectores exteriores (definidos como vectores largos) y el vector nulo, cubriendo de esta manera todo el espacio vectorial. Es importante mencionar que, los vectores largos son proyectados como los vectores de tensión más pequeños en el plano ($x - y$), produciendo una reducción de los componentes de corriente en dicho plano.

$$J_{[k+2|k]} = [(i^{*}_{\alpha s[k+2]} - i^{p}_{\alpha s[k+2|k]})^2 + (i^{*}_{\beta s[k+2]} - i^{p}_{\beta s[k+2|k]})^2$$

$$+\lambda_{xy}((i^{*}_{xs[k+2]} - i^{p}_{xs[k+2|k]})^2 + (i^{*}_{ys[k+2]} - i^{p}_{ys[k+2|k]})^2)]^{\frac{1}{2}} \tag{3.1}$$

Otro aspecto importante que debe considerarse para la implementación de la técnica propuesta es el tiempo de aplicación de los vectores. El cálculo de los ciclos de trabajo de los dos vectores activos de tensión (d_1 y d_2) y del vector nulo (d_0) dentro de cada sector se realiza mediante las ecuaciones (3.2) y (3.3) expresadas a continuación:

$$d_0 = \tfrac{\mu}{J_0} \qquad d_1 = \tfrac{\mu}{J_1} \qquad d_2 = \tfrac{\mu}{J_2} \tag{3.2}$$

$$d_0 + d_1 + d_2 = 1 \tag{3.3}$$

De esta manera, es posible calcular la expresión para μ y los ciclos de trabajo para cada vector. Estos ciclos de trabajo son inversamente proporcionales al valor de la función de costo para el vector de tensión respectivo:

$$d_0 = \frac{J_1 J_2}{J_0 J_1 + J_1 J_2 + J_0 J_2} \tag{3.4}$$

$$d_1 = \frac{J_0 J_2}{J_0 J_1 + J_1 J_2 + J_0 J_2} \tag{3.5}$$

$$d_2 = \frac{J_0 J_1}{J_0 J_1 + J_1 J_2 + J_0 J_2} \tag{3.6}$$

Considerando estas expresiones, la función de costo que finalmente se utiliza para determinar el sector óptimo, el cual es calculado para 12 iteraciones durante T_s, se obtiene de la siguiente manera:

$$G_{[k+2|k]} = d_1 J_1 + d_2 J_2 \tag{3.7}$$

Los dos vectores activos que reducen la función de costo ($G_{[k+2|k]}$) son seleccionados para ser aplicados al convertidor de potencia en el siguiente periodo de muestro. Luego de haber obtenido los ciclos de trabajo para los dos vectores a ser aplicados, es necesario proponer una ecuación que pueda relacionar los ciclos de trabajo y los vectores de tensión seleccionados para ser implementado en un controlador digital. Esto puede realizarse mediante la relación (3.8) con el fin de implementar una modulación PWM simétrica, donde los vectores son sintetizados mediante un cierto patrón de conmutación.

$$D_i = \frac{d_0}{2} + d_1 v_{1(i)} + d_2 v_{2(i)} \tag{3.8}$$

En la ecuación anterior $i = (a, b, c, d, e, f)$ y D_i es el ciclo de trabajo por fase normalizado entre 0 y1. Posteriormente, esta variable es comparada con una forma de onda del tipo triangular para obtener una modulación PWM simétrica y ser aplicado a los correspondientes dispositivos de conmutación, obteniéndose así una frecuencia de conmutación fija cuyo valor es igual a la frecuencia de muestreo.

3.2 Técnica de Modulación basado en Vectores Virtuales (MPCC-VV)

Como una alternativa al control MPCC clásico, recientemente se ha propuesto otra técnica de modulación basada en VV para mitigar los armónicos de corrientes presentes en el plano $(x - y)$ para el accionamiento de una IM de seis fases [16]. La técnica de VV fue propuesta inicialmente para el DTC de una IM de cinco fases [52] y consiste en la formación de un nuevo conjunto de vectores de tensión, denominados VV en la literatura [53], que producen componentes de tensión nulos en el plano $(x - y)$. El nuevo conjunto de vectores (12 en total) se obtienen a partir de la **Figura 3.2** y son formados a partir de la combinación de vectores largos y mediano-largos con la misma fase en el plano $(\alpha - \beta)$. Los ciclos de trabajo de los vectores se obtienen mediante la resolución de un sistema de ecuación lineal donde se consideran sus respectivos módulos. Para el caso del convertidor de potencia de seis fases del tipo 2L-VSI, la expresión general para la implementación de esta técnica teniendo en cuenta los ciclos de trabajo durante un periodo de muestreo, se define a continuación [53]:

$$d_l = 0.73, \qquad d_{ml} = 1 - d_l \tag{3.9}$$

$$VV = d_l V_{largo} + d_{ml} V_{med-largo} \tag{3.10}$$

donde d_l y d_{ml} son los ciclos de trabajo de los vectores largos y mediano-largos, respectivamente.

La implementación de esta técnica en la estrategia MPCC proporciona valores nulos en promedio de los componentes de corriente en el plano $(x - y)$. Esto es posible debido al uso de dos vectores activos en un periodo de muestreo, ya que estos vectores activos poseen proyecciones opuestas en el plano $(x - y)$, a diferencia del MPCC clásico que solamente utiliza un estado de conmutación. Sin embargo, es importante mencionar que

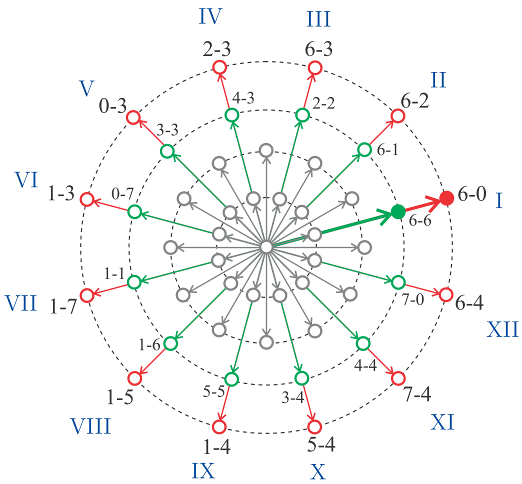

Figura 3.2 Vectores virtuales (círculos rellenos de color verde y rojo) de tensión en el plano $(\alpha - \beta)$.

la longitud alcanzada por los VVs es del 93% del valor real de los vectores largos en el plano $(\alpha - \beta)$.

Adicionalmente, el modelo predictivo empleado en la estrategia MPCC puede ser reducido debido a la ausencia de los componentes $(x - y)$ en el modelo. En ese sentido, es posible definir una nueva función de costo para el seguimiento de corriente, el cual se expresa en la siguiente ecuación:

$$J_{[k+2|k]} = (i^{*}_{\alpha s[k+2]} - i^{p}_{\alpha s[k+2|k]})^2 + (i^{*}_{\beta s[k+2]} - i^{p}_{\beta s[k+2|k]})^2 \tag{3.11}$$

La estrategia MPCC basada en VV evalúa la función de costo para los 13 VVs (incluido el vector nulo), y selecciona el que minimiza la ecuación (3.11) para ser aplicado en el siguiente periodo de muestreo. También es importante mencionar que, la combinación de vectores utilizada en esta técnica produce una frecuencia de conmutación variable.

3.3 Técnica de Modulación basado en MPCC-FSF y MPCC-VV (T3)

En las secciones anteriores se han descritos dos técnicas de modulación empleadas para la reducción de las corrientes en el plano $(x - y)$ en los accionamientos multifásicos. Una característica de la primera técnica de modulación (MPCC-FSF), es que proporciona una frecuencia de conmutación fija y está basada en la combinación de vectores largos con el vector nulo, los cuales se relacionan mediante una ecuación de sintetización que proporciona los ciclos de trabajo. Esta técnica de modulación tiene en cuenta solamente los 12 sectores exteriores para el seguimiento de corriente cubriendo así el área delimitada por los vectores en el plano $(\alpha - \beta)$. Además, estos vectores generan naturalmente una reducción de los componentes de corriente en el plano $(x - y)$. Cabe mencionar que, MPCC-FSF emplea menos vectores de tensión en comparación con la estrategia MPCC clásica, donde el proceso de optimización se realiza 49 veces para el caso del convertidor de potencia de seis fases del tipo 2L-VSI, lo que se traduce en un menor costo computacional.

Para el caso de la segunda técnica de modulación (MPCC-VV), la selección de vectores se realiza de tal manera que los componentes de tensión en el plano $(x - y)$ sea nula, y por lo tanto asegurando que las corrientes en dicho plano sea reducida. MPCC-VV también garantiza un menor costo computacional en comparación con la estrategia MPCC clásica, debido a que en el proceso de modulación se utilizan 13 vectores de tensión y por la ausencia de los componentes $(x - y)$ en el modelo. Sin embargo, la limitación de MPCC-VV radica en generar la tensión óptima en el plano $(\alpha - \beta)$ para el seguimiento de corriente. Esto se debe a que la longitud resultante de la combinación de los vectores largos con los mediano-largos es menor al de los vectores largos.

Por lo mencionado anteriormente, en el Artículo 2 se propone una nueva técnica de modulación que resulta de la combinación de las estrategias MPCC-FSF y MPCC-VV. El principal objetivo de esta propuesta consiste en utilizar las ventajas que ofrecen ambas técnicas de modulación, y en ese sentido, limitar la inyección de los componentes de corriente en el plano $(x - y)$ con un adecuado seguimiento de corriente en el plano $(\alpha - \beta)$, además de proporcionar una frecuencia de conmutación fija.

La técnica propuesta se basa en la estrategia de modulación de vectores espaciales (SVM). De esta manera es posible definir los sectores involucrados en la implementación de la misma. Los sectores se representan en la **Figura 3.3**, donde se resaltan los vectores que se utilizan durante el proceso de modulación (círculos rellenos de color rojo, verde y naranja). Así como en MPCC-FSF se tiene en cuenta los 12 sectores exteriores. Cada sector está compuesto por dos vectores largos adyacentes, dos vectores mediano-largos adyacentes con la misma fase que los vectores largos (respecto al plano $(\alpha - \beta)$) y por el vector nulo. Como se puede notar, se han escogido los vectores de tensión utilizados en las técnicas de modulación descritas anteriormente.

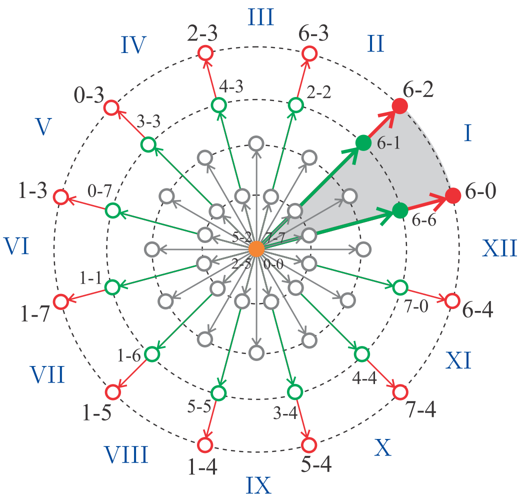

Figura 3.3 Sectores considerados para la técnica de modulación propuesta en el plano $(\alpha - \beta)$.

El tiempo de aplicación o ciclos de trabajo de los vectores son calculados mediante las ecuaciones (3.2) - (3.6), mientras que el sector óptimo se determina a través de la ecuación (3.7). Luego, la sintetización de los vectores de tensión se realiza de la misma manera que en MPCC-FSF por medio de la ecuación (3.8) obteniéndose los ciclos de trabajo para los dispositivos de conmutación de cada fase, y éstos son finalmente comparados con una forma triangular para generar la modulación PWM simétrica.

En la **Figura 3.4** se representa el patrón de aplicación de los vectores en cada periodo de muestreo para generar el porcentaje de tiempo necesario para producir componentes de corriente reducidas en el plano $(x - y)$. Siendo LV_i, MLV_j y NV las abreviaturas correspondientes a los vectores largos, mediano-largos y vector nulo, respectivamente, mientras que T_i representa el periodo de interrupción en el algoritmo de control.

Las validaciones de estas tres técnicas de modulación serán abordadas en la siguiente sección mediante simulaciones y pruebas experimentales. Es importante mencionar que la validación del Artículo 1 fue realizada con el grupo de investigación APET de la

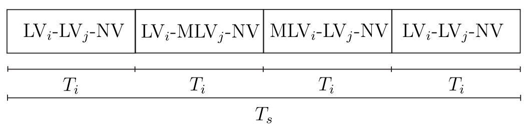

Figura 3.4 Patrón de aplicación de los vectores.

Universidad de Vigo utilizando una IM de seis fases de 2 kW de potencia. Mientras que el Artículo 2 fue validado en el Laboratorio de Sistemas de Potencia y Control (LSPyC) de la Facultad de Ingeniería de la Universidad Nacional de Asunción (UNA) empleando una IM de seis fases de 15 kW de potencia.

3.4 Validación de Resultados

En los siguientes apartados se presentan la validación de los resultados obtenidos a partir de las aportaciones de esta Tesis Doctoral, los cuales se sustentan en los siguientes artículos publicados en revistas internacionales arbitradas e indexadas, con factor de impacto definido:

1. Artículo 1: **Osvaldo González**, Magno Ayala, Jesús Doval-Gandoy, Jorge Rodas, Raúl Gregor, Marcos Rivera, Predictive-Fixed Switching Current Control Strategy Applied to Six-Phase Induction Machine, Energies, 2019, vol. 12, no 12, p. 2294. DOI: 10.3390/en12122294. (Factor de impacto 2.702).

2. Artículo 2: **Osvaldo González**, Magno Ayala, Carlos Romero, Larizza Delorme, Jorge Rodas, Raúl Gregor, Ignacio Gonzalez-Prieto, Mario Javier Duran, Model Predictive Current Control of Six-phase Induction Motor Drives using Virtual Vectors and Space Vector Modulation, IEEE Transactions on Power Electronics, 2021. (Factor de impacto 6.373). (Bajo revisión).

3.4.1 Validación del Artículo 1

Los parámetros eléctricos de la IM de seis fases utilizada para la validación del Artículo 1 se presenta en la **Tabla 3.1**. Los mismos fueron determinados mediante métodos standstill con VSI y técnicas convencionales de AC en el dominio del tiempo [54, 55].

Tabla 3.1 Parámetros Eléctricos y Mecánicos de la IM de Seis Fases (APET).

R_r	6.9 Ω	L_s	654.4 mH
R_s	6.7 Ω	P	1
L_{ls}	5.3 mH	P_w	2 kW
L_{lr}	12.8 mH	J_m	0.07 kg.m^2
L_m	614 mH	B_m	0.0004 kg.m^2/s
L_r	626.8 mH	ω_{r-nom}	3000 rpm

Primeramente, se han realizado pruebas mediante simulaciones en el entorno de programación MATLAB/Simulink R2014a para verificar la viabilidad de la propuesta MPCC-FSF. En ese sentido, se ha utilizado el método de integración numérica basado en la ecuación de Euler de primer orden como estrategia de discretización para calcular el progreso de las variables del sistema en el dominio del tiempo.

Las pruebas de simulación fueron realizadas bajo condiciones de carga, T_L = 2 Nm, para verificar la efectividad de la primera propuesta. La frecuencia de muestreo utilizada fue de 8 kHz, la tensión V_{dc} fue configurada a 400 V, y la corriente encargada de la generación del flujo fue ajustada a 1 A. El factor de peso escogido para las pruebas fue, λ_{xy} = 0.1, con el fin de dar más énfasis al seguimiento de corriente del estátor en el plano $(\alpha - \beta)$.

El rendimiento de la propuesta MPCC-FSF es analizado bajo condiciones de régimen permanente y de régimen transitorio. En ese sentido, los resultados obtenidos por medio de las pruebas de simulación así como de las pruebas experimentales analizan el desempeño del controlador en términos del MSE entre las corrientes de referencia y medidas del estátor en los planos $(\alpha - \beta)$ y $(x - y)$ [56]. Al mismo tiempo, es calculado el THD en el plano $(\alpha - \beta)$. Estas figuras de mérito se definen a continuación:

$$\mathrm{MSE}(i_{s\Phi}) = \sqrt{\frac{1}{N}\sum_{k=1}^{N}(i_{s\Phi}[k] - i^*_{s\Phi}[k])^2} \tag{3.12}$$

donde N es el número de muestras, $i^*_{s\Phi}$ la corriente de referencia del estátor, $i_{s\Phi}$ las corrientes de estátor medidas y $\Phi \in \{\alpha,\ \beta,\ x,\ y\}$.

$$\mathrm{THD}(i_s) = \sqrt{\frac{1}{i_{s1}^2}\sum_{j=2}^{N}(i_{sj})^2} \tag{3.13}$$

donde i_{s1} son las corrientes fundamentales del estátor y i_{sj} son las corrientes armónicas del estátor.

En la **Figura 3.5** se presenta el rendimiento de las corrientes del estátor en los planos $(\alpha - \beta)$ y $(x - y)$ en régimen permanente. De acuerdo a estos resultados de simulación, agrupados en la **Tabla 3.2**, la técnica propuesta presenta un buen desempeño considerando el análisis del MSE y THD de las corrientes del estátor a diferentes velocidades mecánicas. Cabe mencionar que, a velocidades bajas, el rizado de las corrientes del estátor en el plano $(\alpha - \beta)$ es ligeramente más pequeño que a velocidades más altas, de la misma forma que ocurre con las corrientes del estátor en el plano $(x - y)$.

Para la validación experimental de MPCC-FSF se ha utilizado el banco de pruebas mostrado en la **Figura 3.6**. El mismo está compuesto de una IM de seis fases alimentado

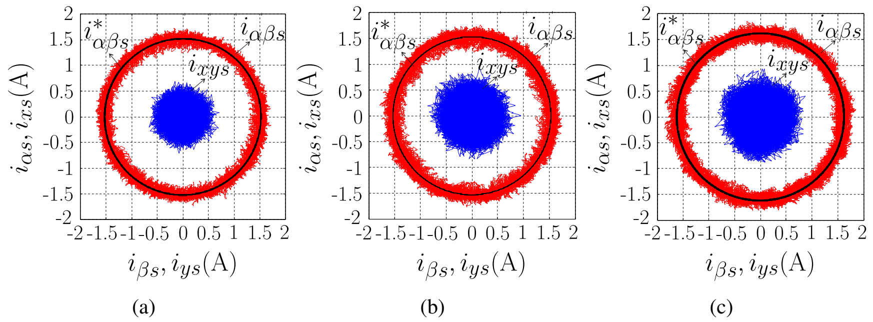

Figura 3.5 Rendimiento de simulación en régimen permanente de las corrientes del estátor en los planos $(\alpha - \beta)$ y $(x - y)$ para una frecuencia de muestreo de 8 kHz a diferentes velocidades (ω_m): (**a**) 500 rpm; (**b**) 1000 rpm; (**c**) 1500 rpm.

por medio de dos 2L-VSI trifásicos convencionales, siendo análogo a un convertidor de potencia de seis fases del tipo 2L-VSI. La tensión V_{dc} es obtenida mediante una fuente de alimentación DC. Para controlar el convertidor de potencia se ha utilizado un prototipo de funciones en tiempo real, denominado dSPACE MABXII DS1401, el mismo incluye Simulink versión 8.2. Los datos adquiridos por el dSPACE son procesados mediante un código desarrollado en MATLAB/Simulink R2014a. Las mediciones experimentales se obtienen mediante sensores de corriente LA 55-P s, con un ancho de banda de frecuencia de DC hasta 200 kHz. Luego, esos valores se convierten a digitales a través de un conversor A/D de 16 bits. El ángulo del rotor se mide a través de un encoder incremental de 1024 rpm, luego la velocidad mecánica es calculada a partir de dicha medición. Finalmente, se utiliza un freno de corriente parásita (eddy current) de 5 HP como carga mecánica variable en la IM de seis fases.

La estimación de las corrientes del rotor se realizan por medio del KF, donde los valores del ruido de proceso y medición se pueden calcular utilizando el método de autocovarianza de mínimos cuadrados (ALS), ya que proporciona estimaciones no sesgadas con

Tabla 3.2 Análisis de rendimiento de simulación de las corrientes del estátor $(\alpha - \beta)$, $(x - y)$, MSE (A), THD (%) a diferentes velocidades del rotor (rpm).

f_s = 8 kHz						
ω_m^*	MSE$_\alpha$	MSE$_\beta$	MSE$_x$	MSE$_y$	THD$_\alpha$	THD$_\beta$
500	0.065	0.064	0.174	0.172	5.73	5.46
1000	0.076	0.075	0.211	0.203	5.43	5.34
1500	0.110	0.110	0.219	0.216	6.46	6.38

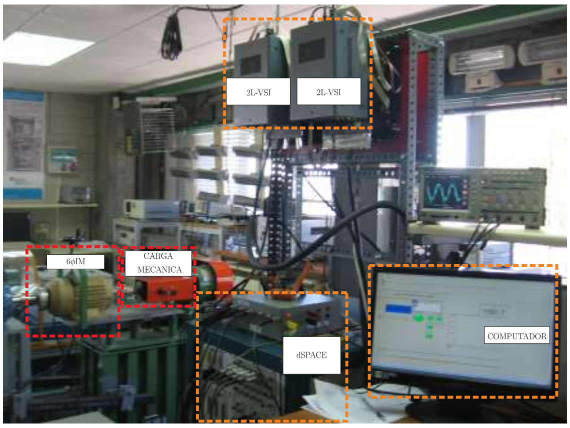

Figura 3.6 Banco de pruebas experimental (APET).

la covarianza más baja, garantizando un ajuste óptimo del filtro. Luego, recopilando los datos del sistema operando en bucle cerrado y utilizando el método propuesto en [44], los valores obtenidos son $\hat{Q}_w = 0.0022$ y $\hat{R}_v = 0.0022$. El rendimiento dinámico de MPCC-FSF ha sido evaluado utilizando dos valores diferentes para λ_{xy}, dando más prioridad al seguimiento de corriente del estátor en el plano $(\alpha - \beta)$. Es importante mencionar que, los valores de λ_{xy} se seleccionan mediante el método heurístico.

Para todas las pruebas experimentales, las corrientes de referencia en el plano $(x - y)$ se establecen a cero ($i^*_{xs} = i^*_{ys} = 0$). La frecuencia de muestreo para MPCC-FSF es de 8 kHz. Los resultados obtenidos mediante MPCC-FSF son comparados con la estrategia MPCC clásica operando a 8 kHz y 16 kHz, respectivamente. Estas pruebas han sido incluidas con el fin de exponer una comparación justa entre MPCC-FSF y el MPCC clásico y mostrar el rendimiento de ambas estrategias, ya que la frecuencia de conmutación en MPCC-FSF es igual a la frecuencia de muestreo, mientras que en el MPCC clásico la frecuencia de conmutación es menor a la frecuencia de muestreo. Bajo condiciones de régimen permanente se han considerado dos puntos de operación para la velocidad mecánica, 500 rpm y 1000 rpm, respectivamente.

Los resultados obtenidos mediante la comparación de MPCC-FSF y el MPCC clásico para diferentes velocidades y frecuencias de muestreo, respecto al MSE en los planos $(\alpha - \beta)$-$(x - y)$ y THD en el plano $(\alpha - \beta)$, se muestran la **Tabla 3.3**.

Los resultados muestran que MPCC-FSF presenta un buen rendimiento en términos de seguimiento de corriente en el plano $(\alpha - \beta)$ y reducidas corrientes en el plano $(x - y)$ en comparación con el MPCC clásico a 8 kHz. Sin embargo, las figuras de mérito del

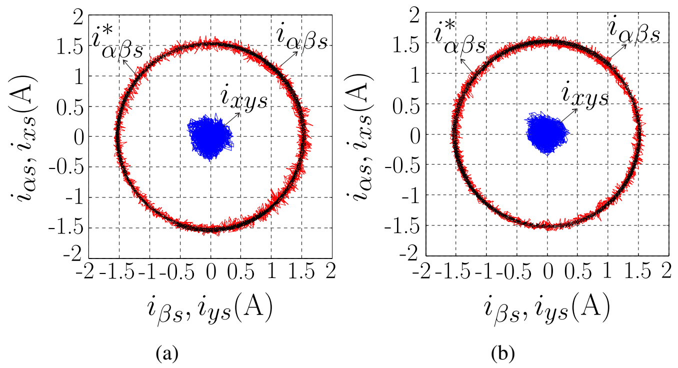

Figura 3.7 Resultados experimentales de las corrientes del estátor en los planos $(\alpha - \beta)$ y $(x - y)$ a 8 kHz de frecuencia de muestreo y 500 rpm de velocidad mecánica, considerando: (**a**) $\lambda_{xy} = 0.05$; (**b**) $\lambda_{xy} = 0.1$.

MPCC clásico presentan una ligera mejora cuando se opera a 16 kHz pero sigue siendo insuficiente en comparación a MPCC-FSF.

En la **Figura 3.7** se presenta las trayectorias de las corrientes del estátor en los planos $(\alpha - \beta)$ y $(x - y)$, considerando dos valores diferentes para λ_{xy}. En la **Figura 3.7** (a) se

Tabla 3.3 Prueba de rendimiento experimental de las corrientes del estátor $(\alpha - \beta)$, $(x - y)$, MSE (A), THD (%) entre el MPCC clásico y MPCC-FSF a diferentes velocidades (rpm).

$f_s =$ 8 kHz para el MPCC clásico						
ω_m^*	MSE$_\alpha$	MSE$_\beta$	MSE$_x$	MSE$_y$	THD$_\alpha$	THD$_\beta$
500	0.140	0.130	0.821	0.822	8.30	8.40
1000	0.147	0.138	0.953	0.934	7.40	7.30
$f_s =$ 16 kHz para el MPCC clásico						
ω_m^*	MSE$_\alpha$	MSE$_\beta$	MSE$_x$	MSE$_y$	THD$_\alpha$	THD$_\beta$
500	0.073	0.072	0.491	0.483	8.40	8.30
1000	0.084	0.082	0.538	0.534	7.50	7.40
$f_s =$ 8 kHz para el MPCC-FSF						
ω_m^*	MSE$_\alpha$	MSE$_\beta$	MSE$_x$	MSE$_y$	THD$_\alpha$	THD$_\beta$
500	0.042	0.045	0.135	0.130	4.89	5.08
1000	0.069	0.068	0.197	0.204	4.69	4.78

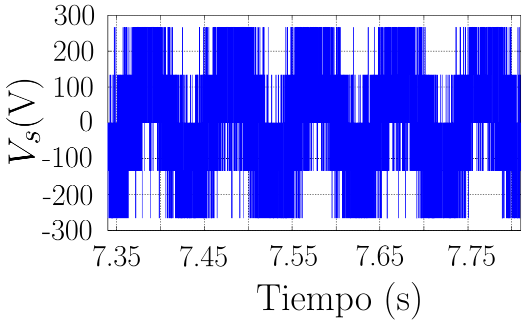

Figura 3.8 Patrón de conmutación del convertidor de potencia para MPCC-FSF a 8 kHz de frecuencia de muestreo y 500 rpm de velocidad mecánica.

ha considerado λ_{xy} = 0.05, mientras que en la **Figura 3.7** (b) λ_{xy} = 0.1. Las pruebas se han realizado a 500 rpm con una frecuencia de muestreo de 8 kHz. De acuerdo a estos resultados se puede notar que los componentes de corriente en el plano $(x - y)$ disminuyen cuando se aumenta el factor de peso, lo que significa que la selección de este parámetro tiene una fuerte influencia en el comportamiento del sistema cuando se utilizan técnicas de modulación en el MPCC. Además, el seguimiento de corriente en el plano $(\alpha - \beta)$ tiene un rendimiento ligeramente mejor considerando λ_{xy} = 0.1.

Adicionalmente, se ha incluido la gráfica de tensión del convertidor de potencia, como se muestra en la **Figura 3.8**, con el fin de mostrar el patrón de conmutación de la estrategia propuesta.

Por otro lado, las pruebas experimentales en régimen transitorio para la estrategia MPCC-FSF se han realizado mediante un escalón de velocidad en el eje q, como se muestra en la **Figura 3.9**. La respuesta transitoria del sistema ha sido verificada por medio de una inversión de giro de la velocidad mecánica (test de reversa) desde 500 rpm a -500 rpm a 8 kHz de muestreo con diferentes valores de λ_{xy}. En ese sentido, ambas pruebas reportan rápidas respuestas dinámicas considerando el sobrepico y el tiempo de establecimiento. La **Figura 3.9** (a) muestra la respuesta transitoria para λ_{xy} = 0.05, donde el sobrepico y el tiempo de establecimiento fueron de, 6.14% y 6 ms, respectivamente. En la segunda prueba, se ha considerado λ_{xy} = 0.1, y se obtuvieron valores de 4.85% y 6.12 ms para el sobrepico y tiempo de establecimiento, como se muestra en la **Figura 3.9** (b). Por lo tanto, la estrategia MPCC-FSF presenta un buen rendimiento dinámico bajo el criterio de análisis transitorio del 5%.

Finalmente, se ha realizado una prueba comparativa de respuesta transitoria de velocidad de 1500 rpm a 200 rpm entre la estrategia MPCC-FSF a 8 kHz y el MPCC clásico a 16 kHz de forma que la comparación sea justa, ya que el MPCC clásico presenta mejor

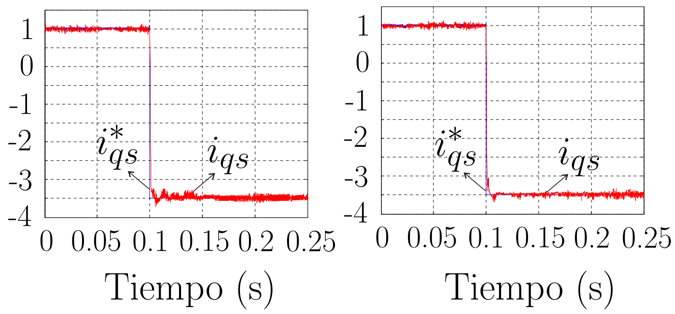

(a) (b)

Figura 3.9 Prueba experimental transitoria de las corrientes del estátor en el eje q para un test de reversa de 500 rpm a -500 rpm a 8 kHz de frecuencia de muestreo, considerando: (**a**) λ_{xy} = 0.05; (**b**) λ_{xy} = 0.1.

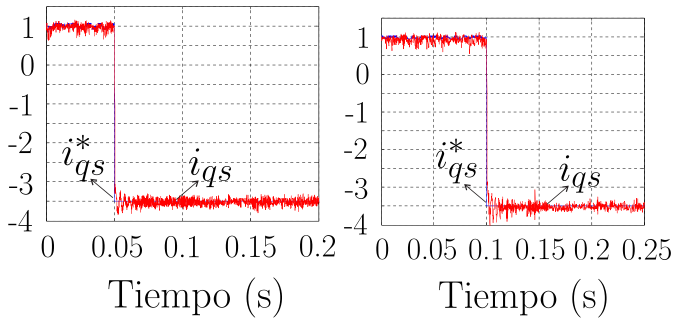

(a) (b)

Figura 3.10 Prueba experimental transitoria de las corrientes del estátor en el eje q para un step de velocidad de 1500 rpm a 200 rpm a 16 kHz y 8 kHz de frecuencia de muestreo, respectivamente: (**a**) MPCC clásico; (**b**) MPCC-FSF.

comportamiento a mayor frecuencia. Los resultados se presentan en la **Figura 3.10** (a) para el MPCC clásico y en la **Figura 3.10** (b) para la propuesta MPCC-FSF, mostrando rendimiento similares.

3.4.2 Validación del Artículo 2

Para la validación del Artículo 2, el cual surge mediante la combinación de las estrategias MPCC-FSF y MPCC-VV, se ha utilizado una IM de seis fases con una mayor potencia en comparación al utilizado en la validación del Artículo 1. Los parámetros eléctricos de la IM de seis fases fueron obtenidos mediante los mismos métodos referenciados en el Artículo 1, los cuales son listados en la **Tabla 3.4**.

El banco de pruebas experimental mostrado en la **Figura 3.11** está compuesto por una IM asimétrica de seis fases de 15 kW también alimentado por dos convertidores de potencia del tipo 2L-VSI cuya alimentación se obtiene de la red eléctrica y está regulada por medio de un transformador para proporcionar la tensión V_{dc} mediante un rectificador de diodos trifásico, obteniéndose un valor DC de 325 V. Los convertidores de potencia son controlados mediante un DSP (TMS320F28335 de Texas Instruments) con un entorno de desarrollo MCK28335 de Technosoft. Los resultados adquiridos son posteriormente procesados utilizando un script desarrollado en MATLAB R2014a.

Las mediciones de corriente se obtienen a través de sensores LA 55-P s con un ancho de banda de frecuencia de DC hasta 200 kHz para luego ser convertidas a valores digitales mediante un conversor A/D de 16 bits. El ángulo del rotor es medido por medio de un encoder incremental de 10000 rpm. Además, para las pruebas se utiliza una pastilla de freno mecánica fija como carga mecánica.

El valor del factor de peso utilizado para las pruebas fue, λ_{xy} = 0.01. Los valores de $\hat{Q}_w = 0.0022$ y $\hat{R}_v = 0.0022$ corresponden al ruido de proceso y medición, respectivamente, empleados en el modelo predictivo. Tanto λ_{xy}, $\hat{Q}_w$ y $\hat{R}_v$ fueron obtenidos de la misma manera en que fue descrita en el Artículo 1.

La técnica de modulación propuesta en el Articulo 2 es sometida a diferentes pruebas, las cuales incluyen el análisis en régimen permanente y en régimen transitorio así como condición de velocidad nominal y análisis de robustez, con el propósito de analizar su rendimiento en comparación con otras estrategias, tales como el MPCC clásico, MPCC-FSF y MPCC-VV. En ese sentido, los resultados obtenidos son analizados mediante las figuras de mérito del MSE y THD.

Primeramente, para el análisis en régimen permanente las corrientes de referencia en el plano $(x - y)$ son fijadas a cero, ($i_{xs}^* = i_{ys}^* = 0$), y la corriente de referencia en el

Tabla 3.4 Parámetros Eléctricos y Mecánicos de la IM de Seis Fases (LSPyC).

Parámetro	Valor	Parámetro	Valor
R_r	0.63 Ω	L_s	206.2 mH
R_s	0.62 Ω	P	3
L_{ls}	6.4 mH	P_w	15 kW
L_{lr}	3.5 mH	J_m	0.27 kg.m^2
L_m	66.6 mH	B_m	0.012 kg.m^2/s
L_r	203.3 mH	ω_{r-nom}	1000 rpm

Figura 3.11 Banco de pruebas experimental compuesto por dos 2L-VSI, unidad de control DSP, IM de seis fases y carga mecánica (LSPyC).

eje d (i_{ds}^*) fue ajustada a 1.5 A. La frecuencia de muestreo utilizada para las pruebas fue de 10 kHz para MPCC clásico y MPCC-FSF, y de 5 kHz para MPCC-VV y la técnica propuesta T3. En ese sentido, se han considerado 5 puntos de operación para la velocidad mecánica: 100 rpm, 200 rpm, 300 rpm, 400 rpm y 500 rpm.

La **Tabla 3.5** muestra los resultados experimentales del MPCC clásico obtenidos para diferentes velocidades mecánicas a una frecuencia de muestreo de 10 kHz, respecto al MSE de las corrientes del estátor en los planos $(\alpha - \beta)$ y $(x - y)$ y THD en el plano $(\alpha - \beta)$. Los resultados muestran un rendimiento aceptable para el MPCC clásico en términos de seguimiento de corriente en el plano $(\alpha - \beta)$ y THD de la corriente del estátor en todos los puntos de operación. Sin embargo, la reducción de los componentes de corriente en el plano $(x - y)$ es insuficiente.

En la **Tabla 3.6** se presenta el rendimiento del MPCC-FSF, el cual mejora notablemente la reducción de las corrientes en el plano $(x - y)$. En términos de THD de la corriente del estátor presenta un comportamiento similar al MPCC clásico a bajas velocidades con una tendencia de mejora a velocidades más elevadas. Sin embargo, su desempeño se ve afectado en términos de seguimiento de corriente en el plano $(\alpha-\beta)$ a velocidades medias.

Por otro lado, la **Tabla 3.7** muestra el resultado del MPCC-VV el cual presenta un rendimiento mucho mejor en términos seguimiento de corriente en el plano $(\alpha-\beta)$ en todos los puntos de operación en comparación con las otras técnicas, con un comportamiento similar al MPCC-FSF en cuanto a la reducción de corriente en el plano $(x-y)$, mientras que el THD de la corriente del estátor presenta un pequeño incremento con el aumento de la velocidad. La **Tabla 3.8** expone el rendimiento de la estrategia propuesta T3 en términos de seguimiento de corriente y THD de la corriente del estátor. Se puede notar que T3 mejora considerablemente la reducción de los componentes de corriente en el plano $(x-y)$ en todos los puntos de operación en comparación con las demás técnicas. T3 presenta un buen rendimiento en términos de seguimiento de corriente en el plano $(\alpha-\beta)$ en comparación con el MPCC-clásico y el MPCC-FSF y muestra un comportamiento similar al MPCC-VV en cuanto a THD.

Tabla 3.5 Corrientes del estátor en los planos $(\alpha-\beta)$ y $(x-y)$, considerando MSE (A) y THD (%) para el MPCC clásico a diferentes velocidades de rotor (rpm).

MPCC clásico a f_s = 10 kHz					
ω_m^*	MSE$_\alpha$	MSE$_\beta$	MSE$_x$	MSE$_y$	THD$_\alpha$
100	3.25	2.65	14.14	13.04	18.68
200	3.23	2.63	12.85	14.38	19.13
300	3.32	2.89	15.05	14.45	15.56
400	3.33	2.95	14.26	14.22	18.09
500	3.57	3.39	15.12	15.68	17.49

Tabla 3.6 Corrientes del estátor en los planos $(\alpha-\beta)$ y $(x-y)$, considerando MSE (A) y THD (%) para la estrategia MPCC-FSF a diferentes velocidades de rotor (rpm).

MPCC-FSF a f_s = 10 kHz					
ω_m^*	MSE$_\alpha$	MSE$_\beta$	MSE$_x$	MSE$_y$	THD$_\alpha$
100	3.23	2.89	2.19	2.51	13.99
200	4.59	4.42	2.23	2.28	11.85
300	5.01	5.41	2.55	2.76	10.18
400	5.16	5.51	2.46	2.98	10.56
500	5.30	5.23	2.36	2.84	10.09

La **Figura 3.12** (a) y la **Figura 3.12** (b) presentan el rendimiento de las corrientes del estátor en los planos $(\alpha - \beta)$ y $(x - y)$ para el MPCC clásico y el MPCC-FSF. Las operaciones fueron analizadas bajo condiciones de carga a 200 rpm de velocidad y 10 kHz de frecuencia de muestreo. Se puede notar que el MPCC-FSF muestra una gran reducción de corriente en el plano $(x - y)$ ($|e_{xy}| < 7$A) respecto al MPCC clásico ($|e_{xy}| < 27$A). Pero, en cuanto a seguimiento de corriente en el plano $(\alpha - \beta)$ su comportamiento es limitado para referencias de velocidad más elevadas. Es importante mencionar que, primeramente, estas pruebas fueron realizadas a 5 kHz de muestreo presentando un buen comportamiento a velocidades bajas, sin embargo, el rendimiento del sistema se vió afectado con el incremento de la velocidad dificultando su análisis. Esto muestra la relación que existe entre la frecuencia de muestreo y la velocidad del rotor.

Por otro lado, el rendimiento de las corrientes del estátor en los planos $(\alpha - \beta)$ y $(x - y)$ para el MPCC-VV y la estrategia T3 se muestran en la **Figura 3.13** (a) y la **Figura 3.13** (b), respectivamente. Para estas pruebas fueron consideradas una velocidad de 200 rpm y 5 kHz de frecuencia de muestreo bajo las mismas condiciones de carga mecánica que la prueba anterior. En términos de seguimiento de corriente en el plano

Tabla 3.7 Corrientes del estátor en los planos $(\alpha - \beta)$ y $(x - y)$, considerando MSE (A) y THD (%) para la estrategia MPCC-VV a diferentes velocidades de rotor (rpm).

MPCC-VV a f_s = 5 kHz					
ω_m^*	MSE$_\alpha$	MSE$_\beta$	MSE$_x$	MSE$_y$	THD$_\alpha$
100	1.28	1.10	2.68	2.90	9.42
200	1.37	1.25	2.69	2.91	10.86
300	1.51	1.32	2.65	2.95	12.43
400	1.66	1.51	2.66	2.87	14.02
500	1.88	1.75	2.58	2.93	17.07

Tabla 3.8 Corrientes del estátor en los planos $(\alpha - \beta)$ y $(x - y)$, considerando MSE (A) y THD (%) para la estrategia T3 a diferentes velocidades de rotor (rpm).

Estrategia T3 a f_s = 5 kHz					
ω_m^*	MSE$_\alpha$	MSE$_\beta$	MSE$_x$	MSE$_y$	THD$_\alpha$
100	2.34	2.07	1.84	1.90	10.11
200	2.48	2.25	1.76	1.74	10.89
300	2.49	2.29	1.95	1.91	12.06
400	2.97	2.76	1.92	1.89	12.04
500	3.01	2.90	2.02	1.91	16.14

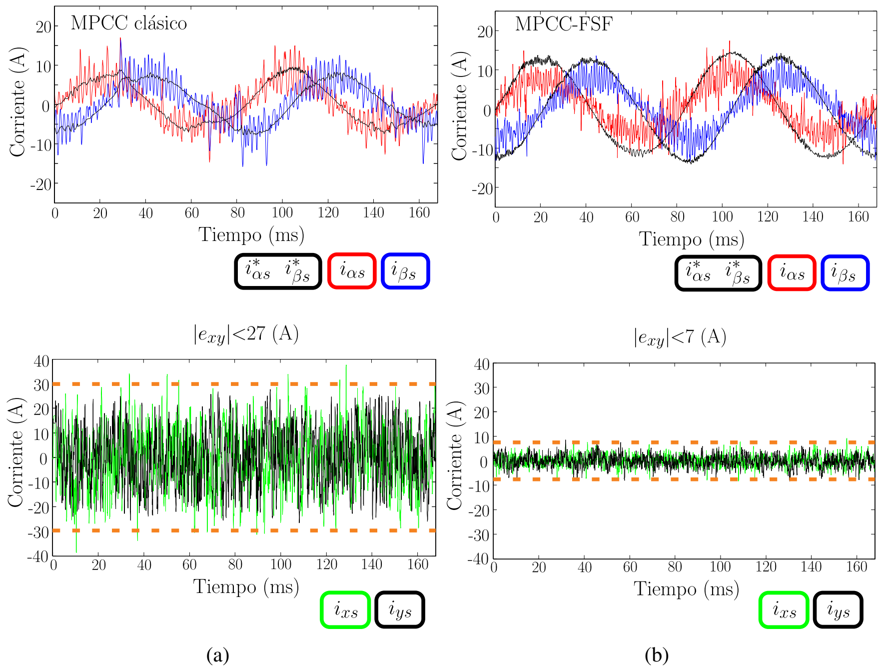

Figura 3.12 Rendimiento de las corrientes del estátor en los planos $(\alpha-\beta)$ y $(x-y)$ para una velocidad de rotor de 200 rpm a 10 kHz de frecuencia de muestreo: (a) MPCC clásico; (b) MPCC-FSF.

$(\alpha-\beta)$ el MPCC-VV presenta una ligera mejora respecto a T3. En cuanto a reducción de corriente en el plano $(x-y)$, la estrategia T3 presenta el mejor rendimiento ($|e_{xy}| < 6$A) respecto al MPCC clásico, MPCC-FSF y al MPCC-VV.

Además, se han incluido las corrientes de fase (i_a e i_d) de las estrategias moduladas para verificar el rendimiento de los mismos en términos de THD operando a 200 rpm. Las estrategias MPCC-VV y T3 presentan un contenido de armónicos similar en sus corrientes de fase, con un rizado menor en comparación al MPCC-FSF, debido al uso de vectores virtuales (**Figura 3.14** (b) y **Figura 3.14** (c)). Sin embargo, el MPCC-FSF presenta un contenido de armónicos ligeramente mayor, lo que se traduce en un aumento en el rizado de la corriente fase, como se muestra en la **Figura 3.14** (a).

Finalmente, la **Tabla 3.9** presenta el rendimiento de la estrategia T3 en comparación con el MPCC clásico, MPCC-FSF y el MPCC-VV, donde los valores positivos (+) y negativos (-) significan mejora y deterioro, respectivamente.

Para el régimen dinámico, se ha considerado una prueba de escalón en la velocidad del rotor de 200 rpm a -200 rpm. La **Figura 3.15** y la **Figura 3.16** presentan pruebas transito-

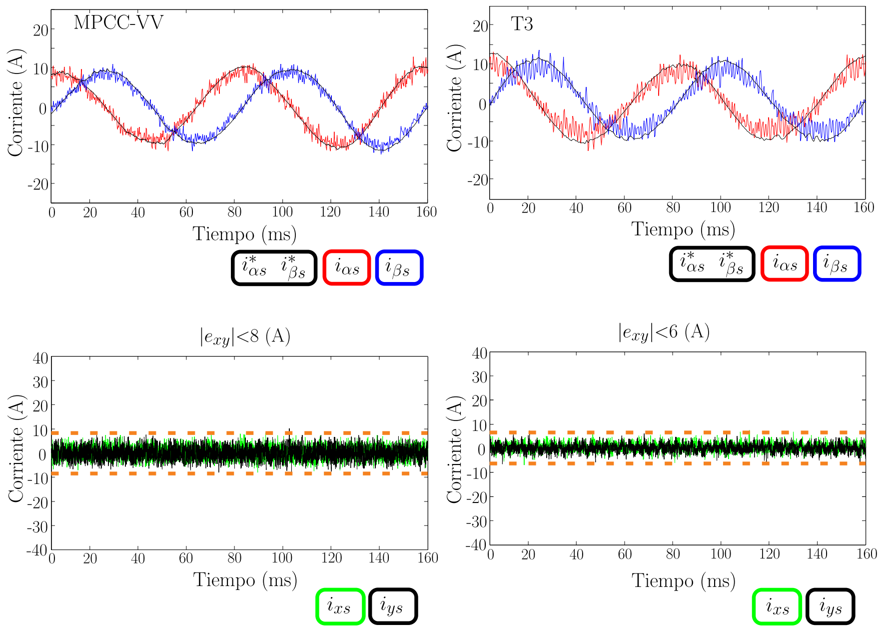

(a) (b)

Figura 3.13 Rendimiento de las corrientes del estátor en los planos ($\alpha - \beta$) y ($x - y$) para una velocidad de rotor de 200 rpm a 5 kHz de frecuencia de muestreo: (a) MPCC-VV; (b) T3.

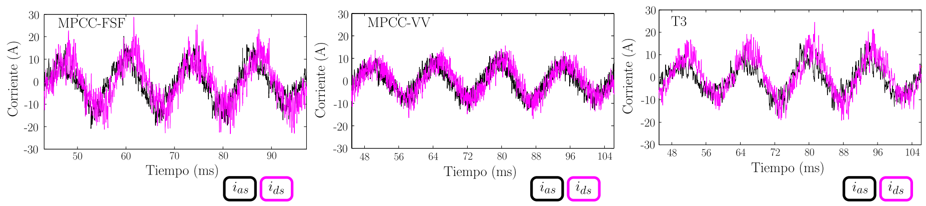

(a) (b) (c)

Figura 3.14 Corrientes de fase en régimen permanente de las técnicas con modulación a 200 rpm; (**a**) MPCC-FSF; (**b**) MPCC-VV; (**c**) Estrategia T3.

rias basada en el seguimiento de corriente en el eje q, los cuales revelan el comportamiento dinámico del MPCC clásico (**Figura 3.15** (a)), MPCC-FSF (**Figura 3.15** (b)), MPCC-VV (**Figura 3.16** (a)) y de la estrategia propuesta (**Figura 3.16** (b)) para un cambio en la corriente q (i^*_{qs}). El rendimiento dinámico es obtenido mediante una condición de reversa de la velocidad del rotor (ω^*_m). El sobrepico y tiempo de establecimiento de todas las técnicas son muy similares, en cuanto a la estrategia propuesta es aproximadamente 12.5% y 0.5 ms, respectivamente.

La **Figura 3.17** presenta el rendimiento de las corrientes del estátor por medio de una representación polar en los planos $(\alpha - \beta)$ y $(x - y)$ para el MPCC clásico, MPCC-FSF y la estrategia propuesta durante el proceso de arranque a 500 rpm. Las pruebas fueron analizadas bajo condiciones de carga. Las figuras muestran que los componentes de corriente en el plano $(x - y)$ son mas reducidos para la estrategia propuesta T3 respecto al MPCC clásico y MPCC-FSF. En cambio el MPCC-VV presenta un mejor desempeño en términos de seguimiento de corriente en el plano $(\alpha - \beta)$, como se ha visto en las pruebas anteriores.

Por otro lado, se ha considerado un análisis de robustez para todas las técnicas. El estudio de robustez consiste en la comparación del rendimiento del controlador al valor nominal de L_m y con una variación del 25% de su valor nominal, ya que L_m es el parámetro más sensible en las IMs [57, 58]. Este estudio se realiza considerando el efecto de la saturación magnética de la IM de seis fases, donde el valor de L_m normalmente varía

Tabla 3.9 Análisis de mejora (%) de la Estrategia T3 sobre las técnicas MPCC clásico, MPCC-FSF y MPCC-VV a diferentes velocidades de rotor (rpm).

Estrategia T3 sobre MPCC clásico			
ω_m^*	MSE$_{\alpha\beta}$	MSE$_{xy}$	THD$_\alpha$
100	+25.25	+86.23	+45.88
200	+19.28	+87.15	+43.07
300	+23.03	+86.92	+22.49
400	+8.76	+86.62	+33.44
500	+15.09	+87.24	+7.72
Estrategia T3 sobre MPCC-FSF			
100	+27.94	+20.43	+27.73
200	+47.50	+22.40	+8.10
300	+54.13	+27.31	-18.47
400	+46.30	+29.96	-14.02
500	+43.87	+24.42	-59.96
Estrategia T3 sobre MPCC-VV			
100	-85.29	+32.98	-7.32
200	-80.53	+37.50	-0.27
300	-68.90	+31.07	+2.98
400	-80.76	+31.10	+14.12
500	-62.81	+28.68	+5.45

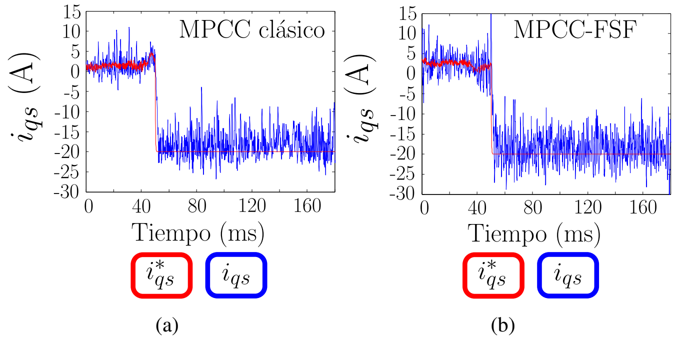

Figura 3.15 Respuesta transitoria de la corriente del estátor en el eje q para un cambio de velocidad de 200 rpm a -200 rpm a una frecuencia de muestreo de 10 kHz: (a) MPCC clásico; (b) MPCC-FSF.

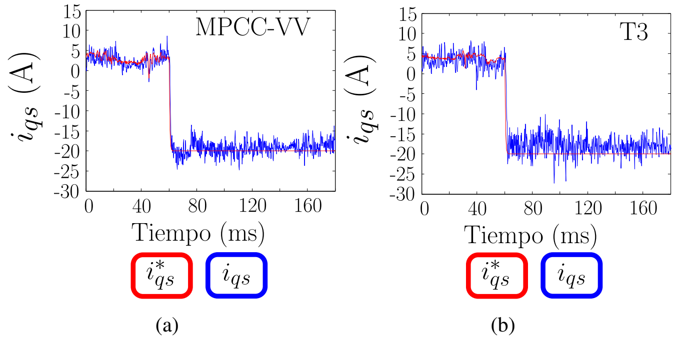

Figura 3.16 Respuesta transitoria de la corriente del estátor en el eje q para un cambio de velocidad de 200 rpm a -200 rpm a una frecuencia de muestreo de 5 kHz: (a) MPCC-VV; (b) Estrategia propuesta.

en aproximadamente esa proporción. La **Tabla 3.10** muestra el desempeño del control con un cambio de L_m del 25% del valor nominal para analizar la sensibilidad del parámetro de robustez del control. Los resultados revelan que las cuatro técnicas presentan una robustez considerable ya que las figuras de mérito no varían mucho en comparación con el valor nominal de L_m. En particular, la estrategia propuesta T3 presenta resultados ligeramente mejores en términos de reducción de corriente en el plano $(x - y)$ y THD, pero en general todos los valores permanecen en un rango similar.

Finalmente, para realizar una operación de alta velocidad para la estrategia propuesta, la tensión V_{dc} es aumentada a 575 V para operar con el flujo magnético nominal. El resultado de esta prueba se muestran en la **Figura 3.18**. El rendimiento del sistema disminuye pero mantiene su funcionamiento, el rizado en la corriente del estátor en el

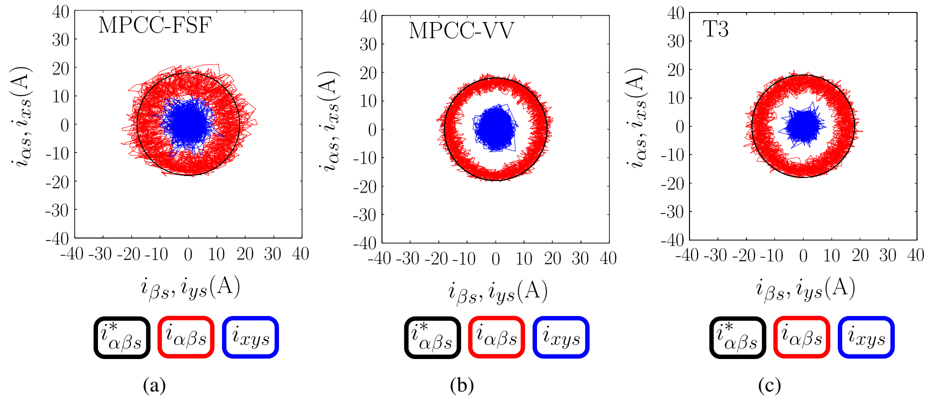

Figura 3.17 Corrientes del estátor en los planos $(\alpha-\beta)$ y $(x-y)$ para una velocidad de arranque de 500 rpm: (**a**) MPCC-FSF; (**b**) MPCC-VV; (**c**) T3.

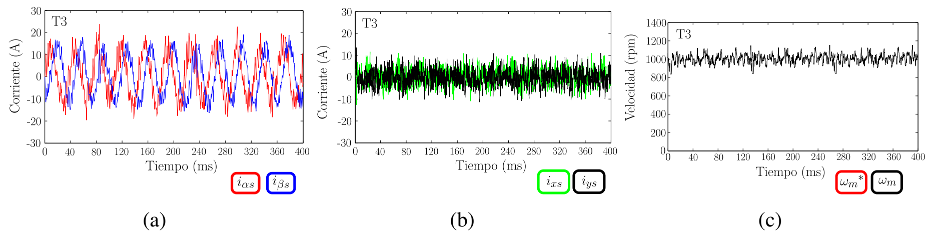

Figura 3.18 Rendimiento de la estrategia propuesta operando a condición de velocidad nominal: (a) Corriente del estátor en el plano $(\alpha-\beta)$; (b) Corriente del estátor en el plano $(x-y)$; (c) Velocidad mecánica (ω_m).

plano $(\alpha-\beta)$ también aumenta a medida que aumenta la velocidad del rotor. Sin embargo, los componentes de corriente en el plano $(x-y)$ se mantienen reducidos en condición de velocidad nominal.

Tabla 3.10 Análisis de las corrientes del estátor bajo variación de L_m.

f_s = 10 kHz[1],	f_s = 5 kHz[2]		y	ω_m^* = 400 rpm	
Techniques	MSE$_\alpha$	MSE$_\beta$	MSE$_x$	MSE$_y$	THD$_\alpha$
MPCC clásico[1]	3.12	2.93	13.92	14.91	20.83
MPCC-FSF[1]	4.46	2.70	2.56	2.59	12.82
MPCC-VV[2]	2.12	1.73	2.83	3.08	14.48
Estrategia T3[2]	3.13	2.52	1.79	1.73	10.27

3.5 Conclusiones

Tanto en el Artículo 1 como en el Artículo 2 se han expuestos y discutidos técnicas de control predictivo basado en el modelo para accionamientos de seis fases de diferentes potencias (2 kW y 15 kw, respectivamente) enfocados en estrategias de modulación para la regulación de la corriente. En el Artículo 1 se propuso una técnica de modulación basada en un cierto patrón de conmutación con el fin de reducir los componentes de corriente en el plano $(x - y)$ utilizando solamente los vectores exteriores del plano $(\alpha - \beta)$, y esto a su vez ha permitido reducir el costo computacional en comparación con el MPCC clásico. El desempeño de esta estrategia ha sido examinado por medio de simulaciones y pruebas experimentales bajo diferentes condiciones de régimen permanente y transitorio, tales como distintos puntos de operación para la velocidad mecánica del rotor, frecuencia de muestreo y factores de peso para las corrientes del estátor en el plano $(x - y)$. En términos de seguimiento de corriente en el plano $(\alpha - \beta)$, la técnica T3 presenta un mejor rendimiento a bajas velocidades y notable reducción de corriente en el plano $(x - y)$ cuando se varía el factor de peso respecto al MPCC clásico. Los resultados obtenidos también han demostrado un buen rendimiento en términos de evolución de corriente en régimen transitorio principalmente si se tiene en cuenta las características en el dominio del tiempo tales como sobrepico y tiempo de establecimiento.

Por otro lado, en el Artículo 2 se ha propuesto una técnica de modulación basada en vectores virtuales utilizando las características de la técnica propuesta en el Artículo 1. Esta estrategia ha sido desarrollada para mejorar el seguimiento de corriente en el plano $(\alpha - \beta)$ y producir reducidas componentes de corriente en el plano $(x - y)$ utilizando vectores de tensión largos, mediano-largos y nulo. En ese sentido, se han realizado pruebas experimentales con el propósito de mostrar la eficacia de la técnica propuesta en comparación con las otras estrategias, tales como el MPCC clásico, MPCC-FSF y el MPCC-VV bajo distintas condiciones de operación tanto en régimen transitorio como en régimen permanente. Las figuras de mérito del MPCC-VV y MPCC-FSF muestran que estas estrategias son una buena alternativa en términos de reducción de corriente en el plano $(x - y)$ en comparación con el MPCC clásico, ya que ambas presentan una notable reducción de corriente en dicho plano. Sin embargo, el MPCC-VV presenta un mejor rendimiento en términos de seguimiento de corriente en el plano $(\alpha - \beta)$ que el MPCC-FSF. Por otro lado, la técnica propuesta ha demostrado ser la mejor alternativa en términos de reducción de corriente en el plano $(x - y)$, sin embargo, en términos de seguimiento de corriente en el plano $(\alpha - \beta)$, el MPCC-VV presenta resultados ligeramente mejores que la estrategia propuesta seguido de las otras estrategias. En régimen transitorio, el resultado obtenido de los cuatro controladores han mostrado un buen comportamiento dinámico.

Además, se ha realizado una prueba de robustez donde los controladores presentaron un buen rendimiento ante la variación de L_m.

CAPÍTULO 4

CONCLUSIONES Y TRABAJOS FUTUROS

4.1 Conclusiones

La presente Tesis Doctoral ha abordado el estudio de esquemas de control predictivo basado en el modelo aplicado a máquinas de inducción de seis fases utilizando estrategias de modulación para la regulación de las corrientes en el plano $(\alpha - \beta)$ y $(x - y)$. Las principales contribuciones y conclusiones se resumen a continuación:

- Se analizó la técnica de modulación basada en un cierto patrón de conmutación (MPCC-FSF) aplicado al control predictivo de corriente proporcionando una frecuencia de conmutación fija. En ese sentido, se han obtenido varios resultados de eficiencia de la técnica de modulación propuesta para el control corriente. Dichos resultados fueron comparados y analizados bajo las figuras de mérito tales como el MSE y la THD. Los resultados teóricos y experimentales son congruentes demostrando ser una propuesta viable en comparación al MPCC clásico en términos de seguimiento y reducción de corriente en los planos $(\alpha-\beta)$ y $(x-y)$, respectivamente.

- Se estudió la modulación basada vectores virtuales (MPCC-VV) aplicado al control predictivo de corriente con el propósito de minimizar los componentes de corriente de estátor en el plano $(x - y)$. Los resultados fueron comparados con el control predictivo de corriente convencional. En este contexto, la implementación de vectores virtuales, además de reducir el costo computacional, demuestra una notable reducción de la corriente de estátor en el plano $(x - y)$.

- Se propuso una técnica de control basada en la combinación de las estrategias MPCC-FSF y MPCC-VV para la regulación de corriente en los planos $(\alpha - \beta)$ y $(x - y)$. Se verificó el comportamiento de la técnica propuesta en comparación con las demás técnicas por medio de pruebas experimentales bajo diferentes condiciones de operación. El mismo resultó ser la mejor alternativa en términos de reducción de corriente en el plano $(x - y)$.

- Los resultados obtenidos han dado como resultado la publicación de varios artículos en revistas y conferencias internacionales. La **Tabla 4.1** contiene las actividades y contribuciones realizadas durante el desarrollo de la presente Tesis.

Tabla 4.1 Resumen de los principales aportes de la Tesis Doctoral.

Producción/Actividad	Número
Artículos de revista internacional Q1 como autor principal	2
Artículos de revista internacional Q1 como coautor	4
Artículos de conferencia internacional como autor principal	2
Artículos de conferencia internacional como coautor	2
Participación en proyectos de investigación y desarrollo	1
Revisión de artículos científicos	9

4.2 Trabajos Futuros

El uso de nuevas técnicas de modulación aplicado a los accionamientos multifásicos para el control predictivo de corriente es un tema de investigación que ha sido abordado recientemente y todavía no ha llegado a su etapa de madurez. Por tal motivo existen varios tópicos que pueden profundizarse dentro de esta línea, entre los que se citan los más relevantes:

- Extender el estudio a otras máquinas multifásicas, con distintos números de fases, y distinto tipo de devanado.
- Validar experimentalmente las estrategias de modulación propuestas en aplicaciones industriales.
- Extender el estudio y análisis de accionamientos eléctricos multifásicos en situación de post-falta para máquinas de imanes permanentes y máquinas de inducción.
- Extender las estrategias de modulación presentadas al control de velocidad sin sensores en los accionamientos eléctricos multifásicos.

REFERENCIAS

[1] E. Levi, “Multiphase electric machines for variable-speed applications,” *IEEE Transactions on Industrial Electronics*, vol. 55, no. 5, pp. 1893–1909, 2008.

[2] R. Bojoi, S. Rubino, A. Tenconi, and S. Vaschetto, “Multiphase electrical machines and drives: A viable solution for energy generation and transportation electrification,” in *Proc. EPE*, 2016, pp. 632–639.

[3] H. A. Toliyat, T. A. Lipo, and J. C. White, “Analysis of a concentrated winding induction machine for adjustable speed drive applications. I. Motor analysis,” *IEEE Transactions on Energy conversion*, vol. 6, no. 4, pp. 679–683, 1991.

[4] F. Barrero and M. J. Duran, “Recent advances in the design, modeling, and control of multiphase machines—Part I,” *IEEE Transactions on Industrial Electronics*, vol. 63, no. 1, pp. 449–458, 2016.

[5] M. Slunjski, O. Dordevic, M. Jones, and E. Levi, “Symmetrical/asymmetrical winding reconfiguration in multiphase machines,” *IEEE Access*, vol. 8, pp. 12 835–12 844, 2020.

[6] L. A. Pereira, C. C. Scharlau, L. F. A. Pereira, and J. F. Haffner, “General model of a five-phase induction machine allowing for harmonics in the air gap field,” *IEEE Transactions on Energy Conversion*, vol. 21, no. 4, pp. 891–899, 2006.

[7] M. J. Duran and F. Barrero, “Recent advances in the design, modeling, and control of multiphase machines—Part II,” *IEEE Transactions on Industrial Electronics*, vol. 63, no. 1, pp. 459–468, 2016.

[8] E. Levi, R. Bojoi, F. Profumo, H. Toliyat, and S. Williamson, “Multiphase induction motor drives–a technology status review,” *IET Electric Power Applications*, vol. 1, no. 4, pp. 489–516, 2007.

[9] L. Comparatore, R. Gregor, J. Rodas, J. Pacher, A. Renault, and M. Rivera, “Model based predictive current control for a three-phase cascade H-bridge multilevel STATCOM operating at fixed switching frequency,” in *Proc. PEDG*, 2017, pp. 1–6.

[10] F. Gavilan, D. Caballero, S. Toledo, E. Maqueda, R. Gregor, J. Rodas, M. Rivera, and I. Araujo-Vargas, “Predictive power control strategy for a grid-connected 2L-VSI with fixed switching frequency,” in *Proc. ROPEC*, 2016, pp. 1–6.

[11] F. Wang, Z. Zhang, X. Mei, J. Rodríguez, and R. Kennel, “Advanced control strategies of induction machine: Field oriented control, direct torque control and model predictive control,” *Energies*, vol. 11, no. 1, p. 120, 2018.

[12] M. Jones, S. N. Vukosavic, D. Dujic, and E. Levi, “A synchronous current control scheme for multiphase induction motor drives,” *IEEE Transactions on Energy Conversion*, vol. 24, no. 4, pp. 860–868, 2009.

[13] F. Barrero, M. R. Arahal, R. Gregor, S. Toral, and M. J. Durán, “A proof of concept study of predictive current control for VSI-driven asymmetrical dual three-phase AC machines,” *IEEE Transactions on Industrial Electronics*, vol. 56, no. 6, pp. 1937–1954, 2009.

[14] S. Kouro, M. A. Perez, J. Rodriguez, A. M. Llor, and H. A. Young, “Model predictive control: MPC’s role in the evolution of power electronics,” *IEEE Industrial Electronics Magazine*, vol. 9, no. 4, pp. 8–21, 2015.

[15] O. Gonzalez, M. Ayala, J. Rodas, R. Gregor, G. Rivas, and J. Doval-Gandoy, “Variable-speed control of a six-phase induction machine using predictive-fixed switching frequency current control techniques,” in *Proc. PEDG*, 2018, pp. 1–6.

[16] I. Gonzalez-Prieto, M. J. Duran, J. J. Aciego, C. Martin, and F. Barrero, “Model predictive control of six-phase induction motor drives using virtual voltage vectors,” *IEEE Transactions on Industrial Electronics*, vol. 65, no. 1, pp. 27–37, 2017.

[17] M. Ayala, J. Rodas, R. Gregor, J. Doval-Gandoy, O. Gonzalez, M. Saad, and M. Rivera, “Comparative study of predictive control strategies at fixed switching frequency for an asymmetrical six-phase induction motor drive,” in *Proc. IEMDC*, 2017, pp. 1–8.

[18] O. Gonzalez, M. Ayala, J. Doval-Gandoy, J. Rodas, R. Gregor, and M. Rivera, “Predictive-fixed switching current control strategy applied to six-phase induction machine,” *Energies*, vol. 12, no. 12, p. 2294, 2019.

[19] M. J. Duran, E. Levi, and F. Barrero, “Multiphase electric drives: Introduction,” *Wiley Encyclopedia of Electrical and Electronics Engineering*, pp. 1–26, 2017.

[20] Y. Zhao and T. A. Lipo, "Space vector PWM control of dual three-phase induction machine using vector space decomposition," *IEEE Transactions on Industry Applications*, vol. 31, no. 5, pp. 1100–1109, 1995.

[21] R. Bojoi, F. Farina, F. Profumo, and A. Tenconi, "Dual-three phase induction machine drives control—A survey," *IEEE Transactions on Industry Applications*, vol. 126, no. 4, pp. 420–429, 2006.

[22] E. Levi, "Power electronics and motor drives," *The Industrial Electronics Handbook*, 2016.

[23] Y. Hu, Z. Zhu, and M. Odavic, "Comparison of two-individual current control and vector space decomposition control for dual three-phase PMSM," *IEEE Transactions on Industry Applications*, vol. 53, no. 5, pp. 4483–4492, 2017.

[24] E. Levi, R. Bojoi, F. Profumo, H. Toliyat, and S. Williamson, "Multiphase induction motor drives–a technology status review," *IET Electric Power Applications*, vol. 1, no. 4, pp. 489–516, 2007.

[25] E. Levi, "Advances in converter control and innovative exploitation of additional degrees of freedom for multiphase machines," *IEEE Transactions on Industrial Electronics*, vol. 63, no. 1, pp. 433–448, 2015.

[26] Y. Zhao and T. A. Lipo, "Space vector PWM control of dual three-phase induction machine using vector space decomposition," *IEEE Transactions on Industry Applications*, vol. 31, no. 5, pp. 1100–1109, 1995.

[27] F. Betin, G.-A. Capolino, D. Casadei, B. Kawkabani, R. I. Bojoi, L. Harnefors, E. Levi, L. Parsa, and B. Fahimi, "Trends in electrical machines control: Samples for classical, sensorless, and fault-tolerant techniques," *IEEE Industrial Electronics Magazine*, vol. 8, no. 2, pp. 43–55, 2014.

[28] R. Kennel, J. Rodriguez, J. Espinoza, and M. Trincado, "High performance speed control methods for electrical machines: An assessment," in *Proc. ICIT*, 2010, pp. 1793–1799.

[29] L. Harnefors, S. E. Saarakkala, and M. Hinkkanen, "Speed control of electrical drives using classical control methods," *IEEE Transactions on Industry Applications*, vol. 49, no. 2, pp. 889–898, 2013.

[30] E. Levi, "Advances in converter control and innovative exploitation of additional degrees of freedom for multiphase machines," *IEEE Transactions on Industrial Electronics*, vol. 63, no. 1, pp. 433–448, 2016.

[31] C. Liu and Y. Luo, "Overview of advanced control strategies for electric machines," *Chinese Journal of Electrical Engineering*, vol. 3, no. 2, pp. 53–61, 2017.

[32] R. Bojoi, F. Farina, G. Griva, F. Profumo, and A. Tenconi, "Direct torque control for dual three-phase induction motor drives," *IEEE Transactions on Industry Applications*, vol. 41, no. 6, pp. 1627–1636, 2005.

[33] H. S. Che, M. J. Duran, E. Levi, M. Jones, W.-P. Hew, and N. A. Rahim, “Postfault operation of an asymmetrical six-phase induction machine with single and two isolated neutral points,” *IEEE Transactions on Power Electronics*, vol. 29, no. 10, pp. 5406–5416, 2013.

[34] I. Gonzalez-Prieto, M. J. Duran, F. Barrero, M. Bermudez, and H. Guzmán, “Impact of postfault flux adaptation on six-phase induction motor drives with parallel converters,” *IEEE Transactions on Power Electronics*, vol. 32, no. 1, pp. 515–528, 2016.

[35] M. J. Duran, I. Gonzalez-Prieto, N. Rios-Garcia, and F. Barrero, “A simple, fast, and robust open-phase fault detection technique for six-phase induction motor drives,” *IEEE Transactions on Power Electronics*, vol. 33, no. 1, pp. 547–557, 2017.

[36] G. K. Singh, K. Nam, and S. Lim, “A simple indirect field-oriented control scheme for multiphase induction machine,” *IEEE Transactions on Industrial Electronics*, vol. 52, no. 4, pp. 1177–1184, 2005.

[37] R. O. Lyra and T. A. Lipo, “Torque density improvement in a six-phase induction motor with third harmonic current injection,” *IEEE Transactions on Industry Applications*, vol. 38, no. 5, pp. 1351–1360, 2002.

[38] T. Geyer, *Model predictive control of high power converters and industrial drives*. John Wiley & Sons, 2016.

[39] S. Vazquez, J. Rodriguez, M. Rivera, L. G. Franquelo, and M. Norambuena, “Model predictive control for power converters and drives: Advances and trends,” *IEEE Transactions on Industrial Electronics*, vol. 64, no. 2, pp. 935–947, 2016.

[40] J. Rodriguez, M. P. Kazmierkowski, J. R. Espinoza, P. Zanchetta, H. Abu-Rub, H. A. Young, and C. A. Rojas, “State of the art of finite control set model predictive control in power electronics,” *IEEE Transactions on Industrial Informatics*, vol. 9, no. 2, pp. 1003–1016, 2013.

[41] C. S. Lim, E. Levi, M. Jones, N. A. Rahim, and W. P. Hew, “FCS-MPC-based current control of a five-phase induction motor and its comparison with PI-PWM control,” *IEEE Transactions on Industrial Electronics*, vol. 61, no. 1, pp. 149–163, 2014.

[42] P. F. Gonçalves, S. M. Cruz, and A. M. Mendes, “Comparison of model predictive control strategies for six-phase permanent magnet synchronous machines,” in *Proc. IECON*, 2018, pp. 5801–5806.

[43] J. Rodas, F. Barrero, M. R. Arahal, C. Martín, and R. Gregor, “Online estimation of rotor variables in predictive current controllers: a case study using five-phase induction machines,” *IEEE Transactions on Industrial Electronics*, vol. 63, no. 9, pp. 5348–5356, 2016.

[44] J. Rodas, C. Martín, M. R. Arahal, F. Barrero, and R. Gregor, “Influence of covariance-based ALS methods in the performance of predictive controllers with rotor current estimation,” *IEEE Transactions on Industrial Electronics*, vol. 64, no. 4, pp. 2602–2607, 2017.

[45] M. Arahal, F. Barrero, S. Toral, M. Duran, and R. Gregor, “Multi-phase current control using finite-state model-predictive control,” *Control Engineering Practice*, vol. 17, no. 5, pp. 579–587, 2009.

[46] J. Rodriguez and P. Cortes, *Predictive control of power converters and electrical drives*. John Wiley & Sons, 2012, vol. 40.

[47] M. Novak, T. Dragicevic, and F. Blaabjerg, “Weighting factor design based on Artificial Neural Network for Finite Set MPC operated 3L-NPC converter,” in *Proc. APEC*, 2019, pp. 77–82.

[48] B. Majmunović, T. Dragičević, and F. Blaabjerg, “Multi objective modulated model predictive control of stand-alone voltage source converters,” *IEEE Journal of Emerging and Selected Topics in Power Electronics*, vol. 8, no. 3, pp. 2559–2571, 2019.

[49] P. Cortés, S. Kouro, B. La Rocca, R. Vargas, J. Rodríguez, J. I. León, S. Vazquez, and L. G. Franquelo, “Guidelines for weighting factors design in model predictive control of power converters and drives,” in *Proc. ICIT*, 2009, pp. 1–7.

[50] M. R. Arahal, F. Barrero, M. J. Duran, M. G. Ortega, and C. Martin, “Trade-offs analysis in predictive current control of multi-phase induction machines,” *Control Engineering Practice*, vol. 81, pp. 105–113, 2018.

[51] R. Gregor, F. Barrero, S. Toral, M. Duran, M. Arahal, J. Prieto, and J. Mora, “Predictive-space vector PWM current control method for asymmetrical dual three-phase induction motor drives,” *IET Electric Power Applications*, vol. 4, no. 1, pp. 26–34, 2010.

[52] L. Gao, J. E. Fletcher, and L. Zheng, “Low-speed control improvements for a two-level five-phase inverter-fed induction machine using classic direct torque control,” *IEEE Transactions on Industrial Electronics*, vol. 58, no. 7, pp. 2744–2754, 2010.

[53] J. J. Aciego, I. G. Prieto, and M. J. Duran, “Model predictive control of six-phase induction motor drives using two virtual voltage vectors,” *IEEE Journal of Emerging and Selected Topics in Power Electronics*, vol. 7, no. 1, pp. 321–330, 2018.

[54] A. G. Yepes, J. A. Riveros, J. Doval-Gandoy, F. Barrero, O. López, B. Bogado, M. Jones, and E. Levi, “Parameter identification of multiphase induction machines with distributed windings—Part 1: Sinusoidal excitation methods,” *IEEE Transactions on Energy Conversion*, vol. 27, no. 4, pp. 1056–1066, 2012.

[55] J. A. Riveros, A. G. Yepes, F. Barrero, J. Doval-Gandoy, B. Bogado, O. Lopez, M. Jones, and E. Levi, “Parameter identification of multiphase induction machines with distributed windings—Part 2: Time-domain techniques,” *IEEE Transactions on Energy Conversion*, vol. 27, no. 4, pp. 1067–1077, 2012.

[56] G. I. Rivas-Martínez, J. Rodas, and J. D. Gandoy, “Statistical Tools to Evaluate the Performance of Current Control Strategies of Power Converters and Drives,” *IEEE Transactions on Instrumentation and Measurement*, vol. 70, pp. 1–11, 2021.

[57] B. Bogado, F. Barrero, M. R. Arahal, S. Toral, and E. Levi, “Sensitivity to electrical parameter variations of predictive current control in multiphase drives,” in *Proc. IECON*, 2013, pp. 5215–5220.

[58] L. Delorme, M. Ayala, J. Rodas, R. Gregor, O. Gonzalez, and J. Doval-Gandoy, “Comparison of the effects on stator currents between continuous model and discrete model of the three-

phase induction motor in the presence of electrical parameter variations," in *Proc. ICIT*, 2020, pp. 151–156.

PARTE III

PUBLICACIONES

4.3 Resumen del Trabajo de Investigación

En este apéndice se realiza una recopilación de los artículos publicados en el marco de este trabajo de investigación, en el siguiente orden:

1. **Osvaldo González**, Magno Ayala, Jesús Doval-Gandoy, Jorge Rodas, Raúl Gregor, Marcos Rivera, Predictive-Fixed Switching Current Control Strategy Applied to Six-Phase Induction Machine, Energies, vol. 12, no 12, p. 2294. DOI: 10.3390/en12122294, 2019.

2. **Osvaldo González**, Magno Ayala, Carlos Romero, Larizza Delorme, Jorge Rodas, Raúl Gregor, Ignacio Gonzalez-Prieto, Mario Javier Duran, Model Predictive Current

Control of Six-phase Induction Motor Drives using Virtual Vectors and Space Vector Modulation, IEEE Transactions on Power Electronics, 2021. (Bajo revisión).

3. **Osvaldo González**, Magno Ayala, Carlos Romero, Jorge Rodas, Raúl Gregor, Larizza Delorme, Ignacio Gonzalez-Prieto, Mario Javier Duran, Marco Rivera, Comparative Assessment of Model Predictive Current Control Strategies applied to Six-Phase Induction Machines, Proc. ICIT, Buenos Aires, Argentina, pp. 1037-1043. DOI: 10.1109/ICIT45562.2020.9067279, 2020

4. **Osvaldo González**, Magno Ayala, Jesus Doval-Gandoy, Raul Gregor, Gustavo Rivas, Variable-Speed Control of a Six-Phase Induction Machine using Predictive-Fixed Switching Frequency Current Control Techniques, Proc. PEDG, Charlotte, US, pp. 1-6, DOI: 10.1109/PEDG.2018.8447837, 2018.

4.4 Otras Contribuciones

Cabe mencionar que, además de las publicaciones de revistas presentadas como contribuciones en el Capítulo 3, otros trabajos publicados en revistas indexadas derivados del trabajo de investigación realizado durante el periodo de la Tesis Doctoral, se listan a continuación:

1. Magno Ayala, Jesús Doval-Gandoy, Jorge Rodas, **Osvaldo González**, Raúl Gregor, Current control designed with model based predictive control for six-phase motor drives, ISA Transactions. DOI: 10.1016/j.isatra.2019.08.052, 2019.

2. Magno Ayala, Jesús Doval-Gandoy, Jorge Rodas, **Osvaldo González**, Raúl Gregor, Marco Rivera, A Novel Modulated Model Predictive Control Applied to Six-Phase Induction Motor Drives, IEEE Transactions on Industrial Electronics. DOI: 10.1109/TIE.2020.2984425, 2020.

3. Magno Ayala, Jesús Doval-Gandoy, **Osvaldo González**, Jorge Rodas, Raúl Gregor, Marcos Rivera, Experimental Stability Study of Modulated Model Predictive Current Controllers Applied to Six-Phase Induction Motor Drives, IEEE Transactions on Power Electronics, 2021. (Aceptado para publicación).

4. Carlos Romero, Larizza Delorme, **Osvaldo González**, Magno Ayala, Jorge Rodas, Raúl Gregor, Algorithm for implementation of Virtual Voltage Vectors in Model Predictive Current Control of Six-Phase Induction Machines, Energies, 2021. (Bajo revisión).

5. Larizza Delorme, Magno Ayala, Jorge Rodas, Raúl Gregor, **Osvaldo González**, Jesús Doval-Gandoy, Comparison of the Effects on Stator Currents Between Continuous Model and Discrete Model of the Three-phase Induction Motor in the Presence of Electrical Parameter Variations, Proc. ICIT, Buenos Aires, Argentina, DOI: 10.1109/ICIT45562.2020.9067265, 2020.

energies

MDPI

Article

Predictive-Fixed Switching Current Control Strategy Applied to Six-Phase Induction Machine

Osvaldo Gonzalez [1,*], Magno Ayala [1], Jesus Doval-Gandoy [2], Jorge Rodas [1], Raul Gregor [1] and Marco Rivera [3]

1 Laboratory of Power and Control Systems (LSPyC), Facultad de Ingeniería, Universidad Nacional de Asunción, Luque 2060, Paraguay; mayala@ing.una.py (M.A.); jrodas@ing.una.py (J.R.); rgregor@ing.una.py (R.G.)

2 Applied Power Electronics Technology Research Group (APET), Universidad de Vigo, 363310 Vigo, Spain; jdoval@uvigo.es

3 Laboratory of Energy Conversion and Power Electronics, Universidad de Talca, 3340000 Curicó, Chile; marcoriv@utalca.cl

* Correspondence: ogonzalez@ing.una.py; Tel.: +59-598-370-1765

Received: 27 April 2019; Accepted: 30 May 2019; Published: 15 June 2019

check for updates

Abstract: In applications such as multiphase motor drives, classical predictive control strategies are characterized by a variable switching frequency which adds high harmonic content and ripple in the stator currents. This paper proposes a model predictive current control adding a modulation stage based on a switching pattern with the aim of generating a fixed switching frequency. Hence, the proposed controller takes into account the prediction of the two adjacent active vectors and null vector in the (α-β) frame defined by space vector modulation in order to reduce the (x-y) currents according to a defined cost function at each sampling period. Both simulation and experimental tests for a six-phase induction motor drive are provided and compared to the classical predictive control to validate the feasibility of the proposed control strategy.

Keywords: multiphase induction machine; model predictive control; fixed switching frequency

1. Introduction

In recent years, multiphase induction machines (IMs) have been considered to be such a viable alternative in comparison to three-phase machines due to their fault tolerance capabilities with no extra hardware, lower torque ripple and better power splitter per phase which result very attractive to the research community for various industrial applications where a high-performance control strategy, as well as, reliability are required [1]. Presently, some applications of multiphase IMs that are being investigated include wind energy generation system [2], hybrid electric vehicles (EV) [3] and ship propulsion. In the applications mentioned above, multiphase IMs can be used under different conditions, such as healthy and post-fault operations [4,5]. From the point of view of control, the most common control strategy to regulate multiphase IMs is the field-oriented control (FOC), which is constituted by an inner current control loop, to obtain the references voltages, and an outer speed control loop for speed regulation [6]. However, several new control approaches have been carried out for the inner current control loop in multiphase IMs, some of them are: sliding mode control [7], resonant control [8] and model predictive control (MPC) [9]. Although there are other controllers such as the well-known proportional-integral (PI) controllers [10], the preferred choice is the MPC due to the fact that it shows a good transient behavior and facilitates the inclusion of nonlinearities in the system as described in [11,12], and in [13] where a comparative study between MPC and PI-PWM control has been addressed. In this context, the MPC strategy produces the reference voltage through the instantaneous discrete states of the power converter according to the minimization of a predefined cost function. However, the classic MPC strategy presents some limitations regarding to the application of only one vector in the whole sampling period. This results in current ripples as well as large voltages at low sampling frequency. Besides, the variable switching frequency develops a spread spectrum, decreasing the performance of the system in terms of useful power [14].

To overcome this subject, a predictive-fixed switching current control strategy, named (PFSCCS) from now on, applied to a two-level six-phase voltage source inverter (VSI) is presented in this paper. The strategy is based on a modulation concept employed with the MPC scheme, which has been studied for different power converters such as the mentioned two-level six-phase VSI described in [15,16] and also other topologies presented in [17,18]. In the proposed current strategy, three vectors have been considered at every sampling period, composed by two active vectors (taking only into account the largest vectors) and null vector, where their corresponding duty cycles are achieved according to the switching states and a switching pattern has also been used before being applied to VSI in order to generate a fixed switching frequency. Whereas, for the speed control loop, a PI controller has been developed by a technique shown in [19].

The main focus of this work is the implementation of the PFSCCS so as to reduce the (x-y) currents compared to the classic MPC strategy using a six-phase IM supplied through a two-level six-phase VSI. In that context, both simulation and experimental validations have been included to demonstrate the capability of the proposed technique. In addition, the effectiveness of the PFSCCS is tested under steady-state and transient requirements, respectively, incorporating the mean square error (MSE) and the total harmonic distortion (THD) analysis.

The paper is organized as follows: the model of the six-phase IM and VSI are presented in Section 2. In Section 3 are described the speed controller, classic MPC and the proposed current controller based on modulated model predictive control. Section 4 shows the performance of the proposed control through simulation and experimental results in steady-state and transient conditions. Finally, Section 5 summarizes the conclusion.

2. Six-Phase IM Drive Model

The six-phase IM, supplied by a two-level six-phase VSI with a DC-Link voltage source (V_{dc}), is taken into account in this work. The simplified topology is presented in Figure 1. The six-phase IM is a dependant of time system, for this reason it is possible to represent it through a group of equations in order to define a model of the real system.

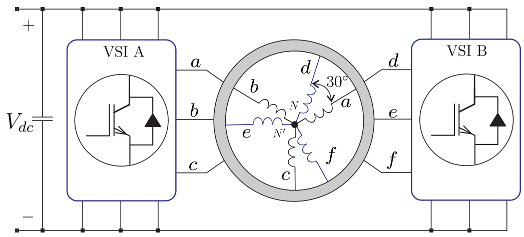

Figure 1. Six-phase IM topology supplied trough a two-level six-phase VSI.

In that sense, vector space decomposition (VSD) strategy [20] has been used to translate the actual six dimensional plane, formed through the six phases of the six-phase IM, into three two dimensional rectangular sub-spaces in the stationary reference frame, named as (α-β), (x-y) and (z_1-z_2) frame, by applying the amplitude invariant decoupling Clarke conversion matrix T [21]. The (α-β) frame contains the variables that provide the torque and flux regulation, unlike the (x-y) frame which is linked with the energy losses. The zero elements mapped in the (z_1-z_2) frame are not examined due to the adopted topology (isolated neutral points).

$$T = \frac{1}{3}\begin{array}{c}\left(\begin{array}{cccccc} \cos(0) & \cos(\frac{\pi}{6}) & \cos(\frac{2\pi}{3}) & \cos(\frac{5\pi}{6}) & \cos(\frac{4\pi}{3}) & \cos(\frac{3\pi}{2}) \\ \sin(0) & \sin(\frac{\pi}{6}) & \sin(\frac{2\pi}{3}) & \sin(\frac{5\pi}{6}) & \sin(\frac{4\pi}{3}) & \sin(\frac{3\pi}{2}) \\ \cos(0) & \cos(\frac{5\pi}{6}) & \cos(\frac{10\pi}{3}) & \cos(\frac{25\pi}{6}) & \cos(\frac{20\pi}{3}) & \cos(\frac{15\pi}{2}) \\ \sin(0) & \sin(\frac{5\pi}{6}) & \sin(\frac{10\pi}{3}) & \sin(\frac{25\pi}{6}) & \sin(\frac{20\pi}{3}) & \sin(\frac{15\pi}{2}) \\ 1 & 0 & 1 & 0 & 1 & 0 \\ 0 & 1 & 0 & 1 & 0 & 1 \end{array}\right)\end{array}\begin{array}{c} \alpha \\ \beta \\ x \\ y \\ z_1 \\ z_2 \end{array} \tag{1}$$

Moreover, the model of the VSI must be included in the system. Thus, due to the discrete nature of the VSI, it is necessary to define an amount of 2^6 different switching states which represent every state of each VSI leg specified as $S_m = (S_a, ..., S_f)$, where S_m is considered as binary number, i.e., $S_m = 0$ or $S_m = 1$. Therefore, the stator phase voltages can be projected into (α-β)-(x-y) frame by considering the vector S_m and the V_{dc} voltage employing the VSD strategy. In Figure 2, the 64 control alternatives (48 active and one null vectors) are depicted in the (α-β)-(x-y) frame.

By considering the mentioned analysis, the six-phase IM can be performed by employing the state-space representation as follows:

$$x'(t) = \underbrace{\left(\begin{array}{cccccc} -R_s r_2 & r_4 L_m \omega_r & 0 & 0 & r_4 R_r & r_4(L_{lr} + L_m)\omega_r \\ r_4 L_m \omega_r & -R_s r_2 & 0 & 0 & r_4(L_{lr} + L_m)\omega_r & r_4\, R_r \\ 0 & 0 & -R_s r_3 & 0 & 0 & 0 \\ 0 & 0 & 0 & -R_s r_3 & 0 & 0 \\ R_s r_4 & -r_5 L_m \omega_r & 0 & 0 & -r_5 R_r & -c_5(L_{lr} + L_m) \\ -r_5 L_m \omega_r & R_s r_4 & 0 & 0 & -r_5(L_{lr} + L_m) & -r_5\, R_r \end{array}\right)}_{M_1(t)} x(t) +$$

$$\underbrace{\left(\begin{array}{cccc} r_2 & 0 & 0 & 0 \\ 0 & r_2 & 0 & 0 \\ 0 & 0 & r_3 & 0 \\ 0 & 0 & 0 & r_3 \\ -r_4 & 0 & 0 & 0 \\ 0 & -r_4 & 0 & 0 \end{array}\right)}_{M_2(t)} u(t) + K_n\, v(t) \tag{2}$$

being $x(t) = (x_1, ..., x_6)^T$ the state vector constituted by stator-rotor currents of the six-phase IM, shown in Equation (3), $u(t) = (u_1, ..., u_4)^T$ is the input vector constituted by the stator voltages, presented in Equation (4). While $M_1(t)$ and $M_2(t)$ are matrices obtained by the electrical parameters of the six-phase IM. The process noise is defined as $v(t)$ and K_n represents the noise weight matrix.

$$x_1 \;=\; i_{\alpha s}, \quad x_2 = i_{\beta s}, \quad x_3 = i_{xs}, \quad x_4 = i_{ys}, \quad x_5 = i_{\alpha r}, \quad x_6 = i_{\beta r}. \tag{3}$$

$$u_1 = u_{\alpha s}, \quad u_2 = u_{\beta s}, \quad u_3 = u_{xs}, \quad u_4 = u_{ys}. \tag{4}$$

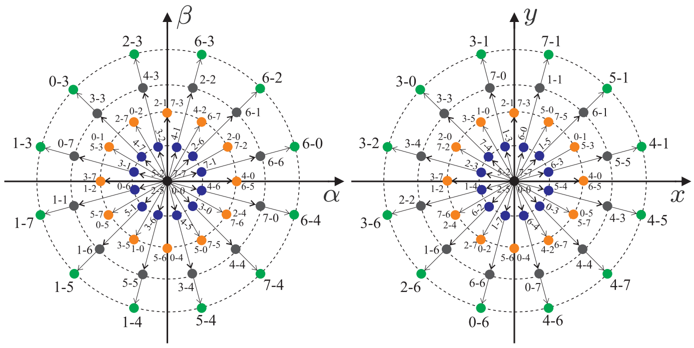

Figure 2. Mapping of the space vectors in the (α-β)-(x-y) frame for a two-level six-phase VSI.

Consequently, by taking into account the state-space representation in Equation (2) and the state vectors, it is feasible to establish the following equations:

$$
\begin{aligned}
x_1' &= -R_s r_2 x_1 + r_4\left[L_m \omega_r x_2 + R_r x_5 + (L_{lr} + L_m)\omega_r x_6\right] + r_2 u_1 \\
x_2' &= -R_s r_2 x_2 + r_4\left[-L_m \omega_r x_1 - (L_{lr} + L_m)\omega_r x_5 + R_r x_6\right] + r_2 u_2 \\
x_3' &= -R_s r_3 x_3 + r_3 u_3 \\
x_4' &= -R_s r_3 x_4 + r_3 u_4 \\
x_5' &= R_s r_4 x_1 + r_5\left[-L_m \omega_r x_2 - R_r x_5 - (L_{lr} + L_m)\omega_r x_6\right] - r_4 u_1 \\
x_6' &= R_s r_4 x_2 + r_5\left[L_m \omega_r x_1 + (L_{lr} + L_m)\omega_r x_5 - R_r x_6\right) - r_4 u_2
\end{aligned}
\tag{5}
$$

where the electrical variables of the six-phase IM are represented by R_s, R_r, L_m, L_{lr} and L_{ls}, ω_r represents the rotor electrical speed and the coefficients $(r_1, ..., r_5)$ are defined as:

$$
r_1 = (L_{ls} + L_m)(L_{lr} + L_m) - L_m^2, \quad r_2 = \tfrac{L_{lr}+L_m}{r_1}, \quad r_3 = \tfrac{1}{L_{ls}}, \quad r_4 = \tfrac{L_m}{r_1}, \quad r_5 = \tfrac{L_{ls}+L_m}{r_1}. \tag{6}
$$

Besides, in order to produce the stator phase voltages, which are dependant of the V_{dc} voltage and the vector S_m, an ideal six-phase VSI has been used [21] as it is defined in Equation (7).

$$
M_{VSI} = \frac{1}{3}\begin{pmatrix} 2 & 0 & -1 & 0 & -1 & 0 \\ 0 & 2 & 0 & -1 & 0 & -1 \\ -1 & 0 & 2 & 0 & -1 & 0 \\ 0 & -1 & 0 & 2 & 0 & -1 \\ -1 & 0 & -1 & 0 & 2 & 0 \\ 0 & -1 & 0 & -1 & 0 & 2 \end{pmatrix}\begin{pmatrix} S_a \\ S_b \\ S_c \\ S_d \\ S_e \\ S_f \end{pmatrix}. \tag{7}
$$

In turn, the stator phase voltages can be mapped into (α-β)-(x-y) frames defined as follows:

$$
\begin{pmatrix} u_{\alpha s} \\ u_{\beta s} \\ u_{xs} \\ u_{ys} \end{pmatrix} = V_{dc}\, T\, M_{VSI} \tag{8}
$$

$$
\begin{pmatrix} i_{\alpha s} \\ i_{\beta s} \\ i_{xs} \\ i_{ys} \end{pmatrix} = \begin{pmatrix} 1 & 0 & 0 & 0 & 0 & 0 \\ 0 & 1 & 0 & 0 & 0 & 0 \\ 0 & 0 & 1 & 0 & 0 & 0 \\ 0 & 0 & 0 & 1 & 0 & 0 \end{pmatrix} x(t) + n(t) \tag{9}
$$

where Equation (9) is considered the output vector, denoted by $y(t)$, and $n(t)$ is the measurement noise. Finally, the mechanical equations of the six-phase IM are specified as:

$$T_e = P\left(\psi_{\alpha s} i_{\beta s} - \psi_{\beta s} i_{\alpha s}\right) 3 \tag{10}$$

$$J_i \omega_m' + B_i \omega_m = (T_e - T_L) \tag{11}$$

where J_i defines the inertia coefficient, B_i is the friction coefficient, T_e represents the generated torque, T_L is the load torque, ω_m is the rotor mechanical speed, which is related to the rotor electrical speed as $\omega_r = P\omega_m$, $\psi_{\alpha s}$ and $\psi_{\beta s}$ are the stator fluxes, and P is the number of pole pairs.

3. Drive Control

A complete diagram of the PFSCCS for the six-phase IM drive is shown in Figure 3, where the outer speed control and the proposed inner current control will be detailed in the following sections.

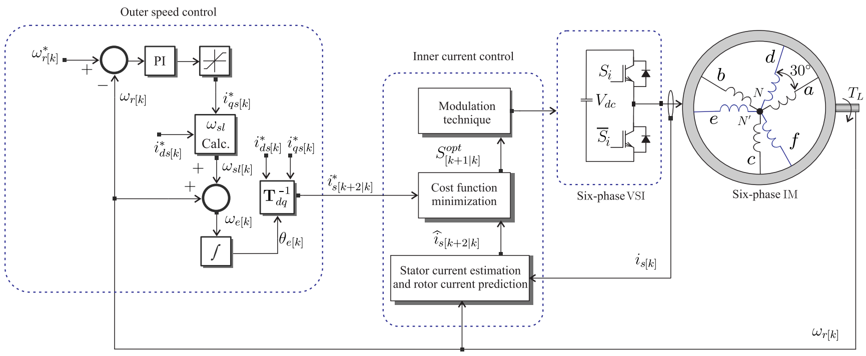

Figure 3. Complete diagram of the PFSCCS applied to six-phase IM.

3.1. Speed Control

For the external speed control loop a two degree PI controller has been incorporated, described in [19], which is based on the FOC strategy due to its easiness. Into the FOC strategy, the reference current is generated by the PI speed controller in the dynamic reference frame, known as *d*-*q* frame. Then, the reference currents are achieved by the calculation of the electric angle employed to convert the current reference, at the beginning in *d*-*q* frame, to the static reference frame (α-β), which are needed for the MPC. This method estimates the slip frequency (ω_{sl}) which is executed in the same manner as the FOC strategies, by using the reference currents in the dynamic reference frame (i_{ds}^*, i_{qs}^*) and the electrical parameters of the IM (R_r, L_r), while the rotor mechanical speed is acquired through an encoder.

3.2. Classic MPC

The MPC is related to the mathematical model of a given system, the six-phase IM in this case, commonly termed as predictive model, which consists of the prediction of the future action (at time k) of the system through measured variables, such as the rotor mechanical speed and the stator currents. Hence, for that purpose a forward Euler discretization strategy has been implemented.

$$x^p[k+1|k] = x[k] + T_s\, f(x[k],\, u[k],\, \omega_r[k]) \tag{12}$$

being k the actual sample and T_s the sampling period. Superscript p represents the predicted variables of the system.

According to the state-space representation (12), the stator currents and the rotor mechanical speed can be measured. Thus, the stator voltages are directly predicted through the switching states of the six-phase VSI. Nevertheless, the rotor currents are not easily measured. This issue can be faced through the estimation of the rotor currents by a reduced order estimator which determines the unmeasured fraction of the state vector. Then, in this work, the rotor currents are estimated by the proposed strategy in [22] which employs a reduced order estimator based on a Kalman Filter (KF). In that sense, uncorrelated process noises and a zero-mean Gaussian measurement have been considered. Finally, the the studied system equations are established as:

$$x^p[k+1|k] = M_1[k]x[k] + M_2[k]u[k] + K_n v[k] \tag{13}$$

$$y[k+1|k] = \begin{pmatrix} 1 & 0 & 0 & 0 & 0 & 0 \\ 0 & 1 & 0 & 0 & 0 & 0 \\ 0 & 0 & 1 & 0 & 0 & 0 \\ 0 & 0 & 0 & 1 & 0 & 0 \end{pmatrix} x[k+1] + n[k+1] \tag{14}$$

where $M_1[k]$ and $M_2[k]$ represent the discretized matrices since (5). $M_1[k]$ is related to the current value of $\omega_r[k]$ and must be included at every sampling period. A completed explanation of the aforementioned reduced order KF is presented in [22,23].

Cost Function

The optimization action is carried out at every sampling period by the MPC strategy. The action is based on the evaluation of a defined cost function, shown in (15), for every feasible stator voltages in order to obtain the control purpose. Since the cost function can be expressed in various manners, in this work, the minimization of the current tracking error has been taken into account specified by the following equation:

$$CF[k+2|k] = \sqrt{(e_{\alpha s})^2 + (e_{\beta s})^2} + \lambda_{xy}\sqrt{(e_{xs})^2 + (e_{ys})^2} \tag{15}$$

being the errors defined as follows:

$$\begin{aligned} e_{\alpha s} &= i^*_{\alpha s}[k+2] - i^p_{\alpha s}[k+2|k], \\ e_{\beta s} &= i^*_{\beta s}[k+2] - i^p_{\beta s}[k+2|k], \\ e_{xs} &= i^*_{xs}[k+2] - i^p_{xs}[k+2|k], \\ e_{ys} &= i^*_{ys}[k+2] - i^p_{ys}[k+2|k]. \end{aligned} \tag{16}$$

considering $i^*_s[k+2]$ as the reference vector for the stator currents and $i^p_s[k+2]$ as the predicted values based on the second-step forward state. At the same time, a tuning parameter is included in the cost function, described as λ_{xy}, in order to provide an extra weight on (α-β) or (x-y) frames [22,23].

3.3. Proposed Current Controller (Pfsccs)

According to the space vector modulation (SVM) strategy, it is feasible to find the available vectors for the six-phase VSI in the (α-β) frame, this produces 64 sectors (48 different ones), which are conformed by two active vectors and a null vector as depicted in Figure 4. The proposed strategy realizes the prediction of the vectors (null vector and two active vectors) that compose every sectors and calculates the cost function independently (G_0, G_1 and G_2) for each prediction at every sampling period. However, the proposed strategy only select the twelve largest vectors including the null vector in order to represent the optimal vector. This current control approach has been adopted in order to reduce the (x-y) currents [24,25].

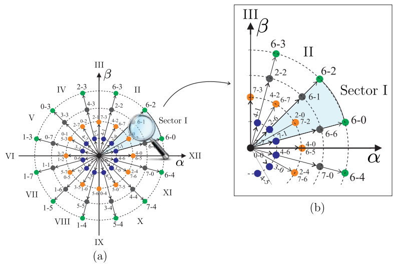

Figure 4. Considered sectors for the six-phase VSI in the (α-β) frame: (**a**) Available vectors; (**b**) A selected specific sector shown as zoom.

The prediction is obtained by Equation (13), but differs in the calculation of the input vector ($u[k]$) [21]. The duty cycles (d_c), considering the null vector and the two active vectors (d_{c-0}, d_{c-1} and d_{c-2}), respectively, are achieved through the following equations:

$$d_{c-0} = \frac{\mu}{G_0}, \qquad d_{c-1} = \frac{\mu}{G_1}, \qquad d_{c-2} = \frac{\mu}{G_2}, \tag{17}$$

$$d_{c-0} + d_{c-1} + d_{c-2} = 1, \tag{18}$$

Hence, it is possible to acquire the relation for μ and the duty cycles for the specified vectors as:

$$d_{c-0} = \frac{G_1G_2}{G_0G_1 + G_1G_2 + G_0G_2}, \tag{19}$$

$$d_{c-1} = \frac{G_0G_2}{G_0G_1 + G_1G_2 + G_0G_2}, \tag{20}$$

$$d_{c-2} = \frac{G_0G_1}{G_0G_1 + G_1G_2 + G_0J_2}. \tag{21}$$

Taking account these relations, the cost function is redefined, as shown in Equation (22), and calculated at each T_s.

$$CF_n[k+2|k] = d_{c-1}G_1 + d_{c-2}G_2. \tag{22}$$

In this way, the two vectors that reduce $CF_n[k+2|k]$ are chosen and then applied to the VSI at the following sampling period. Once the optimal vectors are obtained, the two active vectors (v_1-v_2) and null vector (v_0), their respective duty cycles to be applied and a switching pattern scheme, described in [21], are taken with the aim of producing a fixed switching frequency.

4. Simulation and Experimental Results

First, simulations have been performed in a MATLAB/Simulink R2014a environment so as to verify the feasibility of the PFSCCS using a six-phase IM shown in Figure 1. Numerical integration using first order Euler's algorithm has been applied to calculate the progress of the studied system. The simulation parameters of the six-phase IM are listed in Table 1.

Table 1. Characteristics of the six-phase IM.

R_r	6.9 Ω	L_s	654.4 mH
L_{lr}	12.8 mH	L_r	626.8 mH
L_{ls}	5.3 mH	P_w	2 kW
R_s	6.7 Ω	J_i	0.07 kg.m^2
L_m	614 mH	B_i	0.0004 kg.m^2/s
P	1	ω_{r-nom}	3000 rpm

The effectiveness of the presented control technique for the six-phase IM has been evaluated under a load condition ($T_L = 2$ Nm), the sampling frequency is 8 kHz, V_{dc} is 400 V and the d-axis current reference (i_{ds}^*) has been set in 1 A, while for the gains of the two degree PI controller with a saturation, can be found in [19]. Moreover, for the proposed control, $\lambda_{xy} = 0.1$, defined in (15), has been used in order to give more emphasis to the (α-β) stator current tracking.

The performance of the proposed technique is compared in transient and steady-state conditions. Both proofs, simulation and experimental results, are analyzed in terms of mean squared error (MSE) and total harmonic distortion (THD) obtained between the reference and the measured stator currents in the (α-β) and (x-y) sub-spaces for MSE test and the THD is obtained in the (α-β) sub-space. The MSE is computed as follows:

$$\mathrm{MSE}(i_{\sigma s}) = \sqrt{\frac{1}{N}\sum_{j=1}^{N}(i_{\sigma s} - i_{\sigma s}^*)^2} \quad (23)$$

where the stator current reference is represented through the superscript $*$, the measured stator current is defined by $i_{\sigma s}$ taking into account that σ includes the (α-β)-(x-y) frame and N is the number of studied samples. While, the THD is obtained as follows:

$$\mathrm{THD}(i_s) = \sqrt{\frac{1}{i_{s1}^2}\sum_{k=2}^{N}(i_{sk})^2} \quad (24)$$

where i_{s1} corresponds to the fundamental stator current whereas i_{sk} is the harmonic stator current (multiple of the fundamental stator current).

In Figure 5 the performance of the stator currents in the (α-β)-(x-y) frame can be seen in steady-state condition. According to the simulations results, shown in Table 2, the proposed technique has a good behavior considering the MSE and THD analysis of the stator currents at different rotor mechanical speeds. In addition, it can be noticed that at lower speeds, the stator currents ripple in the (α-β) frame is slightly smaller than at higher mechanical rotor speeds, in the same way that occurs for the (x-y) currents.

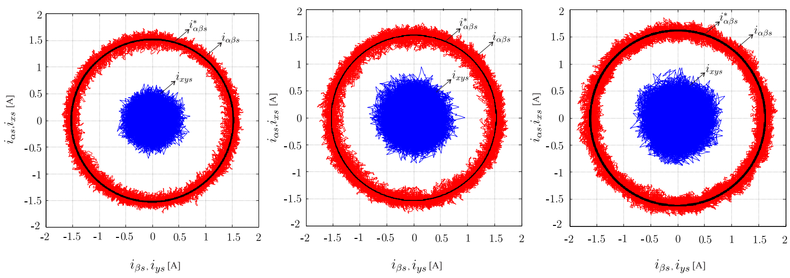

(a) **(b)** **(c)**

Figure 5. Simulation performance in steady-state condition of stator currents in (α-β) and (x-y) sub-spaces for a sampling frequency of 8 kHz at different speeds (ω_m): (**a**) 500 rpm; (**b**) 1000 rpm; (**c**) 1500 rpm.

Table 2. Simulation performance test of stator currents (α-β), (x-y), MSE (A), THD (%) at different rotor speeds (rpm).

f_s = 8 kHz						
ω_m^*	MSE_α	MSE_β	MSE_x	MSE_y	THD_α	THD_β
500	0.065	0.064	0.174	0.172	5.73	5.46
1000	0.076	0.075	0.211	0.203	5.43	5.34
1500	0.110	0.110	0.219	0.216	6.46	6.38

For the experimental proofs the PFSCCS, previously described, is examined in the test rig shown in Figure 6 in order to prove its effectiveness, employing a six-phase IM supplied through two tradictional three-phase VSI, being analogous to a six-phase VSI and the V_{dc} voltage is obtained by means of a DC power source. A dSPACE MABXII DS1401 real-time rapid prototyping bench including Simulink version 8.2 has been used to manage the two-level six VSI. Once the results are acquired, these have been analyzed through MATLAB/Simulink R2014a code. Employing stand-still with VSI proofs and AC time domain strategies, the electrical parameters have been acquired [26,27]. Table 1 summarizes these results. Current sensors LA 55-P s (frequency bandwidth since DC up to 200 kHz) have been used for the experimental measurements. The current measurements have been then turned to digital format by means of a 16-bit A/D converter. The six-phase IM angle has been measured with a 1024-pulses per revolution (ppr) incremental encoder in order to estimate the rotor speed and also a 5 HP eddy current brake has been used to insert a fixed mechanical load on the system.

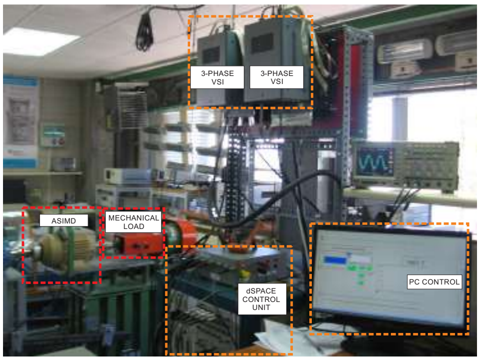

Figure 6. Experimental test rig.

Taking this into account, the experimental results have been analyzed with the same tests that simulations results as figures of merit. The stator currents reference in the (x-y) frame have been established to zero, i.e., $i_{xs}^* = i_{ys}^* = 0$ A so as to decrease the losses in the copper. The amounts for the process noise ($\hat{Q}_w = 0.0022$) and the measurement noise ($\hat{R}_v = 0.0022$) is estimated by means of the strategy proposed in [23]. The dynamic behavior of the proposed technique has been evaluated with two different values of λ_{xy}, defined in (15), giving more weight to (α-β) stator currents tracking. In the developed tests, the sampling frequencies have been fixed in 8 kHz for PFSCCS and 8 kHz and 16 kHz for classic MPC, respectively, due to the fact that the PFSCCS uses two active vectors and null vector twice in a sampling period and this procedure doubles the switching frequency compared to the sampling frequency. In that sense, tests have been included in order to expose a fair comparison between the classic MPC and PFSCCS at the mentioned sampling frequencies and also to show the performance of both techniques. For the rotor mechanical speeds, two operation points have been considered, 500 rpm and 1000 rpm, respectively, in steady-state condition. Furthermore, for a transient response, a reversal rotor mechanical speed test from 500 rpm to -500 rpm has been considered for PFSCCS and from 1500 rpm to 200 rpm for classic MPC and PFSCCS. The obtained results between classic MPC and PFSCCS are reported in Table 3, where the proposed current control technique has demonstrated a good tracking of the current references considering the MSE and THD in the (α-β)-(x-y) frame.

Table 3. Experimental performance test of stator currents (α-β), (x-y), MSE (A), THD (%) between classic MPC and the PFSCCS at different rotor speeds (rpm).

f_s = 8 kHz for Classic MPC						
ω_m^*	MSE$_\alpha$	MSE$_\beta$	MSE$_x$	MSE$_y$	THD$_\alpha$	THD$_\beta$
500	0.140	0.130	0.821	0.822	8.30	8.40
1000	0.147	0.138	0.953	0.934	7.40	7.30
f_s = 16 kHz for Classic MPC						
ω_m^*	MSE$_\alpha$	MSE$_\beta$	MSE$_x$	MSE$_y$	THD$_\alpha$	THD$_\beta$
500	0.073	0.072	0.491	0.483	8.40	8.30
1000	0.084	0.082	0.538	0.534	7.50	7.40
f_s = 8 kHz for PFSCCS						
ω_m^*	MSE$_\alpha$	MSE$_\beta$	MSE$_x$	MSE$_y$	THD$_\alpha$	THD$_\beta$
500	0.042	0.045	0.135	0.130	4.89	5.08
1000	0.069	0.068	0.197	0.204	4.69	4.78

Figure 7 presents the trajectories of the stator currents in the (α-β)-(x-y) frame of the PFSCCS applied to the six-phase IM. In this test two different values of the tuning parameter (λ_{xy}) have been considered, in Figure 7a, λ_{xy} = 0.05 has been considered and λ_{xy} = 0.1 in Figure 7b. The rotor mechanical speed has been set to 500 rpm at 8 kHz. The figure shows that (x-y) currents decrease when λ_{xy} increases, which imply that the selection of this parameter has a strong influence on the behavior of the system. Further, the (α-β) current tracking has a slightly better performance considering λ_{xy} = 0.1.

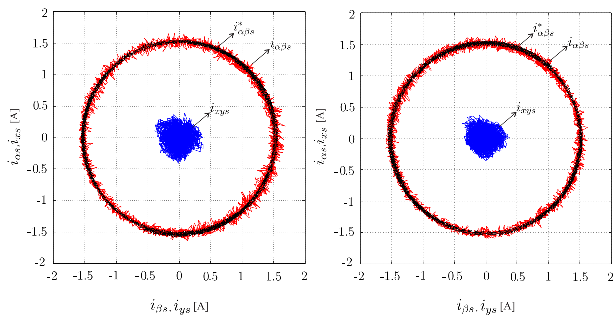

(**a**) (**b**)

Figure 7. Experimental results in the (α-β)-(x-y) frame for stator currents at 8 kHz of sampling frequency and 500 rpm rotor speed considering: (**a**) λ_{xy} = 0.05; (**b**) λ_{xy} = 0.1.

In addition, Figure 8a shows the harmonic content of the measured stator current ($i_{\alpha s}$) through THD analysis and also, in Figure 8b has been included the switching voltage in the six-phase VSI showing the pattern of the proposed modulation strategy.

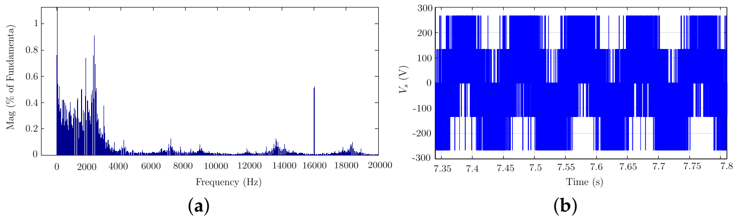

Figure 8. Experimental performance for PFSCCS at 8 kHz of sampling frequency and 500 rpm: (**a**) Spectrum of the measured stator current; (**b**) Switching pattern in the VSI.

On the other hand, Figure 9 exposes the transient response of the proposed control for a step response in q axis. The transient response has been included through a reversal test from rotor mechanical speed (500 rpm to −500 rpm) at 8 kHz. Both cases report fast responses considering the overshoot and settling time, which were of 6.14% and 6 ms, respectively, for Figure 9a and 4.85% and 6.12 ms, respectively for Figure 9b. The criterion of the 5% has been selected. Finally, a experimental transient response from a step change of 1500 rpm to 200 rpm between classic MPC and PFSCCS has been depicted in Figure 10 in order to show the performance of the proposed strategy, which it has demonstrated that it can be used in industrial applications (e.g., regenerating braking).

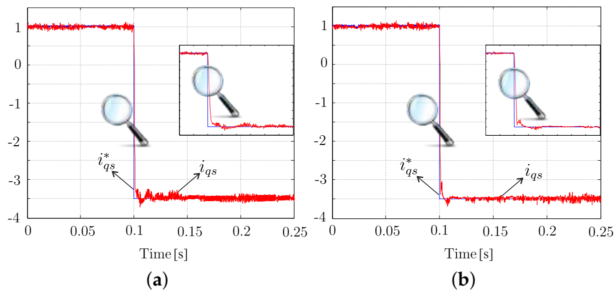

Figure 9. Experimental transient test in q-axis of stator currents from a speed change of 500 rpm to −500 rpm at 8 kHz of sampling frequency considering: (**a**) λ_{xy} = 0.05; (**b**) λ_{xy} = 0.1.

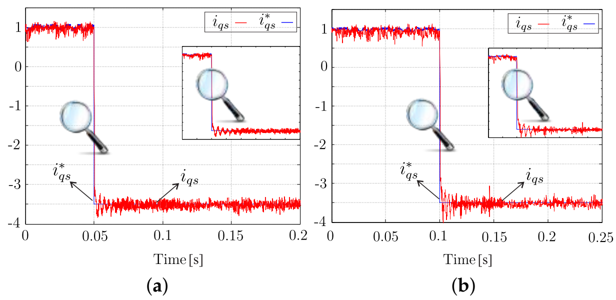

Figure 10. Experimental transient test in q-axis of stator currents from a speed change of 1500 rpm to 200 rpm at 16 kHz and 8 kHz of sampling frequency, respectively: (**a**) Classic MPC; (**b**) PFSCCS.

5. Conclusions

In this paper, a predictive current control technique with a fixed switching frequency applied to a six-phase IM has been proposed. This technique has been developed to reduce the stator currents in the (x-y) frame using the largest vectors of the (α-β) frame with a stage of modulation based on a determined switching pattern in order to produce a fixed switching frequency. The simulation and experimental results have shown the performance of the proposed technique, where the system has been tested under different conditions (steady and transient conditions) including different rotor mechanical speeds, sampling frequency and tuning parameters for (x-y) stator currents, respectively. In terms of (α-β) currents tracking, the presented technique has a better behavior at lower speed and a remarkable reduction of (x-y) stator currents compared to classic MPC. The obtained results have also demonstrated a good transient current behavior in terms of overshoot and settling time. In summary, the proposed current control technique is a good alternative both in low and high speeds for industrial applications.

Author Contributions: Conceptualization, O.G., M.A. and J.R.; methodology, O.G., M.A.; software, M.A. and O.G.; validation, O.G., M.A. and J.D.-G.; formal analysis, O.G., M.A., J.D.-G., J.R., R.G. and M.R.; investigation, O.G. and M.A.; resources, J.D.-G.; data curation, J.D.-G., O.G. and M.A.; writing, original draft preparation, O.G., M.A. and J.R.; writing, review and editing, O.G., M.A., J.R., J.D.-G., R.G. and M.R.; visualization, J.D.-G., M.A., J.R., R.G. and M.R.; project administration, O.G., M.A., J.R., and J.D.-G.; funding acquisition, R.G. and J.R.

Funding: This research has been funded through the Consejo Nacional de Ciencia y Tecnología (CONACYT)-Paraguay, Grant Number POSG16-05 and FONDECYT Regular 1160690 Research Project.

Acknowledgments: The authors would like to thank members of the LSPyC, APET and LECPE for their significant comments on this work.

Conflicts of Interest: The authors declare no conflict of interest.

Abbreviations

The following abbreviations have been employed in this work:

FOC	Field Oriented Control
IM	Induction Machine
MPC	Model Predictive Control
PFSCCS	Predictive-Fixed Switching Current Control Strategy
MSE	Mean Squared Error
PI	Proportional-Integral
PWM	Pulse-Width Modulation
SVM	Space Vector Modulation
THD	Total Harmonic Distortion
VSI	Voltage Source Inverter
VSD	Vector Space Decomposition

References

1. Duran, M.J.; Levi, E.; Barrero, F. Multiphase Electric Drives: Introduction. In *Wiley Encyclopedia of Electrical and Electronics Engineering*. Available online: https://onlinelibrary.wiley.com/doi/abs/10.1002/047134608X.W8364 (accessed on 26 April 2019).
2. Precup, R.E.; Kamal, T.; Hassan, S.Z. *Advanced Control and Optimization Paradigms for Wind Energy Systems*; Springer: Berlin/Heidelberg, Germany, 2019.
3. Subotic, I.; Bodo, N.; Levi, E. Integration of six-phase EV drivetrains into battery charging process with direct grid connection. *IEEE Trans. Energy Conv.* **2017**, *32*, 1012–1022. [CrossRef]
4. Ayala, M.; Gonzalez, O.; Rodas, J.; Gregor, R.; Doval-Gandoy, J. A speed-sensorless predictive current control of multiphase induction machines using a Kalman filter for rotor current estimator. In Proceedings of the 2016 International Conference on Electrical Systems for Aircraft, Railway, Ship Propulsion and Road Vehicles & International Transportation Electrification Conference (ESARS-ITEC), Toulouse, France, 2–4 November 2016; pp. 1–6.

5. Munim, W.N.W.A.; Duran, M.J.; Che, H.S.; Bermúdez, M.; González-Prieto, I.; Rahim, N.A. A unified analysis of the fault tolerance capability in six-phase induction motor drives. *IEEE Trans. Power Electron.* **2017**, *32*, 7824–7836. [CrossRef]
6. Jones, M.; Vukosavic, S.N.; Dujic, D.; Levi, E. A synchronous current control scheme for multiphase induction motor drives. *IEEE Trans. Energy Conv.* **2009**, *24*, 860–868. [CrossRef]
7. Kali, Y.; Ayala, M.; Rodas, J.; Saad, M.; Doval-Gandoy, J.; Gregor, R.; Benjelloun, K. Current Control of a Six-Phase Induction Machine Drive based on Discrete-Time Sliding Mode with Time Delay Estimation. *Energies* **2019**, *12*, 170. [CrossRef]
8. Che, H.S.; Duran, M.J.; Levi, E.; Jones, M.; Hew, W.P.; Rahim, N.A. Postfault operation of an asymmetrical six-phase induction machine with single and two isolated neutral points. *IEEE Trans. Power Electron.* **2014**, *29*, 5406–5416. [CrossRef]
9. Mirzaeva, G.; Goodwin, G.C.; McGrath, B.P.; Teixeira, C.; Rivera, M. A generalized MPC framework for the design and comparison of VSI current controllers. *IEEE Trans. Ind. Electron.* **2016**, *63*, 5816–5826. [CrossRef]
10. Vazquez, S.; Rodriguez, J.; Rivera, M.; Franquelo, L.G.; Norambuena, M. Model Predictive Control for Power Converters and Drives: Advances and Trends. *IEEE Trans. Ind. Electron.* **2016**, *64*, 935–947. [CrossRef]
11. Barrero, F.; Arahal, M.R.; Gregor, R.; Toral, S.; Durán, M.J. A proof of concept study of predictive current control for VSI-driven asymmetrical dual three-phase AC machines. *IEEE Trans. Ind. Electron.* **2009**, *56*, 1937–1954. [CrossRef]
12. Barrero, F.; Prieto, J.; Levi, E.; Gregor, R.; Toral, S.; Durán, M.J.; Jones, M. An enhanced predictive current control method for asymmetrical six-phase motor drives. *IEEE Trans. Ind. Electron.* **2011**, *58*, 3242–3252. [CrossRef]
13. Lim, C.S.; Levi, E.; Jones, M.; Rahim, N.A.; Hew, W.P. FCS-MPC-based current control of a five-phase induction motor and its comparison with PI-PWM control. *IEEE Trans. Ind. Electron.* **2013**, *61*, 149–163. [CrossRef]
14. Vijayagopal, M.; Zanchetta, P.; Empringham, L.; De Lillo, L.; Tarisciotti, L.; Wheeler, P. Modulated model predictive current control for direct matrix converter with fixed switching frequency. In Proceedings of the 2015 17th European Conference on Power Electronics and Applications (EPE'15 ECCE-Europe), Geneva, Switzerland, 8–10 September 2015; pp. 1–10.
15. Gregor, R.; Rodas, J.; Munoz, J.; Ayala, M.; Gonzalez, O.; Gregor, D. Predictive-Fixed Switching Frequency Technique for 5-Phase Induction Motor Drives. In Proceedings of the 2016 International Symposium on Power Electronics, Electrical Drives, Automation and Motion (SPEEDAM), Anacapri, Italy, 22–24 June 2016.
16. Ayala, M.; Gonzalez, O.; Rodas, J.; Gregor, R.; Rivera, M. Predictive control at fixed switching frequency for a dual three-phase induction machine with Kalman filter-based rotor estimator. In Proceedings of the 2016 IEEE International Conference on Automatica (ICA-ACCA), Curico, Chile, 19–21 October 2016; pp. 1–6.
17. Rivera, M.; Toledo, S.; Baier, C.; Tarisciotti, L.; Wheeler, P.; Verne, S. Indirect predictive control techniques for a matrix converter operating at fixed switching frequency. In Proceedings of the 2017 IEEE International Symposium on Predictive Control of Electrical Drives and Power Electronics (PRECEDE), Pucón, Chile, 18–20 October 2017; pp. 13–18.
18. Comparatore, L.; Gregor, R.; Rodas, J.; Pacher, J.; Renault, A.; Rivera, M. Model based predictive current control for a three-phase cascade H-bridge multilevel STATCOM operating at fixed switching frequency. In Proceedings of the 2017 IEEE 8th International Symposium on Power Electronics for Distributed Generation Systems (PEDG), Florianopolis, Brazil, 17–20 April 2017; pp. 1–6.
19. Harnefors, L.; Saarakkala, S.; Hinkkanen, M. Speed Control of Electrical Drives Using Classical Control Methods. *IEEE Trans. Ind. Appl.* **2013**, *49*, 889–898. [CrossRef]
20. Zhao, Y.; Lipo, T. Space vector PWM control of dual three-phase induction machine using vector space decomposition. *IEEE Trans. Ind. Electron.* **1995**, *31*, 1100–1109.
21. Ayala, M.; Rodas, J.; Gregor, R.; Doval-Gandoy, J.; Gonzalez, O.; Saad, M.; Rivera, M. Comparative Study of Predictive Control Strategies at Fixed Switching Frequency for an Asymmetrical Six-Phase Induction Motor Drive. In Proceedings of the 2017 IEEE International Electric Machines and Drives Conference (IEMDC), Miami, FL, USA, 21–24 May 2017; pp. 1–8.
22. Rodas, J.; Barrero, F.; Arahal, M.R.; Martin, C.; Gregor, R. On-Line Estimation of Rotor Variables in Predictive Current Controllers: A Case Study Using Five-Phase Induction Machines. *IEEE Trans. Ind. Electron.* **2016**, *63*, 5348–5356. [CrossRef]

23. Rodas, J.; Martin, C.; Arahal, M.R.; Barrero, F.; Gregor, R. Influence of Covariance-Based ALS Methods in the Performance of Predictive Controllers with Rotor Current Estimation. *IEEE Trans. Ind. Electron.* **2017**, *64*, 2602–2607. [CrossRef]
24. Pandit, J.K.; Aware, M.V.; Nemade, R.V.; Levi, E. Direct torque control scheme for a six-phase induction motor with reduced torque ripple. *IEEE Trans. Power Electron.* **2017**, *32*, 7118–7129. [CrossRef]
25. Gonzalez, O.; Ayala, M.; Rodas, J.; Gregor, R.; Rivas, G.; Doval-Gandoy, J. Variable-Speed Control of a Six-Phase Induction Machine using Predictive-Fixed Switching Frequency Current Control Techniques. In Proceedings of the 2018 9th IEEE International Symposium on Power Electronics for Distributed Generation Systems (PEDG), Charlotte, NC, USA, 25–28 June 2018; pp. 1–6.
26. Yepes, A.G.; Riveros, J.A.; Doval-Gandoy, J.; Barrero, F.; López, O.; Bogado, B.; Jones, M.; Levi, E. Parameter identification of multiphase induction machines with distributed windings Part 1: Sinusoidal excitation methods. *IEEE Trans. Energy Conv.* **2012**, *27*, 1056–1066. [CrossRef]
27. Riveros, J.A.; Yepes, A.G.; Barrero, F.; Doval-Gandoy, J.; Bogado, B.; Lopez, O.; Jones, M.; Levi, E. Parameter identification of multiphase induction machines with distributed windings Part 2: Time-domain techniques. *IEEE Trans. Energy Conv.* **2012**, *27*, 1067–1077. [CrossRef]

Model Predictive Current Control of Six-phase Induction Motor Drives using Virtual Vectors and Space Vector Modulation

O. Gonzalez, M. Ayala, C. Romero, L. Delorme, J. Rodas, *Senior Member, IEEE,* R. Gregor, I. Gonzalez-Prieto and M.J. Durán

***Abstract*—The use of multiphase machines has become a suitable choice in high-performance industry applications through advantages such as lesser torque ripple, enhanced current distribution per phase, and fault-tolerance capability. Among different control approaches for the regulation of multiphase drives, model-based predictive current control (MPCC) is one of the most analyzed strategies due to their adaptability and good dynamic response. However, this approach presents some disadvantages, e.g., high $x-y$ currents and increased harmonic content in the fundamental $\alpha-\beta$ stator currents. Modulation strategies have been combined with MPCC to overcome these shortcomings. This paper proposes a modulated model-predictive current control with virtual vectors and space vector modulation for the regulation of an asymmetrical six-phase induction machine to minimize the $x-y$ currents, reduce the harmonic content and, to perform improved stator currents tracking compared with other MPCC versions. Experimental tests are provided to demonstrate the quality of the proposed current control strategy.**

***Index Terms*—Multiphase induction machine, modulation strategies, predictive current control, space vector modulation, virtual vectors.**

I. Introduction

RECENTLY, the use of electrical machines with a number of phases greater than three ($n > 3$), known as multiphase machines, has emerged in the literature due to their outstanding characteristics such as better phase current redistribution and enhanced torque production. Multiphase machines can operate in the presence of faults in contrast to their three-phase counterparts [1]. Additionally, multiphase machines are being adopted for high-demanding electric drive applications, such as electric ship propulsion, electric vehicles and renewable energy systems [2]. However, multiphase drives require the development of elaborated control strategies to regulate the system variables (e.g. speed, currents, flux). According to control strategies such as direct torque control (DTC), which is based on hysteresis controllers [3] and the field-oriented control (FOC) with multiple inner proportional-integer (PI) current controllers [4], they have been analyzed over the years to produce a decoupled control of the torque and flux.

Furthermore, nonlinear controllers have been recently implemented to improve the control of multiphase machines [5], [6]. Model-based predictive control with finite set control (FSC-MPC) combined with FOC or DTC scheme is one of the most analyzed strategies for its inherent fast dynamic response as well as the capacity to include various control objectives in comparison to linear controllers, addressed in [7]–[10]. Furthermore, the combination of sliding-mode controller with FOC has been also studied in the literature to provide a more robust controller [11], [12].

However, the FSC-MPC, named as MPCC henceforth in the document for the sake of simplicity, faces some disadvantages when it is applied to multiphase machines. Some of them are the large $x-y$ currents which are related to copper losses and large current harmonic content due to the absence of a modulator, resulting in a variable switching frequency. [10], [13]. Recent work has been presented to deal with these drawbacks.

In [14], a comparative study of MPCC variants was presented to mitigate the $x-y$ currents for an asymmetrical six-phase induction machine (IM), however the $\alpha-\beta$ currents tracking got worse. Then an MPCC at a fixed switching frequency (MPCC-FSF) using a switching pattern applied to a two-level six-phase voltage source inverter (2L-6PVSI) was presented in [15], improving the $\alpha-\beta$ currents tracking greatly and the $x-y$ currents reduction, but the improvement is only very effective at a lower mechanical speed of the motor. On the other hand, a new MPCC variant with the name of virtual vectors (VV) was proposed in [16], which it produces an average zero $x-y$ voltages which reduce the $x-y$ currents dramatically, but at the cost of reducing the voltage range in the $\alpha-\beta$ plane. Later an improvement of the MPCC with VV was presented in [17], where a modulation stage regarding two adjacent VV is implemented. However, the modulation is limited to voltage vectors in line with the fixed VV, sparing the control effort of the MPCC. Lastly, a novel modulated MPCC was proposed in [18] to deal with $x-y$ currents and to improve the steady-state quality of stator currents. The improvement was noticed in the steady-state performance and the stability of the whole system, but the improvement of $x-y$ currents reduction was little. So another work regarding a comparative

O. Gonzalez, M. Ayala, C. Romero, J. Rodas and R. Gregor are with the Laboratory of Power and Control Systems, Facultad de Ingenieria, Universidad Nacional de Asuncion, Paraguay e-mail: (ogonzalez@ing.una.py, mayala@ing.una.py, cromero@ing.una.py, jrodas@ing.una.py, rgregor@ing.una.py).

L. Delorme is with the Universidad del Cono Sur de las Americas, Asuncion, Paraguay e-mail:(laridelorme@gmail.com)

I. Gonzalez-Prieto, M. J. Duran are with the Department of Electrical Engineering, Universidad de Malaga, Malaga, Spain e-mail: (ignaciogp87@gmail.com, mjduran@uma.es)

assessment of MPCC with modulation strategies was presented in [19], where the $x-y$ currents reduction was improved over the above-mentioned techniques, but the validation of this work is still missing.

The main contribution of this paper is the implementation of a new scheme of the modulated predictive current control strategy using virtual vectors and space vector modulation (SVM). The latter extends the control effort by encompassing the entire area between two virtual space vectors to perform a better $\alpha-\beta$ current tracking and reduced $x-y$ currents applied to a six-phase (IM) fed by 2L-6PVSI. To demonstrate the effectiveness of the proposed strategy compared to the other state-of-the-art MPCC analyzed in this work, experimental tests are presented in terms of mean square error (MSE) and total harmonic distortion (THD) of stator currents under different system conditions.

This paper is organized as follows. The asymmetrical six-phase IM modeling with 2L-6PVSI supply is analyzed in Section II. The fundamental principles of the classic MPCC and its implementation are presented in Section III. Section IV presents the MPCC with VV. Section V describes the MPCC-FSF design and Section VI presents the proposed MPCC. The experimental tests for the classic MPCC, MPCC with VV, MPCC-FSF and the proposed MPCC are addressed and discussed in Section VII. Conclusions are presented in the last section.

II. Six-Phase IM And 2L-6PVSI Mathematical Model

Before applying the proposed strategy, the mathematical model of the system must be taken into account, which is composed of distributed windings for the asymmetrical six-phase IM fed through a 2L-6PVSI connected to a dc-link voltage source (V_{dc}) as shown in Fig. 1. In that context, the two isolated gate bipolar transistors (IGBT) of the power converter per phase can be defined as S_p, with $S_p = 1$ if the upper IGBT is up and the bottom is down or $S_p = 0$ if the contrary occurs. As a result, the switching states of the 2L-6PVSI per phase can be grouped in a vector ($[S_p] = [S_a, S_d, S_b, S_e, S_c, S_f]$), generating 64 possible switching states according to the number of phases of the machine. Thus, using V_{dc} and the S_p vector, the stator phase voltages are calculated as follows:

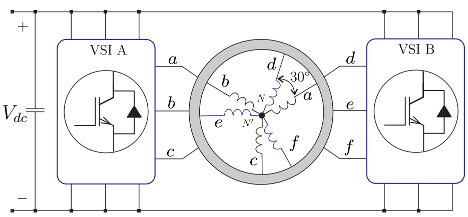

Fig. 1. Six-phase IM fed by 2L-6PVSI.

$$\begin{bmatrix} v_{as} \\ v_{ds} \\ v_{bs} \\ v_{es} \\ v_{cs} \\ v_{fs} \end{bmatrix} = \frac{V_{dc}}{3} \begin{bmatrix} 2 & 0 & -1 & 0 & -1 & 0 \\ 0 & 2 & 0 & -1 & 0 & -1 \\ -1 & 0 & 2 & 0 & -1 & 0 \\ 0 & -1 & 0 & 2 & 0 & -1 \\ -1 & 0 & -1 & 0 & 2 & 0 \\ 0 & -1 & 0 & -1 & 0 & 2 \end{bmatrix} {S_p}^T. \tag{1}$$

where T is the transposed operation. Subsequently, to simplify the system modeling, vector space decomposition (VSD) theory based on an invariant amplitude was employed [20]. Thus, stator phase voltages that initially were expressed in phase variables, as specified in (1), are projected into three two-dimensional orthogonal planes, denoted as $\alpha-\beta$, $x-y$, and z_1-z_2 according to (2). This transformation ensures that the produced planes are entirely decoupled from each other, where the electromechanical energy conversion (flux and torque production) is associated with $\alpha-\beta$ plane, while the system losses are projected in $x-y$ plane and the z_1-z_2 components are neglected due to the isolated neutral points design of the six-phase IM.

$$T_C = \frac{1}{3} \begin{bmatrix} 1 & \frac{\sqrt{3}}{2} & -\frac{1}{2} & -\frac{\sqrt{3}}{2} & -\frac{1}{2} & 0 \\ 0 & \frac{1}{2} & \frac{\sqrt{3}}{2} & \frac{1}{2} & -\frac{\sqrt{3}}{2} & -1 \\ 1 & -\frac{\sqrt{3}}{2} & -\frac{1}{2} & \frac{\sqrt{3}}{2} & -\frac{1}{2} & 0 \\ 0 & \frac{1}{2} & -\frac{\sqrt{3}}{2} & \frac{1}{2} & \frac{\sqrt{3}}{2} & -1 \\ 1 & 0 & 1 & 0 & 1 & 0 \\ 0 & 1 & 0 & 1 & 0 & 1 \end{bmatrix}. \tag{2}$$

Hence, the voltage vectors, which include 15 redundant and 49 non-redundant vectors obtained from the combination of the switching states are represented in Fig. 2. Besides, using the state-space representation, the six-phase IM can be written as:

$$\dot{X}_{(t)} = A_{(t)}\, X_{(t)} + B_{(t)}\, U_{(t)} + H n_{p(t)} \tag{3}$$

defining $X_{(t)}$ as the state vector, formed by stator and rotor currents as shown in (4), $U_{(t)}$ as the input vector constituted by the stator voltages represented by (5), $n_{p(t)}$ as the process noise, and H as the noise weight matrix. At the same time, $A_{(t)}$ and $B_{(t)}$ are the matrices that contain the electrical parameters of the six-phase IM expressed in (6) and (7), respectively.

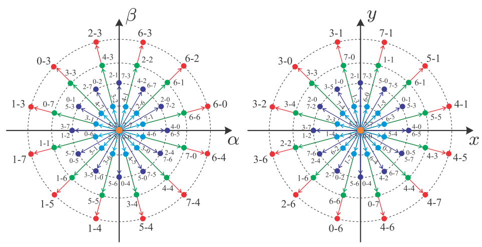

Fig. 2. Voltage vectors for the asymmetrical six-phase IM in the $\alpha-\beta$ and $x-y$ planes.

$$X_{(t)} = [x_1, x_2, x_3, x_4, x_5, x_6]^T = [i_{\alpha s}, i_{\beta s}, i_{xs}, i_{ys}, i_{\alpha r}, i_{\beta r}]^T \quad (4)$$

$$U_{(t)} = [u_1, u_2, u_3, u_4]^T = [u_{\alpha s}, u_{\beta s}, u_{xs}, u_{ys}]^T \quad (5)$$

$$A_{(t)} = \begin{bmatrix} a_{11} & a_{12} & 0 & 0 & a_{15} & a_{16} \\ a_{21} & a_{22} & 0 & 0 & a_{25} & a_{26} \\ 0 & 0 & a_{33} & 0 & 0 & 0 \\ 0 & 0 & 0 & a_{44} & 0 & 0 \\ a_{51} & a_{52} & 0 & 0 & a_{55} & a_{56} \\ a_{61} & a_{62} & 0 & 0 & a_{65} & a_{66} \end{bmatrix} \quad (6)$$

$$B_{(t)} = \begin{bmatrix} b_{11} & 0 & 0 & 0 \\ 0 & b_{22} & 0 & 0 \\ 0 & 0 & b_{33} & 0 \\ 0 & 0 & 0 & b_{44} \\ b_{51} & 0 & 0 & 0 \\ 0 & b_{62} & 0 & 0 \end{bmatrix} \quad (7)$$

taking into account that:

$$a_{11} = a_{22} = -\frac{R_s L_r}{L_s L_r - L_m^2} \qquad a_{12} = -a_{21} = \frac{L_m^2 \omega_r}{L_s L_r - L_m^2}$$
$$a_{15} = a_{26} = \frac{R_r L_m}{L_s L_r - L_m^2} \qquad a_{16} = -a_{25} = \frac{L_m L_r \omega_r}{L_s L_r - L_m^2}$$
$$a_{33} = a_{44} = -\frac{R_s}{L_{ls}} \qquad a_{51} = a_{62} = \frac{R_s L_m}{L_s L_r - L_m^2}$$
$$a_{52} = -a_{61} = -\frac{L_s L_m \omega_r}{L_s L_r - L_m^2} \qquad a_{55} = a_{66} = -\frac{R_r L_s}{L_s L_r - L_m^2}$$
$$a_{56} = -a_{65} = -\frac{L_r L_s \omega_r}{L_s L_r - L_m^2} \qquad b_{11} = b_{22} = \frac{L_r}{L_s L_r - L_m^2}$$
$$b_{33} = b_{44} = \frac{1}{L_{ls}} \qquad b_{51} = b_{62} = -\frac{L_m}{L_s L_r - L_m^2}$$

Consequently, the six-phase IM equations presented in (3) are written as:

$$\begin{aligned} \dot{x_1} &= a_{11}x_1 + a_{12}x_2 + a_{15}x_5 + a_{16}x_6 + b_{11}u_1 \\ \dot{x_2} &= a_{21}x_1 + a_{22}x_2 + a_{25}x_5 + a_{26}x_6 + b_{22}u_2 \\ \dot{x_3} &= a_{33}x_3 + b_{33}u_3 \\ \dot{x_4} &= a_{44}x_4 + b_{44}u_4 \\ \dot{x_5} &= a_{51}x_1 + a_{52}x_2 + a_{55}x_5 + a_{56}x_6 + b_{51}u_1 \\ \dot{x_6} &= a_{61}x_1 + a_{62}x_2 + a_{65}x_5 + a_{66}x_6 + b_{62}u_2 \end{aligned} \quad (8)$$

where $L_s = L_{ls} + L_m$, $L_r = L_{lr} + L_m$, R_s, and R_r are the electrical parameters of the six-phase IM. Then, the input ($U_{(t)}$) and the output ($Y_{(t)}$) vectors, considering the measurement noise ($n_{m(t)}$) in the output, are computed as follows:

$$U_{(t)} = T_C \begin{bmatrix} v_{as} \\ v_{ds} \\ v_{bs} \\ v_{es} \\ v_{cs} \\ v_{fs} \end{bmatrix} \quad (9)$$

$$Y_{(t)} = \begin{bmatrix} 1 & 0 & 0 & 0 & 0 & 0 \\ 0 & 1 & 0 & 0 & 0 & 0 \\ 0 & 0 & 1 & 0 & 0 & 0 \\ 0 & 0 & 0 & 1 & 0 & 0 \end{bmatrix} X_{(t)} + n_{m(t)} \quad (10)$$

The torque ($\mathbf{T_e}$) of the six-phase IM and the load torque ($\mathbf{T_L}$) are calculated through the next equations:

$$\mathbf{T_e} = 3P\left(\psi_{\alpha s} i_{\beta s} - \psi_{\beta s} i_{\alpha s}\right) \quad (11)$$

$$J_i \dot{\omega}_m + B_i \omega_m = (\mathbf{T_e} - \mathbf{T_L}) \quad (12)$$

$$\omega_m = \frac{\omega_r}{P} \quad (13)$$

being J_i, B_i, ω_m, ω_r, $\psi_{\alpha s}$, $\psi_{\beta s}$ and P, the inertia coefficient, the friction coefficient, the rotor mechanical speed, the rotor electrical speed, the stator fluxes and the number of pole pairs, respectively.

III. Classic MPCC

To apply the classic MPCC, a discretization method, obtained from the forward-Euler equation, is applied to (3) to predict the future step of the output variables considering the measurable variables such as the rotor mechanical speed and the stator phase currents. Therefore, the prediction is computed as follows:

$$\hat{X}_{(k+1|k)} = X_{(k)} + f\left(X_{(k)},\, U_{(k)},\, \omega_{r(k)},\, T_s\right) \quad (14)$$

where k and T_s represent the actual sample and the sampling period, respectively.

However, according to (14), rotor currents are non-measurable variables. Thus, to face this difficulty a reduced-order observer needs to be implemented to estimate only the unmeasured variables of $X_{(t)}$. This subject has been addressed in [21]–[23]. In this work, a reduced-order observer based on the Kalman filter (KF) has been implemented because it takes into account the uncorrelated process and the measurement noises to optimize the filter parameters, thus enhancing the predictions in the controller. Therefore, the discrete state-space modeling can be expressed as:

$$\hat{X}_{(k+1|k)} = A_{(k)} X_{(k)} + B_{(k)} U_{(k)} + H n_{p(k)} \quad (15)$$

$$Y_{(k+1|k)} = \begin{bmatrix} 1 & 0 & 0 & 0 & 0 & 0 \\ 0 & 1 & 0 & 0 & 0 & 0 \\ 0 & 0 & 1 & 0 & 0 & 0 \\ 0 & 0 & 0 & 1 & 0 & 0 \end{bmatrix} X_{(k+1)} + n_{m(k+1)}. \quad (16)$$

The discretized matrices $A_{(k)}$ and $B_{(k)}$ are represented in (17) and (18), respectively. $A_{(k)}$ depends on the present amount of the rotor electrical speed and it must be updated every sampling period.

$$A_{(k)} = \begin{bmatrix} a_{11(k)} & a_{12(k)} & 0 & 0 & a_{15(k)} & a_{16(k)} \\ a_{21(k)} & a_{22(k)} & 0 & 0 & a_{25(k)} & a_{26(k)} \\ 0 & 0 & a_{33(k)} & 0 & 0 & 0 \\ 0 & 0 & 0 & a_{44(k)} & 0 & 0 \\ a_{51(k)} & a_{52(k)} & 0 & 0 & a_{55(k)} & a_{56(k)} \\ a_{61(k)} & a_{62(k)} & 0 & 0 & a_{65(k)} & a_{66(k)} \end{bmatrix} \quad (17)$$

$$B_{(k)} = \begin{bmatrix} b_{11(k)} & 0 & 0 & 0 \\ 0 & b_{22(k)} & 0 & 0 \\ 0 & 0 & b_{33(k)} & 0 \\ 0 & 0 & 0 & b_{44(k)} \\ b_{51(k)} & 0 & 0 & 0 \\ 0 & b_{62(k)} & 0 & 0 \end{bmatrix} \quad (18)$$

The coefficients of the matrices are detailed in the Appendix section.

Besides, another important component in the MPCC to be considered is the cost function (J), which can be expressed according to the variables to be optimized, e.g., harmonic content reduction and switching losses [24]. In this work, the current tracking error in the prediction of the stator currents has been considered. In this regard, the cost function is computed for all control signals, i.e., 64 times for the six-phase IM to obtain the lowest one to be applied in the next sampling period. The current tracking error between the reference ($i^*_{s(k+2)}$) and their predicted values ($\hat{i}_{s(k+2)}$) in the $\alpha-\beta$ and $x-y$ planes is calculated as follows:

$$J = \sqrt{(e_{\alpha s})^2 + (e_{\beta s})^2 + \lambda_{xy}[(e_{xs})^2 + (e_{ys})^2]} \tag{19}$$

where

$$\begin{aligned} e_{\alpha s} &= i^*_{\alpha s(k+2)} - \hat{i}_{\alpha s(k+2)} \\ e_{\beta s} &= i^*_{\beta s(k+2)} - \hat{i}_{\beta s(k+2)} \\ e_{xs} &= i^*_{xs(k+2)} - \hat{i}_{xs(k+2)} \\ e_{ys} &= i^*_{ys(k+2)} - \hat{i}_{ys(k+2)}. \end{aligned} \tag{20}$$

which J is based on a four dimension distance formula.

It must be noted that a second-step ahead prediction is implemented to consider the delay compensation. This fact is produced by a notable amount of time in the computation of the control signals comparable to the sampling period [25], [26]. The tuning parameter (λ_{xy}) in (19) is usually considered in the control of the multiphase machines to provide greater weight to the $\alpha-\beta$ currents over the $x-y$ currents.

IV. MPCC WITH VV

The strategy of the MPCC with VV consists in the use of two aligned non-null voltage vectors, composed by the large vector (filled red circle) and the medium-large vector (filled green circle) as shown in Fig. 3, which are implemented at every sampling period. The dwell time of the vectors (d_l and d_{ml}) are obtained from a system of equations considering the modules of the analyzed vectors. Thus, the MPCC with VV can be expressed as follows:

$$\mathbf{VV} = d_l V_{large} + d_{ml} V_{mid-large} \tag{21}$$

being $d_l = 0.73\ T_s$ and $d_{ml} = 0.27\ T_s$, which produces 93% of the actual value of the large vector in $\alpha-\beta$ plane but as well generates zero average value of the $x-y$ currents due to the fact that the two selected vectors have opposite projections in $x-y$ plane [16], [27].

V. MPCC-FSF

The MPCC-FSF establishes each obtainable sector according to the SVM strategy for the 2L-6PVSI in the $\alpha-\beta$ plane. The sectors are formed by two consecutive large vectors or outer vectors (filled red circle) and a null vector (filled orange circle), as depicted in Fig. 4. This strategy calculates the predictions of the two consecutive vectors that minimize the cost function (J) and is performed independently for each vector, whose respective cost functions are named J_0, J_1 and J_2, to find the appropriate sector of the 12 sectors in total and, this procedure is carried out at every sampling period. The predictions are computed according to (19). Also, it can be noted that this procedure only changes in the input vector computation. The MPCC-FSF aims to cover the entire $\alpha-\beta$ plane by using large vectors and these vectors are projected as the smallest ones in the $x-y$ plane providing reduced $x-y$ currents.

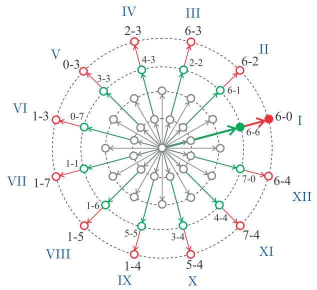

Fig. 3. Space sectors in the $\alpha-\beta$ plane for MPCC with VV.

Hence, the duty cycles for both the pairs of large vectors and for the null vector are represented by the following equations:

$$d_1 = \tfrac{\rho}{J_1} \quad d_2 = \tfrac{\rho}{J_2} \quad d_0 = \tfrac{\rho}{J_0} \tag{22}$$

$$d_1 + d_2 + d_0 = 1. \tag{23}$$

By solving the above equations, it can be calculated the value of ρ and the duty cycles, d_1, d_2 and d_0, respectively, which are related to their corresponding cost functions specified as:

$$d_1 = \frac{J_0 J_2}{J_0 J_1 + J_1 J_2 + J_0 J_2} \tag{24}$$

$$d_2 = \frac{J_0 J_1}{J_0 J_1 + J_1 J_2 + J_0 J_2} \tag{25}$$

$$d_0 = \frac{J_1 J_2}{J_0 J_1 + J_1 J_2 + J_0 J_2}. \tag{26}$$

This strategy assesses the 12 sectors over a sampling period according to a new cost function defined in (27). The two large vectors which minimize the new cost function are considered to be implemented to the 2L-6PVSI at the next sampling period.

$$J'_{(k+2)} = d_1 J_1 + d_2 J_2. \tag{27}$$

Furthermore, it must be provided with the relationships between the duty cycles and the selected vectors to implement this strategy. The latter can be done by using (28).

$$D_j = \frac{d_0}{2} + d_1 v_{1(j)} + d_2 v_{2(j)} \tag{28}$$

being D_j the duty cycles per phase with $j = (a, b, c, d, e, f)$ where the values of D_j are normalized between 0 and 1 and are compared with a triangular signal to produce a symmetric pulse with modulation (PWM) to be applied to the converter.

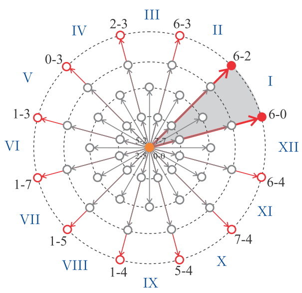

Fig. 4. Space sectors in the $\alpha - \beta$ plane for MPCC-FSF.

VI. Proposed MPCC

The proposed MPCC also uses the SVM strategy. This modulation strategy allows a vector combination from their respective projections in the $\alpha - \beta$ plane producing the obtainable sectors for the 2L-6PVSI. Subsequently, the proposed MPCC employs 5 vectors per sector, where each sector is composed of two consecutive large vectors (filled red circle), two consecutive medium-large vectors (filled green circle), and a null vector (filled orange circle). Fig. 5 shows the resulting 12 sectors. The predictions for the vectors are computed in the same way as the previous strategy (19). Hence, the primary purpose of the proposed MPCC is to generate null $x - y$ currents by incorporating the medium-large vectors in the modulation strategy in the stator currents tracking. This fact arises because the medium-large vectors are aligned with the large vectors and they have the same direction in the $\alpha - \beta$ plane, however, large vectors have opposite directions than medium-large vectors in the $x - y$ plane. Note that the medium-large vectors keep their projections in both planes. Therefore, the proposed MPCC takes advantage of this characteristic to produce the expected results in a similar way to MPCC with VV with the difference that this technique covers the entire area of the voltage space vectors between two VV.

In that sense, to implement the proposed MPCC in a digital signal processor (DSP) using the 5 vectors of each sector and

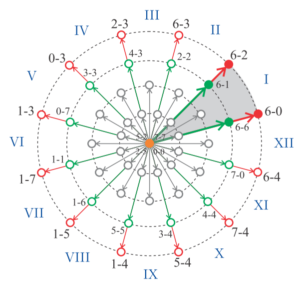

Fig. 5. Space sectors in the $\alpha - \beta$ plane for the proposed MPCC.

considering the dwell time of the MPCC with VV, it has been used a single interrupt routine that is equal to the sampling period. Then, the duty cycles and the cost function are also obtained from the (22) to (26) and (27), respectively.

It is worth mentioning that after obtaining the optimal duty cycles for the large vectors, these are also employed for the medium-large vectors to implement the proposed modulation strategy according to the chosen voltage vectors. However, to generate the percentage of time required (which is a function of T_s) for the considered vectors to produce reduced $x - y$ currents and improved $\alpha - \beta$ currents tracking, each large vector must be applied three times (75% of T_s). While each medium-large vector once (25% of T_s), i.e., to perform the control algorithm once, the interruption routine runs four times, applying the suitable vector combination each time. Note that this approach produces a reduction of four times the original sampling frequency. Moreover, the application of the selected vectors must follow a specific order so they can be synthesized by (28) [15], [18]. For instance, in the sector I, the large vectors are applied from V_1 (6-0) to V_2 (6-2) but the combinations between the large vectors and the medium-large vectors are applied in two different ways, firstly from V_1 (6-0) to V_4 (6-1) and secondly from V_2 (6-2) to V_3 (6-6) as shown in Fig. 6. The procedure is repeated depending on where the current reference is located. This method enables the synthesis of any voltage vector per sector during the modulation by using (28), which represents the relationship between the duty cycles of every leg of the 2L-6PVSI and the selected vectors. At last, the duty cycles are compared with a triangular waveform to generate a symmetric PWM to be applied to the VSI.

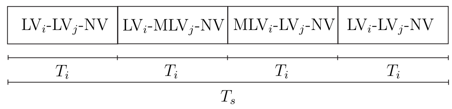

Fig. 6. Applied Vector pattern for the proposed MPCC.

VII. Experimental Results

The proposed MPCC technique is tested to analyze its performance compared to classic MPCC, MPCC at FSF and MPCC with VV through experimental results gathered in the six-phase IM bench.

A. Six-phase IM bench description

The bench is based on a six-phase IM fed by a 2L-6PVSI, using a three phase diode rectifier from the power grid through a step-down transformer obtaining 325 V for the dc-link. The 2L-6PVSI is controlled by a DSP (TMS320F28335 from Texas Instruments), with an MCK28335 development environment from Technosoft. The results are then processed using MATLAB script. Table I shows the parameters of the six-phase IM determined by stand-still with VSI tests and conventional methods of ac time domain [28], [29].

The current measurements were obtained with current sensors LA 55-P s, with many turns to improve precision at low

TABLE I
ELECTRICAL AND MECHANICAL PARAMETERS OF THE SIX-PHASE IM

Parameter	Value	Parameter	Value
R_r	0.63 Ω	L_s	206.2 mH
R_s	0.62 Ω	P	3
L_{ls}	6.4 mH	P_w	15 kW
L_{lr}	3.5 mH	J_i	0.27 kg.m^2
L_m	66.6 mH	B_i	0.012 kg.m^2/s
L_r	203.3 mH	ω_{r-nom}	1000 rpm

Fig. 7. Test bench composed of the 2L-6PVSI, DSP unit control, six-phase IM and the mechanical load.

current amplitude, and it has a frequency bandwidth from DC up to 200 kHz. Those values are then converted to discrete values through a 16-bit A/D converter. The six-phase rotor angle is measured with a 10 000 ppr incremental encoder and the mechanical speed is obtained from it. Finally, a fixed mechanical brake pad, set to approximately 120 Nm, is used as a mechanical load for the six-phase IM. A block diagram of the test bench is shown in Fig. 7.

The defined cost function in (19) with $\lambda_{xy} = 0.01$ was selected to evaluate the performance of the proposed MPCC, prioritizing the $\alpha-\beta$ current tracking. The selection of λ_{xy} is made through a heuristic method. The process and measurement noise covariances, from (15) and (16), can be estimated by using the autocovariance-least-squared (ALS) method proposed in [30]. The obtained values are $\hat{Q}_w = 0.0022$ and $\hat{R}_v = 0.0022$.

B. Figures of merit

The performance of the proposed MPCC is analyzed and compared to classic MPCC, MPCC with VV and MPCC at FSF in steady-state and transient operation. The experimental results show the controllers performance in terms of MSE between the reference and measured stator currents in $\alpha-\beta$ and $x-y$ planes [31]. At last, THD is calculated in $\alpha-\beta$ plane to complete the study. The MSE is defined as:

$$\mathrm{MSE}(i_{s\Phi}) = \sqrt{\frac{1}{N}\sum_{k=1}^{N}(i_{s\Phi}[k] - i^*_{s\Phi}[k])^2} \qquad (29)$$

where N is the number of samples, $i^*_{s\Phi}$ the stator currents reference, $i_{s\Phi}$ the measured stator currents and $\Phi \in \{\alpha, \beta, x, y\}$. At the same time, THD is defined as:

$$\mathrm{THD}(i_s) = \sqrt{\frac{1}{i_{s1}^2}\sum_{j=2}^{N}(i_{sj})^2} \qquad (30)$$

where i_{s1} is the fundamental component of the stator currents and i_{sj} are the harmonic stator currents.

C. Steady-state study

For all cases, $x-y$ current references are fixed to zero ($i^*_{xs} = i^*_{ys} = 0$), and d-axis current ($i^*_{ds} = 1.5$ A) has been considered. The sampling frequency in all tests for classic MPCC and MPCC-FSF is 10 kHz, and 5 kHz for MPCC with VV and the proposed MPCC because the sampling frequency is divided by 4 for both techniques and the hardware limit does not allow the further increase. Five steady-state operating points are considered with mechanical rotor speeds of 100 to 500 rpm.

Table II shows the experimental results for classic MPCC, in terms of MSE of stator currents in $\alpha-\beta$ and $x-y$ planes and THD (%) in $\alpha-\beta$ plane. The results denote good current tracking in $\alpha-\beta$ plane. However, the $x-y$ current reduction is poor, and the performance is similar at higher rotor speed.

Table III presents the results of MPCC-FSF which show a far better performance in terms of $x-y$ current reduction compared to classic MPCC. However, the performance is worse for $\alpha-\beta$ current tracking. At the same time, Table IV depicts the performance of MPCC with VV which significantly improves the tracking and reduction of $\alpha-\beta$ and $x-y$ currents compared to classic MPCC. Table V exposes the proposed MPCC in terms of currents tracking. It can be seen that the proposed MPCC greatly improves the $x-y$ current reduction compared to the other techniques. At the same time the THD is also better, and the $\alpha-\beta$ currents tracking is good compared to classic MPCC.

Fig. 8 shows the stator current tracking in $\alpha-\beta$ and $x-y$ planes for classic MPCC, MPCC-FSF. MPCC with VV and the proposed MPCC. The operations were tested at a rotor speed of 200 rpm for all the techniques. The figures reveal that $x-y$ currents are considerably lower for the proposed MPCC than the other MPCC techniques and proper current tracking in the $\alpha-\beta$ plane.

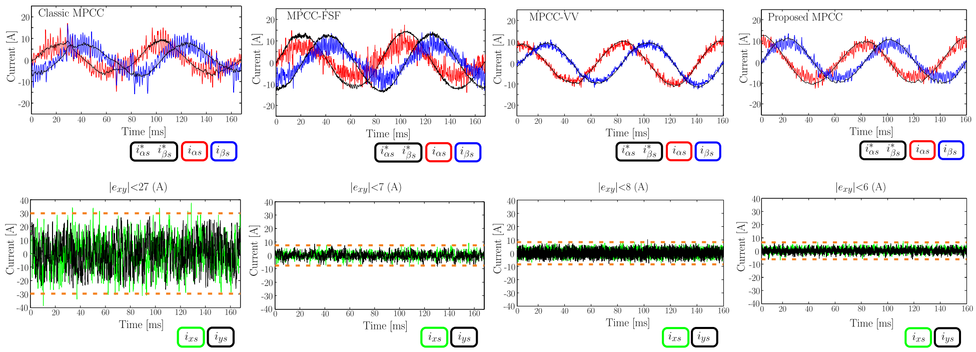

(a) (b) (c) (d)

Fig. 8. Performance of stator currents in $\alpha-\beta$ and $x-y$ planes for a rotor speed of 200 [rpm]: (a) Classic MPCC; (b) MPCC-FSF; (c) MPCC with VV and (d) Proposed MPCC.

TABLE II
STATOR CURRENTS IN $\alpha-\beta$ AND $x-y$ PLANES, CONSIDERING MSE [A] AND THD [%] FOR CLASSIC MPCC AT DIFFERENT ROTOR SPEEDS.

	Classic MPCC	at	f_s = 10 [kHz]		
ω_m^*	MSE$_\alpha$	MSE$_\beta$	MSE$_x$	MSE$_y$	THD$_\alpha$
100	3.25	2.65	14.14	13.04	18.68
200	3.23	2.63	12.85	14.38	19.13
300	3.32	2.89	15.05	14.45	15.56
400	3.33	2.95	14.26	14.22	18.09
500	3.57	3.39	15.12	15.68	17.49

TABLE III
STATOR CURRENTS IN $\alpha-\beta$ AND $x-y$ PLANES, CONSIDERING MSE [A] AND THD [%] FOR MPCC-FSF AT DIFFERENT ROTOR SPEEDS.

	MPCC-FSF	at	f_s = 10 [kHz]		
ω_m^*	MSE$_\alpha$	MSE$_\beta$	MSE$_x$	MSE$_y$	THD$_\alpha$
100	3.23	2.89	2.19	2.51	13.99
200	4.59	4.42	2.23	2.28	11.85
300	5.01	5.41	2.55	2.76	10.18
400	5.16	5.51	2.46	2.98	10.56
500	5.30	5.23	2.36	2.84	10.09

TABLE IV
STATOR CURRENTS IN $\alpha-\beta$ AND $x-y$ PLANES, CONSIDERING MSE [A] AND THD [%] FOR MPCC WITH VV AT DIFFERENT ROTOR SPEEDS.

	MPCC with VV	at	f_s = 5 [kHz]		
ω_m^*	MSE$_\alpha$	MSE$_\beta$	MSE$_x$	MSE$_y$	THD$_\alpha$
100	1.28	1.10	2.68	2.90	9.42
200	1.37	1.25	2.69	2.91	10.86
300	1.51	1.32	2.65	2.95	12.43
400	1.66	1.51	2.66	2.87	14.02
500	1.88	1.75	2.58	2.93	17.07

TABLE V
STATOR CURRENTS IN $\alpha-\beta$ AND $x-y$ PLANES, CONSIDERING MSE [A] AND THD [%] FOR THE PROPOSED MPCC AT DIFFERENT ROTOR SPEEDS.

	Proposed MPCC	at	f_s = 5 [kHz]		
ω_m^*	MSE$_\alpha$	MSE$_\beta$	MSE$_x$	MSE$_y$	THD$_\alpha$
100	2.34	2.07	1.84	1.90	10.11
200	2.48	2.25	1.76	1.74	10.89
300	2.49	2.29	1.95	1.91	12.06
400	2.97	2.76	1.92	1.89	12.04
500	3.01	2.90	2.02	1.91	16.14

D. High-speed operation

A high-speed operation is performed, so the DC-link is increased to 575 V to operate at nominal magnetic flux. The current ripple is also increased as the voltage switching is higher. The rated speed results are shown in Fig. 10 and Fig. 11. The system performance is decreased, but it operates very well with almost nominal torque.

E. Transient study

For a transient operation, a step modification in the rotor speed is considered from 200 to -200 rpm (reversal condition). Fig. 9 presents a dynamic test (q current tracking), which reveals the transient operation of classic MPCC (a), MPCC with VV (b), MPCC-FSF (c) and the proposed MPCC (d) for a step-change in the q current (i_{qs}^*). The dynamic performance is obtained through a reversal condition of the rotor speed (ω_m^*). The overshoot and reaching time of all the techniques are very similar, as for the proposed MPCC is approximately 12.5 % and 0.5 ms, respectively.

F. Robustness study

The robustness study consists of comparing the controllers at the nominal L_m value and a variation of 25% of the nominal value, as L_m is considered the most sensitive parameter in six-phase IM [8], [32]. This study is performed by considering the

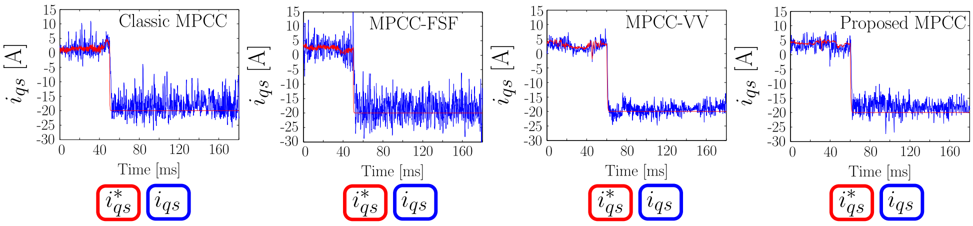

(a) (b) (c) (d)

Fig. 9. Transient response in q-axis of stator current for a rotor speed change from 200 [rpm] to -200 [rpm]: (a) Classic MPCC; (b) MPCC-FSF; (c) MPCC with VV and (d) Proposed MPCC.

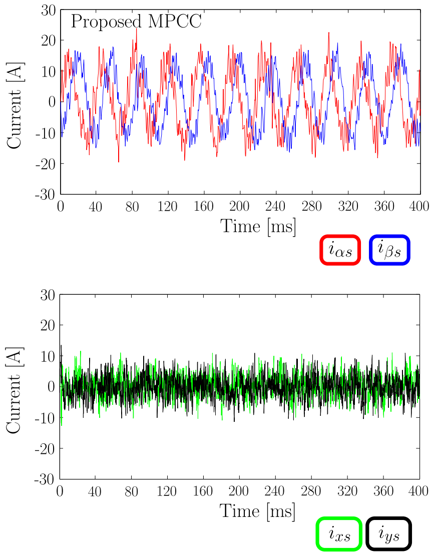

Fig. 10. Performance of stator currents in $\alpha - \beta$ and $x - y$ planes at rated speed.

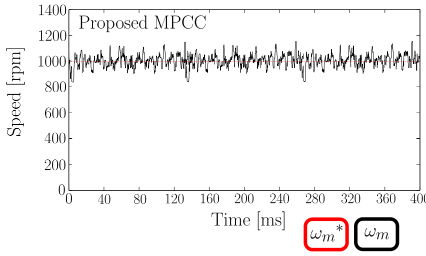

Fig. 11. Performance of the rotor mechanical speed and its reference at nominal condition for the proposed MPCC.

TABLE VI
ANALYSIS OF STATOR CURRENTS UNDER VARIATION OF L_m.

ω_m^* = 400 [rpm]					
Techniques	MSE$_\alpha$	MSE$_\beta$	MSE$_x$	MSE$_y$	THD$_\alpha$
Classic MPCC	3.12	2.93	13.92	14.91	20.83
MPCC with VV	2.12	1.73	2.83	3.08	14.48
MPCC-FSF	4.46	2.70	2.56	2.59	12.82
Proposed MPCC	3.13	2.52	1.79	1.73	10.27

effect of magnetic saturation of the six-phase IM, where L_m value typically changes in approximately that ratio. Table VI shows the control performance with an L_m change of 25 % of the nominal value to analyze the control robustness parameter sensitivity. The results reveal that the four techniques present considerable robustness as the figures of merit do not change much compared to nominal L_m. Notably, the proposed MPCC presents slightly better results in terms of MSE and the THD is moderately worse, but all values remain in a similar range.

G. Comparative analysis

Finally, Table VII presents a comparative analysis of the performance all the analyzed MPCC techniques, in terms of %, where positive (+) and negative ($-$) values mean improvement and deterioration respectively, which is obtained as follows:

$$\text{Imp}\ (\%) = 100\frac{\text{refMPCC}_{\text{data}} - \text{proposedMPCC}_{\text{data}}}{\text{refMPCC}_{\text{data}}} \quad (31)$$

where "data" could be MSE of stator currents in $\alpha - \beta$ and $x - y$ planes or THD of $\alpha - \beta$ stator currents and refMPCC could be classic MPCC, MPCC-FSF and MPCC with VV.

VIII. Conclusion

The paper proposes implementing a modulation strategy with virtual vectors and space vector modulation applied to an asymmetrical six-phase IM. The strategy has been developed to enhance the stator current tracking in the $\alpha-\beta$ plane and to produce null $x-y$ currents using large, medium-large, and null vectors. Experimental tests are done to prove the effectiveness of the proposed MPCC compared to other strategies such as

TABLE VII
COMPARATIVE ANALYSIS (%) OF THE PROPOSED MPCC OVER CLASSIC MPCC, MPCC-FSF AND MPCC WITH VV.

Proposed MPCC over classic MPCC			
ω_m^*	MSE$_{\alpha\beta}$	MSE$_{xy}$	THD$_\alpha$
100	+25.25	+86.23	+45.88
200	+19.28	+87.15	+43.07
300	+23.03	+86.92	+22.49
400	+8.76	+86.62	+33.44
500	+15.09	+87.24	+7.72
Proposed MPCC over MPCC-FSF			
100	+27.94	+20.43	+27.73
200	+47.50	+22.40	+8.10
300	+54.13	+27.31	-18.47
400	+46.30	+29.96	-14.02
500	+43.87	+24.42	-59.96
Proposed MPCC over MPCC with VV			
100	-85.29	+32.98	-7.32
200	-80.53	+37.50	-0.27
300	-68.90	+31.07	+2.98
400	-80.76	+31.10	+14.12
500	-62.81	+28.68	+5.45

classic MPCC, MPCC with VV and the MPCC-FSF under diverse conditions such as different rotor mechanical speeds, steady and transient operations. The figures of merit of the MPCC with VV and MPCC-FSF show that these controllers are viable alternatives to classic MPCC. Both presents a notable reduction of the $x-y$ currents, noting that MPCC with VV has better $\alpha-\beta$ current tracking than MPCC-FSF. On the other hand, the proposed MPCC, which uses the characteristics of MPCC with VV and MPCC-FSF, has demonstrated to be the best alternative in terms of $x-y$ currents reduction and THD analysis. But in terms of MSE in the $\alpha-\beta$ plane the MPCC with VV presents slightly better results than the proposed MPCC followed by the other strategies. In transient condition, the results of the four controllers showed good dynamic performance. Finally, a robustness test has been implemented where the controllers presented good behavior to the variation of the parameter under study. It is important to mention that the proposed MPCC has been implemented in a large six-phase IM (15 kW) making it suitable for medium power applications.

IX. APPENDIX

$$a_{11(k)} = a_{22(k)} = 1 - \frac{R_s L_r T_s}{L_s L_r - L_m^2}$$
$$a_{12(k)} = -a_{21(k)} = \frac{L_m^2 \omega_{r(k)} T_s}{L_s L_r - L_m^2}$$
$$a_{15(k)} = a_{26(k)} = \frac{R_r L_m T_s}{L_s L_r - L_m^2}$$
$$a_{16(k)} = -a_{25(k)} = \frac{L_m L_r \omega_{r(k)} T_s}{L_s L_r - L_m^2}$$
$$a_{33(k)} = a_{44(k)} = 1 - \frac{R_s T_s}{L_{ls}}$$
$$a_{51(k)} = a_{62(k)} = \frac{R_s L_m T_s}{L_s L_r - L_m^2}$$
$$a_{52(k)} = -a_{61(k)} = -\frac{L_s L_m \omega_{r(k)} T_s}{L_s L_r - L_m^2}$$
$$a_{55(k)} = a_{66(k)} = 1 - \frac{R_r L_s T_s}{L_s L_r - L_m^2}$$
$$a_{56(k)} = -a_{65(k)} = -\frac{L_r L_s \omega_{r(k)} T_s}{L_s L_r - L_m^2}$$
$$b_{11(k)} = b_{22(k)} = \frac{L_r T_s}{L_s L_r - L_m^2}$$
$$b_{33(k)} = b_{44(k)} = \frac{T_s}{L_{ls}}$$
$$b_{51(k)} = b_{62(k)} = -\frac{L_m T_s}{L_s L_r - L_m^2}$$

REFERENCES

[1] M. J. Duran, E. Levi, and F. Barrero, *Multiphase Electric Drives: Introduction*. Wiley Encyclopedia of Electrical and Electronics Engineering, 2017, pp. 1–26.

[2] R. Bojoi, S. Rubino, A. Tenconi, and S. Vaschetto, "Multiphase electrical machines and drives: A viable solution for energy generation and transportation electrification," in *Proc. EPE*, 2016, pp. 632–639.

[3] E. Levi, R. Bojoi, F. Profumo, H. Toliyat, and S. Williamson, "Multiphase induction motor drives–a technology status review," *IET Electr. Power Appl.*, vol. 1, no. 4, pp. 489–516, 2007.

[4] F. Barrero and M. J. Duran, "Recent advances in the design, modeling, and control of multiphase machines: Part I," *IEEE Trans. Ind. Electron.*, vol. 63, no. 1, pp. 449–458, 2016.

[5] Y. Kali, M. Ayala, J. Rodas, M. Saad, J. Doval-Gandoy, R. Gregor, and K. Benjelloun, "Time delay estimation based discrete-time super-twisting current control for a six-phase induction motor," *IEEE Trans. Power Electron.*, 2020.

[6] A. Gonzalez-Prieto, I. Gonzalez-Prieto, and M. J. Duran, "Smart voltage vectors for model predictive control of six-phase electric drives," *IEEE Trans. Ind. Electron.*, 2020.

[7] F. Barrero, M. R. Arahal, R. Gregor, S. Toral, and M. J. Durán, "A proof of concept study of predictive current control for vsi-driven asymmetrical dual three-phase ac machines," *IEEE Trans. Ind. Electron.*, vol. 56, no. 6, pp. 1937–1954, 2009.

[8] F. Wang, Z. Zhang, X. Mei, J. Rodríguez, and R. Kennel, "Advanced control strategies of induction machine: Field oriented control, direct torque control and model predictive control," *Energies*, vol. 11, no. 1, p. 120, 2018.

[9] O. Gonzalez, M. Ayala, J. Rodas, R. Gregor, G. Rivas, and J. Doval-Gandoy, "Variable-speed control of a six-phase induction machine using predictive-fixed switching frequency current control techniques," in *Proc. PEDG*, 2018, pp. 1–6.

[10] S. Kouro, M. A. Perez, J. Rodriguez, A. M. Llor, and H. A. Young, "Model predictive control: Mpc's role in the evolution of power electronics," *IEEE Ind. Electron. Mag.*, vol. 9, no. 4, pp. 8–21, 2015.

[11] Y. Kali, M. Ayala, J. Rodas, M. Saad, J. Doval-Gandoy, R. Gregor, and K. Benjelloun, "Current control of a six-phase induction machine drive based on discrete-time sliding mode with time delay estimation," *Energies*, vol. 12, no. 1, p. 170, 2019.

[12] Y. Kali, M. Saad, J. Doval-Gandoy, J. Rodas, and K. Benjelloun, "Discrete sliding mode control based on exponential reaching law and time delay estimation for an asymmetrical six-phase induction machine drive," *IET Electr. Power App.*, vol. 13, no. 11, pp. 1660–1671, 2019.

[13] P. Gonçalves, S. Cruz, and A. Mendes, "Finite control set model predictive control of six-phase asymmetrical machines—An overview," *Energies*, vol. 12, no. 24, p. 4693, 2019.

[14] M. Ayala, J. Doval-Gandoy, J. Rodas, O. Gonzalez, and R. Gregor, "Current control designed with model based predictive control for six-phase motor drives," *ISA Trans.*, vol. 98, pp. 496–504, 2020.

[15] O. Gonzalez, M. Ayala, J. Doval-Gandoy, J. Rodas, R. Gregor, and M. Rivera, "Predictive-fixed switching current control strategy applied to six-phase induction machine," *Energies*, vol. 12, no. 12, p. 2294, 2019.

[16] I. Gonzalez-Prieto, M. J. Duran, J. J. Aciego, C. Martin, and F. Barrero, "Model predictive control of six-phase induction motor drives using virtual voltage vectors," *IEEE Trans. Ind. Electron.*, vol. 65, no. 1, pp. 27–37, 2017.

[17] J. J. Aciego, I. Gonzalez-Prieto, M. Duran, M. Bermudez, and P. Salas-Biedma, "Model predictive control based on dynamic voltage vectors for six-phase induction machines," *IEEE J. Emerg. Sel. Top. Power Electron.*, 2020.

[18] M. Ayala, J. Doval-Gandoy, J. Rodas, O. Gonzalez, R. Gregor, and M. Rivera, "A novel modulated model predictive control applied to six-phase induction motor drives," *IEEE Trans. Ind. Electron.*, 2020.

[19] O. González, M. Ayala, C. Romero, J. Rodas, R. Gregor, L. Delorme, I. González-Prieto, M. J. Durán, and M. Rivera, "Comparative assessment of model predictive current control strategies applied to six-phase induction machines," in *Proc. ICIT*, 2020, pp. 1037–1043.

[20] Y. Zhao and T. Lipo, "Space vector pwm control of dual three-phase induction machine using vector space decomposition," *IEEE Trans. Ind. Electron.*, vol. 31, no. 5, pp. 1100–1109, 1995.

[21] J. Rodas, F. Barrero, M. R. Arahal, C. Martin, and R. Gregor, "On-line estimation of rotor variables in predictive current controllers: A case study using five-phase induction machines," *IEEE Trans. Ind. Electron.*, vol. 63, no. 9, pp. 5348–5356, 2016.

[22] C. Martin, M. R. Arahal, F. Barrero, and M. J. Durán, "Five-phase induction motor rotor current observer for finite control set model predictive control of stator current," *IEEE Trans. Ind. Electron.*, vol. 63, no. 7, pp. 4527–4538, 2016.

[23] J. Rodas, C. Martin, M. R. Arahal, F. Barrero, and R. Gregor, "Influence of covariance-based ALS methods in the performance of predictive controllers with rotor current estimation," *IEEE Trans. Ind. Electron.*, vol. 64, no. 4, pp. 2602–2607, 2017.

[24] J. Rodriguez, M. P. Kazmierkowski, J. R. Espinoza, P. Zanchetta, H. Abu-Rub, H. A. Young, and C. A. Rojas, "State of the art of finite control set model predictive control in power electronics," *IEEE Trans Ind. Informat.*, vol. 9, no. 2, pp. 1003–1016, 2013.

[25] M. Arahal, F. Barrero, S. Toral, M. Duran, and R. Gregor, "Multi-phase current control using finite-state model-predictive control," *Control Eng. Pract.*, vol. 17, no. 5, pp. 579–587, 2009.

[26] J. Rodriguez and P. Cortes, *Predictive control of power converters and electrical drives*. John Wiley & Sons, 2012, vol. 40.

[27] J. J. Aciego, I. G. Prieto, and M. J. Duran, "Model predictive control of six-phase induction motor drives using two virtual voltage vectors," *IEEE J. Emerg. Sel. Top. Power Electron.*, vol. 7, no. 1, pp. 321–330, 2018.

[28] A. G. Yepes, J. A. Riveros, J. Doval-Gandoy, F. Barrero, O. López, B. Bogado, M. Jones, and E. Levi, "Parameter identification of multiphase induction machines with distributed windings Part 1: Sinusoidal excitation methods," *IEEE Trans. Energy Conv.*, vol. 27, no. 4, pp. 1056–1066, 2012.

[29] J. A. Riveros, A. G. Yepes, F. Barrero, J. Doval-Gandoy, B. Bogado, O. Lopez, M. Jones, and E. Levi, "Parameter identification of multiphase induction machines with distributed windings Part 2: Time-domain techniques," *IEEE Trans. Energy Conv.*, vol. 27, no. 4, pp. 1067–1077, 2012.

[30] J. Rodas, C. Martin, M. R. Arahal, F. Barrero, and R. Gregor, "Influence of covariance-based ALS methods in the performance of predictive controllers with rotor current estimation," *IEEE Trans. Ind. Electron.*, vol. 64, no. 4, pp. 2602–2607, 2017.

[31] G. I. Rivas-Martínez, J. Rodas, and J. D. Gandoy, "Statistical Tools to Evaluate the Performance of Current Control Strategies of Power Converters and Drives," *IEEE Trans. Instrum. Meas*, vol. 70, pp. 1–11, 2021.

[32] L. Delorme, M. Ayala, J. Rodas, R. Gregor, O. Gonzalez, and J. Doval-Gandoy, "Comparison of the effects on stator currents between continuous model and discrete model of the three-phase induction motor in the presence of electrical parameter variations," in *Proc. ICIT*. IEEE, 2020, pp. 151–156.

Comparative Assessment of Model Predictive Current Control Strategies applied to Six-Phase Induction Machines

O. González, M. Ayala, C. Romero, J. Rodas, R. Gregor
Lab. of Power and Control Systems
Universidad Nacional de Asunción
Luque, Paraguay
{ogonzalez, mayala, cromero, jrodas, rgregor}@ing.una.py

L. Delorme
Universidad del Cono Sur de las Américas
Asunción, Paraguay
laridelorme@gmail.com

I. González-Prieto, M.J. Durán
Dept. of Electrical Engineering
Universidad de Málaga
Málaga, Spain
ignaciogp87@gmail.com, mjduran@uma.es

M. Rivera
Lab. of Energy Conversion and Power Electronics
Universidad de Talca
Curicó, Chile
marcoriv@utalca.cl

***Abstract*—Nowadays, model predictive current control strategy has become a viable alternative because of its fast response for high-reliability systems, such as multiphase machines. In that regard, this paper proposes a comparative assessment of four current controllers based on the model using different approaches as virtual vectors, modulation techniques and further, combining these strategies in order to deal at the same time with the regulation of the main and secondary currents components, known as (α-β) and (x-y), respectively, applied to six-phase induction machines. Simulation results are presented so as to show the effectiveness of the four model predictive current controllers, taking into account the mean squared error and the total harmonic distortion of the stator currents in both steady and dynamic conditions.**

***Index Terms*—Multiphase machines, predictive current control, six-phase induction machine, virtual vectors.**

NOMENCLATURE

KF	Kalman filter.
MPC	Model predictive control.
MPCCS	Model predictive current control strategy.
MSE	Mean squared error.
PFSCCS	Predictive fixed-switching current control strategy.
SPIM	Six-phase induction machine.
THD	Total harmonic distortion.
VSD	Vector space decomposition.
VSI	Voltage source inverter.
VV	Virtual vector.

I. INTRODUCTION

Recently, the attention of the research community has been focused on multiphase induction machines due to their advantages over the three-phase induction machines, such as, better power split per phase, lower current harmonic content, less torque ripple production and fault tolerance capabilities [1]–[3]. However, the (x-y) secondary current components present in multiphase machines need special consideration due to their relationship with the stator copper losses. Different control strategies over the years have been proposed for multiphase [4]–[11], one of them with promising features is MPC, described in [12]–[16], but they all present a high harmonic content in the stator currents compared to other approaches.

The PFSCCS adds a modulation stage to MPC strategy, in order to use three vectors in each sampling period. Consisting of two active vectors and the null vector, its advantages are: 1. Applying more than one vector in the sampling period helps to obtain voltages in (α-β) sub-spaces closer to the reference and avoids large voltages at low sampling rates that would be obtained by applying a single vector throughout the sampling period. 2. The selected active vectors are the largest, thus decreasing their components in the (x-y) sub-spaces. 3. A fixed switching pattern is applied so that the frequency spectrum of harmonics is reduced [17]–[19].

Another control technique that uses modulation in combination with MPC is proposed in [20]. This technique cancels the components in the (x-y) sub-space by combining two pairs of vectors. Each vector is composed by one large medium and one large vector in the (α-β) sub-space, with the same common direction, and opposite in the secondary sub-space, to form a vector called VV [20], [21]. The application of the VV ensures zero production of average voltage (x-y), and the combination of two VVs provides greater accuracy in the voltage supply. Although, the tracking in the main sub-space may still be improved, for example by increasing the amount of vectors to be used taking advantage of the computational capabilities left over from the digital controllers, such as digital signal processors.

Two predictive control models are proposed in this article. The first one, is a variant of the PFSCCS control model called

5V-PFCCS. It uses 5 vectors to obtain the desired voltage in the (α-β) sub-spaces while trying to reduce the voltage in the (x-y) sub-spaces through their strategic selection. The second predictive control model called PFSCCS-VVs is a variant of the VV-MPC. This control method hopes to take advantage of the voltage cancellation in the (x-y) sub-space and at the same time increase the voltage accuracy in the main sub-space. In this context, the main contribution of this paper is the comparative assessment of four model predictive control strategies by employing modulation techniques through simulation results applied to SPIM taking into account the main and secondary plane, termed as, (α-β) and (x-y), from now on, respectively. The effectiveness of the four current controllers is analyzed by means of the MSE and the THD so as to compare the advantages and limitations of each current control strategy. The four current controllers are examined at different speeds in steady state operation. Further, each strategy has been tested under transient operation to prove the system behavior.

This paper is structured as follows. Modeling of the SPIM including the two-level six-phase VSI employed in this study is analyzed in Section II. The comparative assessment of current controllers based on the laws of the MPC to the presented system is described in Section III. Section IV presents the proposed predictive currents controllers, explaining the behavior of the modulation strategies used in the predictive control. Simulations results of each MPCCS in both steady and dynamic operations are depicted in Section V in order to present their benefits and limitations. Finally, the conclusions are summarized and discussed in Section VI.

II. Modeling of the SPIM and VSI

In this section the main characteristics of the used SPIM drive are presented. The SPIM employed in this comparative assessment is fed by a two-level six-phase VSI. A simplified topology is presented in Fig. 1. Each switching configuration of the VSI is represented by S_p, where S_p can take two possible values that belong to 0 or 1, i.e., $S_p = 1$ if the upper switch is up and the lower switch is down and the opposite takes place if $S_p = 0$. Hence, it is feasible to represent the switching configurations per leg of the two-level six-phase VSI like a vector: $[S_p] = [S_a, S_b, S_c, S_d, S_e, S_f]$, which produces 64 valid switching configurations that include 48 active non redundant vectors and one zero vector.

In this context, stator voltages of the considered VSI can be calculated by the DC-link voltage, known as, (V_{dc}) and the S_p vector, as shown in (1).

$$VSI_{[M]} = \frac{V_{dc}}{3}\begin{bmatrix} 2 & 0 & -1 & 0 & -1 & 0 \\ 0 & 2 & 0 & -1 & 0 & -1 \\ -1 & 0 & 2 & 0 & -1 & 0 \\ 0 & -1 & 0 & 2 & 0 & -1 \\ -1 & 0 & -1 & 0 & 2 & 0 \\ 0 & -1 & 0 & -1 & 0 & 2 \end{bmatrix} {S_p}^T \quad (1)$$

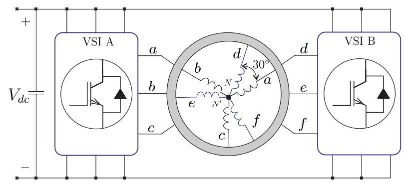

Fig. 1. SPIM fed by two-level six-phase VSI.

Afterwards, by combining the VSD strategy [22] and employing an invariant amplitude transformation matrix criterion [14], depicted in (2), the six-phase stator voltages of the SPIM are mapped into three-two orthogonal stationary sub-spaces, which are (α-β), (x-y) and (z_1-z_2). The (α-β) sub-space is related to the torque and flux contribution. The (x-y) sub-space is associated with the copper losse. The (z_1-z_2) sub-space is not taken into account because of the isolated neutral points topology considered.

$$T = \frac{1}{3}\begin{bmatrix} 1 & \frac{\sqrt{3}}{2} & -\frac{1}{2} & -\frac{\sqrt{3}}{2} & -\frac{1}{2} & 0 \\ 0 & \frac{1}{2} & \frac{\sqrt{3}}{2} & \frac{1}{2} & -\frac{\sqrt{3}}{2} & -1 \\ 1 & -\frac{\sqrt{3}}{2} & -\frac{1}{2} & \frac{\sqrt{3}}{2} & -\frac{1}{2} & 0 \\ 0 & \frac{1}{2} & -\frac{\sqrt{3}}{2} & \frac{1}{2} & \frac{\sqrt{3}}{2} & -1 \\ 1 & 0 & 1 & 0 & 1 & 0 \\ 0 & 1 & 0 & 1 & 0 & 1 \end{bmatrix} \begin{matrix} \alpha \\ \beta \\ x \\ y \\ z_1 \\ z_2 \end{matrix} \quad (2)$$

Therefore, the sixty-four switching configurations in the (α-β) and (x-y) sub-spaces are represented in Fig. 2. Further, the SPIM mathematical model can be expressed by means of state-space approach, which is established by:

$$X'_{(t)} = A_{(t)}\,X_{(t)} + B_{(t)}\,U_{(t)} + Hn_{p(t)} \quad (3)$$

where the input vector of the considered state-space model is represented by $U_{(t)}$, the mentioned state vector is $X_{(t)}$ and the electrical parameters of the SPIM are represented through the matrices $A_{(t)}$ and $B_{(t)}$. While the process noise is established as $n_{p(t)}$ and the noise weight matrix by H.

According to the equation (3), which expresses the state-space model of the SPIM, and choosing the (α-β), (x-y) stator currents and (α-β) rotor currents as state vectors ($x_1 = i_{\alpha s}$, $x_2 = i_{\beta s}$, $x_3 = i_{xs}$, $x_4 = i_{ys}$, $x_5 = i_{\alpha r}$ and $x_6 = i_{\beta r}$), the SPIM equations can be represented in the next way:

$$\begin{aligned} x'_1 &= -R_s q_2 x_1 + q_4\left(L_m\omega_r x_2 + R_r x_5 + L_r\omega_r x_6\right) + q_2 u_1 \\ x'_2 &= -R_s q_2 x_2 + q_4\left(-L_m\omega_r x_1 - L_r\omega_r x_5 + R_r x_6\right) + q_2 u_2 \\ x'_3 &= -R_s q_3 x_3 + q_3 u_3 \\ x'_4 &= -R_s q_3 x_4 + q_3 u_4 \\ x'_5 &= R_s q_4 x_1 + q_5\left(-L_m\omega_r x_2 - R_r x_5 - L_r\omega_r x_6\right) - q_4 u_1 \\ x'_6 &= R_s q_4 x_2 + q_5\left(L_m\omega_r x_1 + L_r\omega_r x_5 - R_r x_6\right) - q_4 u_2 \end{aligned} \quad (4)$$

where the coefficients are defined as follows:

$$q_1 = L_s L_r - L_m^2,\; q_2 = \frac{L_r}{q_1} \quad (5)$$

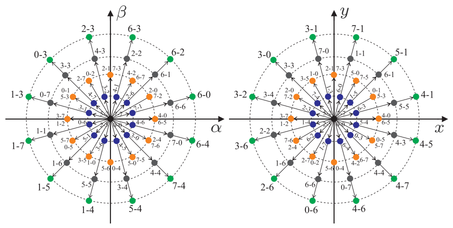

Fig. 2. Space vector representations in the (α-β) and (x-y) sub-spaces for a SPIM.

$$q_3 = \frac{1}{L_{ls}},\ q_4 = \frac{L_m}{q_1},\ q_5 = \frac{L_s}{q_1} \tag{6}$$

being R_s, R_r, L_m, $L_r = L_{lr} + L_m$ and $L_s = L_{ls} + L_m$ the electrical parameters of the SPIM. The input vector is composed of the applied stator voltages, which are $u_1 = v_{\alpha s}$, $u_2 = v_{\beta s}$, $u_3 = v_{xs}$ and $u_4 = v_{ys}$. Further, the SPIM equations contain the rotor electrical speed ω_r.

Since the drive of the SPIM is also composed of the VSI model, it is achievable to convert the gating signals into stator voltages which can be mapped to (α-β) and (x-y) sub-spaces represented in the vector $U_{(t)} = [u_1,\, u_2,\, u_3,\, u_4]^T$ and calculated through the next expressions:

$$U_{(t)} = V_{dc}\, T\, VSI_{[M]} \tag{7}$$

$$Y_{(t)} = \begin{bmatrix} 1 & 0 & 0 & 0 & 0 & 0 \\ 0 & 1 & 0 & 0 & 0 & 0 \\ 0 & 0 & 1 & 0 & 0 & 0 \\ 0 & 0 & 0 & 1 & 0 & 0 \end{bmatrix} X_{(t)} + n_{m(t)} \tag{8}$$

where the output vector is expressed by $Y_{(t)}$ and the measurement noise through $n_{m(t)}$.

Finally, the mechanical expressions of the SPIM are:

$$T_e = 3P\left(\psi_{\alpha s} i_{\beta s} - \psi_{\beta s} i_{\alpha s}\right) \tag{9}$$

$$J_i \omega'_m + B_i \omega_m = (T_e - T_L) \tag{10}$$

where the variables B_i, J_i, T_e, T_L, ω_m, ω_r, $\psi_{\alpha s}$, $\psi_{\beta s}$ and P are, the friction coefficient, the inertia coefficient, the generated torque, the load torque, the rotor mechanical speed, the rotor electrical speed, the stator fluxes and the number of pole pairs, respectively.

III. Assessment of Current Controllers

A. Classic MPCCS

The MPCCS for the SPIM control and the VSI drive in the paper have been developed. A comprehensive block diagram of the strategy is shown in Fig. 3. In order to follow the reference stator current it employs a discrete mathematical model of the SPIM to predict the future action of the considered output variables using the measurable variables, which are the stator currents, stator voltages and the rotor mechanical speed.

$$\hat{X}_{(k+1|k)} = X_{(k)} + T_s f\left(X_{(k)},\, U_{(k)},\, \omega_{r(k)}\right) \tag{11}$$

Taking into account the state-space model represented in the equation (11), the rotor currents are not directly measured. A reduced order estimator has been employed to estimate the unmeasured variables (rotor currents) of the state vector. This strategy has been proposed in [23], [24], which is based on KF. Hence, the SPIM mathematical model can be expressed by the equations (12) and (13), respectively, using uncorrelated process and zero-mean Gaussian measurement noises.

$$\hat{X}_{(k+1|k)} = A_{(k)} X_{(k)} + B_{(k)} U_{(k)} + H n_{p(k)} \tag{12}$$

$$Y_{(k+1|k)} = \begin{bmatrix} 1 & 0 & 0 & 0 & 0 & 0 \\ 0 & 1 & 0 & 0 & 0 & 0 \\ 0 & 0 & 1 & 0 & 0 & 0 \\ 0 & 0 & 0 & 1 & 0 & 0 \end{bmatrix} X_{(k+1)} + n_{m(k+1)} \tag{13}$$

It is worth noting that $A_{(k)}$ and $B_{(k)}$ constitute the discretized matrices from (4), where $A_{(k)}$ depends on the present value of the rotor electrical speed. Therefore, the matrix $A_{(k)}$ must be actualized at each sampling period considering the measured rotor electrical speed.

Moreover, in the MPCCS an optimization control process at every sampling period is carried out to minimize an established cost function J. This process is done by evaluating all possible control signals (64 stator voltages for SPIM) and then selecting the one that reduces the cost function to be applied in the next sampling period. Since this work deals with the current control, the tracking error (e) in the (α-β) and (x-y) sub-spaces between the reference stator currents ($i^*_{s(k+2)}$) and their predicted values ($\hat{i}_{s(k+2)}$) is considered. The tracking error is computed by the second-step ahead prediction for delay compensation, as shown in the next equations:

$$J = (e_{\alpha s})^2 + (e_{\beta s})^2 + \lambda_{xy}[(e_{xs})^2 + (e_{ys})^2] \tag{14}$$

where

$$\begin{aligned} e_{\alpha s} &= i^*_{\alpha s(k+2)} - \hat{i}_{\alpha s(k+2)} \\ e_{\beta s} &= i^*_{\beta s(k+2)} - \hat{i}_{\beta s(k+2)} \\ e_{xs} &= i^*_{xs(k+2)} - \hat{i}_{xs(k+2)} \\ e_{ys} &= i^*_{ys(k+2)} - \hat{i}_{ys(k+2)}. \end{aligned} \tag{15}$$

Also, the tuning parameter (λ_{xy}) has been included that provides more weight on (α-β) or (x-y) sub-spaces according to the optimization control [25]–[27].

B. PFSCCS

This current control method is based on the selected sector defined by the two-level six-phase VSI in the (α-β) sub-space, which are formed by the outer 12 vectors, as depicted in Fig. 4. The current strategy computes the prediction of the two adjacent vectors that compose the considered sector at every sampling period and performs the cost function (J) individually for every prediction [17]. The performed prediction is based on (11). Nevertheless, they differ in the computation of the input vector $U_{(k)}$ [18]. The duty cycles for

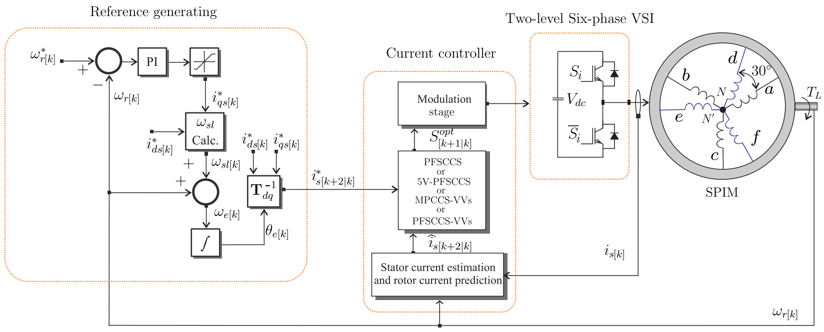

Fig. 3. Scheme of the MPCCS applied to SPIM.

the adjacent vectors, d_1 and d_2, respectively, are obtained by solving the following equations:

$$d_0 = \frac{\sigma}{\sqrt{J_0}} \qquad d_1 = \frac{\sigma}{\sqrt{J_1}} \qquad d_2 = \frac{\sigma}{\sqrt{J_2}} \tag{16}$$

$$d_0 + d_1 + d_2 = T_s \tag{17}$$

where d_0 corresponds to the duty cycle of a zero vector. Then, it is possible to obtain the expression for σ and the duty cycles for each vector given as:

$$d_0 = \frac{T_s\sqrt{J_1}\sqrt{J_2}}{\sqrt{J_0}\sqrt{J_1}+\sqrt{J_1}\sqrt{J_2}+\sqrt{J_0}\sqrt{J_2}} \tag{18}$$

$$d_1 = \frac{T_s\sqrt{J_0}\sqrt{J_2}}{\sqrt{J_0}\sqrt{J_1}+\sqrt{J_1}\sqrt{J_2}+\sqrt{J_0}\sqrt{J_2}} \tag{19}$$

$$d_2 = \frac{T_s\sqrt{J_0}\sqrt{J_1}}{\sqrt{J_0}\sqrt{J_1}+\sqrt{J_1}\sqrt{J_2}+\sqrt{J_0}\sqrt{J_2}} \tag{20}$$

Analyzing the above mathematical expressions, a new cost function, which is evaluated at every sampling period, is defined as:

$$J_{n(k+2)} = d_1\sqrt{J_1} + d_2\sqrt{J_2} \tag{21}$$

The two vectors which minimize $J_{n(k+2)}$ are selected and applied to the VSI at the next sampling period. After computing the duty cycles and selecting the optimal two vectors to be applied, a switching pattern diagram, detailed in [14], [18], is adopted with the aim of applying the active vectors $(v_1 - v_2)$ and zero vector (v_0), considering the calculated duty cycles achieving a fixed-switching frequency.

C. MPCCS-VVs

The implementation of MPCCS-VVs consists on the use of two active voltage vectors, one is the large vector and another is the mid-large vector as shown in Fig. 5, in every sampling time. This virtual vector is applied as follows:

$$VV = d_1 V_{large} + d_2 V_{mid-large} \tag{22}$$

where $d_1 = 0.73T_s$ and $d_2 = 0.27T_s$ which generate approximately 93% of the actual value of the large vector in (α-β) sub-space but it also obtains zero average value of the (x-y) currents due to the fact that those two vectors are opposite in (x-y) sub-space [21].

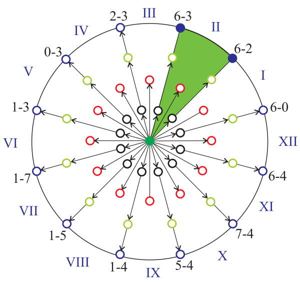

Fig. 4. Space sectors in the (α-β) sub-space for PFSCCS.

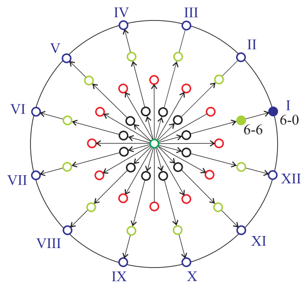

Fig. 5. Space sectors in the (α-β) sub-space for MPCCS-VVs.

IV. Proposed Predictive Current Controllers

A. 5V-PFSCCS

This technique is based on PFSCCS, so the duty cycles are calculated in the same way, with the difference that this technique has five vectors per sector, as shown in Fig. 6.

The duty cycles, for the five vectors d_0, d_1, d_2, d_3 and d_4, are obtained by solving the following equations:

$$d_i = \frac{\sigma}{\sqrt{J_i}} \tag{23}$$

$$d_0 + d_1 + d_2 + d_3 + d_4 = T_s \tag{24}$$

where $i = \{0,1,2,3,4\}$ and J_i are the corresponding cost functions (14) for the vectors in the selected sector. As PFSCCS, it is possible to obtain the expression for σ and the duty cycles for each vector given as:

$$J_{T0} = \sqrt{J_1}\sqrt{J_2}\sqrt{J_3}\sqrt{J_4} \tag{25}$$

$$J_{T1} = \sqrt{J_0}\sqrt{J_2}\sqrt{J_3}\sqrt{J_4} + \sqrt{J_0}\sqrt{J_1}\sqrt{J_3}\sqrt{J_4} \tag{26}$$

$$J_{T2} = \sqrt{J_0}\sqrt{J_1}\sqrt{J_2}\sqrt{J_4} + \sqrt{J_0}\sqrt{J_1}\sqrt{J_2}\sqrt{J_3} \tag{27}$$

$$d_1 = \frac{T_s\sqrt{J_0}\sqrt{J_2}\sqrt{J_3}\sqrt{J_4}}{J_{T0} + J_{T1} + J_{T2}} \tag{28}$$

$$d_2 = \frac{T_s\sqrt{J_0}\sqrt{J_1}\sqrt{J_3}\sqrt{J_4}}{J_{T0} + J_{T1} + J_{T2}} \tag{29}$$

$$d_3 = \frac{T_s\sqrt{J_0}\sqrt{J_1}\sqrt{J_2}\sqrt{J_4}}{J_{T0} + J_{T1} + J_{T2}} \tag{30}$$

$$d_4 = \frac{T_s\sqrt{J_0}\sqrt{J_1}\sqrt{J_2}\sqrt{J_3}}{J_{T0} + J_{T1} + J_{T2}} \tag{31}$$

$$d_0 = T_s - d_1 - d_2 - d_3 - d_4 \tag{32}$$

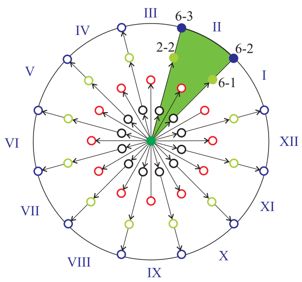

Fig. 6. Space sectors in the (α-β) sub-space for 5V-PFSCCS.

B. PFSCCS-VVs

In this strategy a combination between PFSCCS and MPCCS-VVs has been proposed so as to improve the current tracking in the (α-β) sub-space and also reducing the (x-y) currents. Hence, to reduce the (x-y) currents, the equation presented in (22) has been employed. While for (α-β) currents tracking, the V_1, V_2 and V_0 vectors, which in turn are composed by (v_1^a, v_1^b) and (v_2^a, v_2^b) for the active vectors, respectively, and according to the selected sector, the duty cycles for these vectors are computed as (18), (19) and (20). Finally, once the vectors are selected and before they are applied to the two-level six-phase VSI, a modulation diagram depicted in Fig. 7 is performed to guarantee a fixed-switching frequency at every sampling period.

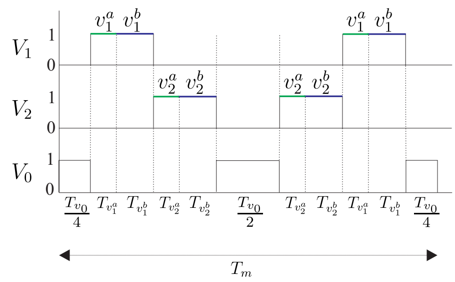

Fig. 7. Switching diagram of each selected sector in the (α-β) sub-space for PFSCCS-VVs.

V. Simulation Results

The SPIM is powered by two-level six-phase VSI, using a constant DC voltage of 200 V. The simulation results are analyzed and processed through MATLAB R2014a employing the electrical and mechanical parameters of the SPIM (Table I). The performance of each current controller is evaluated through the MSE between the reference and measured stator currents in the (α-β) and (x-y) sub-spaces. Further, the THD analysis has been presented, where the MSE and THD, respectively, are calculated as follows:

$$\mathrm{MSE}(i_{\delta s}) = \sqrt{\frac{1}{m}\sum_{l=1}^{m}(i_{\delta s} - i_{\delta s}^*)^2} \tag{33}$$

considering m as the total analyzed samples, $i_{\delta s}^*$ as the reference stator current and $i_{\delta s}$ as the measured stator currents where $\delta \in (\alpha, \beta, x, y)$.

$$\mathrm{THD}(i_s) = \sqrt{\frac{1}{i_{s1}^2}\sum_{f=2}^{m}(i_{sf})^2} \tag{34}$$

where i_{s1} represents the fundamental stator current and the harmonic stator currents are represented by i_{sf}.

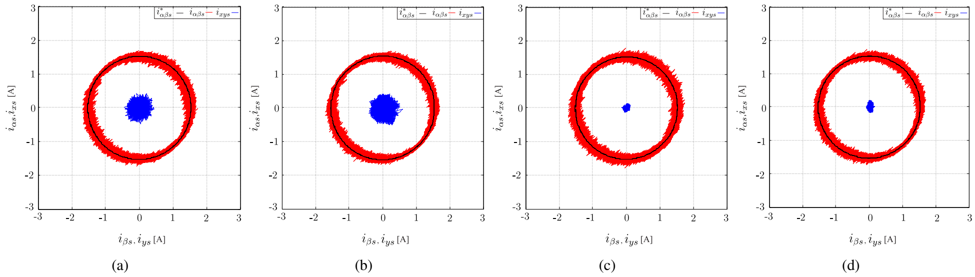

Fig. 8. Comparative performance of stator currents in (α-β) and (x-y) sub-spaces for a rotor speed of 500 [rpm] at 10 [kHz] of sampling frequency: (a) PFSCCS; (b) 5V-PFSCCS; (c) MPCCS-VVs and (d) PFSCCS-VVs.

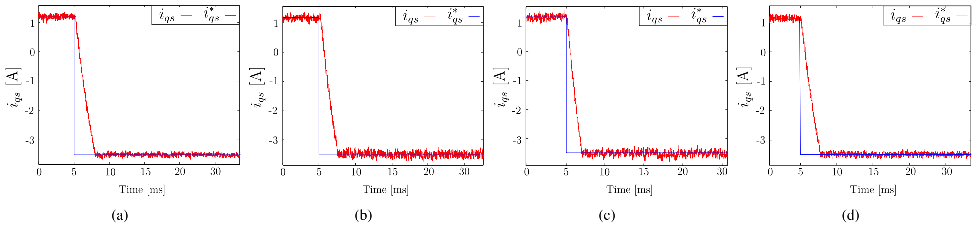

Fig. 9. Dynamic response in q-axis of stator current for a rotor speed change from 500 [rpm] to -500 [rpm] and a sampling frequency of 10 [kHz]: (a) PFSCCS; (b) 5V-PFCCS; (c) MPCCS-VVs and (d) PFSCCS-VVs.

In Table II, Table III, Table IV and Table V, a steady state analysis for stator currents under different rotor speed references (ω_m^*), are shown with PFSCCS, 5V-PFSCCS, MPCCS-VVs and PFSCCS-VVs, respectively. The MSE for (α-β) and (x-y) stator currents as well as the THD for (α) stator currents are included.

TABLE I
ELECTRICAL AND MECHANICAL CHARACTERISTICS OF THE SPIM

R_r	6.9 Ω	L_s	654.4 mH
R_s	6.7 Ω	P	1
L_{ls}	5.3 mH	P_w	2 kW
L_{lr}	12.8 mH	J_i	0.07 kg.m^2
L_m	614 mH	B_i	0.0004 kg.m^2/s
L_r	626.8 mH	ω_{r-nom}	3000 rpm

Fig. 8 exposes the (α-β) and (x-y) stator currents tracking, for PFSCCS, 5V-PFSCCS, MPCCS-VVs and PFSCCS-VVs, in steady state for a rotor speed of 500 rpm and a sampling frequency of 10 kHz. Fig. 9 shows the transient response for q stator current in a reversal test (speed reference changes from 500 [rpm] to -500 [rpm]) where PFSCCS, 5V-PFSCCS, MPCCS-VVs and PFSCCS-VVs show similar response speed which are denoted on Table VI.

TABLE II
ASSESSMENT OF STATOR CURRENTS IN (α-β) AND (x-y) SUB-SPACES, CONSIDERING MSE [A] AND THD [%] FOR PFSCCS AT 500 [RPM] AND 1000 [RPM].

	PFSCCS	at	f_s = 10 [kHz]		
ω_m^*	MSE$_\alpha$	MSE$_\beta$	MSE$_x$	MSE$_y$	THD$_\alpha$
500	0.0628	0.0602	0.0999	0.1013	5.58
1000	0.0982	0.0966	0.1438	0.1403	5.41

TABLE III
ASSESSMENT OF STATOR CURRENTS IN (α-β) AND (x-y) SUB-SPACES, CONSIDERING MSE [A] AND THD [%] FOR 5V-PFSCCS AT 500 [RPM] AND 1000 [RPM].

	5V-PFSCCS	at	f_s = 10 [kHz]		
ω_m^*	MSE$_\alpha$	MSE$_\beta$	MSE$_x$	MSE$_y$	THD$_\alpha$
500	0.0571	0.0544	0.1151	0.1194	4.68
1000	0.0999	0.0954	0.1558	0.1554	5.14

TABLE IV
ASSESSMENT OF STATOR CURRENTS IN (α-β) AND (x-y) SUB-SPACES, CONSIDERING MSE [A] AND THD [%] FOR MPCCS-VVS AT 500 [RPM] AND 1000 [RPM].

	MPCCS-VVs	at	f_s = 10 [kHz]		
ω_m^*	MSE$_\alpha$	MSE$_\beta$	MSE$_x$	MSE$_y$	THD$_\alpha$
500	0.0662	0.0616	0.0381	0.0395	6.14
1000	0.0772	0.0676	0.0455	0.0488	6.41

TABLE V
ASSESSMENT OF STATOR CURRENTS IN (α-β) AND (x-y) SUB-SPACES, CONSIDERING MSE [A] AND THD [%] FOR PFSCCS-VVS AT 500 [RPM] AND 1000 [RPM].

PFSCCS-VVs		at	f_s = 10 [kHz]		
ω_m^*	MSE$_\alpha$	MSE$_\beta$	MSE$_x$	MSE$_y$	THD$_\alpha$
500	0.0594	0.0529	0.0372	0.0776	5.04
1000	0.0690	0.0630	0.0331	0.0405	5.94

TABLE VI
RESPONSE ANALYSIS OF PFSCCS, 5V-PFSCCS, MPCCS-VVS AND PFSCCS-VVS, CONSIDERING OVERSHOOT (%) AND SETTLING TIME (MS) IN A REVERSAL TEST (500 [RPM] TO −500 [RPM]).

MPCCS	Overshoot	Settling time
PFSCCS	4.85 %	3 ms
5V-PFSCCS	4.8 %	3.2 ms
MPCCS-VVs	3.3 %	2.7 ms
PFSCCS-VVs	4.9 %	3 ms

VI. CONCLUSION

In this paper a comparative assessment of four model predictive current control strategies applied to SPIM are presented. The simulation results show a good performance on the four analyzed techniques, highlighting MPCCS-VVs and PFSCCS-VVs for its (x-y) currents reduction. At the same time, PFSCCS-VVs presents better (α-β) stator currents tracking and a better THD, presenting an excellent performance as a predictive current controller.

ACKNOWLEDGMENT

The authors would like to thank the financial support from the Paraguayan Science and Technology National Council (CONACYT) through programs POSG16-5 and POS17-69.

REFERENCES

[1] E. Levi, R. Bojoi, F. Profumo, H. A. Toliyat, and S. Williamson, “Multiphase induction motor drives - A technology status review,” *IET Electr. Power Appl.*, vol. 1, no. 4, pp. 489–516, 2007.

[2] F. Barrero and M. J. Duran, “Recent advances in the design, modeling, and control of multiphase machines: Part I,” *IEEE Trans. Ind. Electron.*, vol. 63, no. 1, pp. 449–458, 2016.

[3] M. J. Duran and F. Barrero, “Recent advances in the design, modeling, and control of multiphase machines: Part II,” *IEEE Trans. Ind. Electron.*, vol. 63, no. 1, pp. 459–468, 2016.

[4] Y. Kali, M. Ayala, J. Rodas, M. Saad, J. Doval-Gandoy, R. Gregor, and K. Benjelloun, “Current control of a six-phase induction machine drive based on discrete-time sliding mode with time delay estimation,” *Energies*, vol. 1, no. 1, p. 170, 2019.

[5] Y. Kali, M. Saad, J. Doval-Gandoy, J. Rodas, and K. Benjelloun, “Discrete sliding mode control based on exponential reaching law and time delay estimation for an asymmetrical six-phase induction machine drive,” *IET Electr. Power Appl.*, vol. 13, pp. 1660–1671, 2019.

[6] Y. Kali, J. Rodas, M. Saad, J. Doval-Gandoy, and R. Gregor, “Nonlinear backstepping with time delay estimation for six-phase induction machine,” in *Proc. IEMDC*, May 2019, pp. 1798–1804.

[7] Y. Kali, J. Rodas, M. Ayala, M. Saad, R. Gregor, K. Benjelloun, J. Doval-Gandoy, and G. Goodwin, “Discrete-time sliding mode with time delay estimation of a six-phase induction motor drive,” in *Proc. IECON*, 2018, pp. 5807–5812.

[8] Y. Kali, J. Rodas, M. Saad, R. Gregor, K. Benjielloun, J. Doval-Gandoy, and G. Goodwin, “Speed control of a five-phase induction motor drive using modified super-twisting algorithm,” in *Proc. SPEEDAM*, 2018, pp. 938–943.

[9] Y. Kali, J. Rodas, M. Saad, R. Gregor, K. Benjelloun, and J. Doval-Gandoy, “Current control based on super-twisting algorithm with time delay estimation for a five-phase induction motor drive,” in *Proc. IEMDC*, 2017, pp. 1–8.

[10] O. Gonzalez, J. Rodas, R. Gregor, M. Ayala, and M. Rivera, “Speed sensorless predictive current control of a five-phase induction machine,” in *Proc. ICIEA*, 2017, pp. 343–348.

[11] O. Gonzalez, J. Rodas, M. Ayala, R. Gregor, M. Rivera, M. J. Duran, and I. Gonzlez-Prieto, “Predictive current control with kalman filter observer for a five-phase induction machine operating at fixed switching frequency,” in *Proc. ICIEA*, 2017, pp. 349–354.

[12] R. Gregor, J. Rodas, J. Muoz, M. Ayala, O. Gonzalez, and D. Gregor, “Predictive-fixed switching frequency technique for 5-phase induction motor drives,” in *Proc. SPEEDAM*, 2016, pp. 761–767.

[13] C. S. Lim, E. Levi, M. Jones, N. A. Rahim, and W. P. Hew, “FCS-MPC-Based Current Control of a Five-Phase Induction Motor and its Comparison with PI-PWM Control,” *IEEE Tran. Ind. Electron.*, vol. 61, no. 1, pp. 149–163, 2014.

[14] M. Ayala, J. Rodas, R. Gregor, J. Doval-Gandoy, O. Gonzalez, M. Saad, and M. Rivera, “Comparative study of predictive control strategies at fixed switching frequency for an asymmetrical six-phase induction motor drive,” in *Proc. IEMDC*, 2017, pp. 1–8.

[15] M. Ayala, O. Gonzalez, J. Rodas, R. Gregor, and J. Doval-Gandoy, “A speed-sensorless predictive current control of multiphase induction machines using a Kalman filter for rotor current estimator,” in *Proc. ESARS-ITEC*, 2016, pp. 1–6.

[16] M. Ayala, J. Doval-Gandoy, J. Rodas, O. Gonzalez, and R. Gregor, “Current control designed with model based predictive control for six-phase motor drives,” *ISA Trans.*, 2019.

[17] M. Ayala, O. Gonzalez, J. Rodas, R. Gregor, and M. Rivera, “Predictive control at fixed switching frequency for a dual three-phase induction machine with Kalman filter-based rotor estimator,” in *Proc. ICA-ACCA*, 2016, pp. 1–6.

[18] O. Gonzalez, M. Ayala, J. Doval-Gandoy, J. Rodas, R. Gregor, and M. Rivera, “Predictive-fixed switching current control strategy applied to six-phase induction machine,” *Energies*, vol. 12, no. 12, p. 2294, 2019.

[19] O. Gonzalez, M. Ayala, J. Rodas, R. Gregor, G. Rivas, and J. Doval-Gandoy, “Variable-speed control of a six-phase induction machine using predictive-fixed switching frequency current control techniques,” in *Proc. PEDG*, 2018, pp. 1–6.

[20] J. J. Aciego, I. G. Prieto, and M. J. Duran, “Model predictive control of six-phase induction motor drives using two virtual voltage vectors,” *IEEE J. Emerg. Sel. Top. Power Electron.*, vol. 7, no. 1, pp. 321–330, 2018.

[21] I. Gonzalez-Prieto, M. J. Duran, J. J. Aciego, C. Martin, and F. Barrero, “Model predictive control of six-phase induction motor drives using virtual voltage vectors,” *IEEE Trans. Ind. Electron.*, vol. 65, no. 1, pp. 27–37, 2017.

[22] Y. Zhao and T. Lipo, “Space vector PWM control of dual three-phase induction machine using vector space decomposition,” *IEEE Trans. Ind. Electron.*, vol. 31, no. 5, pp. 1100–1109, 1995.

[23] J. Rodas, F. Barrero, M. R. Arahal, C. Martin, and R. Gregor, “On-line estimation of rotor variables in predictive current controllers: A case study using five-phase induction machines,” *IEEE Trans. Ind. Electron.*, vol. 63, no. 9, pp. 5348–5356, 2016.

[24] J. Rodas, C. Martin, M. R. Arahal, F. Barrero, and R. Gregor, “Influence of covariance-based ALS methods in the performance of predictive controllers with rotor current estimation,” *IEEE Trans. Ind. Electron.*, vol. 64, no. 4, pp. 2602–2607, 2017.

[25] C. S. Lim, E. Levi, M. Jones, N. A. Rahim, and W. P. Hew, “FCS-MPC-based current control of a five-phase induction motor and its comparison with PI-PWM control,” *IEEE Trans. Ind. Electron.*, vol. 61, no. 1, pp. 149–163, 2013.

[26] M. Novak, T. Dragicevic, and F. Blaabjerg, “Weighting factor design based on Artificial Neural Network for Finite Set MPC operated 3L-NPC converter,” in *Proc. APEC*, 2019, pp. 77–82.

[27] B. Majmunović, T. Dragičević, and F. Blaabjerg, “Multi objective modulated model predictive control of stand-alone voltage source converters,” *IEEE J. Emerg. Sel. Top. Power Electron.*, 2019.

Variable-Speed Control of a Six-Phase Induction Machine using Predictive-Fixed Switching Frequency Current Control Techniques

Osvaldo Gonzalez[1], Magno Ayala[1], Jesus Doval-Gandoy[2], Jorge Rodas[1], Raul Gregor[1] and Gustavo Rivas[1]
[1]Laboratory of Power and Control Systems, Facultad de Ingeniería, Universidad Nacional de Asunción, Paraguay,
ogonzalez@ing.una.py, mayala@ing.una.py, jrodas@ing.una.py, rgregor@ing.una.py, gusyri@hotmail.com
[2]Applied Power Electronics Technology Research Group, Universidad de Vigo, Spain, jdoval@uvigo.es

***Abstract*—Model predictive control method has been recently introduced as an alternative to inner current controllers of multiphase drives using rotor field oriented control methods. Model predictive controllers are distinguished by a variable switching frequency which causes noise, large voltage and current ripples at low sampling frequency. Therefore, this paper proposes a variable-speed control for six-phase induction motor drives by using an inner loop of predictive-fixed switching frequency current control scheme. Experimental results are provided in order to prove the feasibility of the proposed control technique, considering mean squared error as well as the total harmonic distortion of the stator currents as figure of merit. The efficiency of the proposed control could be verified by applying the non-parametric Mann-Whitney statistical test on the experimentally obtained data.**

***Index Terms*—Fixed switching frequency, multiphase machines, predictive control.**

I. Introduction

Multiphase induction machine (IM) has gained higher attention compared to its three-phase counterparts due to its fault tolerance, lower torque pulsation and better power distribution per phase which are very attractive to the research community for industrial applications where a high-performance control is required [1]. In recent times, several applications of multiphase IMs are being studied, such as wind power generation system, electric vehicles (EV) and hybrid EV [2]. In all these applications, multiphase IM would be performed under variable-speed conditions, including speed sensorless operations [3]. The most common speed control structure for multiphase IM is the field-oriented control (FOC) technique, a cascaded scheme with an inner current control loop and an outer speed control loop [4]. Several new control strategies have been developed for the inner current control loop for multiphase IM such as: model predictive control (MPC), resonant and direct torque control and also its extension to post-fault operation [5]. The implemented solution of MPC shows excellent transient performance as well as the easy inclusion of nonlinearities in the model comparing with traditional proportional-integral (PI) controllers [6]. The main obstacle of the MPC methods is that the control can only select from a finite number of valid switching states because of the absence of a modulator. This generates distortion and also large voltage and current ripples at low sampling frequency. The variable switching frequency produces a spread spectrum, decreasing the performance of the system in terms of power quality [7]. To overcome this issue, an enhanced predictive controller with fixed switching frequency is presented in this paper. This method is based on a modulation scheme incorporated to the conventional MPC for different power converters [8]–[11]. This method is applied to a two-level voltage source inverter (VSI), where for a selected number of switching states the duty cycles are generated by using two active vectors and two zero vectors which are applied to the converter using a given switching pattern in order to obtain an efficient dynamic of the system. For the external speed control loop, a PI controller is designed by a technique detailed in [12].

The main contribution of this paper is the experimental validation of the aforementioned predictive-fixed switching frequency technique used as an inner current control applied to a variable-speed six-phase IM drive. The efficiency of the predictive-fixed current control technique is analyzed by using the mean square error (MSE) and the total harmonic distortion (THD) as indices of performance. The figures of merit used are not of constant magnitude. This is easily appreciated when a replication of the experiment is performed. In such cases, we have a probability distribution function for each variable considered (MSE and THD). When sample sizes are small it is more appropriate to make no assumption about the distribution of variables when comparisons are to be made. This results in the application of non-parametric statistical techniques [13]. Specifically, the Mann-Whitney test is used to compare the central tendencies of the values obtained through the experimental results for each scenario described in Section IV.

II. Six-Phase Induction Machine Drive

A six-phase IM associated with a six-phase VSI and a DC voltage source (V_{dc}) is considered where the phase propagation angles of this IM are:

$$[\theta_p] = \begin{bmatrix} 0 & \frac{\pi}{6} & \frac{2\pi}{3} & \frac{5\pi}{6} & \frac{4\pi}{3} & \frac{3\pi}{2} \end{bmatrix} \quad (1)$$

The electrical scheme of the VSI drive is shown in Fig. 1. The six-phase IM is a continuous system which can be described by a group of differential equations. By applying the vector space decomposition (VSD) technique [14], the

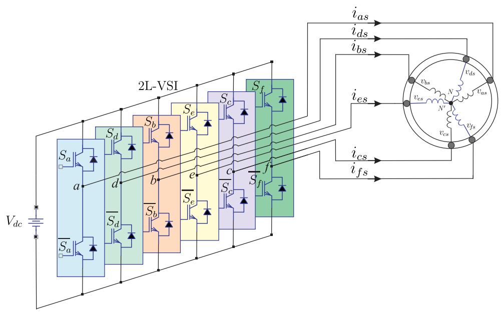

Fig. 1. Scheme of a six-phase IM connected to a six-phase VSI.

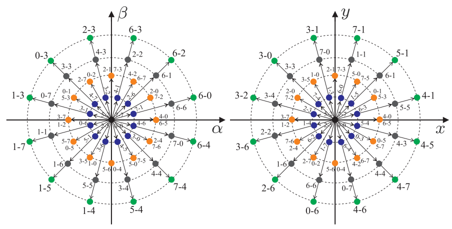

Fig. 2. Voltage space vectors and switching states in the (α-β) and (x-y) sub-spaces for a six-phase IM.

original six dimensional space of the six-phase IM, defined by its six phases (a, b, c, d, e, f), is converted into three two dimensional orthogonal sub-spaces in the stationary reference frame, represented as (α-β), (x-y) and (z_1-z_2), by using the transformation matrix $\mathbf{T}$ [15] and an invariant amplitude criterion was selected, where only (α-β) components contribute to the torque and flux production. The (z_1-z_2) components are not considered due to the isolated neutral points configuration.

$$\mathbf{T} = \frac{1}{3}\begin{array}{c}\left[\begin{array}{cccccc} \multicolumn{6}{c}{\cos([\theta_p])} \\ \multicolumn{6}{c}{\sin([\theta_p])} \\ \multicolumn{6}{c}{\cos(5\,[\theta_p])} \\ \multicolumn{6}{c}{\sin(5\,[\theta_p])} \\ 1 & 0 & 1 & 0 & 1 & 0 \\ 0 & 1 & 0 & 1 & 0 & 1 \end{array}\right]\end{array}\begin{array}{c} \alpha \\ \beta \\ x \\ y \\ z_1 \\ z_2 \end{array} \tag{2}$$

The VSI has a discrete nature with an amount of $64 = 2^6$ different switching states defined by six switching functions corresponding to the six inverter legs $[S_a, S_b, S_c, S_d, S_e, S_f]$, where $\mathbf{S}_i \in \{0, 1\}$. The different switching states and the voltage of the V_{dc} define the phase voltages which can be mapped to the (α-β)-(x-y) sub-spaces according to the VSD approach. Fig. 2 shows the 64 possibilities which lead only to 48 different active voltage vectors plus one null vector in the (α-β)-(x-y) sub-spaces. The six-phase IM can be written by using a state-space model, based on the VSD technique and the dynamic reference transformation which is defined by:

$$\frac{d\mathbf{X}_{(t)}}{dt} = \mathbf{A}_{(t)}\,\mathbf{X}_{(t)} + \mathbf{B}_{(t)}\,\mathbf{U}_{(t)} + \mathbf{H}\,\varpi_{(t)} \tag{3}$$

being $\mathbf{U}_{(t)}$ the input vector of the state-space model, $\mathbf{X}_{(t)}$ the state vector and $\mathbf{A}_{(t)}$ and $\mathbf{B}_{(t)}$ are matrices determined by the electrical parameters of the six-phase IM. The process noise is defined as $\varpi_{(t)}$ and $\mathbf{H}$ is the noise weight matrix.

The state-space model, expressed in (3), and $\mathbf{X}_{(t)} = [x_1, x_2, x_3, x_4, x_5, x_6]^T$ defines the following equations:

$$\begin{aligned}
\frac{dx_1}{dt} &= -R_s c_2 x_1 + c_4\left(L_m\omega_r x_2 + R_r x_5 + L_r\omega_r x_6\right) + c_2 u_1 \\
\frac{dx_2}{dt} &= -R_s c_2 x_2 + c_4\left(-L_m\omega_r x_1 - L_r\omega_r x_5 + R_r x_6\right) + c_2 u_2 \\
\frac{dx_3}{dt} &= -R_s c_3 x_3 + c_3 u_3 \\
\frac{dx_4}{dt} &= -R_s c_3 x_4 + c_3 u_4 \\
\frac{dx_5}{dt} &= R_s c_4 x_1 + c_5\left(-L_m\omega_r x_2 - R_r x_5 - L_r\omega_r x_6\right) - c_4 u_1 \\
\frac{dx_6}{dt} &= R_s c_4 x_2 + c_5\left(L_m\omega_r x_1 + L_r\omega_r x_5 - R_r x_6\right) - c_4 u_2
\end{aligned} \tag{4}$$

where ω_r is the rotor electrical speed, R_s, R_r, L_m, $L_r = L_{lr} + L_m$ and $L_s = L_{ls} + L_m$ are the electrical parameters of the six-phase IM. The coefficients are determined as $c_1 = L_s L_r - L_m^2$, $c_2 = \frac{L_r}{c_1}$, $c_3 = \frac{1}{L_{ls}}$, $c_4 = \frac{L_m}{c_1}$ and $c_5 = \frac{L_s}{c_1}$. The input vector is constituted of the applied voltages to the stator $u_1 = v_{\alpha s}$, $u_2 = v_{\beta s}$, $u_3 = v_{xs}$, $u_4 = v_{ys}$ and the state vector corresponds to the six-phase IM stator and rotor currents $x_1 = i_{\alpha s}$, $x_2 = i_{\beta s}$, $x_3 = i_{xs}$, $x_4 = i_{ys}$, $x_5 = i_{\alpha r}$ and $x_6 = i_{\beta r}$.

Stator voltages are dependant of the input control signals. In this particular case, the simplest VSI model has been considered to achieve a good optimization process. Through this model the stator voltages can be obtained from the ideal six-phase VSI model $\mathbf{M}_{[\mathbf{S}]}$ [15].

$$\mathbf{M}_{[\mathbf{S}]} = \frac{1}{3}\begin{bmatrix} 2 & 0 & -1 & 0 & -1 & 0 \\ 0 & 2 & 0 & -1 & 0 & -1 \\ -1 & 0 & 2 & 0 & -1 & 0 \\ 0 & -1 & 0 & 2 & 0 & -1 \\ -1 & 0 & -1 & 0 & 2 & 0 \\ 0 & -1 & 0 & -1 & 0 & 2 \end{bmatrix}\mathbf{S}^T \tag{5}$$

Taking into account the ideal six-phase VSI, is possible to transform the gating signals into stator voltages which can be mapped to (α-β) and (x-y) sub-spaces and defined in $\mathbf{U}_{(t)} = [u_1,\, u_2,\, u_3,\, u_4]^T$ which yields to the following equations:

$$\mathbf{U}_{(t)} = V_{dc}\,\mathbf{T}\,\mathbf{M}_{[\mathbf{S}]} \tag{6}$$

$$\mathbf{Y}_{(t)} = \mathbf{C}\,\mathbf{X}_{(t)} + \nu_{(t)} \tag{7}$$

being $\mathbf{Y}$ the output vector, $\nu_{(t)}$ the measurement noise and $\mathbf{C}$:

$$\mathbf{C} = \begin{bmatrix} 1 & 0 & 0 & 0 & 0 & 0 \\ 0 & 1 & 0 & 0 & 0 & 0 \\ 0 & 0 & 1 & 0 & 0 & 0 \\ 0 & 0 & 0 & 1 & 0 & 0 \end{bmatrix}$$

The mechanical equations of the six-phase IM are:

$$T_e = 3P\left(\psi_{\alpha s} i_{\beta s} - \psi_{\beta s} i_{\alpha s}\right) \tag{8}$$

$$J_i \frac{d\omega_m}{dt} + B_i \omega_m = (T_e - T_L) \tag{9}$$

where B_i is the friction coefficient, J_i the inertia coefficient, T_e defines the generated torque, T_L is the load torque, ω_m is the rotor mechanical speed, $\psi_{\alpha s}$ and $\psi_{\beta s}$ are the stator fluxes, and P is the number of pole pairs.

III. Proposed Speed Controller

A two degree PI controller with saturator, proposed in [12], is utilized as the external speed control loop, based on FOC control technique due to its easiness. In the FOC scheme, PI speed controller is utilized to create the reference current in dynamic reference frame. The current reference utilized by the MPC are obtained from the calculation of the electric angle used to change the current reference, initially in dynamic reference frame (d-q), to static reference frame (α-β). The process of calculation of the slip frequency (ω_{sl}) is achieved in the same way as the FOC techniques, from the reference currents in dynamic reference frame (i^*_{ds}, i^*_{qs}) and the electrical parameters of the machine (R_r, L_r), and the mechanical speed is acquired by using an encoder. A detailed block diagram of the proposed speed control technique for the six-phase IM drive is presented in Fig. 3.

A. Classic MPC

MPC uses the mathematical model of the system, namely predictive model, to predict at time $[k]$ the future values $[k+1]$, by using measured variables such as the stator currents and the mechanical speed.

$$\hat{\mathbf{X}}_{[k+1|k]} = \mathbf{X}_{[k]} + T_s\, f\left(\mathbf{X}_{[k]},\, \mathbf{U}_{[k]},\, \omega_{r[k]}\right) \tag{10}$$

In the state-space representation (10) only the stator currents, voltages and mechanical speed are measured. The stator voltages are easily predicted from the switching commands issued to the VSI, however, the rotor currents cannot be directly measured. This fact can be solve by means of estimating the rotor current using a reduced order estimators where the reduced order estimators provide an estimate for only the unmeasured part of the state vector. Then, in this work, the rotor current is estimated by the method proposed in [16] by using a reduced order estimator based on a Kalman filter (KF). In that sense, considering a zero-mean Gaussian measurement and uncorrelated process noises, the system's equations can be written as:

$$\hat{\mathbf{X}}_{[k+1|k]} = \mathbf{A}_{[k]}\mathbf{X}_{[k]} + \mathbf{B}_{[k]}\mathbf{U}_{[k]} + \mathbf{H}\varpi_{[k]} \tag{11}$$

$$\mathbf{Y}_{[k+1|k]} = \mathbf{C}\,\mathbf{X}_{[k+1]} + \nu_{[k+1]} \tag{12}$$

where $\mathbf{A}_{[k]}$ and $\mathbf{B}_{[k]}$ are discretized matrices from (4). $\mathbf{A}_{[k]}$ depends on the present value of $\omega_{r[k]}$ and must be considered at every sampling time. A detailed description of the dynamics of the reduced order KF can be found in [16], [17] which has not been exhibit for the sake of conciseness.

B. Cost Function

Then, the MPC performs a optimization process at every sampling time. This process consists in the evaluation of a cost function (13) for all possible stator voltages in order to achieve its control objective. As the cost function can be represented in several ways, in this paper, it is selected the minimization of the current tracking error, defined as the following equation:

$$\begin{aligned} J_{[k+2|k]} =& \| i^*_{\alpha s[k+2]} - \hat{i}_{\alpha s[k+2|k]} \|^2 + \| i^*_{\beta s[k+2]} - \hat{i}_{\beta s[k+2|k]} \|^2 \\ &+ \lambda_{xy}\left(\| i^*_{xs[k+2]} - \hat{i}_{xs[k+2|k]} \|^2 + \| i^*_{ys[k+2]} - \hat{i}_{ys[k+2|k]} \|^2 \right) \end{aligned} \tag{13}$$

being $i^*_{s[k+2]}$ the vector containing the reference for the stator currents and $\hat{i}_{s[k+2]}$ the vector containing the predictions based on the second-step ahead state. In order to put more emphasis on (α-β) or (x-y) sub-spaces a tuning parameter (λ_{xy}) is used [16], [17].

C. Modulated model predictive control (M2PC)

It is feasible to determine each available vector for the VSI in the (α-β) plane, which defines 64 sectors (48 different), which are given by two adjacent vectors. The proposed technique evaluates the prediction of the two active vectors that conform each sector at every sampling time and evaluates the cost function separately for each prediction. Each prediction is evaluated based on (10) and the only difference is in the calculation of the input vector $\mathbf{U}_{[k]}$ [15]. The duty cycles, for the two active vectors d_1 and d_2, are calculated by solving the following equations:

$$d_0 = \tfrac{\sigma}{J_0} \qquad d_1 = \tfrac{\sigma}{J_1} \qquad d_2 = \tfrac{\sigma}{J_2} \tag{14}$$

$$d_0 + d_1 + d_2 = T_s \tag{15}$$

where d_0 corresponds to the duty cycle of a zero vector. Then, it is possible to obtain the expression for σ and the duty cycles for each vector given as:

$$d_0 = \frac{T_s J_1 J_2}{J_0 J_1 + J_1 J_2 + J_0 J_2} \tag{16}$$

$$d_1 = \frac{T_s J_0 J_2}{J_0 J_1 + J_1 J_2 + J_0 J_2} \tag{17}$$

$$d_2 = \frac{T_s J_0 J_1}{J_0 J_1 + J_1 J_2 + J_0 J_2} \tag{18}$$

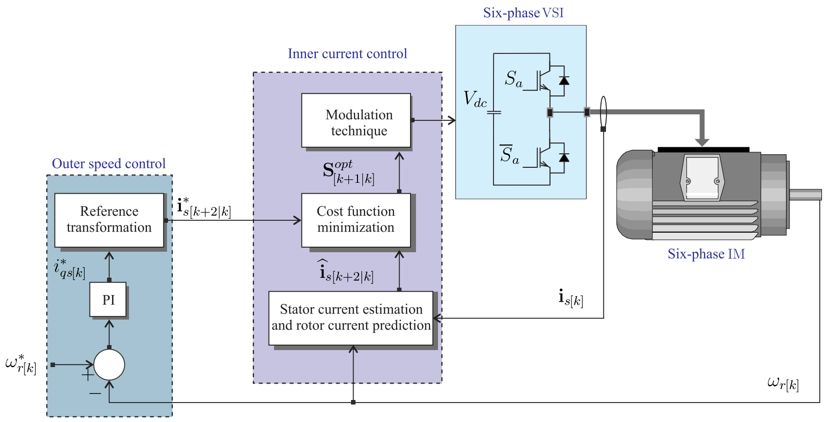

Fig. 3. Speed control with an inner current control based on predictive-fixed control and using KF for rotor current estimation.

Considering these expressions, the new cost function, which is evaluated at every T_s, is defined as:

$$G_{[k+2|k]} = d_1 J_1 + d_2 J_2 \tag{19}$$

The two vectors which minimize $G_{[k+2|k]}$ are selected and applied to the VSI at the next sampling time. After obtaining the duty cycles and selecting the optimal two vectors to be applied, a switching pattern procedure, shown in [15], is adopted with the goal of applying the two active vectors $(v_1 - v_2)$ and two zero vectors (v_0), considering the calculated duty cycles obtaining a fixed-switching frequency.

IV. Experimental Results

A detailed block diagram of the MPC technique for the six-phase IM is provided in Fig. 3. The six-phase IM is powered by two typical three-phase VSI, using a constant DC voltage of 400 V from a DC power supply. The VSI are controlled by a dSPACE MABXII DS1401 real-time prototyping platform. The experimental results are captured and processed using MATLAB R2013b. The motor position is measured with a 1024-pulses-per-revolution incremental encoder, and then, the speed is estimated from it. A 5 HP eddy current brake is used to connect a variable mechanical load. Table I shows the electrical and mechanical parameters for the six-phase IM.

TABLE I
Electrical and Mechanical Parameters of the six-phase IM

R_r	6.9 Ω	L_s	654.4 mH
R_s	6.7 Ω	P	1
L_{ls}	5.3 mH	P_w	2 kW
L_{lr}	12.8 mH	J_i	0.07 kg.m^2
L_m	614 mH	B_i	0.0004 kg.m^2/s
L_r	626.8 mH	ω_{r-nom}	3000 rpm

In Table II and Table III, a steady state analysis for stator currents under different rotor speed references (ω_r^*), are shown with M2PC and classic MPC, respectively. A total of 7 samples are obtained to measure the MSE for (α-β), (x-y) stator currents and the mechanical rotor speed (ω_r) as well as the THD for (α-β) stator currents.

TABLE II
Analysis of N Samples of Stator Currents (α-β), (x-y), MSE [A], THD [%] for M2PC at Different Rotor Speeds [rpm].

		Speed	ω_r^* =	500	[rpm]		
N	MSE$_\alpha$	MSE$_\beta$	MSE$_x$	MSE$_y$	THD$_\alpha$	THD$_\beta$	MSE$_{\omega_r}$
1	0.1140	0.1226	0.1662	0.2060	10.7	9.6	1.9233
2	0.1210	0.1199	0.1508	0.2037	10.5	9.5	1.6378
3	0.1151	0.1207	0.1653	0.2084	10.7	9.4	1.8141
4	0.1233	0.1183	0.1458	0.1981	11.0	9.7	1.8051
5	0.1171	0.1141	0.1529	0.1969	10.1	8.8	1.6634
6	0.1196	0.1158	0.1590	0.1958	10.3	9.0	1.8145
7	0.1111	0.1184	0.1691	0.2027	10.6	9.5	1.5835
		Speed	ω_r^* =	1000	[rpm]		
N	MSE$_\alpha$	MSE$_\beta$	MSE$_x$	MSE$_y$	THD$_\alpha$	THD$_\beta$	MSE$_{\omega_r}$
1	0.1546	0.1470	0.1644	0.2615	12.4	9.9	2.3932
2	0.1491	0.1432	0.1761	0.2599	12.3	9.7	2.6218
3	0.1583	0.1465	0.1677	0.2648	12.3	9.7	2.3217
4	0.1596	0.1480	0.1666	0.2630	12.5	9.9	2.3814
5	0.1594	0.1487	0.1797	0.2650	12.0	9.7	2.6432
6	0.1508	0.1487	0.1807	0.2685	12.0	10.0	2.7061
7	0.1487	0.1485	0.1771	0.2656	12.6	9.9	2.3885
		Speed	ω_r^* =	1500	[rpm]		
N	MSE$_\alpha$	MSE$_\beta$	MSE$_x$	MSE$_y$	THD$_\alpha$	THD$_\beta$	MSE$_{\omega_r}$
1	0.2044	0.1895	0.1875	0.3331	17.5	11.7	3.5112
2	0.2182	0.1908	0.1864	0.3199	18.0	12.1	2.9387
3	0.2193	0.1938	0.1820	0.3220	18.6	12.6	3.2329
4	0.2068	0.1921	0.1863	0.3204	17.8	12.0	2.9350
5	0.2197	0.1909	0.1920	0.3131	17.5	12.0	3.0535
6	0.2106	0.1926	0.1953	0.3277	17.1	12.0	3.2980
7	0.2094	0.1924	0.1907	0.3350	18.3	12.2	2.9544

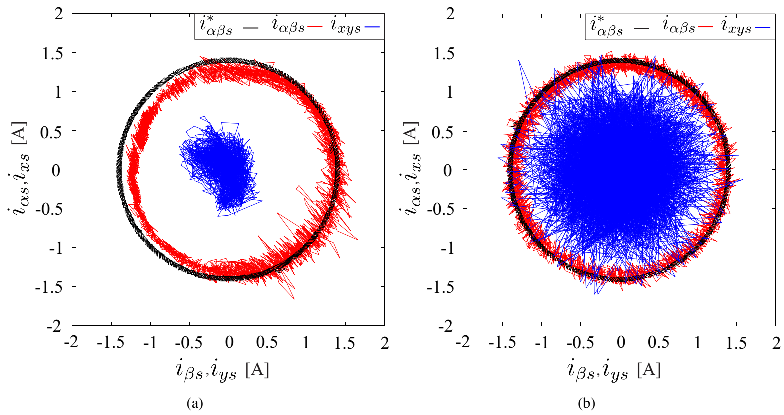

Fig. 4. Stator currents in (α-β) and (x-y) sub-spaces for rotor speed of 500 [rpm] and a sampling frequency of 16 [kHz]: (a) Amplitude of 1.5 [A] for M2PC; (b) Amplitude of 1.5 [A] for classic MPC.

TABLE III
ANALYSIS OF N SAMPLES OF STATOR CURRENTS (α-β), (x-y), MSE [A], THD [%] FOR CLASSIC MPC AT DIFFERENT ROTOR SPEEDS [RPM].

		Speed	ω_r^* =	500	[rpm]		
N	MSE_α	MSE_β	MSE_x	MSE_y	THD_α	THD_β	MSE_{ω_r}
1	0.0730	0.0719	0.4849	0.4929	8.3	8.3	1.7649
2	0.0713	0.0718	0.4825	0.4729	8.3	8.3	1.7851
3	0.0717	0.0713	0.4766	0.4771	8.5	8.2	1.9413
4	0.0726	0.0710	0.4868	0.4791	8.4	8.3	1.6323
5	0.0728	0.0713	0.4839	0.4800	8.5	8.3	1.9156
6	0.0731	0.0722	0.4835	0.4868	8.1	8.3	1.6481
7	0.0731	0.0726	0.4911	0.4839	8.2	8.0	1.6629
		Speed	ω_r^* =	1000	[rpm]		
N	MSE_α	MSE_β	MSE_x	MSE_y	THD_α	THD_β	MSE_{ω_r}
1	0.0847	0.0837	0.5332	0.5322	7.4	7.3	2.1235
2	0.0851	0.0827	0.5298	0.5407	7.5	7.1	2.2418
3	0.0841	0.0808	0.5386	0.5408	7.4	7.1	2.2721
4	0.0848	0.0813	0.5405	0.5327	7.4	7.2	2.1209
5	0.0845	0.0833	0.5356	0.5326	7.4	7.4	1.9444
6	0.0830	0.0822	0.5434	0.5340	7.3	7.3	2.1001
7	0.0844	0.0827	0.5385	0.5347	7.5	7.3	2.1238
		Speed	ω_r^* =	1500	[rpm]		
N	MSE_α	MSE_β	MSE_x	MSE_y	THD_α	THD_β	MSE_{ω_r}
1	0.0720	0.0706	0.5283	0.5144	7.0	6.9	3.0061
2	0.0726	0.0728	0.5190	0.5214	7.0	7.0	3.1270
3	0.0726	0.0703	0.5211	0.5101	7.6	6.9	2.9781
4	0.0706	0.0721	0.5238	0.5180	6.8	6.6	2.7550
5	0.0727	0.0727	0.5328	0.5241	7.0	6.8	3.1873
6	0.0720	0.0703	0.5239	0.5221	6.9	6.7	2.9386
7	0.0682	0.0698	0.5180	0.5134	6.8	6.7	2.5484

TABLE IV
EFFICIENCY ANALYSIS OF BOTH CONTROLLERS BASED ON STATISTICAL TEST.

AH1:	M2PC/Speed	AH2:	Classic MPC/Speed
Variables	p-value	Variables	p-value
MSE_α	0.001	MSE_α	0.001
MSE_β	0.001	MSE_β	0.001
MSE_x	0.001	MSE_x	0.001
MSE_y	0.001	MSE_y	0.001
THD_α	0.001	THD_α	0.001
THD_β	0.001	THD_β	0.001
MSE_{ω_r}	0.001	MSE_{ω_r}	0.001
AH3:	M2PC/Classic MPC 500 [rpm]	AH4:	M2PC/Classic MPC 1500 [rpm]
Variables	p-value	Variables	p-value
MSE_α	0.002	MSE_α	0.001
MSE_β	0.002	MSE_β	0.001
MSE_x	0.002	MSE_x	0.001
MSE_y	0.002	MSE_y	0.001
THD_α	0.002	THD_α	0.001
THD_β	0.001	THD_β	0.001
MSE_{ω_r}	0.949	MSE_{ω_r}	0.259

Fig. 4 exposes the (α-β) and (x-y) stator currents tracking, for M2PC and classic MPC, in steady state for the rotor speed. Fig. 5 shows the transient response for q stator current in a reversal test (speed reference changes from 500 [rpm] to -500 [rpm]) where the M2PC and classic MPC show similar response speed. The presented results in Table IV were obtained by the Mann-Whitney non-parametric statistical test using the software SPSS version 20.0. AH1 is a alternative hypothesis where the variables (MSE and THD) equality is verified for M2PC at different rotor speeds (500 [rpm] and 1000 [rpm]). By considering the obtained probability value (p-value) it can be deducted that the M2PC efficiency is better for a rotor speed of 500 [rpm] in comparison to 1000 [rpm]. After processing other data revolving different rotor speeds, it is obtained a similar result where M2PC has better performance with lower rotor speeds. AH2 is defined as the same analysis than AH1 for classic MPC, where the results are the same, a better performance at lower speed. AH3 and AH4

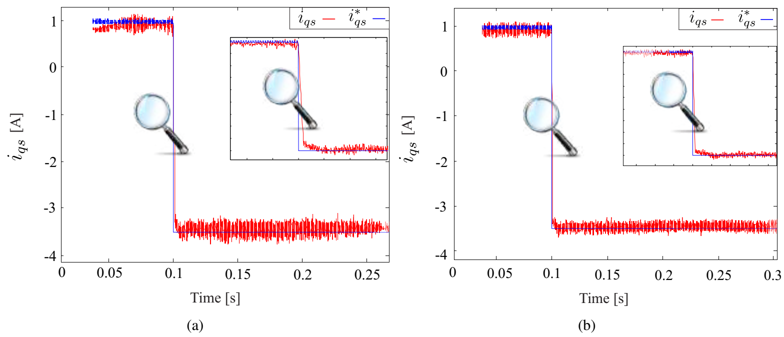

Fig. 5. Transient response in q-axis stator current for rotor speed of 500 [rpm] to -500 [rpm] and a sampling frequency of 16 [kHz]: (a) For M2PC; (b) For classic MPC.

are alternative hypothesis that compare the efficiency of both techniques (M2PC and classic MPC) at rotor speeds of 500 and 1500 [rpm], respectively. The registered p-values demonstrate a different efficiency, particularly better for classic MPC over M2PC in terms of MSE_{α}, MSE_{β}, THD_{α} and THD_{β}. While M2PC efficiency is far superior for MSE_{x} and MSE_{y}. On the other hand, for MSE_{ω_r} the p-value shows that there is not sufficient statistical evidence to reject the same efficiency for both techniques.

V. Conclusion

In this paper a variable-speed control with a modified predictive current control technique with fixed switching frequency (M2PC) applied to the six-phase IM is presented. The experimental and statistical results were compared between M2PC and the classic MPC and showed a better performance in the (x-y) currents reduction for M2PC. However, in the (α-β) currents tracking, M2PC had a worse performance compared to classic MPC due to a saturation effect in the measured currents. In terms of speed tracking both techniques had similar results and in the transient analysis, the response was almost the same for both techniques. It can be concluded that M2PC is a good alternative to classic MPC to improve the (x-y) currents reduction.

Acknowledgment

The authors wish to thank the financial support from the Paraguayan Science and Technology National Council (CONACYT) through project 14-INV-101.

References

[1] E. Levi, "Advances in converter control and innovative exploitation of additional degrees of freedom for multiphase machines," *IEEE Trans. Ind. Electron.*, vol. 63, no. 1, pp. 433–448, 2016.

[2] I. Subotic, N. Bodo, and E. Levi, "Integration of six-phase EV drivetrains into battery charging process with direct grid connection," *IEEE Trans. Energy Convers.*, vol. 32, no. 3, pp. 1012–1022, 2017.

[3] M. Ayala, O. Gonzalez, J. Rodas, R. Gregor, and J. Doval-Gandoy, "A speed-sensorless predictive current control of multiphase induction machines using a Kalman filter for rotor current estimator," in *Proc. ESARS-ITEC*, pp. 1–6, 2016.

[4] M. Jones, S. N. Vukosavic, D. Dujic, and E. Levi, "A synchronous current control scheme for multiphase induction motor drives," *IEEE Trans. Energy Convers.*, vol. 24, no. 4, pp. 860–868, 2009.

[5] H. S. Che, M. J. Duran, E. Levi, M. Jones, W.-P. Hew, and N. A. Rahim, "Postfault operation of an asymmetrical six-phase induction machine with single and two isolated neutral points," *IEEE Trans. Power Electron.*, vol. 29, no. 10, pp. 5406–5416, 2014.

[6] S. Vazquez, J. Rodriguez, M. Rivera, L. G. Franquelo, and M. Norambuena, "Model predictive control for power converters and drives: Advances and trends," *IEEE Trans. on Ind. Electron.*, vol. 64, no. 2, pp. 935–947, 2016.

[7] M. Vijayagopal, P. Zanchetta, L. Empringham, L. De Lillo, L. Tarisciotti, and P. Wheeler, "Modulated model predictive current control for direct matrix converter with fixed switching frequency," in *Proc. EPE*, 2015, pp. 1–10, 2015.

[8] F. Gavilan, D. Caballero, S. Toledo, E. Maqueda, R. Gregor, J. Rodas, M. Rivera, and I. Araujo-Vargas, "Predictive power control strategy for a grid-connected 2L-VSI with fixed switching frequency," in *Proc. ROPEC*, pp. 1–6, 2016.

[9] S. Toledo, M. Rivera, J. Muñoz, R. Peña, J. Riveros, and R. Gregor, "Fixed switching frequency predictive control for a multi-drive indirect matrix converter system," in *Proc. SPEC*, pp. 1–6, 2017.

[10] M. Rivera, S. Toledo, C. Baier, L. Tarisciotti, P. Wheeler, and S. Verne, "Indirect predictive control techniques for a matrix converter operating at fixed switching frequency," in *Proc. PRECEDE*, pp. 13–18, 2017.

[11] L. Comparatore, R. Gregor, J. Rodas, J. Pacher, A. Renault, and M. Rivera, "Model based predictive current control for a three-phase cascade H-bridge multilevel STATCOM operating at fixed switching frequency," in *Proc. PEDG*, pp. 1–6, 2017.

[12] L. Harnefors, S. Saarakkala, and M. Hinkkanen, "Speed control of electrical drives using classical control methods," *IEEE Trans. Ind. Appl.*, vol. 49, no. 2, pp. 889–898, 2013.

[13] H. B. Mann and D. R. Whitney, "On a test of whether one of two random variables is stochastically larger than the other," *The annals of mathematical statistics*, pp. 50–60, 1947.

[14] Y. Zhao and T. Lipo, "Space vector PWM control of dual three-phase induction machine using vector space decomposition," *IEEE Trans. Ind. Electron.*, vol. 31, no. 5, pp. 1100–1109, 1995.

[15] M. Ayala, J. Rodas, R. Gregor, J. Doval-Gandoy, O. Gonzalez, M. Saad, and M. Rivera, "Comparative study of predictive control strategies at fixed switching frequency for an asymmetrical six-phase induction motor drive," in *Proc. IEMDC*, pp. 1–8, 2017.

[16] J. Rodas, F. Barrero, M. R. Arahal, C. Martin, and R. Gregor, "On-line estimation of rotor variables in predictive current controllers: A case study using five-phase induction machines," *IEEE Trans. Ind. Electron.*, vol. 63, no. 9, pp. 5348–5356, 2016.

[17] J. Rodas, C. Martin, M. R. Arahal, F. Barrero, and R. Gregor, "Influence of covariance-based ALS methods in the performance of predictive controllers with rotor current estimation," *IEEE Trans. Ind. Electron.*, vol. 64, no. 4, pp. 2602–2607, 2017.

ISA Transactions 98 (2020) 496–504

Contents lists available at ScienceDirect

ISA Transactions

journal homepage: www.elsevier.com/locate/isatrans

Practice article

Current control designed with model based predictive control for six-phase motor drives

Magno Ayala [a,*], Jesus Doval-Gandoy [b], Jorge Rodas [a], Osvaldo Gonzalez [a], Raul Gregor [a]

[a] Laboratory of Power and Control Systems, Facultad de Ingeniería, Universidad Nacional de Asunción, Paraguay
[b] Applied Power Electronics Technology Research Group, Universidad de Vigo, Spain

ARTICLE INFO

Article history:
Received 6 May 2018
Received in revised form 27 February 2019
Accepted 28 August 2019
Available online 6 September 2019

Keywords:
Model-based predictive control
Multiphase induction machine
Power electronics
Six-phase drives

ABSTRACT

Finite control set model-based predictive control techniques are distinguished by being an interesting alternative to traditional field oriented control techniques for multiphase drives due to their fast dynamic response and flexibility in the introduction of constraints. However, those predictive control techniques have some drawbacks regulating the $(x-y)$ current components which can cause machine losses as well as a high computational burden. This paper presents a comparative study of an enhanced predictive current control technique with a conventional predictive control technique and two hybrid predictive control techniques applied to an asymmetrical six-phase induction motor drive in terms of current tracking, total harmonic distortion of stator currents and computational burden. Experimental results are reported to demonstrate the benefits of the different current control techniques by using the mean squared error and total harmonic distortion of stator currents as quality figures of merit and the number of floating point operations to measure the computational burden of each predictive control, thus concluding the advantages and limitations of each technique at transient and steady regimes.

1. Introduction

Model-based predictive control (MPC) has gained attention in the last years as an alternative to conventional linear control techniques [1–3]. MPC strategies are identified by the requirement of a defined system model in order to predict the next values for the system state variables. Once the future state variables are estimated, the MPC uses an optimization criterion by minimizing a cost function that describes the desired system behavior in every sample time. MPC has a fast dynamic response and can be applied to different systems, such as AC–DC converters [4], controlled grid-connected converters [5,6], permanent magnet synchronous machines [7,8] and induction motors (IMs) [9,10]. MPC is classified in a continuous control set MPC and finite-control-set MPC (FCS–MPC) which is mainly applied, due to its discrete nature, to three-phase and multiphase systems with different voltage source inverters (VSIs) topologies, being the two-level VSI the most studied [7–10].

At the same time, the research in the field of multiphase IM has been growing in the last decade [11–13]. Comparing to the conventional three-phase IM, multiphase IMs have some intrinsic advantages such as major power splitting, lower torque ripple and better fault tolerance [14]. By considering these advantages over three-phase IMs, the applications for multiphase IMs have been increasing in areas such as electric and hybrid vehicles [15] and wind energy conversion systems [11,16]. It is considered that any multiphase IM can be analyzed by the vector space decomposition (VSD) technique, obtaining multiple orthogonal planes, $(\alpha-\beta)$, $(x-y)$ and (z_1-z_2), which represent the electromagnetic energy conversion excluding some higher harmonics of the order $12n \pm 1$ $(n = 1, 2, 3\ldots)$, the machine energy losses and the homopolar plane, respectively [17]. For two isolated neutrals configuration, (z_1-z_2) currents cannot flow, therefore the components of the (z_1-z_2) sub-space can be ignored [18].

FCS–MPC, applied to multiphase IM drives, has been developed for the first time in 2009 in [19,20], verifying its performance as an alternative to conventional control techniques. However, FCS–MPC techniques are known for their high computational cost [20,21]. In addition, some state observers were considered to perform a speed-sensorless control in multiphase machines in [22–24] and also to improve the prediction of the FCS–MPC applied to multiphase induction machines [25–28]. Some restrained vectors techniques were presented in [29,30], which consist in reducing the selection of some space vector voltages as the control output based on a constraint such as avoiding the voltage vectors that generate more harmonics or generate more $(x-y)$ currents, to reduce the computational cost in FCS–MPC and some modulation techniques were described in [31–33], such as pulse width modulation (PWM), based on space vector modulation,

* Corresponding author.
E-mail addresses: mayala@ing.una.py (M. Ayala), jdoval@uvigo.es (J. Doval-Gandoy), jrodas@ing.una.py (J. Rodas), ogonzalez@ing.una.py (O. Gonzalez), rgregor@ing.una.py (R. Gregor).

https://doi.org/10.1016/j.isatra.2019.08.052
0019-0578/© 2019 ISA. Published by Elsevier Ltd. All rights reserved.

added to FCS–MPC to reduce $(x-y)$ currents. It can be noticed that in these cited works there is not an exhaustive comparison between different predictive current control techniques in order to analyze their advantages and limitations for implementation of predictive control techniques applied to multiphase motor drives.

The main contribution of this paper is a comparative study of four FCS–MPC applied as a predictive current control (PCC) technique, with a Kalman filter (KF) as a state observer to operate an asymmetrical six-phase induction motor drive (ASIMD) in terms of current tracking, THD of stator currents and computational burden. The four PCC techniques, which differ each other by the method to select the optimal vector and the modulation technique applied in some of them, are compared by using the mean square error (MSE), THD and the number of floating point operations (FPOs), to measure the computational burden of each PCC, as figures of merit. These techniques are tested for different operating conditions, in steady-state and transient conditions.

This paper is organized as follows: the ASIMD state-space model is presented in Section 2. In Section 3, the PCC design is shown, where it describes the traditional PCC which will be used as a reference for the comparative study. Sections 4–6 describe the three PCC techniques to be compared. The experimental results show the transient and steady-state behavior, for the four PCC where the figures of merit are compared, in Section 7. Section 8 summarizes the conclusion.

2. Asymmetrical six-phase IM model

The system is composed of an ASIMD connected to a six-phase VSI and a DC voltage source (V_{dc}). An electrical scheme of the VSI drive is shown in Fig. 1. The ASIMD is a continuous system which can be described by a group of differential equations. By applying the VSD approach, the six-dimensional space of the ASIMD, defined by its six-phases (a, b, c, d, e, f), is transformed into three two-dimensional orthogonal planes in the stationary reference frame, represented as $(\alpha-\beta)$, $(x-y)$ and (z_1-z_2), by using the transformation matrix $\mathbf{T}$ [32]. The studied ASIMD has isolated neutrals configuration, thus (z_1-z_2) currents are not considered, simplifying the mathematical model used by only considering $(\alpha-\beta)$ and $(x-y)$ planes.

$$\mathbf{T}=\frac{1}{3}\begin{array}{c} \begin{array}{cccccc} a & d & b & e & c & f \end{array} \\ \begin{bmatrix} 1 & \frac{\sqrt{3}}{2} & -\frac{1}{2} & -\frac{\sqrt{3}}{2} & -\frac{1}{2} & 0 \\ 0 & \frac{1}{2} & \frac{\sqrt{3}}{2} & \frac{1}{2} & -\frac{\sqrt{3}}{2} & -1 \\ 1 & -\frac{\sqrt{3}}{2} & -\frac{1}{2} & \frac{\sqrt{3}}{2} & -\frac{1}{2} & 0 \\ 0 & \frac{1}{2} & -\frac{\sqrt{3}}{2} & \frac{1}{2} & \frac{\sqrt{3}}{2} & -1 \\ 1 & 0 & 1 & 0 & 1 & 0 \\ 0 & 1 & 0 & 1 & 0 & 1 \end{bmatrix} \end{array} \begin{array}{c} \alpha \\ \beta \\ x \\ y \\ z_1 \\ z_2 \end{array} \tag{1}$$

where an invariant amplitude criterion was selected.

The six-phase VSI has a discrete behavior and a total number of 2^6 = 64 switching states defined by the six VSI legs $\mathbf{S}=[S_a, S_b, S_c, S_d, S_e, S_f]$, where $S_i \in \{0,1\}$. The different switching states and V_{dc} determine the phase voltages, which can be represented into the $(\alpha-\beta)$ and $(x-y)$ planes according to the VSD approach [17]. Fig. 2 shows the 64 possibilities which lead only to 49 different vectors (48 vectors + 1 null vector) in the $(\alpha-\beta)$ and $(x-y)$ planes. The state-space model of the ASIMD is defined by:

$$\dot{\mathbf{X}}_{(t)}=\mathbf{A}_{(t)}\,\mathbf{X}_{(t)}+\mathbf{B}_{(t)}\,\mathbf{U}_{(t)}+\mathbf{H}\,\varpi_{(t)} \tag{2}$$

where $\mathbf{U}_{(t)}$ is the input vector of the state-space model, $\mathbf{X}_{(t)}$ the state vector and $\mathbf{A}_{(t)}$ and $\mathbf{B}_{(t)}$ are matrices determined by the electrical parameters of the ASIMD. The process noise is defined as $\varpi_{(t)}$ and $\mathbf{H}$ is the noise weight matrix. The state-space model

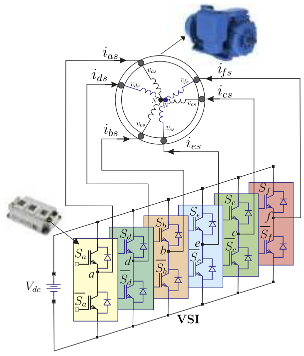

Fig. 1. Scheme of an ASIMD connected to a six-phase VSI.

described by (2) and $\mathbf{X}_{(t)}=[x_1, x_2, x_3, x_4, x_5, x_6]^T$, define the following equation:

$$\begin{bmatrix}\dot{x}_1\\ \dot{x}_2\\ \dot{x}_3\\ \dot{x}_4\\ \dot{x}_5\\ \dot{x}_6\end{bmatrix}=\begin{bmatrix}A_{11} & A_{12} & 0 & 0 & A_{15} & A_{16}\\ A_{21} & A_{22} & 0 & 0 & A_{25} & A_{26}\\ 0 & 0 & A_{33} & 0 & 0 & 0\\ 0 & 0 & 0 & A_{44} & 0 & 0\\ A_{51} & A_{52} & 0 & 0 & A_{55} & A_{56}\\ A_{61} & A_{62} & 0 & 0 & A_{65} & A_{66}\end{bmatrix}\begin{bmatrix}x_1\\ x_2\\ x_3\\ x_4\\ x_5\\ x_6\end{bmatrix}$$
$$+\begin{bmatrix}B_{11} & 0 & 0 & 0 & 0 & 0\\ 0 & B_{22} & 0 & 0 & 0 & 0\\ 0 & 0 & B_{33} & 0 & 0 & 0\\ 0 & 0 & 0 & B_{44} & 0 & 0\\ B_{55} & 0 & 0 & 0 & 0 & 0\\ 0 & B_{66} & 0 & 0 & 0 & 0\end{bmatrix}\begin{bmatrix}u_1\\ u_2\\ u_3\\ u_4\\ 0\\ 0\end{bmatrix} \tag{3}$$

being

$A_{11}=A_{22}=-R_s c_2$ $\quad A_{12}=-A_{21}=c_4 L_m \omega_r$
$A_{15}=A_{26}=c_4 R_r$ $\quad A_{16}=-A_{25}=c_4 L_r \omega_r$
$A_{33}=A_{44}=-R_s c_3$ $\quad A_{51}=A_{62}=R_s c_4$
$A_{52}=-A_{61}=-c_5 L_m \omega_r$ $\quad A_{55}=A_{66}=-c_5 R_r$
$A_{56}=-A_{65}=-c_5 L_r \omega_r$ $\quad B_{11}=B_{22}=c_2$
$B_{33}=B_{44}=c_3$ $\quad B_{55}=B_{66}=-c_4$

where R_s, R_r, L_m, $L_r=L_{lr}+L_m$ and $L_s=L_{ls}+L_m$ are the electrical parameters of the ASIMD. The coefficients are determined as $c_1=L_sL_r-L_m^2$, $c_2=\frac{L_r}{c_1}$, $c_3=\frac{1}{L_{ls}}$, $c_4=\frac{L_m}{c_1}$ and $c_5=\frac{L_s}{c_1}$. The input vector is composed of the applied voltages to the stator $u_1=v_{\alpha s}$, $u_2=v_{\beta s}$, $u_3=v_{xs}$, $u_4=v_{ys}$ and the state vector corresponds to the ASIMD stator and rotor currents $x_1=i_{\alpha s}$, $x_2=i_{\beta s}$, $x_3=i_{xs}$, $x_4=i_{ys}$, $x_5=i_{\alpha r}$ and $x_6=i_{\beta r}$. Stator voltages are dependent on the input control signals $\mathbf{S}$. In this particular case, the simplest VSI model has been considered to obtain a good optimization process. The stator voltages can be calculated from the ideal six-phase VSI model $\mathbf{M}_{[\mathbf{S}]}$ [32].

$$\mathbf{M}_{[\mathbf{S}]}=\frac{1}{3}\begin{bmatrix}2 & 0 & -1 & 0 & -1 & 0\\ 0 & 2 & 0 & -1 & 0 & -1\\ -1 & 0 & 2 & 0 & -1 & 0\\ 0 & -1 & 0 & 2 & 0 & -1\\ -1 & 0 & -1 & 0 & 2 & 0\\ 0 & -1 & 0 & -1 & 0 & 2\end{bmatrix}\mathbf{S}^T \tag{4}$$

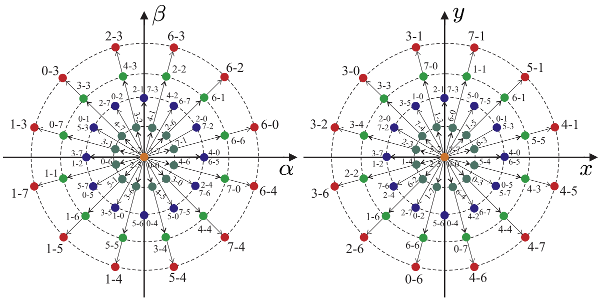

Fig. 2. Voltage space vectors and switching states in $(\alpha-\beta)$ and $(x-y)$ planes for an ASIMD.

An ideal six-phase VSI transforms gating signals into stator voltages which can be projected to $(\alpha-\beta)$ and $(x-y)$ planes and defined in $\mathbf{U}_{(t)} = [u_1,\ u_2,\ u_3,\ u_4]^T$, determined with the following equation:

$$\mathbf{U}_{(t)} = V_{dc}\,\mathbf{T}\,\mathbf{M}_{[\mathbf{S}]} \tag{5}$$

The output vector, **Y**, is:

$$\mathbf{Y}_{(t)} = \mathbf{C}\mathbf{X}_{(t)} + \nu_{(t)} \tag{6}$$

being $\nu_{(t)}$ is the measurement noise and

$$\mathbf{C} = \begin{bmatrix} 1 & 0 & 0 & 0 & 0 & 0 \\ 0 & 1 & 0 & 0 & 0 & 0 \\ 0 & 0 & 1 & 0 & 0 & 0 \\ 0 & 0 & 0 & 1 & 0 & 0 \end{bmatrix}$$

The mechanical equations of the ASIMD are given by:

$$T_e = 3\,P\left(\psi_{\alpha s} i_{\beta s} - \psi_{\beta s} i_{\alpha s}\right) \tag{7}$$

$$J_i\,\dot{\omega}_m + B_i\,\omega_m = (T_e - T_L) \tag{8}$$

$$\omega_r = P\omega_m \tag{9}$$

where B_i is the friction coefficient, J_i the inertia coefficient, T_e defines the produced torque, T_L is the load torque, ω_r is the rotor electrical speed, ω_m is the rotor mechanical speed, $\psi_{\alpha s}$ and $\psi_{\beta s}$ are the stator fluxes and P is the number of pole pairs.

3. FCS–MPC method for an asymmetrical six-phase IM model (PC1)

This section presents the conventional PCC technique equipped with KF for rotor current estimator proposed in [25] (PC1 in what follows). The equations of the ASIMD (3) and (6) have to be discretized so it can be adapted for the PC1. A forward-Euler discretization method is selected to maintain a low computational cost. The resulting equations will be in a digital control form with predicted variables only dependent on the variables past values. Hence, a prediction of the future next-sample state $\hat{\mathbf{X}}_{[k+1|k]}$ is:

$$\hat{\mathbf{X}}_{[k+1|k]} = \mathbf{X}_{[k]} + \mathrm{f}\left(\mathbf{X}_{[k]},\ \mathbf{U}_{[k]},\ T_s,\ \omega_{r[k]}\right) \tag{10}$$

being $[k]$ the current sample and T_s is the sampling time.

3.1. Reduced order observer

The state-space representation in (3) has six state variables, where only stator currents can be measured. Stator voltages are easily calculated from (5), where the switching commands cause the output voltage from the VSI. On the other hand, rotor currents cannot be directly measured. This can be overcome by a reduced order observer to estimate the rotor currents. The reduced order observers estimate a calculation for only the unmeasured part of the state vector. This is the main issue which has been recently covered by the application of the Luenberger observer (LO) and KF techniques, where the KF shows better results due to the observer gains are computed online by considering the measurement and process noises of the ASIMD. However, LO has gains which are not so optimized and it has a deterministic setting [25,28]. Therefore, a reduced order KF is implemented in this work for rotor currents estimation. By considering a zero-mean Gaussian measurement and uncorrelated process noises, the system's equations can be:

$$\hat{\mathbf{X}}_{[k+1|k]} = \mathbf{A}_{[k]}\mathbf{X}_{[k]} + \mathbf{B}_{[k]}\mathbf{U}_{[k]} + \mathbf{H}\varpi_{[k]} \tag{11}$$

$$\mathbf{Y}_{[k+1|k]} = \mathbf{C}\mathbf{X}_{[k+1]} + \nu_{[k+1]} \tag{12}$$

where $\mathbf{A}_{[k]}$ and $\mathbf{B}_{[k]}$ are discretized matrices from (3). $\mathbf{A}_{[k]}$ is also dependable on the present value of $\omega_{r[k]}$ and must be considered at every sampling period. The error dynamics of the reduced order observer is presented as:

$$e_{[k+1]} = \boldsymbol{\lambda}_{[k]} e_{[k]} = \left\{ \begin{bmatrix} 1 + A_{55}T_s & A_{56}T_s \\ A_{65}T_s & 1 + A_{66}T_s \end{bmatrix} - \mathbf{K}_{[k]} \begin{bmatrix} A_{15}T_s & A_{16}T_s \\ A_{25}T_s & A_{26}T_s \end{bmatrix} \right\} e_{[k]} \tag{13}$$

where $e_{[k]}$ is the error between the estimated rotor currents and the real rotor currents while $\mathbf{K}_{[k]}$ is the KF gain. For a fast error convergence to zero, the real parts of the eigenvalues of $\boldsymbol{\lambda}_{[k]}$ should be as negative as possible. It can also be considered that rotor currents have a very low dynamic facilitating the KF speed convergence. A detailed description of the convergence and dynamics of the reduced order KF (and LO) can be found in [25,26] and it was not included for the sake of conciseness.

3.2. Cost function

The cost function design can grant the optimization of many important variables such as machine torque ripple minimization, VSI switching losses and harmonic content reduction [2]. As consequence, by including more terms in the cost function the controller can easily include other variables or constraints. In PC1 the parameter is the tracking error in the predicted stator currents for the next sample. Therefore, the cost function is determined as:

$$J_{[k+2|k]} = \|i^*_{\alpha s[k+2]} - \hat{i}_{\alpha s[k+2|k]}\|^2 + \|i^*_{\beta s[k+2]} - \hat{i}_{\beta s[k+2|k]}\|^2 + \lambda_{xy}\left(\|i^*_{xs[k+2]} - \hat{i}_{xs[k+2|k]}\|^2 + \|i^*_{ys[k+2]} - \hat{i}_{ys[k+2|k]}\|^2\right) \tag{14}$$

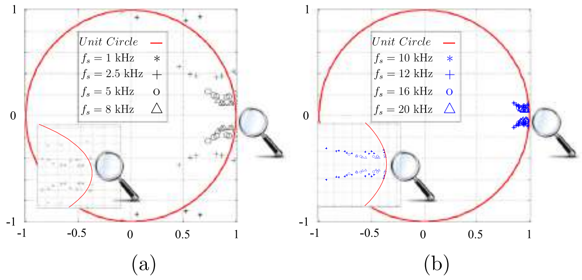

Fig. 3. Eigenvalues of $(\mathbf{A}_{[k]} - \mathbf{B}_{[k]}\mathbf{L}_{[k]})$ matrix at different sampling frequencies: (a) lower than 10 kHz; (b) higher than 10 kHz.

A second-step ahead prediction of the stator current $\hat{i}_{s[k+2|k]}$ is required for the delay compensation of the computational burden and $i^*_{s[k+2]}$ exhibits the reference trajectory of the stator currents. The tuning parameter λ_{xy} is related to the ASIMD losses [25,32]. As a result, through an iterative algorithm PC1 obtains the optimal output control vector $\mathbf{S}^{opt}$, which is the one that minimizes (14). Then, this optimal switching state is used in (5) and it is applied during the next sampling period. Taking into account the computational cost, it is considered the 49 no redundant voltage vectors to be selected for PC1 which is the number of iterations performed in every sample time. In every iteration there are 48 FPOs related to the prediction calculation, the cost function minimization and the second step prediction process, giving a total amount of 2352 FPOs, while the KF has 450 FPOs.

3.3. Stability analysis

There are many MPC techniques presented in the literature, which have some common properties which formalize the stability field [34]. The main common property is a defined cost function to forecast the future behavior of the system. Hence, one of the most used methods to prove the stability of FCS–MPC is by considering the defined cost function as a candidate-Lyapunov function [35,36], another approach, presented in [35,37] consists in produce a determined gain $\mathbf{L}_{[k]}$ to obtain a stable matrix $(\mathbf{A}_{[k]} - \mathbf{B}_{[k]}\mathbf{L}_{[k]})$ whose eigenvalues are less than 1. The second method is used due to its simplicity and by considering that FCS–MPC has a limited control effort, i.e. 49 voltage vectors in the particular case of the six-phase VSI. For a limited current reference (due to security issues), there is a finite number of $\mathbf{L}_{[k]}$ values through the cost function minimization and it shows guaranteed asymptotic stability with a high sampling frequency (f_s), above 10 kHz, as it shows in Fig. 3(a) and Fig. 3(b).

4. FCS–MPC technique with PWM (PC2)

PC1 technique selects an optimal vector $\mathbf{S}^{opt}$ by minimizing the cost function in (14). Instead of applying the optimal vector to the ASIMD during the entire switching period, PC2 method, presented in [38], uses an optimal vector combining it with the VSD theory to obtain the duty cycles as follows:

$$\boldsymbol{\tau} = \frac{1}{2} + \frac{3}{4}\mathbf{M}_{[\mathbf{S}^{opt}]} \tag{15}$$

where $\boldsymbol{\tau} = \left[\tau_a,\ \tau_b,\ \tau_c,\ \tau_d,\ \tau_e,\ \tau_f\right]^T$ and $\mathbf{M}_{[\mathbf{S}^{opt}]}$ is the ideal VSI model from (4) with the optimal vector selected. The duty cycles, defined as $\boldsymbol{\tau}$, are related with the VSI phases and are normalized between 0 and 1. $\mathbf{S}^{opt}$ produces a certain level of voltage for each phase and this technique, through the duty cycles calculation, allows the VSI to generate a similar level of voltage (75% of the optimal vector value) with a combination of space vectors. This technique can be considered as the application of several vectors in order to reduce the voltage vector amplitude in order to minimize the stator currents in $(x - y)$ plane in one sampling period as shown (with an example for optimal vector $6 - 4$) in Fig. 4. As for the computational cost, it is slightly higher than PC1, since the modulation stage has 90 FPOs.

5. FCS–MPC with computation load reduction method (PC3)

PC3 technique is based on the conventional PC1, which selects an optimal vector through the cost function minimization in (14) for a sample time, and a restrained vector technique which will be applied in the next sample time. The main target of this technique is to reduce the $(x - y)$ stator currents by limiting the selected vectors to a determined region depending on the previously selected vector, in order to give priority to an optimal vector which will generate an opposite voltage vector in the $(x - y)$ plane. However, this technique will limit the $(\alpha - \beta)$ stator currents regulation due to the fact that PC3 uses restrained vectors prioritizing the $(x - y)$ stator currents reduction.

As shown in Fig. 5, the $(x - y)$ plane can be subdivided into four regions, where each region contains 12 not redundant voltage vectors. PC3 will operate as the conventional PC1, where an optimal vector will be selected from the minimization of the cost function. Then the algorithm will reduce the possible vectors for the next sample time, being the selected region, the opposite of the previously selected vector.

This PCC technique is a restrained voltage vector technique, thus it gets a computational load reduction due to the limited iterations executed to process comparing to PC1, being a total of 61 iterations comparing to 98 from PC1 in two sample times. This restrained technique reduces the computational cost by approximately 888 FPOs in every sampling time.

6. FCS–MPC with computation load reduction and PWM (PC4)

PC4 is a combination between PC2 and PC3, where there is a restriction in the voltage vectors selection and a PWM modulation applied in the final stage of the control, as shown in Fig. 6. The main objective of this technique is to improve the $(x - y)$ stator currents reduction by combining the two techniques and still managing to get a PCC with a reduced computational cost due to the limited executed iterations, just adding 90 FPOs for the modulation stage comparing to PC3.

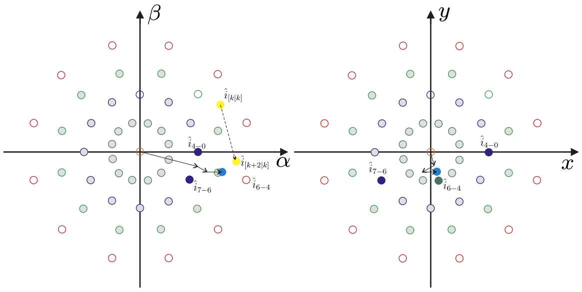

Fig. 4. Stator currents predictions projected by PC2 in the $(\alpha - \beta)$ and $(x - y)$ planes.

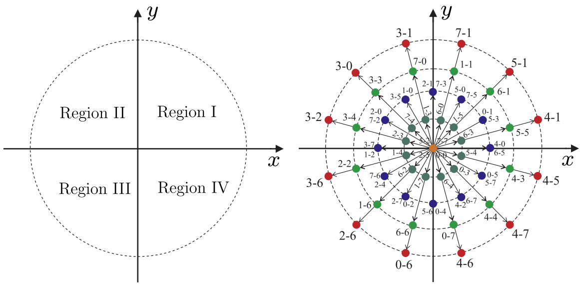

Fig. 5. Voltage space vectors regions in the $(x - y)$ plane determined by PC3 for an ASIMD.

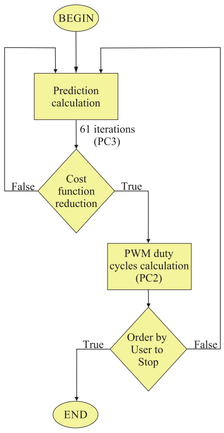

Fig. 6. Block diagram of the PC4 algorithm.

7. Experimental results

7.1. Experimental setup description

The previously described PCC techniques are tested in order to compare the experimental results obtained in the same test bench. The parameters of the ASIMD used in these tests have been obtained using conventional, AC-time domain and stand-still with VSI supply tests [39,40], and the obtained values are described in Table 1. The ASIMD is powered by two conventional three-phase VSI, using a constant DC voltage of 400 V from a DC power supply system. The VSIs are finally controlled by a dSPACE MABXII DS1401 real-time rapid prototyping platform. This platform is designed to perform controllers of the electric motor for automotive applications. As a consequence, this platform is comparable, in robustness and immunity to electromagnetic noise, to any industrial ones. The experimental results included are captured and then processed using MATLAB R2013b. In the experimental tests, the phase currents are measured with the current sensors LA 55-P s, which have a frequency bandwidth from DC up to 200 kHz. The analog measurements are converted to digital with 16-bit A/D converters. The motor position is measured with a 1024-pulses-per-revolution incremental encoder, and then, the speed is calculated from it. Finally, a 5 HP eddy current brake, based on Foucault currents, is used to introduce a variable mechanic load in the system. This brake is able to emulate typical loads attached to the ASIMD, from positive or negative loading steps to linear or quadratic load variations. It is important to mention that the brake control is made externally to the converter's control. A block diagram of the test bench is shown in Fig. 7, including some photos of the equipment.

7.2. Performance parameters

The performance of the three enhanced PCC techniques and the conventional PCC are compared in transient and steady-state conditions. The experimental results show a comparison of the

Table 1
Electrical and mechanical parameters of the ASIMD.

PARAMETER	VALUE	PARAMETER	VALUE
R_r (Ω)	6.9	L_s (mH)	654.4
R_s (Ω)	6.7	P	1
L_{ls} (mH)	5.3	P_w (kW)	2
L_m (mH)	614	J_i (kg m^2)	0.07
L_r (mH)	626.8	B_i (kg m^2/s)	0.0004
ω_{r-nom} (rpm)	3000	V_{dc} (V)	400

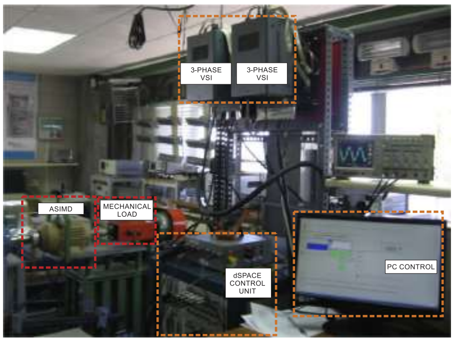

Fig. 7. Block diagram of the test bench including the ASIMD, the VSI, the dSPACE and the mechanical load.

MSE and THD obtained in stator currents in the $(\alpha-\beta)$ and $(x-y)$ planes for all PCC techniques. The MSE is computed as:

$$\mathrm{MSE}(i_{\phi s}) = \sqrt{\frac{1}{N}\sum_{j=1}^{N}(i_{\phi s}-i_{\phi s}^{*})^2} \tag{16}$$

being N the number of analyzed samples, $i_{\phi s}^{*}$ the stator current reference, $i_{\phi s}$ the measured stator current and $\phi \in \{\alpha, \beta, x, y\}$. On the other hand, the THD is computed as:

$$\mathrm{THD}(i_s) = \sqrt{\frac{1}{i_{s1}^2}\sum_{j=2}^{N}(i_{sj})^2} \tag{17}$$

being i_{s1} the fundamental stator current and i_{sj} is the harmonic stator current. The defined cost function in (14) with λ_{xy} = 0.01, was selected to evaluate the dynamic performance of the proposed PCC techniques, prioritizing the $(\alpha-\beta)$ stator current tracking over the $(x-y)$ currents reduction [32]. The process noise and the measurement noise values can be estimated by using the method proposed in [26], as $\hat{Q}_w$ = 0.0022 and $\hat{R}_v$ = 0.0022. In every case, the $(x-y)$ current references are set to zero ($i_{xs}^{*} = i_{ys}^{*} = 0$) and the sampling frequency used in the tests are 12, 16 and 20 kHz.

7.3. Analysis of experimental results

The comparison among the three proposed PCC techniques, defined as PC2, PC3 and PC4, and the conventional PCC, described as PC1, is first analyzed under a steady-state condition, a mechanical load condition based on Foucault currents brake of 5 CV and different rotor speeds (ω_m). Table 2 reports the experimental results obtained for PC1, at different rotor speeds and sampling frequencies, regarding the MSE and THD of stator currents in the $(\alpha-\beta)$ and $(x-y)$ planes. The results demonstrate a good tracking

Table 2
Performance Analysis of Stator Currents $(\alpha-\beta)$, $(x-y)$, MSE (A), THD (%) for PC1 at different rotor speeds (rpm).

ω_m^*	MSE$_\alpha$	MSE$_\beta$	MSE$_x$	MSE$_y$	THD$_\alpha$	THD$_\beta$
		Sampling	frequency	12 kHz		
500	0.0856	0.0874	0.6008	0.5859	8.3101	8.6441
1000	0.0975	0.0952	0.7127	0.7293	6.8383	6.8663
1500	0.0988	0.1006	0.7344	0.7140	5.8643	6.0550
		Sampling	frequency	16 kHz		
500	0.0717	0.0730	0.4707	0.4747	8.9044	8.9615
1000	0.0853	0.0855	0.5505	0.5538	6.1956	6.1703
1500	0.0783	0.0790	0.5736	0.5710	4.4041	4.4777
		Sampling	frequency	20 kHz		
500	0.0641	0.0661	0.4137	0.4103	6.4833	7.1390
1000	0.0745	0.0791	0.4764	0.4813	5.4602	5.8339
1500	0.0726	0.0737	0.4701	0.4649	4.0989	4.3228

Table 3
Performance Analysis of Stator Currents $(\alpha-\beta)$, $(x-y)$, MSE (A), THD (%) for PC2 at different rotor speeds (rpm).

ω_m^*	MSE$_\alpha$	MSE$_\beta$	MSE$_x$	MSE$_y$	THD$_\alpha$	THD$_\beta$
		Sampling	frequency	12 kHz		
500	0.1259	0.1095	0.4862	0.4796	13.2002	11.5178
1000	0.1100	0.1010	0.5360	0.5380	7.6581	7.0963
1500	0.1539	0.1465	0.5092	0.5547	10.1893	9.6681
		Sampling	frequency	16 kHz		
500	0.0827	0.0807	0.3801	0.3652	9.8252	9.3829
1000	0.0927	0.0886	0.4086	0.4058	6.7514	6.5256
1500	0.1102	0.1075	0.4685	0.4627	5.2311	5.3378
		Sampling	frequency	20 kHz		
500	0.0944	0.0877	0.3262	0.3139	10.7465	10.2255
1000	0.1072	0.1025	0.3566	0.3677	7.5919	7.0918
1500	0.1114	0.1096	0.4202	0.4271	5.7400	5.6312

of the current references in the $(\alpha-\beta)$ plane, but a low reduction of the stator currents in the $(x-y)$ plane. Table 3 exposes the results for PC2, considering the MSE and THD of stator currents. For PC2, there is an improvement in the $(x-y)$ stator currents reduction over PC1 of 24 % in average, but there is a decrease of the $(\alpha-\beta)$ current tracking of approximately 21 %.

Table 4 shows the results of the system performance with PC3. From the comparison between PC3 and PC1, there is an improvement of 13 % in average regarding the $(x-y)$ stator currents reduction, however it shows a decrease in the $(\alpha-\beta)$ current tracking of 41 %. At last it is presented in Table 5 the results for PC4 at different rotor speeds and sampling frequencies.

If the results are compared to PC1, it can be seen an improvement of 30 % in average for the $(x-y)$ stator current reduction and a decrease of the $(\alpha-\beta)$ current tracking of approximately 52 %.

Fig. 8 exposes the polar trajectories of the stator currents in the $(\alpha-\beta)$ and $(x-y)$ planes. The obtained results with PC1, PC2, PC3 and PC4 techniques are shown in Fig. 8(a), 8(b), 8(c) and 8(d) respectively. Fig. 9(a), 9(b), 9(c) and 9(d) report the stator phase currents in time domain for PC1, PC2, PC3 and PC4 respectively. By considering the MSE and root mean square (RMS) of the stator currents ripple in the $(\alpha-\beta)$ and $(x-y)$ planes for the four PCC techniques, it can be defined that PC1 has the lowest MSE and RMS current ripple in the $(\alpha-\beta)$ plane, where PC2 has 83 % of RMS ripple and 56 % of MSE greater than PC1, but PC2 has lesser RMS current ripple and MSE in the $(x-y)$ plane comparing to PC1 of approximately 23 % and 44 % respectively. On the other hand, by comparing with PC1, PC3 and PC4 present a lower RMS ripple (12 % and 19 % approximately) and MSE (10 % and 19 % approximately) regarding the currents in the $(x-y)$ plane.

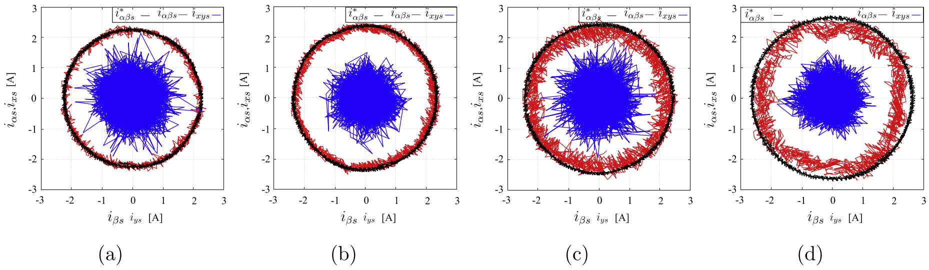

Fig. 8. Stator currents in $(\alpha-\beta)$ and $(x-y)$ planes for a frequency of 25 Hz and ω_m being 1500 rpm: (a) for PC1; (b) for PC2; (c) for PC3; (d) for PC4.

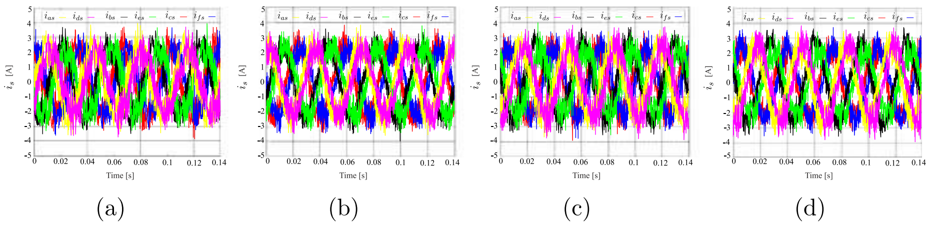

Fig. 9. Stator phase currents in time domain for a frequency of 25 Hz and ω_m being 1500 rpm.: (a) for PC1; (b) for PC2; (c) for PC3; (d) for PC4.

Table 4
Performance Analysis of Stator Currents $(\alpha-\beta)$, $(x-y)$, MSE (A), THD (%) for PC3 at different rotor speeds (rpm).

ω_m^*	MSE_α	MSE_β	MSE_x	MSE_y	THD_α	THD_β
		Sampling	frequency	12 kHz		
500	0.1699	0.1749	0.4996	0.5063	16.2516	16.8039
1000	0.2162	0.2203	0.5759	0.5867	12.9967	13.0654
1500	0.2734	0.2722	0.6339	0.6288	11.4490	11.8897
		Sampling	frequency	16 kHz		
500	0.1419	0.1386	0.3983	0.4023	14.5515	15.0068
1000	0.1798	0.1826	0.4800	0.4792	11.2449	11.1217
1500	0.2133	0.2195	0.5225	0.5345	9.9848	9.9575
		Sampling	frequency	20 kHz		
500	0.1101	0.1223	0.3525	0.3547	11.3357	12.7361
1000	0.1444	0.1557	0.4051	0.4197	9.3282	10.1117
1500	0.1935	0.1827	0.4504	0.4648	8.3290	8.5807

Table 5
Performance Analysis of Stator Currents $(\alpha-\beta)$, $(x-y)$, MSE (A), THD (%) for PC4 at different rotor speeds (rpm).

ω_m^*	MSE_α	MSE_β	MSE_x	MSE_y	THD_α	THD_β
		Sampling	frequency	12 kHz		
500	0.2544	0.2125	0.3685	0.3844	22.3211	17.6980
1000	0.2627	0.2528	0.4467	0.4587	13.7984	13.3634
1500	0.3440	0.3262	0.4961	0.4908	17.4150	16.7115
		Sampling	frequency	16 kHz		
500	0.1716	0.1605	0.3057	0.2980	14.2297	13.3001
1000	0.2113	0.1934	0.3909	0.3742	10.6151	9.8541
1500	0.2882	0.2846	0.4814	0.4773	9.8225	9.5776
		Sampling	frequency	20 kHz		
500	0.1641	0.1463	0.2856	0.2695	15.2786	13.5077
1000	0.1937	0.1817	0.3376	0.3545	11.2976	10.4904
1500	0.2895	0.2719	0.4689	0.4668	10.3093	9.6217

Table 6
Computational cost of the four PCC in terms of FPOs.

PCC	FPOs	PCC	FPOs
PC1	2802	PC3	1914
PC2	2892	PC4	2004

A dynamic comparison test is carried out as shown in Fig. 10 which consists in the transient behavior of the different PCC techniques for a step response in the q axis current reference (i_{qs}^*). The step response is obtained through a modification of the rotor mechanical speed (ω_m) from 500 to −500 rpm, making a reversal condition. In all the figures [Fig. 10(a) to Fig. 10(d)] it is observed the transient performance of PC1 is approximately 2.8 ms, for PC2 is approximately 4.2 ms, PC3 is 10 ms and PC4 is 18 ms for a 5% criterion, showing that PC1 has the highest response speed to reach the new reference (i_{qs}^*). PC2, PC3 and PC4 present a better efficiency regarding the $(x-y)$ currents reduction showing a good performance in terms of energy losses in the ASIMD. However, they present an increased steady-state error in the $(d-q)$ currents tracking of 7%, 12% and 14% respectively, compromising the torque/flux regulation. In this particular subject, PC1 presents the best performance in the $(d-q)$ currents tracking but it has the least efficient current reduction in the $(x-y)$ plane. On the other hand, Table 6 shows the computational cost of the four studied PCC techniques in terms of FPOs, where PC2 has the highest computational cost of all the techniques, while PC3 has the lowest computational cost.

8. Conclusion

A comparative study of four PCC techniques (PC1, PC2, PC3, PC4) is presented. By comparing the currents performance in terms of MSE (with the reference), THD with different operating conditions and the computational burden, it can be determined

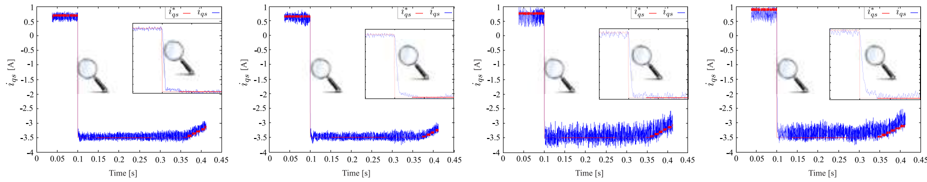

(a) (b) (c) (d)

Fig. 10. Transient step response of i_{qs} from a step response of 500 to −500 rpm from ω_m at a frequency sample of 16 kHz: (a) for PC1; (b) for PC2; (c) for PC3; (d) for PC4.

the advantages and limitations of each proposed technique compared to traditional PCC technique (PC1). PC1 presents a better performance regarding the $(\alpha - \beta)$ currents tracking, comparing to the other PCC techniques, however, it has a decreased capacity in the $(x - y)$ currents reduction. On the other hand, PC2 has an improved performance in terms of $(x - y)$ currents reduction comparing to PC1, and the $(\alpha - \beta)$ currents tracking is a little inferior to PC1. For PC3 and PC4, there is a notorious improvement on the $(x-y)$ currents reduction comparing to PC1, however the performance on the $(\alpha - \beta)$ currents tracking is vastly decreased, consequently worsening the steady-state error eclipsing their $(x - y)$ currents reduction performance. Still, PC3 and PC4 are viable options if considered the lower computational cost compared to PC1 and PC2 in terms of lesser FPOs executed.

Declaration of competing interest

The authors declare that they have no known competing financial interests or personal relationships that could have appeared to influence the work reported in this paper.

Acknowledgments

This research has been funded through the Consejo Nacional de Ciencia y Tecnología (CONACYT)-Paraguay, Grant Numbers 14-INV-101 and POSG16-05.

References

[1] Barrero F, Duran MJ. Recent advances in the design, modeling, and control of multiphase machines: Part I. IEEE Trans Ind Electron 2016;63(1):449–58. http://dx.doi.org/10.1109/TIE.2015.2447733.

[2] Vazquez S, Rodriguez J, Rivera M, Franquelo LG, Norambuena M. Model predictive control for power converters and drives: Advances and trends. IEEE Trans Ind Electron 2017;64(2):935–47. http://dx.doi.org/10.1109/TIE.2016.2625238.

[3] Arahal M, Barrero F, Toral S, Duran M, Gregor R. Multi-phase current control using finite-state model-predictive control. Control Eng Pract 2009;17(5):579–87. http://dx.doi.org/10.1016/j.conengprac.2008.10.005.

[4] Kim S-K, Choi D-K, Lee K-B, Lee YI. Offset-free model predictive control for the power control of three-phase AC/DC converters. IEEE Trans Ind Electron 2015;62(11):7114–26. http://dx.doi.org/10.1109/TIE.2015.2436353.

[5] Rohten JA, Espinoza JR, Muñoz JA, Pérez MA, Melin PE, Silva JJ, Espinosa EE, Rivera M. Model predictive control for power converters in a distorted three-phase power supply. IEEE Trans Ind Electron 2016;63(9):5838–48. http://dx.doi.org/10.1109/TIE.2016.2527732.

[6] Mirzaeva G, Goodwin GC, McGrath BP, Teixeira C, Rivera M. A generalized MPC framework for the design and comparison of VSI current controllers. IEEE Trans Ind Electron 2016;63(9):5816–26. http://dx.doi.org/10.1109/TIE.2016.2578283.

[7] Fuentes E, Silva CA, Kennel RM. MPC implementation of a quasi-time-optimal speed control for a PMSM drive, with inner modulated- FS-MPC torque control. IEEE Trans Ind Electron 2016;63(6):3897–905. http://dx.doi.org/10.1109/TIE.2016.2519326.

[8] Preindl M. Robust control invariant sets and Lyapunov-based MPC for IPM synchronous motor drives. IEEE Trans Ind Electron 2016;63(6):3925–33. http://dx.doi.org/10.1109/TIE.2016.2527722.

[9] Karamanakos P, Stolze P, Kennel RM, Manias S, du Toit Mouton H. Variable switching point predictive torque control of induction machines. IEEE Trans Emerg Sel Topics Power Electron 2014;2(2):285–95. http://dx.doi.org/10.1109/JESTPE.2013.2296794.

[10] Zbede YB, Gadoue SM, Atkinson DJ. Model predictive MRAS estimator for sensorless induction motor drives. IEEE Trans Ind Electron 2016;63(6):3511–21. http://dx.doi.org/10.1109/TIE.2016.2521721.

[11] Duran MJ, Barrero F. Recent advances in the design, modeling, and control of multiphase machines: Part II. IEEE Trans Ind Electron 2016;63(1):459–68. http://dx.doi.org/10.1109/TIE.2015.2448211.

[12] Levi E. Advances in converter control and innovative exploitation of additional degrees of freedom for multiphase machines. IEEE Trans Ind Electron 2016;63(1):433–48. http://dx.doi.org/10.1109/TIE.2015.2434999.

[13] Martín C, Bermúdez M, Barrero F, Arahal MR, Kestelyn X, Durán MJ. Sensitivity of predictive controllers to parameter variation in five-phase induction motor drives. Control Eng Pract 2017;68:23–31. http://dx.doi.org/10.1016/j.conengprac.2017.08.001.

[14] Che HS, Duran MJ, Levi E, Jones M, Hew W-P, Rahim NA. Postfault operation of an asymmetrical six-phase induction machine with single and two isolated neutral points. IEEE Trans Power Electron 2014;29(10):5406–16. http://dx.doi.org/10.1109/TPEL.2013.2293195.

[15] Yeoh SS, Yang T, Tarisciotti L, Hill CI, Bozhko S, Zanchetta P. More electric aircraft starter-generator system with utilization of hybrid modulated model predictive control. In: Proc. ESARS/ITEC; 2016, p. 1–6, http://dx.doi.org/10.1109/ESARS-ITEC.2016.7841399.

[16] Gonzalez-Prieto I, Duran MJ, Che H, Levi E, Bermúdez M, Barrero F. Fault-tolerant operation of six-phase energy conversion systems with parallel machine-side converters. IEEE Trans Power Electron 2016;31(4):3068–79. http://dx.doi.org/10.1109/TPEL.2015.2455595.

[17] Zhao Y, Lipo T. Space vector PWM control of dual three-phase induction machine using vector space decomposition. IEEE Trans Ind Electron 1995;31(5):1100–9. http://dx.doi.org/10.1109/28.464525.

[18] Che HS, Hew WP. Dual three-phase operation of single neutral symmetrical six-phase machine for improved performance. In: Proc. IECON; 2015, p. 1176–81, http://dx.doi.org/10.1109/IECON.2015.7392259.

[19] Arahal M, Barrero F, Toral S, Duran M, Gregor R. Multi-phase current control using finite-state model-predictive control. Control Eng Pract 2009;17(5):579–87. http://dx.doi.org/10.1016/j.conengprac.2008.10.005.

[20] Barrero F, Arahal MR, Gregor R, Toral S, Duran MJ. A proof of concept study of predictive current control for VSI-driven asymmetrical dual three-phase AC machines. IEEE Trans Ind Electron 2009;56(6):1937–54. http://dx.doi.org/10.1109/TIE.2008.2011604.

[21] Rodriguez J, Kazmierkowski MP, Espinoza JR, Zanchetta P, Abu-Rub H, Young HA, Rojas CA. State of the art of finite control set model predictive control in power electronics. IEEE Trans Ind Inf 2013;9(2):1003–16. http://dx.doi.org/10.1109/TII.2012.2221469.

[22] Hosseyni A, Trabelsi R, Mimouni MF, Iqbal A, Alammari R. Sensorless sliding mode observer for a five-phase permanent magnet synchronous motor drive. ISA Trans 2015;58:462–73. http://dx.doi.org/10.1016/j.isatra.2015.05.007.

[23] Ayala M, Gonzalez O, Rodas J, Gregor R, Doval-Gandoy J. A speed-sensorless predictive current control of multiphase induction machines using a Kalman filter for rotor current estimator, In: Proc. ESARS/ITEC; 2016. http://dx.doi.org/10.1109/ESARS-ITEC.2016.7841385.

[24] Mengoni M, Zarri L, Tani A, Serra G, Casadei D. Sensorless speed observer based on third-order spatial field harmonic for multiphase induction motor drives. In: Proc SLED; 2016, p. 1–6. http://dx.doi.org/10.1109/SLED.2016.7518792.

[25] Rodas J, Barrero F, Arahal MR, Martin C, Gregor R. On-line estimation of rotor variables in predictive current controllers: A case study using five-phase induction machines. IEEE Trans Ind Electron 2016;63(9):5348–56. http://dx.doi.org/10.1109/TIE.2016.2559420.

[26] Rodas J, Martin C, Arahal MR, Barrero F, Gregor R. Influence of covariance-based ALS methods in the performance of predictive controllers with rotor current estimation. IEEE Trans Ind Electron 2017;64(4):2602–7. http://dx.doi.org/10.1109/TIE.2016.2636205.

[27] Martin C, Arahal M, Barrero F, Duran M. Five-phase induction motor rotor current observer for finite control set model predictive control of stator current. IEEE Trans Ind Electron 2016;63(7):4527–38. http://dx.doi.org/10.1109/TIE.2016.2536578.

[28] Martín C, Arahal MR, Barrero F, Duran MJ. Multiphase rotor current observers for current predictive control: A five-phase case study. Control Eng Pract 2016;49:101–11. http://dx.doi.org/10.1016/j.conengprac.2016.01.011.

[29] Duran MJ, Prieto J, Barrero F, Toral S. Predictive current control of dual three-phase drives using restrained search techniques. IEEE Trans Ind Electron 2011;58(8):3253–63. http://dx.doi.org/10.1109/TIE.2010.2087297.

[30] Gonzalez-Prieto I, Duran MJ, Aciego JJ, Martin C, Barrero F. Model predictive control of six-phase induction motor drives using virtual voltage vectors. IEEE Trans Ind Electron 2017. http://dx.doi.org/10.1109/TIE.2017.2714126.

[31] Gregor R, Barrero F, Toral S, Duran M, Arahal M, Prieto J, Mora J. Predictive-space vector PWM current control method for asymmetrical dual three-phase induction motor drives. IET Electr Power App 2010;4(1):26–34. http://dx.doi.org/10.1049/iet-epa.2008.0274.

[32] Ayala M, Rodas J, Gregor R, Doval-Gandoy J, Gonzalez O, Saad M, Rivera M. Comparative study of predictive control strategies at fixed switching frequency for an asymmetrical six-phase induction motor drive. In: Proc. IEMDC; 2017, p. 1–8. http://dx.doi.org/10.1109/IEMDC.2017.8002121.

[33] Lu H, Li J, Qu R, Ye D. Fault-tolerant predictive current control with two-vector modulation for six-phase PMSM drives. IET Electr Power App 2018;12(2):169–78. http://dx.doi.org/10.1049/iet-epa.2017.0331.

[34] Mayne DQ, Rawlings JB, Rao CV, Scokaert PO. Constrained model predictive control: Stability and optimality. Automatica 2000;36(6):789–814. http://dx.doi.org/10.1016/S0005-1098(99)00214-9.

[35] Aguilera RP, Quevedo DE. On stability and performance of finite control set MPC for power converters. In: 2011 workshop on predictive control of electrical drives and power electronics. IEEE; 2011, p. 55–62. http://dx.doi.org/10.1109/PRECEDE.2011.6078688.

[36] Aguilera RP, Quevedo DE. On the stability of MPC with a finite input alphabet. IFAC Proc Vol 2011;44(1):7975–80. http://dx.doi.org/10.3182/20110828-6-IT-1002.02705.

[37] Aguilera RP, Quevedo DE. Stability analysis of quadratic MPC with a discrete input alphabet. IEEE Trans Automat Control 2013;58(12):3190–6. http://dx.doi.org/10.1109/TAC.2013.2264551.

[38] Gregor R, Rodas J, Muñoz J, Ayala M, Gonzalez O, Gregor D. Predictive-fixed switching frequency technique for 5-phase induction motor drives. In: Proc. SPEEDAM; 2016, p. 761–7. http://dx.doi.org/10.1109/SPEEDAM.2016.7525849.

[39] Yepes AG, Riveros JA, Doval-Gandoy J, Barrero F, López O, Bogado B, Jones M, Levi E. Parameter identification of multiphase induction machines with distributed windings Part 1: Sinusoidal excitation methods. IEEE Trans Energy Convers 2012;27(4):1056–66. http://dx.doi.org/10.1109/TEC.2012.2220967.

[40] Riveros JA, Yepes AG, Barrero F, Doval-Gandoy J, Bogado B, Lopez O, Jones M, Levi E. Parameter identification of multiphase induction machines with distributed windings part 2: Time-domain techniques. IEEE Trans Energy Convers 2012;27(4):1067–77. http://dx.doi.org/10.1109/TEC.2012.2219862.

Magno Ayala received the B.Eng. degree in electronic engineering from the Universidad Nacional de Asunción (UNA), Paraguay, in 2014 and his M.Sc. in 2017. He joined the Laboratory of Power and Control System at the UNA, in 2015, working as a Research Assistant. Mr. Ayala is a recipient of the training program for university lecturers from the CONACYT of Paraguay for his Ph.D. studies.

Jesús Doval-Gandoy (M99) received the M.Sc. degree from Polytechnic University of Madrid, Madrid, Spain, in 1991 and the Ph.D. degree from the University of Vigo, Vigo, Spain in 1999. From 1991 till 1994 he worked at industry. He is currently an Associate Professor at the University of Vigo. His research interests are in the areas of ac power conversion.

Jorge Rodas (S'08–M'12) was born in Asunción, Paraguay in 1984. He received his B.Eng. degree in Electronic Engineering from the Universidad Nacional de Asunción (UNA), Paraguay, in 2009. He received his M.Sc. degrees from the Universidad de Vigo, Spain, in 2012 and from the Universidad de Sevilla, Spain, in 2013, and his joint-university Ph.D. degree between the Universidad Nacional de Asunción and the Universidad de Sevilla in 2016.

In 2011, he joined the Laboratory of Power and Control System at the UNA, where he is currently an Associate Professor. His main research areas are predictive control, multiphase drives, matrix converters and control of power converters for renewable energy applications.

Osvaldo Gonzalez was born in Paraguay in 1987. B.Eng. degree in electronic engineering from the Universidad Nacional de Asunción (UNA), in 2014 and the M.Sc. degree in Power Electronics in 2017. His research interests include the area of control of multiphase motors. Mr. Gonzalez is a recipient of the training program for university lecturers from the CONACYT of Paraguay for his Ph.D. studies.

Raúl Gregor was born in Asunción, Paraguay, in 1979. He received the Bachelor Degree in Electronic Engineering from the Catholic University of Asunción, Paraguay, in 2005. He received the M.Sc. and Ph.D. degrees in Electronic, Signal Processing and Communications from the Higher Technical School of Engineering (ETSI), University of Seville, Spain, in 2008 and 2010, respectively. Since March 2010, Prof. Gregor is Head of the Laboratory of Power and Control System (LSPyC) of the Engineering Faculty in the National University of Asunción, Paraguay.

Prof. Gregor has authored or coauthored about 40 technical papers in the field of power electronics and control systems, six of which have been published in high impact factor journals. He obtained the Best Paper Award from the IEEE TRANSACTIONS ON INDUSTRIAL ELECTRONICS, Industrial Electronics Society, in 2010, and the Best Paper Award from the IET ELECTRIC POWER APPLICATIONS, in 2012. His research interests include; Multiphase Drives, Advanced Control of Power Converters Topologies, Quality of Electrical Power, Renewable Energy, Modeling, Simulation, Optimization and Control of Power Systems, Smart Metering & Smart Grids and Predictive Control.

A Novel Modulated Model Predictive Control Applied to Six-Phase Induction Motor Drives

Magno Ayala, Jesus Doval-Gandoy, *Member*, *IEEE*, Jorge Rodas, *Senior Member*, *IEEE*, Osvaldo Gonzalez, Raúl Gregor, and Marco Rivera, *Senior Member*, *IEEE*

***Abstract*—Model-based predictive control techniques, with finite set control, are considered an interesting option to control multiphase drives due to their control flexibility and fast dynamic response. However, those techniques have some drawbacks such as a high computational cost, poor ($x-y$) currents reduction and steady-state error, especially at high speeds. To improve some of these drawbacks, modulation stages have been presented as an alternative. However, some of those drawbacks have not been improved. This paper proposes a novel approach to the classic predictive current control applied to an asymmetrical six-phase induction machine where a space vector modulation with specific vectors is used in order to improve the ($x-y$) currents, the steady-state error and total harmonic distortion at high operation speeds. Experimental results are presented to demonstrate the characteristics of the proposed control technique in terms of current tracking, ($x-y$) currents reduction and total harmonic distortion of stator currents compared to the classic predictive current control.**

***Index Terms*—Model-based predictive control, multiphase induction machine, space vector modulation.**

I. Introduction

MULTIPHASE machines have received great attention from the power electronics community due to their good features such as lower current per phase, availability, lower torque ripple and fault tolerant capabilities in comparison with traditional three-phase machines [1]. In the last few years, they were extensively applied especially in high-power applications such as electric vehicles and wind energy conversion systems [1], [2]. The majority of the control approaches applied to multiphase drives are commonly an extension of the control techniques applied to three-phase drives such as field oriented control (FOC) based on proportional-integral (PI) current control, direct torque control, among others [3], [4].

Lately, some new nonlinear control methods were developed to be applied in multiphase machines such as finite control set model predictive control (FCS-MPC), which presents fast transient response in comparison to linear controllers, addressed in [5]–[7], which has some variants already presented in the literature [8]–[10], i.e. MPC with virtual vectors (VV) which nullify the $(x-y)$ currents but with a limited voltage range proposed in [11]–[13]. Another example of these variants is the modulated model predictive control (M2PC) [14], [15]. In the remainder of the paper MPC will be used instead of the cumbersome FCS-MPC as the context makes the notation clear. M2PC is designed as a conventional MPC and a modulation stage, which is based on space vector modulation (SVM). This method was presented for different power converters [16]–[18]. This technique is applied by selecting two optimal active vectors and two zero vectors, where the duty cycles are calculated through their respective cost functions. These vectors are applied by a predetermined switching pattern in order to obtain an efficient performance for the system [18]. Recently, this technique was applied to an asymmetrical six-phase induction machine (ASIMD) in [19] and it showed some improvements over classic MPC, by obtaining a fixed switching frequency and a major reduction of $(x{-}y)$ stator currents. Still, the main drawback of classic MPC, which is the steady-state error [20], [21], was not improved with M2PC especially at high mechanical speeds.

This paper proposes a novel modulated MPC (N-M2PC) that improves the steady-state error, compared to M2PC, and reduces effectively the $(x-y)$ stator currents in an ASIMD. Experimental results are presented to show the advantages of this method in terms of current tracking by considering the mean squared error (MSE), mean value and total harmonic distortion (THD) of the stator currents. This method is tested under different operation points, considering transient and steady-state conditions.

The rest of this document is organized as follows: the ASIMD mathematical model is shown in Section II. In Section III, the classic MPC design is presented as a predictive current control (PCC), where it describes the traditional PCC which will be used as a reference to the obtained results. Section IV describes the M2PC design and Section V presents the proposed N-M2PC. The experimental results show the transient and steady-state performance, for the classic PCC, PCC-VV, M2PC and N-M2PC, where the figures of merit

Manuscript received April 30, 2019; revised July 19, 2019, November 13, 2019 and January 24, 2020; accepted March 17, 2020. This work was supported by the Paraguayan Government through the CONACYT Number POSG16-05 and the Chilean Government through the FONDECYT Regular 1160690 Research Project.

M. Ayala, J. Rodas, O. Gonzalez and R. Gregor are with the Laboratory of Power and Control Systems, Facultad de Ingeniería, Universidad Nacional de Asunción, 2060 Luque, Paraguay (e-mail: mayala,jrodas,ogonzalez,rgregor@ing.una.py).

J. Doval-Gandoy is with the Applied Power Electronics Technology (APET) Research Group, University of Vigo, Vigo 36310, Spain (e-mail: jdoval@uvigo.es).

M. Rivera is with the Laboratory of Energy Conversion and Power Electronics, University of Talca, 3341717, Curicó, Chile (e-mail: marcoriv@utalca.cl).

are analyzed, in Section VI. Finally, conclusions and special remarks are presented in the last section.

II. ASIMD Mathematical Model

The selected system is composed of an ASIMD connected to a six-leg voltage source inverter (VSI) and a DC voltage source. An electrical scheme of the six-phase VSI drive, based on isolated gate bipolar transistor (IGBT), is presented in Fig. 1. The ASIMD has a continuous model which can be analyzed by differential equations. By considering the six-dimensional space of the ASIMD defined by the six-phases (a, b, c, d, e, f) and the vector space decomposition (VSD) technique, the model can be represented into three two-dimensional orthogonal planes in the stationary reference frame, $(\alpha-\beta)$, $(x-y)$ and (z_1-z_2), by using (1), where the invariant amplitude criterion has been applied [15]. The ASIMD has a phase shift of 30° between the three phases and has an isolated neutral configuration, thus (z_1-z_2) currents are assumed to be null.

$$\mathbf{T}=\frac{1}{3}\begin{array}{c} \begin{array}{cccccc} a & d & b & e & c & f \end{array} \\ \left[\begin{array}{cccccc} 1 & \frac{\sqrt{3}}{2} & -\frac{1}{2} & -\frac{\sqrt{3}}{2} & -\frac{1}{2} & 0 \\ 0 & \frac{1}{2} & \frac{\sqrt{3}}{2} & \frac{1}{2} & -\frac{\sqrt{3}}{2} & -1 \\ 1 & -\frac{\sqrt{3}}{2} & -\frac{1}{2} & \frac{\sqrt{3}}{2} & -\frac{1}{2} & 0 \\ 0 & \frac{1}{2} & -\frac{\sqrt{3}}{2} & \frac{1}{2} & \frac{\sqrt{3}}{2} & -1 \\ 1 & 0 & 1 & 0 & 1 & 0 \\ 0 & 1 & 0 & 1 & 0 & 1 \end{array}\right] \end{array} \begin{array}{c} \\ \alpha \\ \beta \\ x \\ y \\ z_1 \\ z_2 \end{array} \tag{1}$$

The six-phase VSI has a discrete output and a total number of $2^6=64$ switching possible states defined by the six-legs. The different switching states and the DC voltage source determine the phase voltages, which can be represented into $(\alpha-\beta)$ and $(x-y)$ planes according to the VSD approach [22]. Fig. 2 denotes the 64 possibilities which only 49 different vectors (48 vectors + 1 null vector) are considered different in the $(\alpha-\beta)$ and $(x-y)$ planes. The state-space mathematical model of the ASIMD is modeled by:

$$\dot{\mathbf{X}}_{(t)}=\mathbf{A}_{(t)}\,\mathbf{X}_{(t)}+\mathbf{B}_{(t)}\,\mathbf{U}_{(t)}+\mathbf{H}\,\varpi_{(t)} \tag{2}$$

where $\mathbf{X}_{(t)}=[x_1,\,x_2,\,x_3,\,x_4,x_5,\,x_6]^T$ is the state vector that represents the stator and rotor currents $x_1=i_{\alpha s}$, $x_2=i_{\beta s}$, $x_3=i_{xs}$, $x_4=i_{ys}$, $x_5=i_{\alpha r}$ and $x_6=i_{\beta r}$, $\mathbf{U}_{(t)}=[u_1,\,u_2,\,u_3,\,u_4]^T=[v_{\alpha s},\,v_{\beta s},\,v_{xs},\,v_{ys}]^T$ is the input vector applied to the stator coils, the process noise is represented as $\varpi_{(t)}$, $\mathbf{H}$ is considered the noise weight matrix and $\mathbf{A}_{(t)}$ and $\mathbf{B}_{(t)}$ are matrices defined by the physical parameters of the ASIMD as follows:

$$\mathbf{A}_{(t)}=\begin{bmatrix} -R_sc_2 & c_4L_m\omega_r & 0 & 0 & c_4R_r & c_4L_r\omega_r \\ c_4L_m\omega_r & -R_sc_2 & 0 & 0 & c_4L_r\omega_r & c_4R_r \\ 0 & 0 & -R_sc_3 & 0 & 0 & 0 \\ 0 & 0 & 0 & -R_sc_3 & 0 & 0 \\ R_sc_4 & -c_5L_m\omega_r & 0 & 0 & -c_5R_r & -c_5L_r \\ -c_5L_m\omega_r & R_sc_4 & 0 & 0 & -c_5L_r & -c_5R_r \end{bmatrix}$$

$$\mathbf{B}_{(t)}=\begin{bmatrix} c_2 & 0 & 0 & 0 \\ 0 & c_2 & 0 & 0 \\ 0 & 0 & c_3 & 0 \\ 0 & 0 & 0 & c_3 \\ -c_4 & 0 & 0 & 0 \\ 0 & -c_4 & 0 & 0 \end{bmatrix}$$

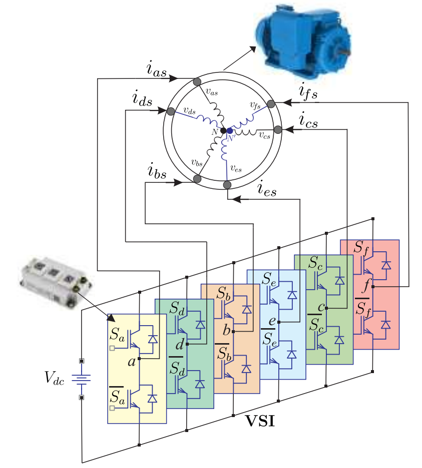

Fig. 1. Scheme of an ASIMD controlled by a six-leg VSI.

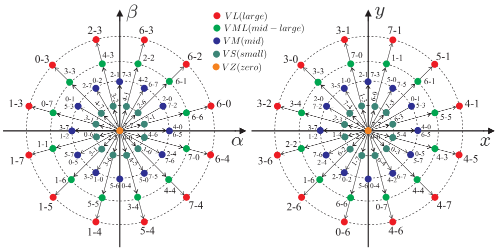

Fig. 2. Voltage space vectors and 64 switching states in $(\alpha-\beta)$ and $(x-y)$ planes for an ASIMD.

being R_s, R_r, L_m, $L_r=L_{lr}+L_m$ and $L_s=L_{ls}+L_m$ are the electrical parameters of the ASIMD. The coefficients are defined as $c_1=L_sL_r-L_m^2$, $c_2=\frac{L_r}{c_1}$, $c_3=\frac{1}{L_{ls}}$, $c_4=\frac{L_m}{c_1}$ and $c_5=\frac{L_s}{c_1}$. Stator voltages depend on the input control signals $\mathbf{S}$, which is considered the switching state. The ideal VSI model has been considered to obtain a good optimization process. Stator voltages can be estimated from the ideal six-leg VSI model $\mathbf{M}_{[\mathbf{S}]}$ [15].

$$\mathbf{M}_{[\mathbf{S}]}=\frac{1}{3}\begin{bmatrix} 2 & 0 & -1 & 0 & -1 & 0 \\ 0 & 2 & 0 & -1 & 0 & -1 \\ -1 & 0 & 2 & 0 & -1 & 0 \\ 0 & -1 & 0 & 2 & 0 & -1 \\ -1 & 0 & -1 & 0 & 2 & 0 \\ 0 & -1 & 0 & -1 & 0 & 2 \end{bmatrix}\mathbf{S}^T. \tag{3}$$

where $\mathbf{S}=[S_a,\,S_b,\,S_c,\,S_d,\,S_e,\,S_f]$, where $\mathbf{S}_i\in\{0,1\}$. The ideal six-leg VSI converts the switching gating signals into stator voltages which are converted to $(\alpha - \beta)$ and $(x - y)$ planes and they are determined in $\mathbf{U}_{(t)}$, defined by:

$$\mathbf{U}_{(t)} = V_{dc}\,\mathbf{T}\,\mathbf{M}_{[\mathbf{S}]}. \tag{4}$$

where V_{dc} is the DC voltage source. The output vector, $\mathbf{Y}$, is:

$$\mathbf{Y}_{(t)} = \mathbf{C}\,\mathbf{X}_{(t)} + \nu_{(t)} \tag{5}$$

where $\nu_{(t)}$ is considered the measurement noise and

$$\mathbf{C} = \begin{bmatrix} 1 & 0 & 0 & 0 & 0 & 0 \\ 0 & 1 & 0 & 0 & 0 & 0 \\ 0 & 0 & 1 & 0 & 0 & 0 \\ 0 & 0 & 0 & 1 & 0 & 0 \end{bmatrix}.$$

The mechanical variables of the ASIMD are related by:

$$T_e = 3\,P\,(\psi_{\alpha s} i_{\beta s} - \psi_{\beta s} i_{\alpha s}) \tag{6}$$

$$J_i\,\dot{\omega}_m + B_i\,\omega_m = (T_e - T_L) \tag{7}$$

$$\omega_r = P\omega_m \tag{8}$$

where J_i is the inertia coefficient, B_i is considered the friction coefficient, T_e represents the electromagnetic torque, T_L is the load torque, ω_r is the rotor electrical angular speed, ω_m the rotor mechanical speed, $\psi_{\alpha s}$ and $\psi_{\beta s}$ are considered the stator fluxes and P the number of pole pairs.

III. Classic PCC

The mathematical model of the ASIMD (2) and (5) must be in discrete form so it can be applied for the PCC. A forward-Euler method is considered to maintain a low computational cost for the controller. The equations will be in digital form with predicted variables only depending on past values of the variables and not on present values. Thus, a prediction of the next sample state $\hat{\mathbf{X}}_{[k+1|k]}$ is defined as:

$$\hat{\mathbf{X}}_{[k+1|k]} = \mathbf{X}_{[k]} + \mathrm{f}\left(\mathbf{X}_{[k]},\, \mathbf{U}_{[k]},\, T_s,\, \omega_{r[k]}\right) \tag{9}$$

being $[k]$ the current sample, f the function nomenclature and T_s is the sampling time.

A. Reduced Order Observers

In the state-space modeling (2), only the stator currents and mechanical rotor speed are measured. The stator voltages are easily estimated from the switching commands sent to the six-phase VSI. However, the rotor currents are rarely measured in real system and they have to be estimated. This issue can be solved by the estimation of the rotor currents through the concept of reduced order observers. The reduced order observers only estimate the value of the unmeasured parts of the state vector. This is an important topic which has been recently solved by the use of Luenberger Observer (LO) [23] and Kalman Filter (KF) [9], [24] techniques, where the KF is considered a better selection due to the fact that the observer gains are optimized taking into account the noise input to the sensors. In LO-based estimator, the gains are not so optimized and the setting is deterministic [9]. Therefore, KF is designed and implemented in this paper to improve the control performance of PCC, by increasing the accuracy of the predictions. By considering zero-mean Gaussian measurement noises and uncorrelated process, the equations of the system state-space mathematical model can be defined as:

$$\hat{\mathbf{X}}_{[k+1|k]} = \mathbf{A}_{[k]}\mathbf{X}_{[k]} + \mathbf{B}_{[k]}\mathbf{U}_{[k]} + \mathbf{H}\varpi_{[k]} \tag{10}$$

$$\mathbf{Y}_{[k+1|k]} = \mathbf{C}\,\mathbf{X}_{[k+1]} + \nu_{[k+1]} \tag{11}$$

where $\mathbf{A}_{[k]}$ and $\mathbf{B}_{[k]}$ are defined by (12)-(14). It can be noted that $\mathbf{A}_{[k]}$ is also dependable on the present value of $\omega_{r[k]}$ and consequently must be considered at every sampling period. A detailed explanation of the dynamics and error convergence of the KF can be found in [9], [24] and it was not included in this work for the sake of conciseness. The aforementioned matrices are defined as:

$$\mathbf{A}_{[k]} = \begin{bmatrix} A_{11} & A_{12} & 0 & 0 & A_{15} & A_{16} \\ A_{21} & A_{22} & 0 & 0 & A_{25} & A_{26} \\ 0 & 0 & A_{33} & 0 & 0 & 0 \\ 0 & 0 & 0 & A_{44} & 0 & 0 \\ A_{51} & A_{52} & 0 & 0 & A_{55} & A_{56} \\ A_{61} & A_{62} & 0 & 0 & A_{65} & A_{66} \end{bmatrix} \tag{12}$$

where $\mathbf{A}_{[k]}$ parameters are defined as follows:

$$\begin{aligned} A_{11} &= A_{22} = 1 - T_s c_2 R_s \\ A_{12} &= -A_{21} = T_s c_4 L_m \omega_{r[k]} \\ A_{15} &= A_{26} = T_s c_4 R_r \\ A_{16} &= -A_{25} = T_s c_4 L_r \omega_{r[k]} \\ A_{33} &= A_{44} = 1 - T_s c_3 R_s \\ A_{51} &= A_{62} = -T_s c_4 R_s \\ A_{52} &= -A_{61} = -T_s c_5 L_m \omega_{r[k]} \\ A_{55} &= A_{66} = 1 - T_s c_5 R_r \\ A_{56} &= -A_{65} = -c_5 \omega_{r[k]} T_s L_r \end{aligned} \tag{13}$$

$$\mathbf{B}_{[k]} = \begin{bmatrix} B_{11} & 0 & 0 & 0 & 0 & 0 \\ 0 & B_{22} & 0 & 0 & 0 & 0 \\ 0 & 0 & B_{33} & 0 & 0 & 0 \\ 0 & 0 & 0 & B_{44} & 0 & 0 \\ 0 & 0 & 0 & 0 & B_{55} & 0 \\ 0 & 0 & 0 & 0 & 0 & B_{66} \end{bmatrix} \tag{14}$$

being $\mathbf{B}_{[k]}$ parameters the following: $B_{11} = B_{22} = T_s c_2$, $B_{33} = B_{44} = T_s c_3$ and $B_{55} = B_{66} = -T_s c_4$

B. Cost Function

The cost function problem can allow the optimization of several important variables such as machine torque ripple minimization, VSI switching losses and harmonic content minimization [20]. However in current control, the most important figure of merit is the tracking error in the predicted stator currents in $(\alpha - \beta)$ and $(x - y)$ planes. PCC analyses the cost function for 49 iterations with the following:

$$J_{[k+2|k]} = \Big[(i^*_{\alpha s[k+2]} - \hat{i}_{\alpha s[k+2|k]})^2 + (i^*_{\beta s[k+2]} - \hat{i}_{\beta s[k+2|k]})^2 + \lambda_{xy} \left((i^*_{xs[k+2]} - \hat{i}_{xs[k+2|k]})^2 + (i^*_{ys[k+2]} - \hat{i}_{ys[k+2|k]})^2 \right) \Big]^{\frac{1}{2}} \tag{15}$$

By using (16), a second-step ahead prediction of the stator currents $\hat{i}_{s[k+2|k]}$ is computed for delay compensation [25]. The desired reference trajectory of the stator currents is represented by $i^*_{s[k+2]}$. The weighting factor optimization is a hot research topic and some recent works tackled this issue [7], [26], [27]. Typically, for multiphase machines, λ_{xy} allows to prioritize the stator currents in $(\alpha - \beta)$ plane [9], [28].

$$\hat{\mathbf{X}}_{[k+2|k]} = \mathbf{A}_{[k]}\mathbf{X}_{[k+1]} + \mathbf{B}_{[k]}\mathbf{U}_{[k+1]} + \mathbf{H}\varpi_{[k]} \tag{16}$$

IV. M2PC

This technique consists in the determination of each available sector for the six-leg VSI in the $(\alpha - \beta)$ plane, being 48 sectors in total, which are composed of two adjacent active vectors and a null vector (VZ), as shown in Fig. 3. This technique, which is based on SVM, estimates the prediction of two active vectors that conform the 12 outside sectors at every sampling time and analyses their respective cost functions (J_0, J_1 and J_2) separately. Each prediction is evaluated based on (15) and the only difference is in the calculation of the input voltage vector $\mathbf{U}_{[k]}$ [15], [19]. The main goal of this modulation technique is to obtain any voltage vector in the $(\alpha - \beta)$ plane by using the large vectors (VL) and the VZ, covering the entire space vector, and at the same time, note that the outside vectors are the smallest voltage vectors in $(x - y)$ plane, managing a reduction of $(x - y)$ currents [19].

The duty cycles, for the two active vectors d_1 and d_2, are obtained by solving the following equations, related to their respective cost functions (24 for every sample time):

$$d_0 = \frac{\sigma}{J_0} \qquad d_1 = \frac{\sigma}{J_1} \qquad d_2 = \frac{\sigma}{J_2} \tag{17}$$

$$d_0 + d_1 + d_2 = 1 \tag{18}$$

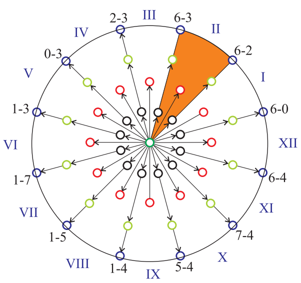

Fig. 3. Available sectors for the six-leg VSI.

where d_0 is the duty cycle of a null vector. Then, it is possible to calculate the expression for σ and the duty cycles for each vector given as:

$$J_T = J_1 J_2 + J_0 J_1 + J_0 J_2 \tag{19}$$

$$d_0 = \frac{J_1 J_2}{J_T} \tag{20}$$

$$d_1 = \frac{J_0 J_2}{J_T} \tag{21}$$

$$d_2 = \frac{J_0 J_1}{J_T} \tag{22}$$

Considering these expressions, the final cost function, which is calculated for 12 iterations during T_s, is considered as:

$$G_{[k+2|k]} = d_1 J_1 + d_2 J_2 \tag{23}$$

The two vectors, which reduce $G_{[k+2|k]}$, are selected and applied to the six-phase VSI at the next sampling time. After calculating the duty cycles for the two vectors to be applied, it is necessary to propose an equation relating the duty cycles and the selected voltage vectors, in order to implement a symmetric pulse width modulation (PWM):

$$\tau_i = \frac{d_0}{2} + d_1 v_{1(i)} + d_2 v_{2(i)} \tag{24}$$

where $i = [a, b, c, d, e, f]$ and τ_i is the duty cycle per phase. This variable is compared to a triangular waveform to obtain the respective symmetric PWM, accomplishing a fixed switching frequency fixing the sampling frequency.

V. N-M2PC

As well as M2PC, N-M2PC is also based on SVM. The main difference is that M2PC only uses 2 VL per sector and N-M2PC uses 4 which include 2 mid vectors (VM) and 2 VL. The main goal of this modulation is to improve further the steady-state error of the stator currents tracking in $(d - q)$ plane by including these adjacent VM per sector in order to avoid the application of VZ which limits the range. This is due to the fact that the desired optimal vector is within the corresponding sector and a certain combination of vector can represent that particular optimal vector. However, VZ reduces the range of the combination of vectors with its corresponding duty cycle, reducing the controller's capacity of tracking the desired stator current in $(\alpha - \beta)$ plane, due to the fact that the duty cycle of VZ increases when the $(x - y)$ currents are being reduced in M2PC. In summary, N-M2PC does not have the same limitation as M2PC, due to the fact that it does not apply VZ and the used vectors add any point in the upper area of the $(\alpha - \beta)$ plane.

The duty cycles, for the four active vectors d_1, d_2, d_3 and d_4, are obtained by solving the following equations:

$$d_1 = \frac{\sigma}{J_1} \qquad d_2 = \frac{\sigma}{J_2} \qquad d_3 = \frac{\sigma}{J_3} \qquad d_4 = \frac{\sigma}{J_4} \tag{25}$$

$$d_1 + d_2 + d_3 + d_4 = 1 \tag{26}$$

where J_1, J_2, J_3 and J_4 are the corresponding cost function (15) for the vectors in the selected sector. As M2PC, it is

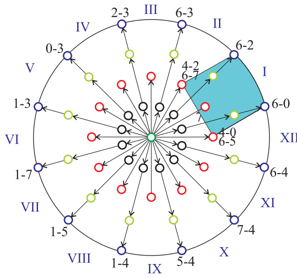

Fig. 4. Available sectors of N-M2PC for the six-leg VSI.

possible to calculate the expression for σ and the duty cycles for each vector given as:

$$J_{T1} = J_1 J_3 J_4 + J_2 J_3 J_4 \tag{27}$$

$$J_{T2} = J_1 J_2 J_4 + J_1 J_2 J_3 \tag{28}$$

$$d_1 = \frac{J_2 J_3 J_4}{J_{T1} + J_{T2}} \tag{29}$$

$$d_2 = \frac{J_1 J_3 J_4}{J_{T1} + J_{T2}} \tag{30}$$

$$d_3 = \frac{J_1 J_2 J_4}{J_{T1} + J_{T2}} \tag{31}$$

$$d_4 = \frac{J_1 J_2 J_3}{J_{T1} + J_{T2}} \tag{32}$$

N-M2PC evaluates all the 12 sectors, as shown in Fig. 4, by calculating the corresponding cost function for each vector (48 in total), then the duty cycles of each vector is calculated as in M2PC, at last, the final cost function is computed as:

$$G_{[k+2|k]} = d_1 J_1 + d_2 J_2 + d_3 J_3 + d_4 J_4 \tag{33}$$

It can be noticed that the VM used to obtain the 12 sectors are the redundant ones, giving the possibility to select each of those vectors in order to apply a certain switching pattern, as the one shown in Fig. 5. This allows the use of a simple equation to calculate the duty cycles $\tau_{(i)}$ for the switching devices of each leg of the VSI, as follows:

$$\tau_{(i)} = d_1 v_{1(i)} + d_2 v_{2(i)} + d_3 v_{3(i)} + d_4 v_{4(i)} \tag{34}$$

where $\tau_{(i)}$ is normalized between 0 and 1, for the switching devices for the six-phase legs VSI. At last, a triangular carrier waveform is used to apply the value of $\tau_{(i)}$ in the corresponding switching devices.

VI. Experimental Results

The proposed N-M2PC technique is validated in order to compare its performance with M2PC and classic PCC through experimental results obtained in the test bench.

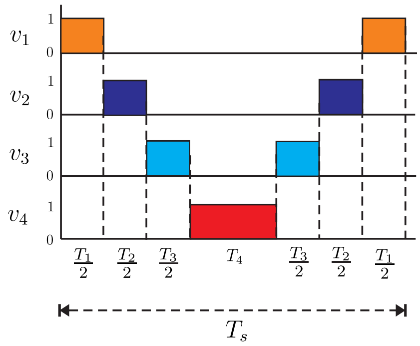

Fig. 5. Switching pattern for the selected optimal vectors.

A. Test bench composition

The test bench is composed of an ASIMD connected to two conventional three-phase VSI, using a constant DC-bus voltage from a DC power supply. The six-phase VSI is controlled by a dSPACE MABXII DS1401 real-time rapid prototyping platform, with MATLAB/Simulink. The results are processed using MATLAB R2013b script. Table I shows the electrical and mechanical parameters of the ASIMD obtained using stand-still with VSI tests and conventional methods of AC time domain [29], [30]. The experimental measurements were obtained with current sensors LA 55-P s, with several turns to improve precision at low current measurement, which have a frequency bandwidth from DC up to 200 kHz. Those values are then converted to digital through 16-bit A/D converter. The ASIMD rotor angle is measured with a 1024 ppr incremental encoder and the mechanical speed is calculated from it. Finally, a 5 HP eddy current brake is used as a variable mechanical load on the ASIMD which is fixed at 1 A. A block diagram of the test bench is shown in Fig. 6. The defined cost function in (15) with λ_{xy} = 0.05 was selected to evaluate the performance of classic PCC, which its influence in the performance is minimal, and M2PC giving more priority to $(\alpha - \beta)$ stator currents tracking over the $(x - y)$ currents reduction. As for N-M2PC, λ_{xy} = 0.1 is selected, due to the fact that it does not use the null vector and the $(x - y)$ currents reduction is obtained through the active vectors combination. It is worth

TABLE I
Parameters of the ASIMD.

PARAMETER	VALUE	PARAMETER	VALUE
R_r (Ω)	6.9	R_s (Ω)	6.7
L_s (mH)	654.4	L_r (mH)	626.8
L_m (mH)	614	L_{ls} (mH)	5.3
ω_{m-nom} (rpm)	3 000	P_w (kW)	2
J_i (kg.m^2)	0.07	B_i (kg.m^2/s)	0.0004
P	1	V_{dc} (V)	400

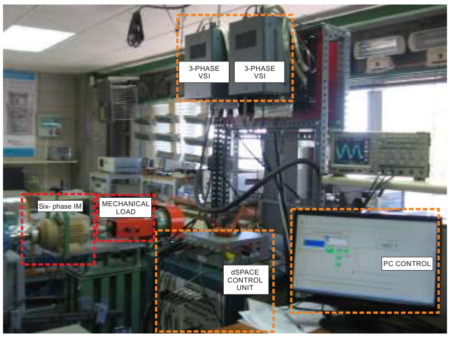

Fig. 6. Block diagram of the test bench including the ASIMD, the dSPACE platform, the eddy current brake and the six-phase VSI.

mentioning that these values of λ_{xy} are selected through heuristic method by focusing on obtaining a sub-optimal system. The process and measurement noise values can be calculated by using the autocovariance-least-squared (ALS) method since provides unbiased estimates with the lowest covariance, guaranteeing optimal KF tuning. By collecting data from a closed-loop operation of the system and then using the method proposed in [24]. The obtained values are $\hat{Q}_w = 0.0022$ and $\hat{R}_v = 0.0022$.

B. Figures of merit

The performance of the proposed N-M2PC is analyzed and compared to classic PCC and M2PC in transient and steady-state conditions. The experimental results analyze the controller performance in terms of MSE between the reference and measured stator currents in $(\alpha - \beta)$ and $(x - y)$ planes. At the same time, the mean value error of $(d - q)$ currents are analyzed to obtain the steady-state error in current tracking for the three techniques. At last, THD is calculated in $(\alpha - \beta)$ plane to complete the analysis. The MSE is defined as:

$$\mathrm{MSE}(i_{s\Phi}) = \sqrt{\frac{1}{N}\sum_{k=1}^{N}(i_{s\Phi}[k] - i_{s\Phi}^{*}[k])^2} \tag{35}$$

where N is the number of analyzed samples, $i_{s\Phi}^{*}$ the stator current reference, $i_{s\Phi}$ the measured stator currents and $\Phi \in \{\alpha,\ \beta,\ x,\ y\}$. On the other hand, the mean value is calculated as:

$$\mathrm{Error}(\%)(i_{s\theta}) = |\frac{100}{N}\sum_{k=1}^{N} i_{s\theta}[k] - i_{s\theta}^{*}[k]| \tag{36}$$

where $i_{s\theta}^{*}$ is $(d - q)$ stator currents reference and $i_{s\theta}$ the measured $(d - q)$ stator currents. At last, THD is defined as:

$$\mathrm{THD}(i_s) = \sqrt{\frac{1}{i_{s1}^2}\sum_{j=2}^{N}(i_{sj})^2} \tag{37}$$

TABLE II
PERFORMANCE ANALYSIS OF STATOR CURRENTS, MSE (A), MEAN ERROR (%) FOR CLASSIC PCC AT DIFFERENT ROTOR SPEEDS (RPM).

		Sampling	frequency	8 kHz		
ω_m^*	MSE$_\alpha$	MSE$_\beta$	MSE$_x$	MSE$_y$	Error$_d$	Error$_q$
500	0.1437	0.1282	0.8228	0.8158	1.48	9.41
1000	0.1443	0.1372	0.9605	0.9570	0.54	7.02
1500	Uns	Uns	Uns	Uns	Uns	Uns
2000	Uns	Uns	Uns	Uns	Uns	Uns
		Sampling	frequency	16 kHz		
ω_m^*	MSE$_\alpha$	MSE$_\beta$	MSE$_x$	MSE$_y$	Error$_d$	Error$_q$
500	0.0831	0.0755	0.4676	0.4763	0.70	3.70
1000	0.0974	0.0858	0.5087	0.5072	0.24	3.79
1500	0.0812	0.0771	0.5185	0.5057	1.48	3.45
2000	Uns	Uns	Uns	Uns	Uns	Uns

TABLE III
PERFORMANCE ANALYSIS OF STATOR CURRENTS, MSE (A), MEAN ERROR (%) FOR PCC-VV AT DIFFERENT ROTOR SPEEDS (RPM).

		Sampling	frequency	8 kHz		
ω_m^*	MSE$_\alpha$	MSE$_\beta$	MSE$_x$	MSE$_y$	Error$_d$	Error$_q$
500	0.1623	0.1620	0.0856	0.0784	0.94	6.23
1000	0.1682	0.1691	0.0905	0.0904	1.02	6.52
1500	Uns	Uns	Uns	Uns	Uns	Uns
2000	Uns	Uns	Uns	Uns	Uns	Uns
		Sampling	frequency	16 kHz		
ω_m^*	MSE$_\alpha$	MSE$_\beta$	MSE$_x$	MSE$_y$	Error$_d$	Error$_q$
500	0.1256	0.1182	0.0640	0.0600	0.86	4.11
1000	0.1299	0.1231	0.0810	0.0638	0.89	4.46
1500	0.1445	0.1231	0.0760	0.0714	6.26	5.89
2000	0.1455	0.1309	0.0860	0.0838	6.50	8.95

where i_{s1} is the fundamental stator currents and i_{sj} is the harmonic stator currents.

C. Steady state analysis

For all cases, $(x - y)$ current references are set to zero ($i_{xs}^{*} = i_{ys}^{*} = 0$). A fixed d current ($i_{ds}^{*} = 1$ A) has been used. The sampling frequencies used in the tests are 8 kHz and 16 kHz. Four steady-state operations are set for mechanical speed: 500 rpm, 1 000 rpm, 1 500 rpm and 2 000 rpm.

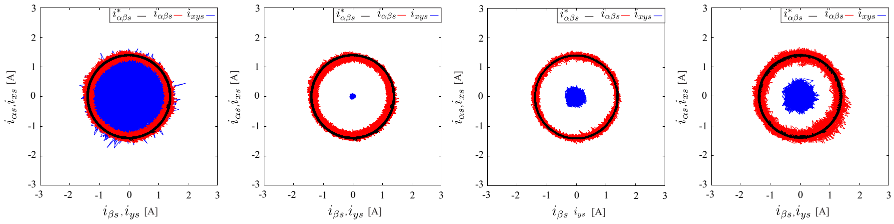

(a) (b) (c) (d)

Fig. 7. Stator currents in $(\alpha-\beta)$ and $(x-y)$ planes at 500 rpm for: (a)classic PCC; (b)PCC-VV; (c)M2PC; (d)N-M2PC.

TABLE V
PERFORMANCE ANALYSIS OF STATOR CURRENTS, MSE (A), MEAN ERROR (%) FOR N-M2PC AT DIFFERENT ROTOR SPEEDS (RPM).

		Sampling	frequency	8 kHz		
ω_m^*	MSE$_\alpha$	MSE$_\beta$	MSE$_x$	MSE$_y$	Error$_d$	Error$_q$
500	0.1977	0.1998	0.2490	0.2553	1.8	2.6
1000	0.2135	0.2159	0.2659	0.2684	3.3	6.9
1500	0.1983	0.1924	0.3012	0.2956	2.25	13.8
2000	0.2033	0.2062	0.3020	0.3020	5.32	18.2
		Sampling	frequency	16 kHz		
ω_m^*	MSE$_\alpha$	MSE$_\beta$	MSE$_x$	MSE$_y$	Error$_d$	Error$_q$
500	0.1004	0.1003	0.2009	0.2130	0.81	2.52
1000	0.1051	0.1049	0.2091	0.2064	1.04	4.84
1500	0.1030	0.1097	0.2172	0.2125	1.97	5.72
2000	0.1084	0.1081	0.2325	0.2287	1.99	8.71

TABLE IV
PERFORMANCE ANALYSIS OF STATOR CURRENTS, MSE (A), MEAN ERROR (%) FOR M2PC AT DIFFERENT ROTOR SPEEDS (RPM).

		Sampling	frequency	8 kHz		
ω_m^*	MSE$_\alpha$	MSE$_\beta$	MSE$_x$	MSE$_y$	Error$_d$	Error$_q$
500	0.0562	0.0592	0.1241	0.1130	1.34	2.69
1000	0.0861	0.0903	0.1485	0.1545	1.9	7.03
1500	0.1039	0.0958	0.1960	0.1944	2.2	7.33
2000	Uns	Uns	Uns	Uns	Uns	Uns
		Sampling	frequency	16 kHz		
ω_m^*	MSE$_\alpha$	MSE$_\beta$	MSE$_x$	MSE$_y$	Error$_d$	Error$_q$
500	0.1046	0.1094	0.1332	0.1334	0.51	3.04
1000	0.1037	0.1059	0.1401	0.1417	0.14	4.59
1500	0.0972	0.0986	0.1038	0.1069	0.4	5.93
2000	0.0976	0.0989	0.1150	0.1182	0.26	9.04

Table II shows the experimental results obtained for different mechanical speeds and sampling frequencies for classic PCC, regarding the MSE of stator currents in $(\alpha-\beta)$ and $(x-y)$ planes and Mean Error (%) in $(d-q)$ planes. The results show good performance of classic PCC in terms of $(\alpha-\beta)$ current tracking and steady-state error for $(d-q)$ currents at a higher sampling frequency compared to lower sampling frequency. However, the $(x-y)$ reduction is insufficient, and the performance is worse at higher mechanical speed to the point of becoming unstable (Uns) at low sampling frequency, where the error system is tending towards infinity due to the fact that parameters such as sampling time, rotor speed, electrical parameters have a direct impact on the poles placement of the ASIMD [31].

Table III presents the performance of PCC-VV which improves the reduction of $(x-y)$ currents compared to classic PCC. On the other hand, Table IV shows the results of M2PC which show a far better performance at lower sampling frequency and lower mechanical speed in all the figures of merit, compared to classic PCC. However, the performance also worsens at higher sampling frequency and mechanical speed, specially in steady-state error for $(d-q)$ currents. Table V exposes the N-M2PC performance in terms of the current tracking and steady-state error in $(d-q)$ currents. It can be seen that N-M2PC improves the steady-state error in $(d-q)$ currents and $(x-y)$ currents reduction compared to classic PCC, but M2PC is better in every aspect, except at high mechanical speeds where N-M2PC is the only stable controller. At higher sampling frequency, N-M2PC is better in every figure of merit in comparison lower sampling frequency and is comparable to M2PC in every figure of merit.

TABLE VI
PERFORMANCE ANALYSIS OF STATOR CURRENTS, THD (%) FOR CLASSIC PCC, PCC-VV, M2PC AND N-M2PC AT DIFFERENT SPEEDS (RPM).

Sampling frequency of 8 kHz				
	PCC	PCC-VV	M2PC	N-M2PC
ω_m^*	THD$_{\alpha\beta}$	THD$_{\alpha\beta}$	THD$_{\alpha\beta}$	THD$_{\alpha\beta}$
500	12.84	13.78	5.39	15.78
1000	14.27	14.85	7.38	14.42
1500	Uns	Uns	8.16	17.98
2000	Uns	Uns	Uns	17.65
Sampling frequency of 16 kHz				
	PCC	PCC-VV	M2PC	N-M2PC
ω_m^*	THD$_{\alpha\beta}$	THD$_{\alpha\beta}$	THD$_{\alpha\beta}$	THD$_{\alpha\beta}$
500	7.55	12.57	10.61	9.95
1000	8.41	12.49	10.17	9.73
1500	7.27	12.70	8.10	9.78
2000	Uns	13.23	7.65	9.54

Table VI shows the THD in $(\alpha-\beta)$ stator currents for Classic PCC, M2PC and N-M2PC for different mechanical speeds. The results present a reduction on the THD

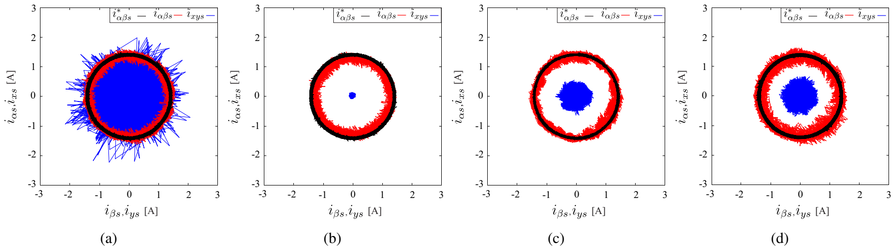

Fig. 8. Stator currents in $(\alpha - \beta)$ and $(x - y)$ planes at 1500 rpm for: (a)classic PCC; (b)PCC-VV; (c)M2PC; (d)N-M2PC.

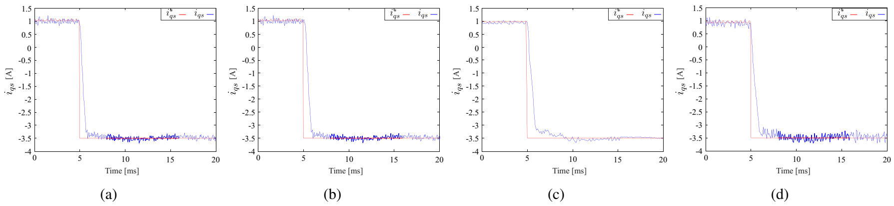

Fig. 9. Transient response of stator current (q) from a step response of 1 A to -3.5 A for different techniques: (a)classic PCC; (b)PCC-VV; (c)M2PC; (d)N-M2PC.

TABLE VII
IMPROVEMENT ANALYSIS (%) OF M2PC AND N-M2PC OVER CLASSIC PCC AT DIFFERENT SPEEDS (RPM).

ω_m^*	MSE$_{\alpha\beta}$	MSE$_{xy}$	Error$_d$	Error$_q$	THD$_{\alpha\beta}$
	Sampling	frequency	8 kHz	(M2PC)	
500	57.36	85.53	9.46	71.41	57.73
1000	37.26	84.20	-251.85	-0.14	46.86
1500	100	100	100	100	100
2000	–	–	–	–	–
	Sampling	frequency	8 kHz	(N-M2PC)	
500	-46.71	69.22	-21.62	72.37	-23.38
1000	-52.66	72.14	-511.11	1.71	-1.12
1500	100	100	100	100	100
2000	100	100	100	100	100
	Sampling	frequency	16 kHz	(M2PC)	
500	-35.39	71.75	27.14	17.84	-41.25
1000	-14.95	72.94	41.67	-21.11	-21.76
1500	-23.80	79.42	72.97	-71.88	-11.74
2000	100	100	100	100	100
	Sampling	frequency	16 kHz	(N-M2PC)	
500	-26.83	56.16	-15.71	31.89	-32.59
1000	-15.08	59.10	-333.33	-27.70	-16.50
1500	-34.57	58.04	-33.11	-65.80	-35.21
2000	100	100	100	100	100

stator currents with higher sampling frequency and higher mechanical speed for classic PCC. For M2PC, the currents THD are better at lower mechanical speed at low sampling frequency, M2PC changes its tendency at high sampling frequency. As for N-M2PC, the THD improves at high sampling frequency and is consistent for every operation.

Fig. 7 and Fig. 8 present the stator currents performance with a polar representation in $(\alpha - \beta)$ and $(x - y)$ planes for classic PCC, PCC-VV, M2PC and N-M2PC. The operations were tested with different eddy current (mechanical load), thus the value of $(\alpha - \beta)$ amplitude is the same at different mechanical speeds. The figures show that $(x - y)$ currents are lower for N-M2PC and especially for M2PC and PCC-VV compared to classic PCC. At last, Table VII presents the performance of M2PC and N-M2PC compared to classic PCC in terms of $\%$, where positive $(+)$ and negative $(-)$ values mean improvement and deterioration respectively.

D. Transient analysis

For a transient condition, a step modification in mechanical speed is considered from 500 to -500 rpm (reversal operation). Fig. 9 exposes a dynamic test (performance of q axis current), which consists of the transient behavior of classic PCC, PCC-VV, M2PC and N-M2PC for a step response in the q axis current (i_{qs}^*). The dynamic response is generated through a reversal operation of the mechanical speed (ω_m) from 500 to -500 rpm. Fig. 9(a) and Fig. 9(b) show a transient test for classic PCC and PCC-VV where the time to reach the new reference is approximately 1 ms. Fig. 9(c) and Fig. 9(d) show the dynamic response of M2PC and N-M2PC, which they present a reaching time of 4 and 3 ms respectively.

E. Robustness analysis

The robustness analysis consists in the performance comparison of the controller at a nominal L_m value and with a variation of 25% of its nominal value, being L_m

TABLE VIII
PERFORMANCE ANALYSIS OF STATOR CURRENTS FOR N-M2PC UNDER 25% OF VARIATION OF THE NOMINAL L_m.

		Sampling	frequency	8 kHz		
ω_m^*	MSE$_\alpha$	MSE$_\beta$	MSE$_x$	MSE$_y$	Error$_d$	Error$_q$
500	0.2175	0.2270	0.2706	0.2721	1.48	11.07
1000	0.2332	0.2389	0.3061	0.3009	6.43	13.82
1500	0.2006	0.2027	0.3019	0.3000	1.87	16.2
2000	0.2094	0.2065	0.3120	0.3096	4.70	19.66
		Sampling	frequency	16 kHz		
ω_m^*	MSE$_\alpha$	MSE$_\beta$	MSE$_x$	MSE$_y$	Error$_d$	Error$_q$
500	0.1145	0.1057	0.2056	0.2130	0.21	3.23
1000	0.1168	0.1157	0.2027	0.2014	0.21	5.30
1500	0.1199	0.1195	0.2042	0.2118	0.95	6.77
2000	0.1219	0.1181	0.2125	0.2200	2.26	8.09

TABLE IX
COMPARATIVE ANALYSIS OF COMPUTATIONAL COST OF CLASSIC PCC, PCC-VV, M2PC AND N-M2PC IN TERMS OF FPOS.

	PCC	PCC-VV	M2PC	N-M2PC
FPOs	2352	1452	1968	2736

the most sensitive parameter in induction machines [32], [33]. This is analyzed by taking in consideration the effect of magnetic saturation of the ASIMD, where L_m value typically changes in approximately that ratio. Table VIII presents the control performance with a L_m change of 25% of the nominal value to analyze the control robustness to uncertainties. The results show that at low speed, the control performance presents a good tracking of stator currents with a variation of approximately 12% and 11%, compared to the unmodified L_m value, for 500 and 1000 rpm respectively, showing an low sensibility in these operation points. On the other hand, at higher speed, the control performance also shows a good current tracking with a variation of approximately 14% and 8%, showing a good robustness at 1500 and 2000 rpm. However, the steady state error in $(d-q)$ currents is severely affected in all the mechanical speeds at 8 kHz, being approximately 5 and 2 times higher, but minimal change in steady state error is obtained, at 16 kHz, of approximately 16%, presenting a good performance at that sampling frequency.

F. Comparative analysis

A comparative analysis regarding computational cost for classic PCC, M2PC and N-M2PC. It is considered the number of floating point operations (FPOs) per technique and then summarized on Table IX. For classic PCC, it is considered 49 iterations to perform correctly, and every iteration has 48 FPOs related to the prediction estimation, the cost function reduction and the second step prediction process. For PCC-VV, it is considered 13 iterations with 121 FPOs and for M2PC and N-M2PC, it is considered 12 iterations with 164 and 228 FPOs respectively.

TABLE X
COMPARATIVE ANALYSIS OF AVERAGE SWITCHING FREQUENCY (KHZ) OF CLASSIC PCC, PCC-VV, M2PC AND N-M2PC AT DIFFERENT SPEEDS (RPM) AND SAMPLING FREQUENCIES (KHZ).

ω_m^*	PCC	PCC-VV	M2PC	N-M2PC
	Sampling frequency of 8 kHz			
500	2.8	3.7	8	1.35
1000	2.7	3.5	8	1.32
1500	–	3.2	8	1.3
2000	–	–	–	1.28
	Sampling frequency of 16 kHz			
500	5.3	6.9	16	2.63
1000	5.15	6.5	16	2.6
1500	4.75	6.2	16	2.5
2000	–	5.8	16	2.37

At last, Table X shows a comparative analysis of the average switching frequency for classic PCC, PCC-VV, M2PC and N-M2PC at different rotor speeds, where the results show a lower switching frequency for lower sampling frequency and higher speeds, due to the fact that the larger voltage vectors are more used in those operation points. As presented in [34], M2PC is a fixed switching frequency technique which maintains the amount of the sampling frequency, due to the fact that it uses null vector, generating less harmonic content, but limiting the sampling range according to the transistor type. As for N-M2PC, the switching frequency is lower, due to the fact it only uses the large and mid vectors, diminishing the semiconductor stress and losses.

VII. CONCLUSION

This paper proposed a novel modulated MPC technique applied to an ASIMD. This technique has been designed to improve the steady-state error in the $(d-q)$ stator currents and effectively reducing the $(x-y)$ sub-space using VL and VM of the $(\alpha-\beta)$ sub-space. The experimental results showed the performance of the proposed technique compared to another modulated technique presented as M2PC, PCC-VV and to classic PCC, where the tests have been done under different operation points (steady and transient conditions) including low and high mechanical speeds, sampling frequencies and tuning parameters for $(x-y)$ stator currents, respectively. As shown in the results, M2PC and PCC-VV are excellent alternatives to classic PCC for low mechanical speeds, specially M2PC which performs excellent in the $(\alpha-\beta)$ sub-space, where all the figures of merit prove a better performance than classic PCC and N-M2PC. However, there is a limitation in terms of high mechanical speeds and higher sampling frequencies, where M2PC worsens its performance, due to the fact that it fixes the switching frequency from the sampling frequency, aggravating the switching losses. On the other hand, N-M2PC is proven to be a great alternative to classic PCC, PCC-VV and M2PC in high mechanical speeds, specially at higher sampling frequencies, where the performance in terms of steady-state error and $(x-y)$ currents minimization are good proving that at lower sampling frequency, it can still perform with stability, unlike classic PCC and M2PC. In transient condition, the results demonstrated a good transient current behavior in terms of response time, where classic PCC is the fastest, followed by N-M2PC. In summary, M2PC presents an excellent performance to be a good alternative in low mechanical speeds up to 1500 rpm (25 Hz, 1 pole pair) and N-M2PC is proven to be a great alternative for high speeds, above 1500 rpm, for industrial applications.

Acknowledgment

The authors would like to thank the Consejo Nacional de Ciencia y Tecnología (CONACYT)-Paraguay, Grant Number POSG16-05 and FONDECYT Regular 1160690 Research Project.

References

[1] E. Levi, "Advances in converter control and innovative exploitation of additional degrees of freedom for multiphase machines," *IEEE Trans. Ind. Electron.*, vol. 63, DOI 10.1109/TIE.2015.2434999, no. 1, pp. 433–448, 2016.

[2] I. Subotic, N. Bodo, E. Levi, B. Dumnic, D. Milicevic, and V. Katic, "Overview of fast on-board integrated battery chargers for electric vehicles based on multiphase machines and power electronics," *Elect. Power Appl.*, vol. 10, DOI 10.1049/iet-epa.2015.0292, no. 3, pp. 217–229, 2016.

[3] E. Levi, R. Bojoi, F. Profumo, H. Toliyat, and S. Williamson, "Multiphase induction motor drives–a technology status review," *Elect. Power Appl.*, vol. 1, DOI 10.1049/iet-epa:20060342, no. 4, pp. 489–516, 2007.

[4] A. G. Yepes, A. Vidal, J. Malvar, O. López, and J. Doval-Gandoy, "Tuning method aimed at optimized settling time and overshoot for synchronous proportional-integral current control in electric machines," *IEEE Trans. Power Electron.*, vol. 29, DOI 10.1109/TPEL.2013.2276059, no. 6, pp. 3041–3054, 2014.

[5] F. Barrero, J. Prieto, E. Levi, R. Gregor, S. Toral, M. J. Durán, and M. Jones, "An enhanced predictive current control method for asymmetrical six-phase motor drives," *IEEE Trans. Ind. Electron.*, vol. 58, DOI 10.1109/TIE.2010.2089943, no. 8, pp. 3242–3252, 2010.

[6] F. Barrero, M. R. Arahal, R. Gregor, S. Toral, and M. J. Durán, "A proof of concept study of predictive current control for VSI-driven asymmetrical dual three-phase AC machines," *IEEE Trans. Ind. Electron.*, vol. 56, DOI 10.1109/TIE.2008.2011604, no. 6, pp. 1937–1954, 2009.

[7] C. S. Lim, E. Levi, M. Jones, N. A. Rahim, and W. P. Hew, "FCS-MPC-based current control of a five-phase induction motor and its comparison with PI-PWM control," *IEEE Trans. Ind. Electron.*, vol. 61, DOI 10.1109/TIE.2013.2248334, no. 1, pp. 149–163, 2013.

[8] E. Fuentes, C. A. Silva, and R. M. Kennel, "MPC implementation of a quasi-time-optimal speed control for a PMSM drive, with inner modulated-fs-mpc torque control," *IEEE Trans. Ind. Electron.*, vol. 63, DOI 10.1109/TIE.2016.2519326, no. 6, pp. 3897–3905, 2016.

[9] J. Rodas, F. Barrero, M. R. Arahal, C. Martín, and R. Gregor, "Online estimation of rotor variables in predictive current controllers: a case study using five-phase induction machines," *IEEE Trans. Ind. Electron.*, vol. 63, DOI 10.1109/TIE.2016.2559420, no. 9, pp. 5348–5356, 2016.

[10] I. Gonzalez-Prieto, M. J. Duran, J. J. Aciego, C. Martin, and F. Barrero, "Model predictive control of six-phase induction motor drives using virtual voltage vectors," *IEEE Trans. Ind. Electron.*, vol. 65, DOI 10.1109/TIE.2017.2714126, no. 1, pp. 27–37, 2018.

[11] I. Gonzalez-Prieto, M. J. Duran, J. J. Aciego, C. Martin, and F. Barrero, "Model predictive control of six-phase induction motor drives using virtual voltage vectors," *IEEE Trans. Ind. Electron.*, vol. 65, DOI 10.1109/TIE.2017.2714126, no. 1, pp. 27–37, 2017.

[12] J. J. Aciego, I. G. Prieto, and M. J. Duran, "Model predictive control of six-phase induction motor drives using two virtual voltage vectors," *IEEE Journal of Emerging and Selected Topics in Power Electronics*, vol. 7, DOI 10.1109/JESTPE.2018.2883359, no. 1, pp. 321–330, 2018.

[13] I. González-Prieto, M. Durán, M. Bermúdez, F. Barrero, and C. Martín, "Assessment of Virtual-Voltage-based Model Predictive Controllers in Six-phase Drives under Open-Phase Faults," *IEEE Journal of Emerging and Selected Topics in Power Electronics*, DOI 10.1109/JESTPE.2019.2915666, 2019.

[14] S. Toledo, M. Rivera, J. Muñoz, R. Peña, J. Riveros, and R. Gregor, "Fixed switching frequency predictive control for a multi-drive indirect matrix converter system," in *Proc. SPEC*, DOI 10.1109/SPEC.2017.8333672, 2017, pp. 1–6.

[15] M. Ayala, J. Rodas, R. Gregor, J. Doval-Gandoy, O. Gonzalez, M. Saad, and M. Rivera, "Comparative study of predictive control strategies at fixed switching frequency for an asymmetrical six-phase induction motor drive," in *Proc. IEMDC*, DOI 10.1109/IEMDC.2017.8002121, 2017, pp. 1–8.

[16] F. Gavilan, D. Caballero, S. Toledo, E. Maqueda, R. Gregor, J. Rodas, M. Rivera, and I. Araujo-Vargas, "Predictive power control strategy for a grid-connected 2l-vsi with fixed switching frequency," in *Proc. ROPEC*, DOI 10.1109/ROPEC.2016.7830631, 2016, pp. 1–6.

[17] L. Comparatore, R. Gregor, J. Rodas, J. Pacher, A. Renault, and M. Rivera, "Model based predictive current control for a three-phase cascade H-bridge multilevel statcom operating at fixed switching frequency," in *Proc. PEDG*, DOI 10.1109/PEDG.2017.7972540, 2017, pp. 1–6.

[18] M. Rivera, S. Toledo, C. Baier, L. Tarisciotti, P. Wheeler, and S. Verne, "Indirect predictive control techniques for a matrix converter operating at fixed switching frequency," in *Proc. PRECEDE*, DOI 10.1109/PRECEDE.2017.8071101, 2017, pp. 13–18.

[19] O. Gonzalez, M. Ayala, J. Rodas, R. Gregor, G. Rivas, and J. Doval-Gandoy, "Variable-speed control of a six-phase induction machine using predictive-fixed switching frequency current control techniques," in *Proc. PEDG*, DOI 10.1109/PEDG.2018.8447837, 2018, pp. 1–6.

[20] J. Rodriguez, M. P. Kazmierkowski, J. R. Espinoza, P. Zanchetta, H. Abu-Rub, H. A. Young, and C. A. Rojas, "State of the art of finite control set model predictive control in power electronics," *IEEE Trans. Ind. Inform.*, vol. 9, DOI 10.1109/TII.2012.2221469, no. 2, pp. 1003–1016, 2013.

[21] S. Vazquez, J. Rodriguez, M. Rivera, L. G. Franquelo, and M. Norambuena, "Model predictive control for power converters and drives: Advances and trends," *IEEE Trans. Ind. Electron.*, vol. 64, DOI 10.1109/TIE.2016.2625238, no. 2, pp. 935–947, 2017.

[22] Y. Zhao and T. Lipo, "Space vector PWM control of dual three-phase induction machine using vector space decomposition," *IEEE Trans. Ind. Electron.*, vol. 31, DOI 10.1109/28.464525, no. 5, pp. 1100–1109, 1995.

[23] C. Martín, M. R. Arahal, F. Barrero, and M. J. Durán, "Multiphase rotor current observers for current predictive control: A five-phase case study," *Control Eng. Prac.*, vol. 49, DOI 10.1016/j.conengprac.2016.01.011, pp. 101–111, 2016.

[24] J. Rodas, C. Martin, M. R. Arahal, F. Barrero, and R. Gregor, "Influence of covariance-based ALS methods in the performance of predictive controllers with rotor current estimation," *IEEE Trans. Ind. Electron.*, vol. 64, DOI 10.1109/TIE.2016.2636205, no. 4, pp. 2602–2607, 2017.

[25] J. Rodriguez and P. Cortes, *Predictive control of power converters and electrical drives*. John Wiley & Sons, 2012, DOI 10.1002/9781119941446, vol. 40.

[26] M. Novak, T. Dragicevic, and F. Blaabjerg, "Weighting factor design based on Artificial Neural Network for Finite Set MPC operated 3L-NPC converter," in *Proc. APEC)*, DOI 10.1109/APEC.2019.8722062. IEEE, 2019, pp. 77–82.

[27] B. Majmunović, T. Dragičević, and F. Blaabjerg, "Multi Objective Modulated Model Predictive Control of Stand-Alone Voltage Source Converters," *IEEE Journal of Emerging and Selected Topics in Power Electronics*, DOI 10.1109/JESTPE.2019.2925603, 2019.

[28] C. Martin, M. Arahal, F. Barrero, and M. Duran, "Five-phase induction motor rotor current observer for finite control set model predictive control of stator current," *IEEE Trans. Ind. Electron.*, vol. 63, DOI 10.1109/TIE.2016.2536578, no. 7, pp. 4527–4538, 2016.

[29] A. G. Yepes, J. A. Riveros, J. Doval-Gandoy, F. Barrero, O. López, B. Bogado, M. Jones, and E. Levi, "Parameter identification of multiphase induction machines with distributed windings Part 1: Sinusoidal excitation methods," *IEEE Trans. Energy Conv.*, vol. 27, DOI 10.1109/TEC.2012.2220967, no. 4, pp. 1056–1066, 2012.

[30] J. A. Riveros, A. G. Yepes, F. Barrero, J. Doval-Gandoy, B. Bogado, O. Lopez, M. Jones, and E. Levi, "Parameter identification of multiphase induction machines with distributed windings Part 2: Time-domain techniques," *IEEE Trans. Energy Conv.*, vol. 27, DOI 10.1109/TEC.2012.2219862, no. 4, pp. 1067–1077, 2012.

[31] M. Ayala, J. Doval-Gandoy, J. Rodas, O. Gonzalez, and R. Gregor, "Current control designed with model based predictive control for six-phase motor drives," *ISA transactions*, DOI 10.1016/j.isatra.2019.08.052, 2019.

[32] B. Bogado, F. Barrero, M. Arahal, S. Toral, and E. Levi, "Sensitivity to electrical parameter variations of predictive current control in multiphase drives," in *Proc. IECON*, DOI 10.1109/IECON.2013.6699982. IEEE, 2013, pp. 5215–5220.
[33] F. Wang, Z. Zhang, X. Mei, J. Rodríguez, and R. Kennel, "Advanced control strategies of induction machine: Field oriented control, direct torque control and model predictive control," *Energies*, vol. 11, DOI 10.3390/en11010120, no. 1, p. 120, 2018.
[34] O. Gonzalez, M. Ayala, J. Doval-Gandoy, J. Rodas, R. Gregor, and M. Rivera, "Predictive-Fixed Switching Current Control Strategy Applied to Six-Phase Induction Machine," *Energies*, vol. 12, DOI 10.3390/en12122294, no. 12, p. 2294, 2019.

Magno Ayala received the B.Eng. degree in electronic engineering from the Universidad Nacional de Asunción (UNA), Paraguay, in 2014 and his M.Sc. in 2017. He joined the Laboratory of Power and Control System at the UNA, in 2015, working as a Research Assistant. Mr. Ayala is a recipient of the training program for university lecturers from the CONACYT of Paraguay for his Ph.D. studies.

Jesús Doval-Gandoy (M'99) received the M.Sc. degree from Polytechnic University of Madrid, Madrid, Spain, in 1991 and the Ph.D. degree from the University of Vigo, Vigo, Spain in 1999.

From 1991 till 1994 he worked at industry. He is currently a Professor and the head of the Applied Power Electronics Technology Research Group, University of Vigo. His research interests are in the areas of ac power conversion.

Jorge Rodas (S'08–M'12–SM'19) was born in Asunción, Paraguay in 1984. He received his B.Eng. degree in Electronic Engineering from the Universidad Nacional de Asunción (UNA), Paraguay, in 2009. He received his M.Sc. degrees from the Universidad de Vigo, Spain, in 2012 and from the Universidad de Sevilla, Spain, in 2013, and his joint-university Ph.D. degree between the Universidad Nacional de Asunción and the Universidad de Sevilla in 2016.

In 2011, he joined the Laboratory of Power and Control Systems, Faculty of Engineering, UNA, where he currently serves as a Full Professor.

Osvaldo Gonzalez was born in Paraguay in 1987. B.Eng. degree in electronic engineering from the Universidad Nacional de Asunción (UNA), in 2014 and the M.Sc. degree in Power Electronics in 2017. His research interests include the area of control of multiphase motors. Mr. Gonzalez is a recipient of the training program for university lecturers from the CONACYT of Paraguay for his Ph.D. studies.

Raúl Gregor was born in Asunción, Paraguay, in 1979. He received the Bachelor Degree in Electronic Engineering from the Catholic University of Asunción, Paraguay, in 2005. He received the M.Sc. and Ph.D. degrees in Electronic, Signal Processing and Communications from the Higher Technical School of Engineering (ETSI), University of Seville, Spain, in 2008 and 2010, respectively. Since March 2010, Prof. Gregor is Head of the Laboratory of Power and Control System (LSPyC) of the Engineering Faculty in the National University of Asunción, Paraguay.

Marco Rivera was born in Talca, Chile, in 1982. He received the B.Sc. degree in electronics engineering and the M.Sc. degree in electrical engineering from the Universidad de Concepción, Concepción, Chile, in 2007 and 2008, respectively, and the Ph.D. degree from the Department of Electronics Engineering, Universidad Técnica Federico Santa María, Valparaíso, Chile, in 2011. Prof. Rivera is Head of the Laboratory of Energy Conversion and Power Electronics (LCEEP) and the Technology Center for Energy Conversion (CTCE).

Experimental Stability Study of Modulated Model Predictive Current Controllers Applied to Six-Phase Induction Motor Drives

Magno Ayala[1], Jesus Doval-Gandoy[2], *Member, IEEE,* Osvaldo Gonzalez[1], Jorge Rodas[1], *Senior Member, IEEE,* Raul Gregor[1], and Marco Rivera[3], *Senior Member, IEEE*

***Abstract*—Modulated model predictive current control techniques are considered an interesting option to control multiphase drives due to their control flexibility and fast dynamic response. However, a practical stability study of those techniques is still missing. This paper presents an experimental stability study, to quantify the limits of stability, to modulated predictive current controllers applied to an asymmetrical six-phase induction machine. Experimental results are presented to verify the theoretical analysis results in terms of stability ranges regarding sampling frequency and rotor speed.**

***Index Terms*—Model predictive control, multiphase induction machine, practical stability, space vector modulation.**

I. Introduction

MODULATED model predictive current controllers have gained attention in the last years as valid alternatives to conventional model predictive current control (MPCC) techniques [1]–[4] as MPCC has shown very good results in comparison to linear PI controllers, in terms of faster transient dynamics, easier inclusions of constraints, among others, applied in electrical machines [5]–[7]. At the same time, the field of multiphase induction machines (IMs) has been growing significantly in the last years [8], [9] Comparing to the conventional three-phase IM, multiphase IMs have some intrinsic advantages such as lower torque ripple, lower current/power per phase, availability and fault-tolerant capabilities [8], [10]–[12]. By considering these advantages, they were extensively applied in the high-power applications such as renewable energies and electric vehicles [13], [14].

As the research of multiphase IM has been growing, new nonlinear control methods were developed to apply to these machines such as sliding mode control [15], [16], fuzzy logic [17], [18], backstepping [19], [20], model referenced adaptation system [21] and new variants of modulated finite control set model predictive control (FCS-MPC) [22]–[25]. Some examples of these variants are the modulated model predictive control (M2PC) [26] and a novel variation named N-M2PC [27] which are considered great alternatives for low and high rotor speed operations respectively in terms of steady-state operations and $(x-y)$ plane (related to IM losses) currents reduction.

Furthermore, PCC stability analysis applied to different systems were approached in previous works [28], such as Buck converters and three-phase inverters [29] and synchronous machines [30]. The main common property is a defined cost function to optimize the future behaviour of the system. Hence, one of the most popular methods to prove the stability of PCC is the consideration of the optimized cost function as a candidate-Lyapunov function [31]–[33]. However, this method presents many complications as to find a candidate-Lyapunov function requires complex proof. Therefore, a practical stability study of modulated PCC applied to multiphase machines in terms of sampling frequency and rotor speed has not been presented.

The main contribution of this paper is an experimental stability study for M2PC and N-M2PC applied to an asymmetrical six-phase induction motor (SPIM) in terms of stability limits regarding sampling frequency and rotor speed to define the critical operating points of both techniques from the stability point of view, complementing the proposal in [27]. Experimental results are presented to verify the results of the theoretical analysis. Considering that the stability of MPCC techniques has not been analyzed in terms of sampling frequency and motor speed, it is considered that this study presents interesting results from the point of view of the design and implementation of modulated predictive control techniques. The rest of this paper is organized as follows: the SPIM mathematical model is shown in Section II. In Section III, the traditional PCC design is presented and their two variants named M2PC and N-M2PC. Section IV describes the proposed theoretical stability study. Section V presents the experimental results of the system performance verifying the theoretical analysis in terms of stability ranges regarding sampling frequency and rotor speed. Finally, conclusions are summarized in the last section.

II. SPIM Mathematical Model

The studied system is made of a SPIM fed by a six-phase voltage source inverter (VSI) energized by a dc voltage source (V_{dc}). The electrical scheme of the six-phase VSI, based on

M. Ayala, O. Gonzalez, J. Rodas and R. Gregor are with the Laboratory of Power and Control Systems, Facultad de Ingeniería, Universidad Nacional de Asunción, Paraguay (e-mail: mayala@ing.una.py, ogonzalez@ing.una.py, jrodas@ing.una.py, rgregor@ing.una.py).
J. Doval-Gandoy is with the Applied Power Electronics Technology Research Group, Universidad de Vigo, Spain (e-mail: jdoval@uvigo.es)
M. Rivera is with the Department of Electrical Engineering, Universidad de Talca, Chile (e-mail: marcoriv@utalca.cl)

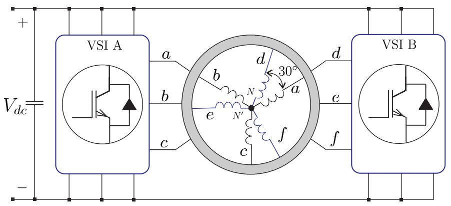

Fig. 1. Electrical scheme of a six-phase VSI connected to a SPIM.

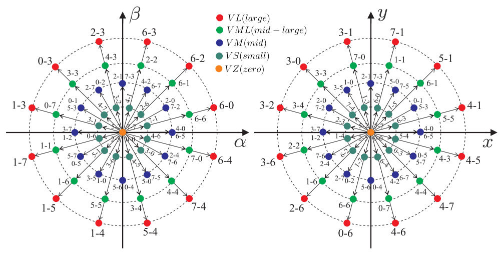

Fig. 2. Voltage space vectors of 64 switching states in $(\alpha-\beta)$ and $(x-y)$ planes for the SPIM.

isolated gate bipolar transistors (IGBT), is illustrated in Fig. 1. The SPIM is considered as a continuous model which can be represented by differential equations. The six-dimensional space of the SPIM, which is defined by its six-phases (a, b, c, d, e, f), and the vector space decomposition (VSD) technique are considered. Then, the model can be represented into three different two-dimensional orthogonal planes in stationary reference planes, $(\alpha-\beta)$, $(x-y)$ and (z_1-z_2), by using (1), where the invariant amplitude criteria has been considered [34]. The SPIM is asymmetrical, so it has a phase shift of 30° between the three phases and has an isolated neutral configuration. Thus (z_1-z_2) currents are considered null.

$$\mathbf{T} = \frac{1}{3} \begin{array}{c} \begin{array}{cccccc} a & d & b & e & c & f \end{array} \\ \left[\begin{array}{cccccc} 1 & \frac{\sqrt{3}}{2} & -\frac{1}{2} & -\frac{\sqrt{3}}{2} & -\frac{1}{2} & 0 \\ 0 & \frac{1}{2} & \frac{\sqrt{3}}{2} & \frac{1}{2} & -\frac{\sqrt{3}}{2} & -1 \\ 1 & -\frac{\sqrt{3}}{2} & -\frac{1}{2} & \frac{\sqrt{3}}{2} & -\frac{1}{2} & 0 \\ 0 & \frac{1}{2} & -\frac{\sqrt{3}}{2} & \frac{1}{2} & \frac{\sqrt{3}}{2} & -1 \\ 1 & 0 & 1 & 0 & 1 & 0 \\ 0 & 1 & 0 & 1 & 0 & 1 \end{array}\right] \end{array} \begin{array}{c} \\ \alpha \\ \beta \\ x \\ y \\ z_1 \\ z_2 \end{array} \tag{1}$$

The six-leg VSI has a digital output that depends on the different $2^6 = 64$ possible switching states defined by the six-legs. The switching states and V_{dc} determine the phase voltages, which can be drawn into $(\alpha-\beta)$ and $(x-y)$ planes according to the VSD approach [35]. Fig. 2 shows the 64 possibilities with only 49 different vectors (48 vectors + 1 null vector) in the $(\alpha-\beta)$ and $(x-y)$ planes in terms of octal nomenclature. The state-space mathematical model of the SPIM is modelled by:

$$\dot{\mathbf{X}}_{(t)} = \mathbf{A}_{(t)}\,\mathbf{X}_{(t)} + \mathbf{B}_{(t)}\,\mathbf{U}_{(t)} + \mathbf{H}\,\varpi_{(t)} \tag{2}$$

where $\mathbf{X}_{(t)} = [x_1,\, x_2,\, x_3,\, x_4, x_5,\, x_6]^T$ is the state vector which represents the stator and rotor currents $x_1 = i_{\alpha s}$, $x_2 = i_{\beta s}$, $x_3 = i_{xs}$, $x_4 = i_{ys}$, $x_5 = i_{\alpha r}$ and $x_6 = i_{\beta r}$, $\mathbf{U}_{(t)} = [u_1,\, u_2,\, u_3,\, u_4]^T = [v_{\alpha s},\, v_{\beta s},\, v_{xs},\, v_{ys}]^T$ is the input voltage vector applied to the stator windings, $\mathbf{H}$ represents the noise weight matrix, the process noise is considered as $\varpi_{(t)}$ and $\mathbf{A}_{(t)}$ and $\mathbf{B}_{(t)}$ are matrices defined by the electrical parameters of the SPIM as follows:

$$\mathbf{A}_{(t)} = \begin{bmatrix} -R_s c_2 & c_4 L_m \omega_r & 0 & 0 & c_4 R_r & c_4 L_r \omega_r \\ c_4 L_m \omega_r & -R_s c_2 & 0 & 0 & c_4 L_r \omega_r & c_4 R_r \\ 0 & 0 & -R_s c_3 & 0 & 0 & 0 \\ 0 & 0 & 0 & -R_s c_3 & 0 & 0 \\ R_s c_4 & -c_5 L_m \omega_r & 0 & 0 & -c_5 R_r & -c_5 L_r \\ -c_5 L_m \omega_r & R_s c_4 & 0 & 0 & -c_5 L_r & -c_5 R_r \end{bmatrix}$$

$$\mathbf{B}_{(t)} = \begin{bmatrix} c_2 & 0 & 0 & 0 \\ 0 & c_2 & 0 & 0 \\ 0 & 0 & c_3 & 0 \\ 0 & 0 & 0 & c_3 \\ -c_4 & 0 & 0 & 0 \\ 0 & -c_4 & 0 & 0 \end{bmatrix}$$

where R_s, R_r, L_m, $L_r = L_{lr} + L_m$ and $L_s = L_{ls} + L_m$ are the electrical parameters of the SPIM. The coefficients are considered as $c_1 = L_s L_r - L_m^2$, $c_2 = \frac{L_r}{c_1}$, $c_3 = \frac{1}{L_{ls}}$, $c_4 = \frac{L_m}{c_1}$ and $c_5 = \frac{L_s}{c_1}$. Stator voltages are dependant on the input control signals $\mathbf{S}$, which is considered the actual switching state. For this analysis, the ideal VSI has been modeled to obtain a good optimization process. The stator voltages can be calculated from the ideal six-leg VSI model $\mathbf{M}_{[\mathbf{S}]}$ [34].

$$\mathbf{M}_{[\mathbf{S}]} = \frac{1}{3} \begin{bmatrix} 2 & 0 & -1 & 0 & -1 & 0 \\ 0 & 2 & 0 & -1 & 0 & -1 \\ -1 & 0 & 2 & 0 & -1 & 0 \\ 0 & -1 & 0 & 2 & 0 & -1 \\ -1 & 0 & -1 & 0 & 2 & 0 \\ 0 & -1 & 0 & -1 & 0 & 2 \end{bmatrix} \mathbf{S}^T \tag{3}$$

where $\mathbf{S} = [S_a,\, S_d,\, S_b,\, S_e,\, S_c,\, S_f]$, and $\mathbf{S}_i \in \{0, 1\}$. The ideal six-phase VSI generates the stator voltages through the switching gating signals and V_{dc} and then they are transformed to $(\alpha-\beta)$ and $(x-y)$ planes, represented by $\mathbf{U}_{(t)}$, calculated in the following equation:

$$\mathbf{U}_{(t)} = V_{dc}\,\mathbf{T}\,\mathbf{M}_{[\mathbf{S}]}. \tag{4}$$

The output vector, $\mathbf{Y}$, is:

$$\mathbf{Y}_{(t)} = \mathbf{C}\,\mathbf{X}_{(t)} + \nu_{(t)} \tag{5}$$

where $\nu_{(t)}$ is the measurement noise and $\mathbf{C}$ is considered as follows:

$$\mathbf{C} = \begin{bmatrix} 1 & 0 & 0 & 0 & 0 & 0 \\ 0 & 1 & 0 & 0 & 0 & 0 \\ 0 & 0 & 1 & 0 & 0 & 0 \\ 0 & 0 & 0 & 1 & 0 & 0 \end{bmatrix}$$

The mechanical variables of the SPIM are considered in the following equations:

$$T_e = 3\,P\,(\psi_{\alpha s} i_{\beta s} - \psi_{\beta s} i_{\alpha s}) \tag{6}$$

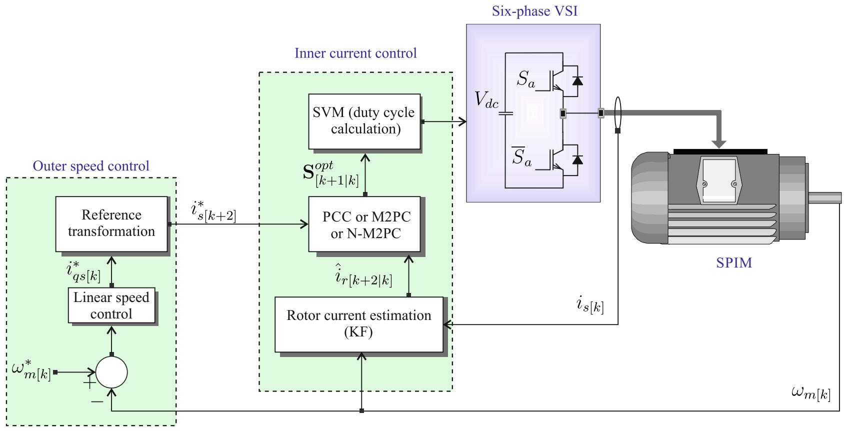

Fig. 3. Block diagram of the controlled system based on FOC and traditional PCC, M2PC and N-M2PC.

$$J_i\,\dot{\omega}_m + B_i\,\omega_m = (T_e - T_L) \tag{7}$$

$$\omega_r = P\omega_m \tag{8}$$

where T_e represents the electromagnetic torque, P the number of pole pairs, $\psi_{\alpha s}$ and $\psi_{\beta s}$ are considered the stator fluxes, J_i is the inertia coefficient, B_i is considered the friction coefficient, T_L is the load torque, ω_r is the rotor electrical angular speed and ω_m is the rotor mechanical speed.

III. Traditional PCC and its Variants

The mathematical model of the SPIM (2) and (5) has to be discretized so it can be considered for the PCC. A forward-Euler method is computed to avoid a high computational cost for the digital controller. The equations will then be in a discrete form with the future variables only depending on past values of the variables and not on present values. Thus, a prediction of the future (next sample state) $\hat{\mathbf{X}}_{[k+1|k]}$ is written as:

$$\hat{\mathbf{X}}_{[k+1|k]} = \mathbf{X}_{[k]} + \mathrm{f}\left(\mathbf{X}_{[k]},\, \mathbf{U}_{[k]},\, T_s,\, \omega_{r[k]}\right) \tag{9}$$

where $[k]$ is the current sample and T_s the sampling time. Fig. 3 presents the block diagram of the system with the SPIM and the analyzed current controllers.

A. Rotor Currents Observer

Stator currents and mechanical rotor speed are the only measured variables in the state-space model (9). On the other hand, stator voltages can be calculated from the switching states sent to the VSI. However, rotor currents cannot be easily measured in a real system and they have to be estimated. This can be solved by reduced-order observers of rotor currents. The reduced-order observers only estimate the value of the unmeasured parts of the state vector. The latter is an important issue that has been already solved by using Luenberger Observer (LO) [36] and Kalman Filter (KF) [37], [38]. KF is considered a superior option because their observer gains are estimated and optimized in every sampling time by considering the noise input in the system. For LO, gains are not so optimized and the setting is deterministic [37]. Therefore, KF is considered and implemented in this work to improve the control performance of PCC by reducing the prediction errors. Zero-mean Gaussian measurement noises and uncorrelated processes are considered. Now, the predictive model of the SPIM in state-space representation is defined as follows:

$$\hat{\mathbf{X}}_{[k+1|k]} = \mathbf{A}_{[k]}\mathbf{X}_{[k]} + \mathbf{B}_{[k]}\mathbf{U}_{[k]} + \mathbf{H}\varpi_{[k]} \tag{10}$$

$$\mathbf{Y}_{[k+1|k]} = \mathbf{C}\,\mathbf{X}_{[k+1]} + \nu_{[k+1]} \tag{11}$$

where $\mathbf{A}_{[k]}$ and $\mathbf{B}_{[k]}$ are matrices defined by equations (12)-(15). $\mathbf{A}_{[k]}$ also depends on the actual value of $\omega_{r[k]}$ and has to be computed at every sampling time. A more detailed explanation of the error convergence of the KF and its dynamics are described in [37], [38]. The system matrices are defined as:

$$\mathbf{A}_{[k]} = \begin{bmatrix} A_{11} & A_{12} & 0 & 0 & A_{15} & A_{16} \\ A_{21} & A_{22} & 0 & 0 & A_{25} & A_{26} \\ 0 & 0 & A_{33} & 0 & 0 & 0 \\ 0 & 0 & 0 & A_{44} & 0 & 0 \\ A_{51} & A_{52} & 0 & 0 & A_{55} & A_{56} \\ A_{61} & A_{62} & 0 & 0 & A_{65} & A_{66} \end{bmatrix} \tag{12}$$

where $\mathbf{A}_{[k]}$ parameters are:

$$
\begin{aligned}
A_{11} &= A_{22} = 1 - T_s c_2 R_s \\
A_{12} &= -A_{21} = T_s c_4 L_m \omega_{r[k]} \\
A_{15} &= A_{26} = T_s c_4 R_r \\
A_{16} &= -A_{25} = T_s c_4 L_r \omega_{r[k]} \\
A_{33} &= A_{44} = 1 - T_s c_3 R_s \\
A_{51} &= A_{62} = -T_s c_4 R_s \\
A_{52} &= -A_{61} = -T_s c_5 L_m \omega_{r[k]} \\
A_{55} &= A_{66} = 1 - T_s c_5 R_r \\
A_{56} &= -A_{65} = -c_5 \omega_{r[k]} T_s L_r
\end{aligned} \tag{13}
$$

$$
\mathbf{B}_{[k]} = \begin{bmatrix} B_{11} & 0 & 0 & 0 & 0 & 0 \\ 0 & B_{22} & 0 & 0 & 0 & 0 \\ 0 & 0 & B_{33} & 0 & 0 & 0 \\ 0 & 0 & 0 & B_{44} & 0 & 0 \\ 0 & 0 & 0 & 0 & B_{55} & 0 \\ 0 & 0 & 0 & 0 & 0 & B_{66} \end{bmatrix} \tag{14}
$$

being $\mathbf{B}_{[k]}$ parameters:

$$
\begin{aligned}
B_{11} &= B_{22} = T_s c_2 \\
B_{33} &= B_{44} = T_s c_3 \\
B_{55} &= B_{66} = -T_s c_4
\end{aligned} \tag{15}
$$

B. Cost Function Minimization

The cost function is considered as an optimization process of different system variables such as harmonic content minimization, machine torque ripple minimization, VSI switching losses and current tracking error [39]. This last variable is the most important figure of merit in PCC in $(\alpha-\beta)$ and $(x-y)$ planes. PCC evaluates the cost function for 49 iterations regarding 49 different voltage vectors. Therefore, the selected cost function is:

$$
J_{[k+2|k]} = \Big[(i^*_{\alpha s[k+2]} - \hat{i}_{\alpha s[k+2|k]})^2 + (i^*_{\beta s[k+2]} - \hat{i}_{\beta s[k+2|k]})^2 + \lambda_{xy} \left((i^*_{xs[k+2]} - \hat{i}_{xs[k+2|k]})^2 + (i^*_{ys[k+2]} - \hat{i}_{ys[k+2|k]})^2 \right) \Big]^{\frac{1}{2}} \tag{16}
$$

A second-step ahead prediction of stator currents $\hat{i}_{s[k+2|k]}$ is computed for delay compensation, by considering equations (10) and (11). The desired reference trajectory of the stator currents is represented by $i^*_{s[k+2]}$. The weighting factor optimization is tackled in [40]. Typically, for SPIM, λ_{xy} gives more priority to stator currents in $(\alpha-\beta)$ plane than $(x-y)$ to prioritize the flux/torque production plane over the machine losses [37].

C. M2PC

This PCC with a modulation stage consists on determine each available sector for the six-leg VSI in the $(\alpha-\beta)$ plane, being 12 outside sectors in total, which are composed of two adjacent active vectors and the null vector (VZ), as shown in

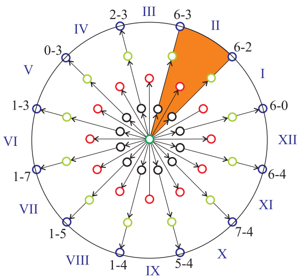

Fig. 4. Space voltage sectors of M2PC.

Fig. 4. Then, it calculates the future prediction of the three vectors at every sampling time and analyses their respective cost functions (J_0, J_1 and J_2) separately. This technique can generate any voltage vector in the $(\alpha-\beta)$ plane using the large vectors (VL) and VZ, covering the entire space vector area. It can be noted that VL are the smallest voltage vectors in $(x-y)$ plane, managing a natural reduction of $(x-y)$ currents [26].

The duty cycles (d_0, d_1 and d_2) are obtained by solving the following equations:

$$
d_0 = \frac{\gamma}{J_0} \qquad d_1 = \frac{\gamma}{J_1} \qquad d_2 = \frac{\gamma}{J_2} \tag{17}
$$

$$
d_0 + d_1 + d_2 = T_s \tag{18}
$$

The duty cycles for each vector are given as:

$$
J_T = J_1 J_2 + J_0 J_1 + J_0 J_2 \tag{19}
$$

$$
d_0 = \frac{T_s J_1 J_2}{J_T} \tag{20}
$$

$$
d_1 = \frac{T_s J_0 J_2}{J_T} \tag{21}
$$

$$
d_2 = \frac{T_s J_0 J_1}{J_T} \tag{22}
$$

At last, the selected sector cost function is considered as:

$$
G_{[k+2|k]} = d_1 J_1 + d_2 J_2 \tag{23}
$$

The sector, which reduces $G_{[k+2|k]}$, is applied to the six-leg VSI at the next sampling time. It is necessary to synthesize the duty cycles, to be able to implement a symmetric pulse width modulation (PWM) as follows:

$$
\tau_{(i)} = \frac{d_0}{2T_s} + \frac{d_1}{T_s} v_{1(i)} + \frac{d_2}{T_s} v_{2(i)} \tag{24}
$$

where $i = [a, d, b, e, c, f]$ and τ_i is the PWM duty cycle per leg, obtaining a fixed switching frequency.

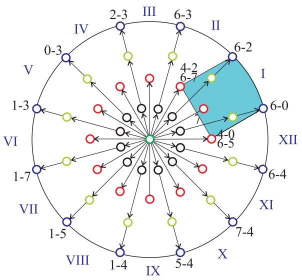

Fig. 5. Space voltage sectors of N-M2PC.

D. N-M2PC

The main difference between N-M2PC and M2PC is the shape of each voltage sector. M2PC uses 2 VL and VZ per sector and N-M2PC uses 4 including 2 mid vectors (VM) and 2 VL. As in M2PC, 12 rectangular sectors are considered and their respective cost functions (J_1, J_2, J_3 and J_4) are calculated separately at every sampling time. The main goal of this modulation is to reduce the steady-state error of the stator currents tracking in $(d-q)$ plane by including these adjacent VM per sector avoiding the use of VZ which limits the voltage range, reducing the tracking capacity of the stator currents in $(\alpha-\beta)$ plane, since VZ has an increased duty cycle when $(x-y)$ currents are being reduced [27].

The duty cycles, for VL and VM d_1, d_2, d_3 and d_4, are obtained as follows:

$$d_1 = \frac{\gamma}{J_1} \quad d_2 = \frac{\gamma}{J_2} \quad d_3 = \frac{\gamma}{J_3} \quad d_4 = \frac{\gamma}{J_4} \tag{25}$$

$$d_1 + d_2 + d_3 + d_4 = T_s \tag{26}$$

where J_1, J_2, J_3 and J_4 are the corresponding cost functions (16) for the four vectors and γ is an auxiliary variable whose value depends directly on the cost function values. Then, the duty cycles for each vector are calculated as:

$$J_{T1} = J_1J_3J_4 + J_2J_3J_4 \tag{27}$$

$$J_{T2} = J_1J_2J_4 + J_1J_2J_3 \tag{28}$$

$$d_1 = \frac{T_sJ_2J_3J_4}{J_{T1}+J_{T2}} \tag{29}$$

$$d_2 = \frac{T_sJ_1J_3J_4}{J_{T1}+J_{T2}} \tag{30}$$

$$d_3 = \frac{T_sJ_1J_2J_4}{J_{T1}+J_{T2}} \tag{31}$$

$$d_4 = \frac{T_sJ_1J_2J_3}{J_{T1}+J_{T2}} \tag{32}$$

At last, the final cost function is computed as:

$$G_{[k+2|k]} = d_1J_1 + d_2J_2 + d_3J_3 + d_4J_4 \tag{33}$$

As in M2PC, the sector which reduces $G_{[k+2|k]}$ the most is applied to the six-leg VSI at the next sampling time with their respective duty cycles for every vector (mid and large) in the selected sector. A simple equation is used to obtain the duty cycles $\tau_{(i)}$ for the switching devices of each phase of the six-leg VSI, as follows:

$$\tau_{(i)} = \frac{d_1}{T_s}v_{1(i)} + \frac{d_2}{T_s}v_{2(i)} + \frac{d_3}{T_s}v_{3(i)} + \frac{d_4}{T_s}v_{4(i)} \tag{34}$$

where $\tau_{(i)}$ is normalized between 0 and 1, for the switching devices for the six-leg VSI.

TABLE I
RANGE VALUES OF DIFFERENT GAINS $(\mathbf{L}_{[k]})$ OF M2PC AND N-M2PC.

Gains	M2PC	N-M2PC
L_1	$[-10, 10]$	$[-10, 10]$
L_2	$[-40, 40]$	$[-40, 40]$
L_3	$[-150, 10]$	$[-760, -300]$
L_4	$[-40, 40]$	$[-40, 40]$

IV. PRACTICAL STABILITY STUDY

Examples of PCC variants are vastly known in the literature, which present some common properties and allow them to formalize the stability analysis [41]. A candidate-Lyapunov function is often considered as a popular method to prove the stability of PCC. Another considered approach, presented in [23], [42] consists in estimate a specific gain $\mathbf{L}_{[k]}$ to obtain a stable matrix $(\mathbf{A}_{[k]}-\mathbf{B}_{[k]}\mathbf{L}_{[k]})$ whose eigenvalues are less than 1. The second method is more practical due to its simplicity and by considering that PCC has a finite control effort, i.e. 49 voltage vectors in the particular case of the SPIM. For a limited current reference (due to security issues), there is a finite number of $\mathbf{L}_{[k]}$ through the cost function minimization and it shows the same behaviour in terms of local stability by analyzing different scenarios, such as typical values of rotor speed and sampling frequency (F_s).

$$\mathbf{U}_{[k]} = -\mathbf{L}_{[k]}\mathbf{X}_{[k]} \tag{35}$$

where $\mathbf{L}_{[k]}$ is selected as follows:

$$\mathbf{L}_{[k]} = \begin{bmatrix} L_1 & L_2 & 0 & 0 & L_3 & L_4 \\ -L_2 & L_1 & 0 & 0 & -L_4 & L_3 \\ 0 & 0 & L_1 & L_2 & 0 & 0 \\ 0 & 0 & -L_2 & L_1 & 0 & 0 \end{bmatrix}$$

It is considered a limited range of $[-3.5, 3.5]$ A, by considering the nominal current value of the SPIM, for state variables ($\mathbf{X}_{[k]}$). Then, by using the separation theorem, the closed-loop eigenvalues are the union of those of the observer and state feedback. Assuming measured states, and finite values of the voltage vector ($\mathbf{U}_{[k]}$) i.e. 49 different values for traditional PCC, a finite number of $\mathbf{L}_{[k]}$ is found through an exhaustive iterative search, as shown in Table I. It is worth mentioning that $\mathbf{L}_{[k]}$ can be defined with infinite different values, so bounded ranges of values for every parameter of $\mathbf{L}_{[k]}$ are considered. It is also noted that PCC is a constraint optimal control method, therefore, the selected control effort should be stable as long as inside the solution region at least one stable solution exists (inside the unit circle). Thus, rotor speed values are increased to obtain unstable solutions, and this value is defined as the upper bound of stable rotor speed. At the same time, Table II presents the maximum stable rotor speed (eigenvalues inside the unit circle) at different sampling frequencies for M2PC and N-M2PC. The theoretical analysis is only considered for M2PC and N-M2PC since they are the main MPCC schemes studying in this work. At last, eigenvalues of $(\mathbf{A}_{[k]} - \mathbf{B}_{[k]}\mathbf{L}_{[k]})$ matrix at 10 kHz of sampling frequency and rotor speed of 2500 rpm for the three techniques are shown in Fig. 6 where, at those conditions, N-M2PC is the only controller with eigenvalues inside the unit circle.

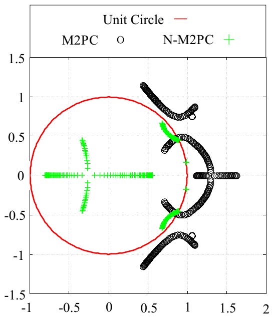

Fig. 6. Eigenvalues of $(\mathbf{A}_{[k]} - \mathbf{B}_{[k]}\mathbf{L}_{[k]})$ matrix at 10 kHz of sampling frequency and rotor speed of 2500 rpm for M2PC and N-M2PC.

V. Experimental Results

The stability analysis is validated through experimental tests for traditional PCC, M2PC and N-M2PC in the experimental test bench. It must be considered that despite not presenting theoretical results for the traditional PCC, experimental tests were carried out to have a comparative pattern.

TABLE II
Stability Theoretical Analysis of M2PC and N-M2PC and their maximum stable speeds (rpm).

F_s (kHz)	M2PC	N-M2PC
	Maximum Stable Speed	
2	850	250
2.5	1000	550
4	1300	1250
5	1400	1650
7.5	1700	2800
8	1850	2850
10	2000	3000
12.5	2300	3000
15	2600	3000
16	2700	3000
17.5	2800	3000
20	3000	3000

A. Experimental test bench

The experimental test bench is composed of a SPIM fed by two conventional three-phase VSI, using a dc voltage source. The six-phase VSI is controlled by a real-time rapid prototyping platform defined as dSPACE MABXII DS1401, with MATLAB/Simulink incorporated. Table III presents the parameters of the SPIM obtained using stand-still VSI tests and typical methods of AC time domain [43], [44].

The measurements were made with current sensors LA 55-P s, with many turns to improve the precision at low current amplitude. They also have a frequency bandwidth from dc up to 200 kHz. The data is converted to digital through a 16-bit A/D converter. The SPIM rotor angle is obtained by a 1024 ppr incremental encoder and the rotor speed is estimated from the angle. At last, a 5 HP eddy current brake is selected as a variable mechanical load on the SPIM which is considered at 1 A, generating a load torque of 1.5 Nm. A block diagram of the experimental test bench is shown in Fig. 7. The cost function in (16) with λ_{xy} = 0.05 is considered to apply the traditional PCC and M2PC. This gives priority to $(\alpha - \beta)$ stator currents tracking over $(x-y)$ currents reduction. As for N-M2PC, λ_{xy} = 0.1 is selected because the null vector is not used and hence $(x-y)$ currents reduction is obtained through combination of the active vectors. It is worth mentioning that λ_{xy} does not influence the maximum stable rotor speed, it only affects the performance of the currents tracking in a range of $[0.01, 0.1]$ which are the tested values. These values of λ_{xy} were obtained through a heuristic method, which consists in a manual tuning checked by trial and error, by focusing on obtaining a sub-optimal system [37]. The covariances of the process $(\varpi_{(t)})$ and measurement $(\nu_{(t)})$ noises, defined as $\hat{Q}_w = 0.0022$ and $\hat{R}_v = 0.0022$, can be estimated by using the proposed method in [38].

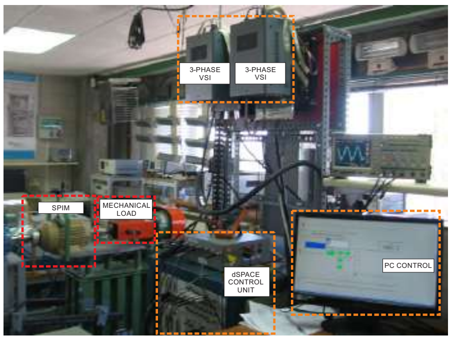

Fig. 7. Setup of the experimental test bench including the dSPACE platform, the SPIM, the six-phase VSI and the eddy current brake.

B. Stability test

In every case, $(x-y)$ current references are considered zero $(i^*_{xs} = i^*_{ys} = 0)$. Then, a fixed d stator current $(i^*_{ds} = 1$ A) has been set. The sampling frequencies, in the tests, are 2.5 kHz,

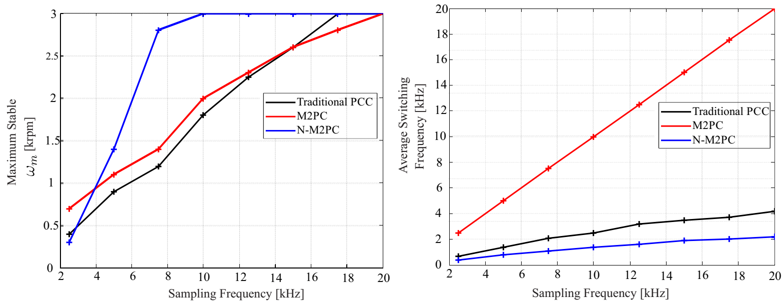

(a) (b)

Fig. 8. Trend chart of traditional PCC, M2PC and N-M2PC regarding different sampling frequencies and: (a) rotor mechanical speed; (b) average switching frequency.

TABLE III
PARAMETERS OF THE SPIM

PARAMETER	VALUE	PARAMETER	VALUE
R_r (Ω)	6.9	R_s (Ω)	6.7
L_s (mH)	654.4	L_r (mH)	626.8
L_m (mH)	614	L_{ls} (mH)	5.3
ω_{m-nom} (rpm)	2 540	P_w (kW)	2
J_i (kg.m^2)	0.07	B_i (kg.m^2/s)	0.0004
P	1	V_{dc} (V)	700

5 kHz, 7.5 kHz, 10 kHz, 12.5 kHz, 15 kHz, 17.5 kHz and 20 kHz.

Fig. 8(a) and Fig. 8(b) show the trend charts of the maximum stable rotor speeds, which is defined as the rotor speed where the stator currents controller can no longer regulate properly as larger oscillations appear destabilizing the system, and average switching frequencies for traditional PCC [37], M2PC and N-M2PC at different sampling frequencies. The results show that N-M2PC has the best performance regarding local stability with the maximum rotor speed of the SPIM, where at lower sampling frequency the performance is not much different to traditional PCC and M2PC although at higher sampling frequency, N-M2PC can operate in the entire speed range of the machine, as for traditional PCC and M2PC, they tend to improve linearly local stability at higher sampling frequency where traditional PCC has a steep slope compared to M2PC. As for average switching frequency, M2PC is a fixed switching frequency technique, so it matches the switching frequency and the sampling frequency. However, traditional PCC and N-M2PC are variable switching frequency techniques, thus the switching states will not necessarily change in two consecutive sampling times, thus the average switching frequencies are lower where N-M2PC has almost half the average switching frequency than traditional PCC, having different pulse ratios under equivalent conditions, increasing the total harmonic distortion of stator currents but reducing the switching losses in the six-phase VSI as shown in [27], as well as the $(x-y)$ currents reduction.

TABLE IV
OPTIMAL VOLTAGE VECTORS AND THEIR CORRESPONDING DUTY CYCLES FOR M2PC AND N-M2PC FOR CONSECUTIVE SAMPLING PERIODS.

M2PC			
Sample	Vector	Switching State	Duty Cycle
1	v_0	0-0	$d_0 = 0.3572T_s$
1	v_1	1-5	$d_1 = 0.3082T_s$
1	v_2	1-7	$d_2 = 0.3346T_s$
2	v_0	0-0	$d_0 = 0.3052T_s$
2	v_1	1-4	$d_1 = 0.4456T_s$
2	v_2	1-5	$d_2 = 0.2492T_s$
3	v_0	0-0	$d_0 = 0.2876T_s$
3	v_1	1-4	$d_1 = 0.3441T_s$
3	v_2	1-5	$d_2 = 0.3683T_s$
N-M2PC			
Sample	Vector	Switching State	Duty Cycle
1	v_1	0-2	$d_1 = 0.1562T_s$
1	v_2	2-3	$d_2 = 0.2586T_s$
1	v_3	6-3	$d_3 = 0.4085T_s$
1	v_4	6-7	$d_4 = 0.1767T_s$
2	v_1	0-1	$d_1 = 0.1727T_s$
2	v_2	0-3	$d_2 = 0.5216T_s$
2	v_3	2-3	$d_3 = 0.1781T_s$
2	v_4	7-3	$d_4 = 0.1276T_s$
3	v_1	0-1	$d_1 = 0.2151T_s$
3	v_2	0-3	$d_2 = 0.4275T_s$
3	v_3	2-3	$d_3 = 0.2010T_s$
3	v_4	7-3	$d_4 = 0.1564T_s$

On the other hand, Table IV presents the selected voltage vectors and their respective duty cycles calculated in consecutive sampling periods for M2PC and N-M2PC showing the performance of both modulated techniques. Then, Fig. 9(a) and Fig. 9(b) present the dynamic behaviour of the rotor speed and stator currents at a stable critical condition for N-M2PC where the measured speed shows oscillations tend to destabilize the system, then the electrical protections are activated.

Last, Table V shows the relative error between theoretical

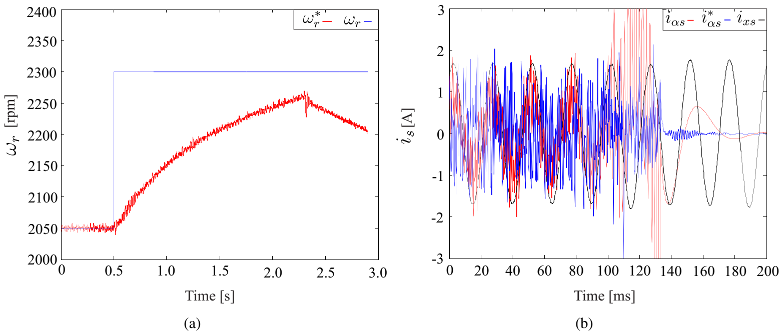

Fig. 9. Dynamic results of rotor speed and stator currents for N-M2PC at a critical stable condition with 2250 rpm and a sampling frequency of 6 kHz: (a) rotor mechanical speed; (b) stator currents.

TABLE V
RELATIVE ERROR (%) BETWEEN THEORETICAL AND EXPERIMENTAL MAXIMUM STABLE ROTOR SPEEDS M2PC AND N-M2PC AND THEIR MAXIMUM STABLE SPEEDS (RPM).

F_s (kHz)	M2PC	N-M2PC
	Error of Maximum Stable Speed	
2.5	30.0	45.5
5	21.4	15.2
7.5	17.6	0.0
10	0.0	0.0
12.5	2.2	0.0
15	0.0	0.0
17.5	0.0	0.0
20	0.0	0.0

and experimental maximum stable rotor speeds obtained at different sampling frequencies for M2PC and N-M2PC. The relative error is significantly low, especially a higher speeds where it matches almost perfectly. However, a difference between the results at low sampling frequencies can be observed as well as a non-linear behaviour between the sampling frequency and the error variation. This can be explained if it is considered that the model parameters have errors that are accentuated with low sampling frequencies since a greater current ripple is generated, degrading the signal-to-noise ratio. In addition, the transport delay of the converter is greater. All these before-mentioned aspects are not considered in the theoretical analysis. Even so, a clear trend of the relationship between the sampling frequency and the maximum stable rotor speed can be observed.

VI. CONCLUSION

This paper has proposed a practical stability study for modulated model predictive controllers applied to an asymmetrical SPIM. The experimental results validated the limits of stability regarding rotor speed and sampling frequencies for the modulated PCCs. From an engineering point of view, a way to obtain these critical operating values can be appreciated in order to apply modulated PCC techniques with the lowest possible sampling frequency which reduce the switching losses in power converters. It was shown an approximately linear relationship between the maximum rotor speed and the sampling frequency and the theoretical analysis showed a very similar behaviour by considering a finite range of gains which represent the different current controllers, even for N-M2PC as shown for frequencies less than 7.5 kHz, although it can be considered that this trend maintains for higher frequencies, it would be necessary to work with speeds higher than 3000 rpm and it is out of the scope of this work, validating the proposed method which can be applied to other systems with PCC.

ACKNOWLEDGMENT

The authors would like to thank the Consejo Nacional de Ciencia y Tecnología (CONACYT)-Paraguay, Grant Number POSG16-05 and ANID/FONDECYT/1191028 Project by SERC Chile (CONICYT/FONDAP/15110019.

REFERENCES

[1] P. Gonçalves, S. Cruz, and A. Mendes, "Finite control set model predictive control of six-phase asymmetrical machines—An overview," *Energies*, vol. 12, DOI 10.3390/en12244693, no. 24, p. 4693, 2019.

[2] I. Gonzalez-Prieto, M. J. Duran, J. J. Aciego, C. Martin, and F. Barrero, "Model predictive control of six-phase induction motor drives using virtual voltage vectors," *IEEE Trans. Ind. Electron.*, vol. 65, DOI 10.1109/TIE.2017.2714126, no. 1, pp. 27–37, 2017.

[3] S. Vazquez, J. Rodriguez, M. Rivera, L. G. Franquelo, and M. Norambuena, "Model predictive control for power converters and drives: Advances and trends," *IEEE Trans. Ind. Electron.*, vol. 64, DOI 10.1109/TIE.2016.2625238, no. 2, pp. 935–947, 2016.

[4] S. Paul and K. Basu, "A three-phase inverter based overmodulation strategy of asymmetrical six-phase induction machine," *IEEE Trans. Power Electron.*, DOI 10.1109/TPEL.2020.3026816, 2020.

[5] F. Barrero, M. R. Arahal, R. Gregor, S. Toral, and M. J. Durán, "A proof of concept study of predictive current control for VSI-driven asymmetrical dual three-phase AC machines," *IEEE Trans. Ind. Electron.*, vol. 56, DOI 10.1109/TIE.2008.2011604, no. 6, pp. 1937–1954, 2009.

[6] F. Barrero, J. Prieto, E. Levi, R. Gregor, S. Toral, M. J. Durán, and M. Jones, "An enhanced predictive current control method for asymmetrical six-phase motor drives," *IEEE Trans. Ind. Electron.*, vol. 58, DOI 10.1109/TIE.2010.2089943, no. 8, pp. 3242–3252, 2010.

[7] C. S. Lim, E. Levi, M. Jones, N. A. Rahim, and W. P. Hew, "FCS-MPC-based current control of a five-phase induction motor and its comparison with PI-PWM control," *IEEE Trans. Ind. Electron.*, vol. 61, DOI 10.1109/TIE.2013.2248334, no. 1, pp. 149–163, 2013.

[8] E. Levi, "Advances in converter control and innovative exploitation of additional degrees of freedom for multiphase machines," *IEEE Trans. Ind. Electron.*, vol. 63, DOI 10.1109/TIE.2015.2434999, no. 1, pp. 433–448, 2016.

[9] F. Barrero and M. J. Duran, "Recent advances in the design, modeling, and control of multiphase machines: Part I," *IEEE Trans. Ind. Electron.*, vol. 63, DOI 10.1109/TIE.2015.2447733, no. 1, pp. 449–458, 2016.

[10] H. S. Che, M. J. Duran, E. Levi, M. Jones, W.-P. Hew, and N. A. Rahim, "Postfault operation of an asymmetrical six-phase induction machine with single and two isolated neutral points," *IEEE Trans. Power Electron.*, vol. 29, DOI 10.1109/TPEL.2013.2293195, no. 10, pp. 5406–5416, 2014.

[11] A. G. Yepes, J. Doval-Gandoy, and H. A. Toliyat, "Strategy With Smooth Transitions and Improved Torque–Speed Region and Stator Copper Loss for Two-Level Asymmetrical Six-Phase Induction Motor Drives Under Switch Faults," *IEEE Trans. Power Electron.*, vol. 36, DOI 10.1109/TPEL.2020.3011852, no. 2, pp. 1954–1969, 2020.

[12] G. Sala, M. Mengoni, G. Rizzoli, M. Degano, L. Zarri, and A. Tani, "Impact of star connection layouts on the control of multiphase induction motor drives under open-phase fault," *IEEE Trans. Power Electron.*, vol. 36, DOI 10.1109/TPEL.2020.3024205, no. 4, pp. 3717–3726, 2020.

[13] M. J. Duran and F. Barrero, "Recent Advances in the Design, Modeling, and Control of Multiphase Machines: Part II," *IEEE Trans. Ind. Electron.*, vol. 63, DOI 10.1109/TIE.2015.2448211, no. 1, pp. 459–468, 2016.

[14] I. Subotic, N. Bodo, E. Levi, B. Dumnic, D. Milicevic, and V. Katic, "Overview of fast on-board integrated battery chargers for electric vehicles based on multiphase machines and power electronics," *Elect. Power Appl.*, vol. 10, DOI 10.1049/iet-epa.2015.0292, no. 3, pp. 217–229, 2016.

[15] Y. Kali, M. Ayala, J. Rodas, M. Saad, J. Doval-Gandoy, R. Gregor, and K. Benjelloun, "Current control of a six-phase induction machine drive based on discrete-time sliding mode with time delay estimation," *Energies*, vol. 12, DOI 10.3390/en12010170, no. 1, p. 170, 2019.

[16] Y. Kali, M. Ayala, J. Rodas, M. Saad, J. Doval-Gandoy, R. Gregor, and K. Benjelloun, "Time delay estimation based discrete-time super-twisting current control for a six-phase induction motor," *IEEE Trans. Power Electron.*, DOI 10.1109/TPEL.2020.2995773, 2020.

[17] M. A. Fnaiech, F. Betin, G.-A. Capolino, and F. Fnaiech, "Fuzzy logic and sliding-mode controls applied to six-phase induction machine with open phases," *IEEE Trans. Ind. Electron.*, vol. 57, DOI 10.1109/TIE.2009.2034285, no. 1, pp. 354–364, 2009.

[18] Z. Liu, Z. Zheng, and Y. Li, "Enhancing fault-tolerant ability of a nine-phase induction motor drive system using fuzzy logic current controllers," *IEEE Trans. Energy Conv.*, vol. 32, DOI 10.1109/TEC.2017.2692528, no. 2, pp. 759–769, 2017.

[19] M. Morawiec, P. Strankowski, A. Lewicki, J. Guziński, and F. Wilczyński, "Feedback control of multiphase induction machines with backstepping technique," *IEEE Trans. Ind. Electron.*, vol. 67, DOI 10.1109/TIE.2019.2931236, no. 6, pp. 4305–4314, 2019.

[20] Y. Kali, J. Rodas, M. Saad, J. Doval-Gandoy, and R. Gregor, "Nonlinear backstepping with time delay estimation for six-phase induction machine," in *Proc. IEMDC*, DOI 10.1109/IEMDC.2019.8785155. IEEE, 2019, pp. 1798–1804.

[21] Y. Wang, J. Yang, S. Li, G. Yang, R. Deng, and H. Hussain, "Multiplane Rotor Resistance Online Estimation Strategy for Multiphase Induction Machine under Non-Sinusoidal Power Supply," *IEEE Trans. Power Electron.*, DOI 10.1109/TPEL.2021.3051213, 2021.

[22] J. J. Aciego, I. G. Prieto, and M. J. Duran, "Model predictive control of six-phase induction motor drives using two virtual voltage vectors," *IEEE Journal of Emerging and Selected Topics in Power Electronics*, vol. 7, DOI 10.1109/JESTPE.2018.2883359, no. 1, pp. 321–330, 2018.

[23] M. Ayala, J. Doval-Gandoy, J. Rodas, O. Gonzalez, and R. Gregor, "Current control designed with model based predictive control for six-phase motor drives," *ISA transactions*, DOI 10.1016/j.isatra.2019.08.052, 2019.

[24] I. González-Prieto, M. Durán, M. Bermúdez, F. Barrero, and C. Martín, "Assessment of Virtual-Voltage-based Model Predictive Controllers in Six-phase Drives under Open-Phase Faults," *IEEE Journal of Emerging and Selected Topics in Power Electronics*, DOI 10.1109/JESTPE.2019.2915666, 2019.

[25] M. Bermúdez, C. Martín, I. González-Prieto, M. J. Durán, M. R. Arahal, and F. Barrero, "Predictive current control in electrical drives: an illustrated review with case examples using a five-phase induction motor drive with distributed windings," *IET Electric Power Appl.*, vol. 14, DOI 10.1049/iet-epa.2019.0667, no. 8, pp. 1291–1310, 2020.

[26] O. Gonzalez, M. Ayala, J. Doval-Gandoy, J. Rodas, R. Gregor, and M. Rivera, "Predictive-fixed switching current control strategy applied to six-phase induction machine," *Energies*, vol. 12, DOI 10.3390/en12122294, no. 12, p. 2294, 2019.

[27] M. Ayala, J. Doval-Gandoy, J. Rodas, O. Gonzalez, R. Gregor, and M. Rivera, "A novel modulated model predictive control applied to six-phase induction motor drives," *IEEE Trans. Ind. Electron.*, DOI 10.1109/TIE.2020.2984425, 2020.

[28] M. Morari and J. H. Lee, "Model predictive control: past, present and future," *Computers & Chemical Engineering*, vol. 23, DOI 10.1016/S0098-1354(98)00301-9, no. 4-5, pp. 667–682, 1999.

[29] R. P. Aguilera and D. E. Quevedo, "Predictive control of power converters: Designs with guaranteed performance," *IEEE Trans. Ind. Inform.*, vol. 11, DOI 10.1109/TII.2014.2363933, no. 1, pp. 53–63, 2014.

[30] M. Preindl, "Robust control invariant sets and Lyapunov-based MPC for ipm synchronous motor drives," *IEEE Trans. Ind. Electron.*, vol. 63, DOI 10.1109/TIE.2016.2527722, no. 6, pp. 3925–3933, 2016.

[31] R. P. Aguilera and D. E. Quevedo, "On the stability of MPC with a finite input alphabet," *Proc. IFAC*, vol. 44, DOI 10.3182/20110828-6-IT-1002.02705, no. 1, pp. 7975–7980, 2011.

[32] M. N. Zeilinger, M. Morari, and C. N. Jones, "Soft constrained model predictive control with robust stability guarantees," *IEEE Trans. Automatic Control*, vol. 59, DOI 10.1109/TAC.2014.2304371, no. 5, pp. 1190–1202, 2014.

[33] L. Zhang, S. Zhuang, and R. D. Braatz, "Switched model predictive control of switched linear systems: Feasibility, stability and robustness," *Automatica*, vol. 67, DOI 10.1016/j.automatica.2016.01.010, pp. 8–21, 2016.

[34] M. Ayala, J. Rodas, R. Gregor, J. Doval-Gandoy, O. Gonzalez, M. Saad, and M. Rivera, "Comparative study of predictive control strategies at fixed switching frequency for an asymmetrical six-phase induction motor drive," in *Proc. IEMDC*, DOI 10.1109/IEMDC.2017.8002121, 2017, pp. 1–8.

[35] Y. Zhao and T. Lipo, "Space vector PWM control of dual three-phase induction machine using vector space decomposition," *IEEE Trans. Ind. Electron.*, vol. 31, DOI 10.1109/28.464525, no. 5, pp. 1100–1109, 1995.

[36] C. Martín, M. R. Arahal, F. Barrero, and M. J. Durán, "Multiphase rotor current observers for current predictive control: A five-phase case study," *Control Eng. Prac.*, vol. 49, DOI 10.1016/j.conengprac.2016.01.011, pp. 101–111, 2016.

[37] J. Rodas, F. Barrero, M. R. Arahal, C. Martín, and R. Gregor, "Online estimation of rotor variables in predictive current controllers: a case study using five-phase induction machines," *IEEE Trans. Ind. Electron.*, vol. 63, DOI 10.1109/TIE.2016.2559420, no. 9, pp. 5348–5356, 2016.

[38] J. Rodas, C. Martin, M. R. Arahal, F. Barrero, and R. Gregor, "Influence of covariance-based ALS methods in the performance of predictive controllers with rotor current estimation," *IEEE Trans. Ind. Electron.*, vol. 64, DOI 10.1109/TIE.2016.2636205, no. 4, pp. 2602–2607, 2017.

[39] J. Rodriguez, M. P. Kazmierkowski, J. R. Espinoza, P. Zanchetta, H. Abu-Rub, H. A. Young, and C. A. Rojas, "State of the art of finite control set model predictive control in power electronics," *IEEE Trans. Ind. Inform.*, vol. 9, DOI 10.1109/TII.2012.2221469, no. 2, pp. 1003–1016, 2013.

[40] B. Majmunović, T. Dragičević, and F. Blaabjerg, "Multi Objective Modulated Model Predictive Control of Stand-Alone Voltage Source Converters," *IEEE Journal of Emerging and Selected Topics in Power Electronics*, DOI 10.1109/JESTPE.2019.2925603, 2019.

[41] D. Q. Mayne, J. B. Rawlings, C. V. Rao, and P. O. Scokaert, "Constrained model predictive control: Stability and optimality," *Automatica*, vol. 36, DOI 10.1016/S0005-1098(99)00214-9, no. 6, pp. 789–814, 2000.

[42] R. P. Aguilera and D. E. Quevedo, "Stability analysis of quadratic MPC with a discrete input alphabet," *IEEE Trans. Automatic Control*, vol. 58, DOI 10.1109/TAC.2013.2264551, no. 12, pp. 3190–3196, 2013.

[43] A. G. Yepes, J. A. Riveros, J. Doval-Gandoy, F. Barrero, O. López, B. Bogado, M. Jones, and E. Levi, "Parameter identification of multiphase induction machines with distributed windings Part 1: Sinusoidal excitation methods," *IEEE Trans. Energy Conv.*, vol. 27, DOI 10.1109/TEC.2012.2220967, no. 4, pp. 1056–1066, 2012.

[44] J. A. Riveros, A. G. Yepes, F. Barrero, J. Doval-Gandoy, B. Bogado, O. Lopez, M. Jones, and E. Levi, "Parameter identification of multiphase induction machines with distributed windings Part 2: Time-domain techniques," *IEEE Trans. Energy Conv.*, vol. 27, DOI 10.1109/TEC.2012.2219862, no. 4, pp. 1067–1077, 2012.

Magno Ayala received the B.Eng. degree in electronic engineering from the Universidad Nacional de Asunción (UNA), Paraguay, in 2014, his M.Sc. and Ph.D in Power Electronics in 2017 and 2020 respectively. He joined the Laboratory of Power and Control System at the UNA, in 2015, working as a Research Assistant. His research interests are in the areas of control of multiphase ac machines.

Jesús Doval-Gandoy (M'99) received the M.Sc. degree from Polytechnic University of Madrid, Madrid, Spain, in 1991 and the Ph.D. degree from the University of Vigo, Vigo, Spain in 1999. From 1991 till 1994 he worked at industry. He is currently an Associate Professor at the University of Vigo. His research interests are in the areas of ac power conversion.

Osvaldo Gonzalez was born in Paraguay in 1987. B.Eng. degree in electronic engineering from the Universidad Nacional de Asunción (UNA), in 2014 and the M.Sc. degree in Power Electronics in 2017. His research interests include the area of control of multiphase motors. Mr. Gonzalez is a recipient of the training program for university lecturers from the CONACYT of Paraguay for his Ph.D. studies.

Jorge Rodas (S'08–M'12) was born in Asunción, Paraguay in 1984. He received his B.Eng. degree in Electronic Engineering from the Universidad Nacional de Asunción (UNA), Paraguay, in 2009. He received his M.Sc. degrees from the Universidad de Vigo, Spain, in 2012 and from the Universidad de Sevilla, Spain, in 2013, and his joint-university Ph.D. degree between the Universidad Nacional de Asunción and the Universidad de Sevilla in 2016.

In 2011, he joined the Laboratory of Power and Control System at the UNA, where he is currently an Associate Professor. His main research areas are predictive control, multiphase drives, matrix converters and control of power converters for renewable energy applications.

Raúl Gregor was born in Asunción, Paraguay, in 1979. He received the Bachelor Degree in Electronic Engineering from the Catholic University of Asunción, Paraguay, in 2005. He received the M.Sc. and Ph.D. degrees in Electronic, Signal Processing and Communications from the Higher Technical School of Engineering (ETSI), University of Seville, Spain, in 2008 and 2010, respectively. Since March 2010, Prof. Gregor is Head of the Laboratory of Power and Control System (LSPyC) of the Engineering Faculty in the National University of Asunción, Paraguay.

Prof. Gregor has authored or coauthored about 40 technical papers in the field of power electronics and control systems, six of which have been published in high impact factor journals. He obtained the Best Paper Award from the IEEE TRANSACTIONS ON INDUSTRIAL ELECTRONICS, Industrial Electronics Society, in 2010, and the Best Paper Award from the IET ELECTRIC POWER APPLICATIONS, in 2012. His research interests include; Multiphase Drives, Advanced Control of Power Converters Topologies, Quality of Electrical Power, Renewable Energy, Modeling, Simulation, Optimization and Control of Power Systems, Smart Metering & Smart Grids and Predictive Control.

Marco Rivera was born in Talca, Chile, in 1982. He received the B.Sc. degree in electronics engineering and the M.Sc. degree in electrical engineering from the Universidad de Concepción, Concepción, Chile, in 2007 and 2008, respectively, and the Ph.D. degree from the Department of Electronics Engineering, Universidad Técnica Federico Santa María, Valparaíso, Chile, in 2011. Prof. Rivera is Head of the Laboratory of Energy Conversion and Power Electronics (LCEEP) and the Technology Center for Energy Conversion (CTCE).

Article

Algorithm for implementation of Virtual Voltage Vectors in Model Predictive Current Control of Six-Phase Induction Machines

Carlos Romero [1,*], Larizza Delorme [2], Osvaldo Gonzalez [1], Magno Ayala [1], Jorge Rodas [1] and Raul Gregor [1]

[1] Laboratory of Power and Control Systems (LSPyC), Facultad de Ingeniería, Universidad Nacional de Asunción, Luque, Paraguay; ogonzalez@ing.una.py, mayala@ing.una.py, jrodas@ing.una.py, rgregor@ing.una.py

[2] Facultad Politécnica, Universidad Nacional de Asunción, Paraguay; laridelorme@gmail.com

* Correspondence: cromero@ing.una.py; Tel.: +595981280330

Version May 17, 2021 submitted to Energies

Abstract: The development of new control techniques for multiphase induction motors (IM) has become a point of great interest to exploit the advantages of these machines compared three-phase topology, for example, the reduced phase currents and lower harmonic contents. One of the most analysed techniques is the model-based predictive current control (MPC) with a finite control set. This technique presents high $x-y$ currents because of the application of one switching state throughout the whole sampling period. Nevertheless, it is one of the most used due to its excellent dynamic response. To overcome the aforementioned drawbacks, new techniques called virtual vector have been developed, but although there are several articles with experimental results, the algorithm for implementing the technique has not been described in them. In this document, an implementation algorithm is described through two proposed variants in order to compare the performance in terms of $x-y$ mitigation in a six-phase machine. Experimental tests were evaluated according to performance indicators, such as the total harmonic distortion and the mean square error for both case studies to determine the implementations of proposed techniques behavior.

Keywords: Modulation strategies, multiphase induction machine, predictive current control, virtual vectors.

---

1. Introduction

For decades, three-phase IM was used for most variable speed applications, and control techniques are widely developed. Still, in recent years the strengths of the multiphase IM has encouraged their use and thus the development of new sophisticated control techniques to regulate their speed, flux, torque or current. Multiphase IM stands out from three-phase IM due to the following characteristics: an inherent ability to post-fault operation without additional hardware, lower stator current per phase for the same voltage and lower torque ripple [1–3]. On the other hand, implementing more complex control strategies and the need for careful regulation of secondary currents that appear in multiphase IM also entails a higher computational cost. [4,5]. However, this fact can be addressed through more powerful digital controllers such as DSP.

In this sense, concerning model-based control techniques, there are numerous options with their advantages and disadvantages. Among them is the MPC with finite set control, set control is one of the most widely used [6–8]. This technique employs a cost function to select an optimal vector from the 64 available vectors and apply it during the sampling period. The cost function consists of a configurable weighting factor to prioritize current tracking or loss reduction in the $x-y$ plane. This method has the disadvantage of high tracking error and considerable losses in the $x - y$ plane since it uses a single vector [9,10]. This fact produces high harmonic content in the stator currents compared to other approaches that integrate modulation strategies in MPC to face this weakness [11].

An alternative to mitigate the $x - y$ currents was presented in [9], called virtual voltage vectors (VV). This method minimizes current losses by using a zero vector (ZV), a large vector (LV), and the corresponding medium-large collinear vector (MLV) at each sampling time (T_s), since in the $x - y$ plane these vectors are 180 degrees out of phase and tend to be eliminated. Thus, to obtain a zero voltage on average in the $x - y$ plane it is necessary to apply the vectors in a certain proportion of time, which means, the LV is applied 0.73 of T_s and the MLV 0.27 of T_s. This technique uses less computational resources due to the fact that it analyzes only 12 vectors, however, combining the vectors decreases the scope, covering only 93% of the LV module in the $\alpha - \beta$ plane.

Another MPC called M2PC based on space vector modulation (SVM), it uses a cost function to determine a pair of optimal LV at each T_s, and the selected optimal LV along with the ZV a combination is performed, this allows to represent more accurately the target voltage, being able to cover 96% of the entire $\alpha - \beta$ plane. This method allows to cover an area, and therefore minimizes the tracking error and naturally reduces the losses because the LV are mapped as the smallest in the $x - y$ plane [12,13].

Recently, other MPC techniques have been developed such as NM2PC, which uses up to 4 active vectors at each T_s and does not use the ZV. By means of a cost function it selects up to 4 vectors, two LV and two medium vectors (MV) in order to reduce the losses in the $x - y$ plane. It is important to mention that in M2PC the cost function implements a weighting factor between current tracking and $x - y$ loss reduction, and to some extent it is common that the algorithm tends to use the zero vector to reduce losses, even if the current tracking decreases in the $\alpha - \beta$ plane, so the NM2PC presents an advantage by not using the ZV, but on the other hand, the tracking ability of the controller for small currents deteriorates [14].

Although several works, as described above, have reported implementations of MPC techniques for multiphase IM drives, few works have described how to implement these techniques in digital controllers. In that sense, the main goal of this paper is to describe the implementation of VV into MPC technique focused on two study situations called virtual vectors with 4 application times (VV4) and virtual vectors with 11 application times (VV11). In both cases, two active vectors with different duty cycles are used in order to effectively reducing the $x - y$ currents, as well as to improve the current tracking capability using an asymmetrical six-phase IM. Experimental results are presented to contrast both study situations, comparing in terms of current tracking considering the mean square error (MSE) and total harmonic distortion (THD) of the stator currents, in order to analyze the performance of the system. The proposed method is tested at different operating points, considering transient and steady state conditions.

The sections that compose this document are the following: the mathematical model of the six-phase IM is shown in Section 2, as well as the voltage source inverter (VSI) used. Section 3 presents the description of the classic MPC, which will be used for the proposed MPC design. Section 4 describes the VV implementation into MPC using two study scenarios. Section 5 shows the experimental results of both proposed methods. Conclusions and special remarks are presented in the last section.

2. Six-Phase IM Mathematical Model

The system is composed of an asymmetrical six-phase IM and a six-phase VSI based on isolated gate bipolar transistors (IGBT) connected as shown in the electrical diagram in Fig. 1.

The stator phase voltages of the six-phase IM depend on the switching states and the DC-link voltage source (V_{dc}). In this regards, complementary signals are applied to each leg of the six-phase VSI and thus it is possible to obtain $2^6 = 64$ different switching states. These states are represented by a six-dimensional vector $[S] = [S_a, S_d, S_b, S_e, S_c, S_f]$. Assuming this, the stator phase voltages can be calculated from the ideal six-phase VSI model as shown below:

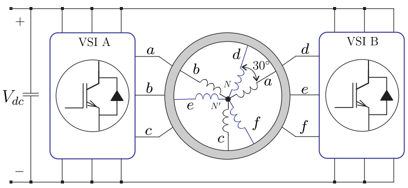

Figure 1. Six-phase IM fed by two level six-phase VSI.

$$\begin{bmatrix} v_{as} \\ v_{ds} \\ v_{bs} \\ v_{es} \\ v_{cs} \\ v_{fs} \end{bmatrix} = \frac{V_{dc}}{3} \begin{bmatrix} 2 & 0 & -1 & 0 & -1 & 0 \\ 0 & 2 & 0 & -1 & 0 & -1 \\ -1 & 0 & 2 & 0 & -1 & 0 \\ 0 & -1 & 0 & 2 & 0 & -1 \\ -1 & 0 & -1 & 0 & 2 & 0 \\ 0 & -1 & 0 & -1 & 0 & 2 \end{bmatrix} \begin{bmatrix} S_a \\ S_d \\ S_b \\ S_e \\ S_c \\ S_f \end{bmatrix} \tag{1}$$

Employing the vector space decomposition (VSD) technique, it is possible to simplify the system model, making transformations through the amplitude invariant Clarke conversion matrix (C), in this way is easy to represent the six-dimensional space defined by the six phases (a, d, b, e, c, f) in three two-dimensional orthogonal planes in the stationary reference frame, $\alpha - \beta$, $x - y$, and $z_1 - z_2$. The $\alpha - \beta$ plane is related to the torque and flux production, the $x - y$ plane is linked to the copper losses, while the components projected in the $z_1 - z_2$ plane are not examined due to the adopted topology (isolated neutral points). The transformation matrix is shown below:

$$C = \frac{1}{3} \begin{bmatrix} 1 & \frac{\sqrt{3}}{2} & -\frac{1}{2} & -\frac{\sqrt{3}}{2} & -\frac{1}{2} & 0 \\ 0 & \frac{1}{2} & \frac{\sqrt{3}}{2} & \frac{1}{2} & -\frac{\sqrt{3}}{2} & -1 \\ 1 & -\frac{\sqrt{3}}{2} & -\frac{1}{2} & \frac{\sqrt{3}}{2} & -\frac{1}{2} & 0 \\ 0 & \frac{1}{2} & -\frac{\sqrt{3}}{2} & \frac{1}{2} & \frac{\sqrt{3}}{2} & -1 \\ 1 & 0 & 1 & 0 & 1 & 0 \\ 0 & 1 & 0 & 1 & 0 & 1 \end{bmatrix} \tag{2}$$

Hence, using the transformation matrix defined in (2) the stator phase voltages are converted into orthogonal planes through the following equation:

$$\begin{bmatrix} v_{\alpha s} \\ v_{\beta s} \\ v_{xs} \\ v_{ys} \\ v_{z1s} \\ v_{z2s} \end{bmatrix} = [C] \begin{bmatrix} v_{as} \\ v_{ds} \\ v_{bs} \\ v_{es} \\ v_{cs} \\ v_{fs} \end{bmatrix} \tag{3}$$

It must be noted that the 64 switching states can be projected at the same time in both planes as shown in Fig. 2, where 49 of them are different. Vectors can be classified into large vectors (LV), medium-large vectors (MLV), medium vectors (MV), and small vectors (SV), which are marked as red, green, blue, and light blue circles, respectively.

Furthermore, the mathematical model of the system by using the state-space representation is expressed as follows:

$$\dot{X}_{(t)} = A_{(t)}\, X_{(t)} + B_{(t)}\, U_{(t)} + H n_{p(t)} \tag{4}$$

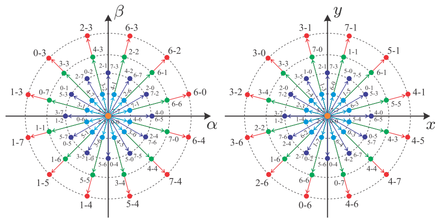

Figure 2. Voltage vectors of the six-phase IM in the $\alpha-\beta$ and $x-y$ planes.

defining $X_{(t)}$ as the state vector, formed by stator and rotor currents as shown in (5), $U_{(t)}$ as the input vector constituted by the stator voltages represented by (6), while $A_{(t)}$ and $B_{(t)}$ are the matrices that contain the electrical parameters of the six-phase IM expressed in (7) and (8), respectively. By considering the Gaussian process noises ($n_{p(t)}$), and its corresponding noise weighting matrix (H) have been considered in the model.

$$X_{(t)} = [x_1, ..., x_6]^T = [i_{\alpha s}, i_{\beta s}, i_{xs}, i_{ys}, i_{\alpha r}, i_{\beta r}]^T \tag{5}$$

$$U_{(t)} = [u_1, ..., u_4]^T = [u_{\alpha s}, u_{\beta s}, u_{xs}, u_{ys}]^T \tag{6}$$

$$A_{(t)} = \begin{bmatrix} a_{11} & a_{12} & 0 & 0 & a_{15} & a_{16} \\ a_{21} & a_{22} & 0 & 0 & a_{25} & a_{26} \\ 0 & 0 & a_{33} & 0 & 0 & 0 \\ 0 & 0 & 0 & a_{44} & 0 & 0 \\ a_{51} & a_{52} & 0 & 0 & a_{55} & a_{56} \\ a_{61} & a_{62} & 0 & 0 & a_{65} & a_{66} \end{bmatrix} \tag{7}$$

$$B_{(t)} = \begin{bmatrix} b_{11} & 0 & 0 & 0 \\ 0 & b_{22} & 0 & 0 \\ 0 & 0 & b_{33} & 0 \\ 0 & 0 & 0 & b_{44} \\ b_{51} & 0 & 0 & 0 \\ 0 & b_{62} & 0 & 0 \end{bmatrix} \tag{8}$$

where the coefficients are defined as:

$$\begin{aligned}
a_{11} &= a_{22} = -\frac{R_s L_r}{L_s L_r - L_m^2} & a_{12} &= -a_{21} = \frac{L_m^2 \omega_r}{L_s L_r - L_m^2} \\
a_{15} &= a_{26} = \frac{R_r L_m}{L_s L_r - L_m^2} & a_{16} &= -a_{25} = \frac{L_m L_r \omega_r}{L_s L_r - L_m^2} \\
a_{33} &= a_{44} = -\frac{R_s}{L_{ls}} & & \\
a_{51} &= a_{62} = \frac{R_s L_m}{L_s L_r - L_m^2} & a_{52} &= -a_{61} = -\frac{L_s L_m \omega_r}{L_s L_r - L_m^2} \\
a_{55} &= a_{66} = -\frac{R_r L_s}{L_s L_r - L_m^2} & a_{56} &= -a_{65} = -\frac{L_r L_s \omega_r}{L_s L_r - L_m^2} \\
b_{11} &= b_{22} = \frac{L_r}{L_s L_r - L_m^2} & b_{33} &= b_{44} = \frac{1}{L_{ls}} \\
b_{51} &= b_{62} = -\frac{L_m}{L_s L_r - L_m^2} & &
\end{aligned}$$

being $L_s = L_{ls} + L_m$, $L_r = L_{lr} + L_m$, R_s, and R_r the electrical parameters of the six-phase IM.

The output vector, including zero-mean Gaussian measurement noises ($n_{m(t)}$) and uncorrelated process, in the model, is calculated as follows:

$$Y_{(t)} = \begin{bmatrix} 1 & 0 & 0 & 0 & 0 & 0 \\ 0 & 1 & 0 & 0 & 0 & 0 \\ 0 & 0 & 1 & 0 & 0 & 0 \\ 0 & 0 & 0 & 1 & 0 & 0 \end{bmatrix} X_{(t)} + n_{m(t)} \tag{9}$$

Finally, the torque (T_e) and the load torque (T_L) of the six-phase IM are obtained using the following equations:

$$T_e = 3P\left(\psi_{\alpha s} i_{\beta s} - \psi_{\beta s} i_{\alpha s}\right) \tag{10}$$

$$J_i \dot{\omega}_m + B_i \omega_m = (T_e - T_L) \tag{11}$$

$$\omega_m = \frac{\omega_r}{P} \tag{12}$$

being J_i, B_i, ω_m, ω_r, $\psi_{\alpha s}$, $\psi_{\beta s}$ and P, the inertia coefficient, the friction coefficient, the rotor mechanical speed, the rotor electrical speed, the stator fluxes and the number of pole pairs, respectively.

3. Classic MPC

In order to implement the classic MPC in a digital controller, the mathematical model of the system must be in a discrete version. For this purpose, a discretization technique derived from the forward-Euler equation is used to obtain the predictive model. Note that the predicted variables only depending on past values of the variables and not on present values. As a result, the predictive model is described as:

$$\hat{X}_{(k+1|k)} = X_{(k)} + f\left(X_{(k)}, U_{(k)}, \omega_{r(k)}, T_s\right) \tag{13}$$

being k the actual sample.

3.1. Reduced Order Observer

Rotor currents can be estimated by means of the reduced order observer. There are two well known techniques, the Luenberger Observer (LO) and the Kalman Filter (KF) [15–17], the latter being the more optimal as it takes into account the noise input to the sensors thus optimizing the gain of the observer. Therefore, the KF is designed and implemented in this document, increasing the accuracy of the predictions. The equations of the mathematical model of system state space can be defined as:

$$\hat{X}_{(k+1|k)} = A_{(k)} X_{(k)} + B_{(k)} U_{(k)} + H n_{p(k)} \tag{14}$$

$$Y_{(k+1|k)} = \begin{bmatrix} 1 & 0 & 0 & 0 & 0 & 0 \\ 0 & 1 & 0 & 0 & 0 & 0 \\ 0 & 0 & 1 & 0 & 0 & 0 \\ 0 & 0 & 0 & 1 & 0 & 0 \end{bmatrix} X_{(k+1)} + n_{m(k+1)} \tag{15}$$

where k represent the actual sample, $n_{p(k)}$ as the process noise, and H as the noise weight matrix

The discretized matrices $A_{(k)}$ and $B_{(k)}$ are represented in (16) and (17) respectively. $A_{(k)}$ depends on the present amount of the rotor electrical speed and it must be actualized at every sampling period.

$$A_{(k)} = \begin{bmatrix} a_{11(k)} & a_{12(k)} & 0 & 0 & a_{15(k)} & a_{16(k)} \\ a_{21(k)} & a_{22(k)} & 0 & 0 & a_{25(k)} & a_{26(k)} \\ 0 & 0 & a_{33(k)} & 0 & 0 & 0 \\ 0 & 0 & 0 & a_{44(k)} & 0 & 0 \\ a_{51(k)} & a_{52(k)} & 0 & 0 & a_{55(k)} & a_{56(k)} \\ a_{61(k)} & a_{62(k)} & 0 & 0 & a_{65(k)} & a_{66(k)} \end{bmatrix} \tag{16}$$

$$B_{(k)} = \begin{bmatrix} b_{11(k)} & 0 & 0 & 0 \\ 0 & b_{22(k)} & 0 & 0 \\ 0 & 0 & b_{33(k)} & 0 \\ 0 & 0 & 0 & b_{44(k)} \\ b_{51(k)} & 0 & 0 & 0 \\ 0 & b_{62(k)} & 0 & 0 \end{bmatrix} \tag{17}$$

The discretized matrix coefficients were included in the Appendix.

3.2. Cost Function

The objective of the cost function is to obtain a numerical value that allows a decision to be made by prioritizing one or more variables. The minimization of switching losses, torque ripple, harmonic content, or tracking error of stator currents could be optimized. The latter is usually the priority, so the current tracking error calculations are made in the $\alpha - \beta$ and $x - y$ plane. The current tracking error between the reference ($i^*_{s(k+2)}$) and their predicted values ($\hat{i}_{s(k+2)}$) in the $\alpha - \beta$ and $x - y$ planes is calculated as follows:

$$J = \sqrt{(e_{\alpha s})^2 + (e_{\beta s})^2 + \lambda_{xy}[(e_{xs})^2 + (e_{ys})^2]} \tag{18}$$

where

$$\begin{aligned} e_{\alpha s} &= i^*_{\alpha s(k+2)} - \hat{i}_{\alpha s(k+2)} \\ e_{\beta s} &= i^*_{\beta s(k+2)} - \hat{i}_{\beta s(k+2)} \\ e_{xs} &= i^*_{xs(k+2)} - \hat{i}_{xs(k+2)} \\ e_{ys} &= i^*_{ys(k+2)} - \hat{i}_{ys(k+2)} \end{aligned} \tag{19}$$

It must be noted that a second-step ahead prediction is implemented to consider the delay compensation. This fact is produced by a notable amount of time in the computation of the control signals which is similar to the sampling period [6,18]. The tuning parameter (λ_{xy}) in (18) is usually considered in the control of the multiphase machines to provide greater weight to the $\alpha - \beta$ currents over the $x - y$ currents.

4. Proposed Algorithm

This section aims to describe the proposed algorithm implementation in a digital controller based on VV characteristics into MPC.

4.1. Case 1: VV4

The first MPC strategy based on virtual vectors to be discussed in this paper is called VV4. It uses 2 vectors per sampling time, a long vector and the nearest collinear medium-large vector. The Fig. 3 exemplifies the selection of two vectors, LV and MLV, from the I-sector of the $\alpha - \beta$ plane. Advantage is taken of the fact that the LV and collinear MLV are 180 degrees out of phase in the $x - y$ plane, and although they have different modulus as shown in Fig. 2, they tend to subtract each other thus decreasing the losses in this plane.

The VV4 technique adopts strategies that take into account the ratio of the modulus of LV and MLV to calculate their application times, in order to obtain a zero average value in the $x - y$ plane. This virtual vector is applied as follows:

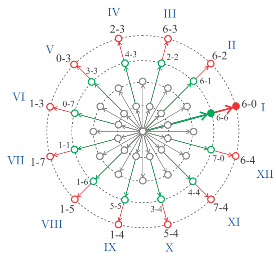

Figure 3. Space sectors in the $\alpha - \beta$ plane for MPC with VV.

$$VV4 = d_l LV + d_{ml} MLV \tag{20}$$

being $d_l = 0.75\ T_{sv}$ and $d_{ml} = 0.25\ T_{sv}$

On the other hand, in VV4 there is a decrease in the maximum final voltage that can be reached, since it conditions the use of the LV and MLV vectors, obtaining a resulting vector of lower modulus.

The process for the implementation of VV4 is shown in Fig 4 and detailed below:

- Step 1: The algorithm starts with the variables initialization and calculation of the electrical parameters of IM.
- Step 2: The basic control technique, in this case the classical MPC, acquires measurements of the stator currents every sampling time (Ts). To implement the VV4 technique, the original sampling time (Ts) is increased by 4, hereafter referred to as (Tsv), consequently the sampling frequency is reduced by 4. On the other hand, an interrupt is used to control current readings, calculations and transforms, vector selection and application. The input period to the routines contained in this interrupt is every $T_{sv}/4$, and they are called interrupt time (T_i), so the interrupt is entered 4 times per sampling time.
- Step 3: In the first interval (T_i) of the sampling time, the measurements are considered to proceed to perform the transformations and calculations.
- Step 4: The 12 external vectors (LV) are evaluated using a cost function and the optimal vector is obtained. The MLV vector corresponding to the optimal LV is identified, and both will be applied during the sampling time.
- Step 5: Only one vector is applied at each interrupt time, making use of conditional statements and a counter to identify the 4 interrupts in a sampling period. To reduce the losses in the $x - y$ plane, the total application time of the active vectors is distributed between the LV and the MLV in a proportion of 75% and 25% respectively, so that the LV is applied 3 times and the MLV once. The final pattern of applied vectors is shown in Fig. 5.

4.2. Case 2: VV11

The second case study is the technique called VV11, based on the MPC strategy with virtual vectors. Unlike VV4, in VV11 the LVand MLV are applied 73%and 27% of the time, so that the average loss in the $x - y$ plane tends to zero. In order to achieve the latter, the sampling period is divided into 11 equal intervals by an interruption, so that T_i=$T_{sv}/11$.

Similar to VV4, measurements are taken in each sampling period, calculations and transformations are performed, optimal vectors are selected and applied in each T_i. In total, 8 times the LV and 3 times the MLV are applied, resulting in approximately 72.73% of T_{sv} for LV and 27.27% of T_{sv} for MLV. The final applied vector pattern for VV11 is shown in Fig. 6. This extra processes implies higher computational costs compared to VV4.

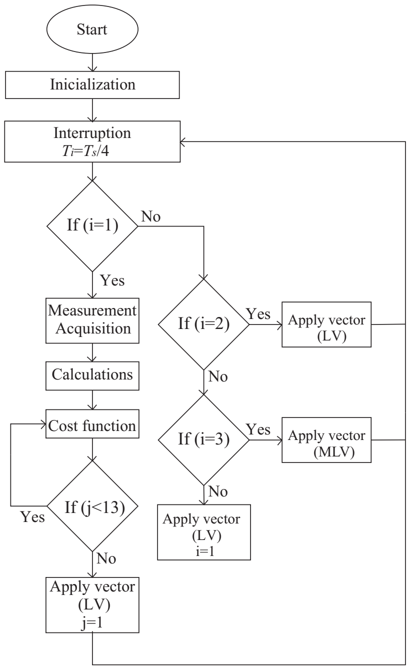

Figure 4. Algorithm diagram for VV4 technique.

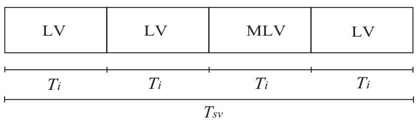

Figure 5. Timing diagram for VV4 technique.

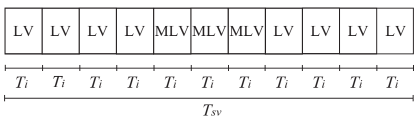

Figure 6. Timing diagram for VV11 technique.

5. Experimental Results

The case studies are implemented to analyze their performance by comparing them with each other through the experimental results collected in the six-phase IM bench.

5.1. Six-phase IM test bench description

The control system is based on Six-Phase VSI, driven by a DSP (TMS320F28335 from Texas Instruments), with a Technosoft MCK28335 development environment. The IM parameters are shown in Table 1 determined by the tests described in [19,20].

Table 1. Electrical and mechanical parameters of the six-phase IM

Parameter	Value	Parameter	Value
R_r	0.63 Ω	L_s	206.2 mH
R_s	0.62 Ω	P	3
L_{ls}	6.4 mH	P_w	15 kW
L_{lr}	3.5 mH	J_i	0.27 kg.m^2
L_m	66.6 mH	B_i	0.012 kg.m^2/s
L_r	203.3 mH	ω_{r-nom}	1000 rpm

Figure 7. Test bench composed of the 2L-6PVSI, DSP unit control, six-phase IM and the mechanical load.

The periodic measurements of the rotor currents and speed, necessary to perform the calculations and implement the control techniques, are made by a series of sensors. A 10000 ppr encoder is used to obtain the mechanical speed of the motor.

A matching board is provided to amplify the signals coming from 4 LA 55-P sensors used to measure the stator currents. The digitalization is performed by means of a 16-bit A/D converter of the DSP. A DC-link is set to 325 V through a three phase rectifier and the power grid with a step-down transformer. A mechanical brake pad was installed to simulate mechanical loading of approximately 120 Nm. A block diagram of the test bench is shown in Fig. 7.

5.2. Figures of merit

In order to analyze the performance of the modulation techniques under study, VV4 and VV11, experimental tests are performed where steady state and transient results are obtained. The MSE between the reference and stator current measured in the $\alpha-\beta$ and $x-y$ planes is obtained in order to compare current and loss tracking. On the other hand, the THD in the $\alpha-\beta$ plane is calculated to quantify the harmonic distortion obtained with both techniques. In this context, the MSE is defined as:

$$\mathrm{MSE}(i_{s\Phi}) = \sqrt{\frac{1}{N}\sum_{k=1}^{N}(i_{s\Phi}[k]-i^{*}_{s\Phi}[k])^2} \tag{21}$$

where N is the number of samples, $i^*_{s\Phi}$ the stator current reference, $i_{s\Phi}$ the measured stator currents and $\Phi \in \{\alpha, \beta, x, y\}$. At the same time, THD is defined as:

$$\mathrm{THD}(i_s) = \sqrt{\frac{1}{i^2_{s1}} \sum_{j=2}^{N} (i_{sj})^2} \tag{22}$$

where i_{s1} is the fundamental stator currents and i_{sj} is the harmonic stator currents.

5.3. Steady state study

For the purpose of analyzing the performance of the $x - y$ current references are set to zero ($i^*_{xs} = i^*_{ys} = 0$), and the d axis current ($i^*_{ds} = 1.5$) has been considered for all cases.

For the VV4 and V11 technique, the sampling frequency is 2.5 kHz, the tests are performed at mechanical speeds of 100 rpm to 600 rpm. The results obtained from VV4 and VV11 at the different speeds are shown in Table 2 and Table 3. At the same time, Fig. 8 and Fig. 9 show the stator currents tracking in $\alpha - \beta$ and $x - y$ planes for classic MPC, VV4 and VV11 respectively. The operations were tested at a sampling frequency of 2.5 kHz and a rotor speed of 200 rpm for the techniques.

The results show good current tracking in the $\alpha - \beta$ plane for both techniques, with a slight advantage for VV11, showing lower MSE values for all speeds. In terms of MSE in the $x - y$ plane, higher values are observed for VV4, corroborating the decrease of the resultant vector in the $x - y$ plane also for all speeds. In terms of THD, it is observed that the VV11 technique leads to higher harmonic distortion.

Table 2. Performance indicators for the drive operating from 100 [rpm] to 600 [rpm] for VV4.

VV4 at f_s = 2.5 [kHz]					
ω^*_m	MSE_α	MSE_β	MSE_x	MSE_y	THD_α
100	1.95	1.65	2.97	3.29	14.22
200	2.15	1.94	3.10	3.26	15.43
300	2.52	2.44	3.05	3.28	13.64
400	2.87	2.83	3.10	3.35	16.13
500	3.27	3.15	3.14	3.37	18.04
600	3.56	3.67	3.16	3.38	16.67

Table 3. Performance indicators for the drive operating from 100 [rpm] to 600 [rpm] for VV11.

VV11 at f_s = 2.5 [kHz]					
ω^*_m	MSE_α	MSE_β	MSE_x	MSE_y	THD_α
100	1.58	1.26	2.55	2.84	19.59
200	1.53	1.27	2.50	2.77	22.22
300	1.65	1.38	2.47	2.79	23.43
400	1.63	1.39	2.56	2.73	24.73
500	2.38	1.86	2.50	2.77	24.56
600	2.60	2.17	2.57	2.86	29.01

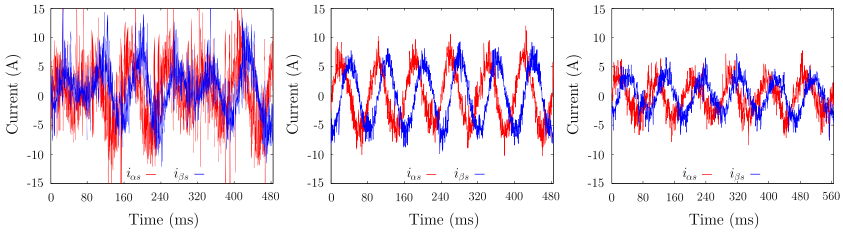

(a) (b) (c)

Figure 8. Performance of stator currents in $\alpha - \beta$ plane for a rotor speed of 200 [rpm] at 2.5 [kHz] of sampling frequency: (a) classic MPC; (b) VV4; (c) VV11.

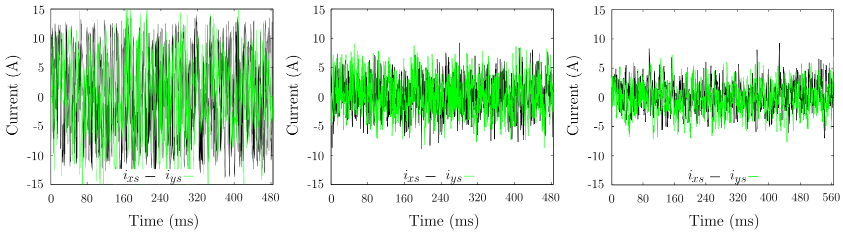

(a) (b) (c)

Figure 9. Performance of stator currents in $x - y$ plane for a rotor speed of 200 [rpm] at 2.5 [kHz] of sampling frequency: (a) classic MPC; (b) VV4; (c) VV11.

5.4. Transient study

For a transient operation, a step modification in the rotor speed is considered from 200 to −200 rpm (reversal condition) as shown in Fig. 10. Fig. 11 presents a dynamic test (q current tracking), which reveals the transient operation of VV4 (a) and VV11 (b) for a step change in the q current (i_{qs}^*). The dynamic performance is obtained through a reversal condition of the rotor speed (ω_m^*). The reaching time is approximately 0.5 ms of both techniques and the overshoot, for VV4 and VV11, are 10 % and 12.5 %, respectively.

6. Conclusion

The paper describes the implementation of two virtual vector modulation techniques applied to a six-phase asymmetrical IM. Among the advantages of both techniques based on the same control strategy are: a) Reduced amount of switching, since only the change of state of the transistor pair of one VSI branch is required to switch from the MLV to the collinear LV. b) Combining LV and their corresponding MLV reduces the losses in the $x - y$ plane. It can be seen in this work that as the combination of LV and MLV is closer to a ratio of 73% and 27% at each sampling time, the $x - y$ currents and the MSE in the $\alpha - \beta$ plane are reduced, although these improvements are negligible compared to the 75% and 25% ratio used in VV4. On the other hand, the VV11, presents higher harmonic distortion and higher computational cost. These observations lead us to conclude that VV11 does not present a higher performance over VV4, so the best alternative in order to achieve good figures of merit and lower computational cost is VV4.

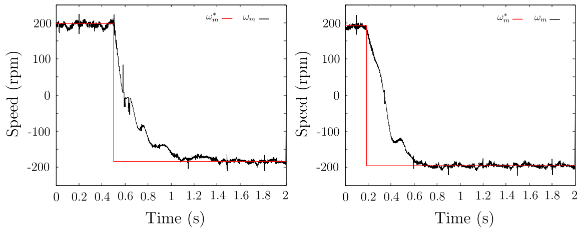

(a) (b)

Figure 10. Reversal condition from 200 [rpm] to −200 [rpm] at 2.5 [kHz] of sampling frequency: (a) VV4; (b) VV11.

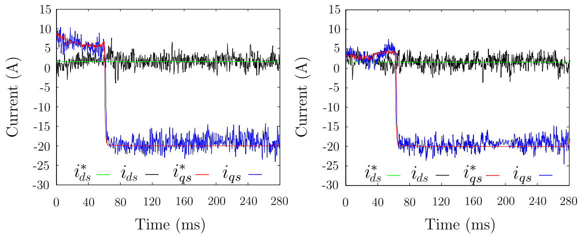

(a) (b)

Figure 11. Transient response in q-axis of stator current for a rotor speed change from 200 [rpm] to −200 [rpm] at 2.5 [kHz] of sampling frequency: (a) VV4; (b) VV11.

7. Appendix

$$
\begin{aligned}
a_{11(k)} &= a_{22(k)} = 1 - \frac{R_s L_r T_s}{L_s L_r - L_m^2} & a_{12(k)} &= -a_{21(k)} = \frac{L_m^2 \omega_{r(k)} T_s}{L_s L_r - L_m^2} \\
a_{15(k)} &= a_{26(k)} = \frac{R_r L_m T_s}{L_s L_r - L_m^2} & a_{16(k)} &= -a_{25(k)} = \frac{L_m L_r \omega_{r(k)} T_s}{L_s L_r - L_m^2} \\
a_{33(k)} &= a_{44(k)} = 1 - \frac{R_s T_s}{L_{ls}} & & \\
a_{51(k)} &= a_{62(k)} = \frac{R_s L_m T_s}{L_s L_r - L_m^2} & a_{52(k)} &= -a_{61(k)} = -\frac{L_s L_m \omega_{r(k)} T_s}{L_s L_r - L_m^2} \\
a_{55(k)} &= a_{66(k)} = 1 - \frac{R_r L_s T_s}{L_s L_r - L_m^2} & a_{56(k)} &= -a_{65(k)} = -\frac{L_r L_s \omega_{r(k)} T_s}{L_s L_r - L_m^2} \\
b_{11(k)} &= b_{22(k)} = \frac{L_r T_s}{L_s L_r - L_m^2} & & \\
b_{33(k)} &= b_{44(k)} = \frac{T_s}{L_{ls}} & & \\
b_{51(k)} &= b_{62(k)} = -\frac{L_m T_s}{L_s L_r - L_m^2} & &
\end{aligned}
$$

Author Contributions: Conceptualization, C.R., L.D., O.G. and M.A.; methodology, C.R., L.D., O.G. and M.A. software, C.R., L.D., O.G. and M.A.; validation, C.R., L.D., O.G. and M.A.; formal analysis, C.R., L.D., O.G., M.A., J.R. and R.G.; investigation, C.R., L.D., O.G. and M.A.; resources, C.R., L.D., O.G., M.A., J.R. and R.G.; data curation, C.R., L.D., O.G. and M.A.; writing, original draft preparation, C.R., L.D., O.G. and M.A.; writing,

review and editing, C.R., L.D., O.G., M.A., J.R. and R.G.; visualization, C.R., L.D., O.G., M.A., J.R. and R.G.; project administration, C.R., L.D., O.G., M.A., J.R. and R.G.; funding acquisition, R.G. and J.R.

Funding: This research has been funded through the Consejo Nacional de Ciencia y Tecnología (CONACYT)-Paraguay, Grant Number POSG16-05.

Conflicts of Interest: The authors declare no conflict of interest.

Abbreviations

The following abbreviations have been employed in this work:

DSP	Digital Signal Processor.
IGBT	Isolated Gate Bipolar Transistors.
IM	Induction Machine.
KF	Kalman Filter.
LO	Luenberger Observer.
LV	Large Vector.
MLV	Medium Large Vector.
MPC	Model Predictive Control.
MSE	Mean Squared Error.
MV	Medium Vector.
SV	Small Vector.
SVM	Space Vector Modulation.
THD	Total Harmonic Distortion.
VSD	Vector Space Decomposition.
VSI	Voltage Source Inverter.
VV	Virtual Vector.
VV11	Virtual Vectors with 11 application times.
VV4	Virtual Vectors with 4 application times.
ZV	Zero Vector.

References

1. Levi, E.; Bojoi, R.; Profumo, F.; Toliyat, H.; Williamson, S. Multiphase induction motor drives–a technology status review. *IET Electric Power Applications* **2007**, *1*, 489–516.
2. Barrero, F.; Duran, M.J. Recent advances in the design, modeling, and control of multiphase machines—Part I. *IEEE Transactions on Industrial Electronics* **2015**, *63*, 449–458.
3. Duran, M.J.; Barrero, F. Recent advances in the design, modeling, and control of multiphase machines—Part II. *IEEE Transactions on Industrial Electronics* **2015**, *63*, 459–468.
4. Kali, Y.; Ayala, M.; Rodas, J.; Saad, M.; Doval-Gandoy, J.; Gregor, R.; Benjelloun, K. Current control of a six-phase induction machine drive based on discrete-time sliding mode with time delay estimation. *Energies* **2019**, *12*, 170.
5. Kali, Y.; Ayala, M.; Rodas, J.; Saad, M.; Doval-Gandoy, J.; Gregor, R.; Benjelloun, K. Time Delay Estimation based Discrete-Time Super-Twisting Current Control for a Six-Phase Induction Motor. *IEEE Trans. Power Electron.* **2020**. doi:10.1109/TPEL.2020.2995773.
6. Arahal, M.; Barrero, F.; Toral, S.; Duran, M.; Gregor, R. Multi-phase current control using finite-state model-predictive control. *Control Eng. Pract.* **2009**, *17*, 579–587.
7. Lim, C.S.; Levi, E.; Jones, M.; Rahim, N.A.; Hew, W.P. A comparative study of synchronous current control schemes based on FCS-MPC and PI-PWM for a two-motor three-phase drive. *IEEE Transactions on Industrial Electronics* **2013**, *61*, 3867–3878.
8. Lim, C.S.; Levi, E.; Jones, M.; Rahim, N.A.; Hew, W.P. FCS-MPC-based current control of a five-phase induction motor and its comparison with PI-PWM control. *IEEE Tran. Ind. Electron.* **2013**, *61*, 149–163.
9. Gonzalez-Prieto, I.; Duran, M.J.; Aciego, J.J.; Martin, C.; Barrero, F. Model predictive control of six-phase induction motor drives using virtual voltage vectors. *IEEE Trans. Ind. Electron.* **2017**, *65*, 27–37.
10. Aciego, J.J.; Prieto, I.G.; Duran, M.J. Model predictive control of six-phase induction motor drives using two virtual voltage vectors. *IEEE J. Emerg. Sel. Top. Power Electron.* **2018**, *7*, 321–330.

11. González, O.; Ayala, M.; Romero, C.; Rodas, J.; Gregor, R.; Delorme, L.; González-Prieto, I.; Durán, M.J.; Rivera, M. Comparative Assessment of Model Predictive Current Control Strategies applied to Six-Phase Induction Machines. Proc. ICIT, 2020, pp. 1037–1043.
12. Ayala, M.; Gonzalez, O.; Rodas, J.; Gregor, R.; Rivera, M. Predictive control at fixed switching frequency for a dual three-phase induction machine with Kalman filter-based rotor estimator. 2016 IEEE International Conference on Automatica (ICA-ACCA). IEEE, 2016, pp. 1–6.
13. Gonzalez, O.; Ayala, M.; Doval-Gandoy, J.; Rodas, J.; Gregor, R.; Rivera, M. Predictive-Fixed Switching Current Control Strategy Applied to Six-Phase Induction Machine. *Energies* **2019**, *12*, 2294.
14. Ayala, M.; Doval-Gandoy, J.; Rodas, J.; Gonzalez, O.; Gregor, R.; Rivera, M. A Novel Modulated Model Predictive Control Applied to Six-Phase Induction Motor Drives. *IEEE Trans. Ind. Electron.* **2020**.
15. Rodas, J.; Barrero, F.; Arahal, M.R.; Martin, C.; Gregor, R. On-Line Estimation of Rotor Variables in Predictive Current Controllers: A Case Study Using Five-Phase Induction Machines. *IEEE Trans. Ind. Electron.* **2016**, *63*, 5348–5356.
16. Martin, C.; Arahal, M.R.; Barrero, F.; Durán, M.J. Five-phase induction motor rotor current observer for finite control set model predictive control of stator current. *IEEE Trans. Ind. Electron.* **2016**, *63*, 4527–4538.
17. Rodas, J.; Martin, C.; Arahal, M.R.; Barrero, F.; Gregor, R. Influence of Covariance-Based ALS Methods in the Performance of Predictive Controllers with Rotor Current Estimation. *IEEE Trans. Ind. Electron.* **2017**, *64*, 2602–2607.
18. Rodriguez, J.; Cortes, P. *Predictive control of power converters and electrical drives*; Vol. 40, John Wiley & Sons, 2012.
19. Yepes, A.G.; Riveros, J.A.; Doval-Gandoy, J.; Barrero, F.; López, O.; Bogado, B.; Jones, M.; Levi, E. Parameter identification of multiphase induction machines with distributed windings Part 1: Sinusoidal excitation methods. *IEEE Trans. Energy Conv.* **2012**, *27*, 1056–1066. doi:10.1109/TEC.2012.2220967.
20. Riveros, J.A.; Yepes, A.G.; Barrero, F.; Doval-Gandoy, J.; Bogado, B.; Lopez, O.; Jones, M.; Levi, E. Parameter identification of multiphase induction machines with distributed windings Part 2: Time-domain techniques. *IEEE Trans. Energy Conv.* **2012**, *27*, 1067–1077. doi:10.1109/TEC.2012.2219862.

Comparison of the Effects on Stator Currents Between Continuous Model and Discrete Model of the Three-phase Induction Motor in the Presence of Electrical Parameter Variations

1st Larizza Delorme
Master Student in Electronic Engineering
Universidad del Cono Sur de las Américas (UCSA)
Asuncion, Paraguay
laridelorme@gmail.com

2nd Magno Ayala
Laboratory of Power and Control Systems (LSPyC)
Universidad Nacional de Asunción
Luque, Paraguay
mayala@ing.una.py

3th Jorge Rodas
Laboratory of Power and Control Systems (LSPyC)
Universidad Nacional de Asunción
Luque, Paraguay
jrodas@ing.una.py

4th Raul Gregor
Laboratory of Power and Control Systems (LSPyC)
Universidad Nacional de Asunción
Luque, Paraguay
rgregor@ing.una.py

5th Osvaldo Gonzalez
Laboratory of Power and Control Systems (LSPyC)
Universidad Nacional de Asunción
Luque, Paraguay
ogonzalez@ing.una.py

6th Jesus Doval-Gandoy
Applied Power Electronics Technology Research Group (APET)
Universidad de Vigo
Vigo, Spain
jdoval@uvigo.es

***Abstract*—Three-phase induction motors are the most widely used electrical energy conversion machines due to their low cost, robustness, and ease of maintenance. Hence, the mathematical model analysis is fundamental to comprehend the behavior of the machine in order to implement a certain type of control. This article presents a comparison between the effects on the current, in steady-state, of electrical parameter variations of a three-phase induction motor model based on discrete-time with a continuous model by considering electrical parameters fixed in nominal values. Side by side comparisons between the application of pure sinusoidal waveforms and PWM waveforms generated by a voltage source inverter to the induction motor are presented. Simulation results are provided to show the parameter with the most significant impact over the machine when varying values.**

***Index Terms*—Induction motors, magnetization inductance, predictive discretized model.**

I. Introduction

Historically, one of the most used drives in industrial applications have been the induction machines due to some specific characteristics such as low cost, robustness and ease of maintenance [1]. As a consequence, the interest in the use of induction motor (IM) drives has allowed the development of well-established control techniques as field oriented control, direct torque control and, more recently, model predictive control (MPC) [2]–[5]. However, to apply control techniques, it is important to have a finished model to describe the properties of the physical system precisely in order to be controlled optimally [6]. In the design of the mathematical model of IMs, it is necessary to know the electrical and mechanical parameters. Some of these can be provided by the manufacturer or can be obtained through standardized tests [7], but in operation, these values, which are assumed as nominal in the equivalent circuit, vary according to different load conditions and effects such as temperature, magnetic saturation, skin effect, harmonics and rotor movement [1], [7], [8].

A precise knowledge of the parameter values is essential to determine a suitable model. When vector control or non-linear control techniques are used [9]–[11], such as the MPC, the control efficiency depends on the model to predict the states and to produce the desired performance [12]. For instance, in accurate speed estimation for the operation of speed-sensorless using machine model-based approaches [13]–[15]. In previous works, parameter identification processes are presented to obtain values focused on the magnetization inductance as in [1], [16]–[18] or focused on rotor and stator resistances as in [16], [19]. In other works, mathematical models are proposed considering magnetic saturation as in [20], [21].

Generally, parameters like stator and rotor resistance as well as magnetization inductance are considered constant in the model for simplicity without knowing how much this affects

978-1-7281-5754-2/20/$31.00 ©2020 IEEE

the performance of the electric drive. This paper aims to present a quantitative analysis of the impact on the currents of the electrical parameter variations in the discrete model concerning the continuous model with nominal values of the IM, in terms of the Mean Square Error (MSE). Variations are applied by taking into account several values in a range and comparisons of the effect between an operation of the IM with pure sinusoidal waveforms and voltage source inverter are presented.

The rest of this paper is organized as follows. The IM mathematical model in continuous time is presented in Section II. Then, in Section III, the model of the IM in discrete-time is described. In order to compare the effects of the variations, two types of power supply are exposed in Section IV. In Section V, simulation tests are described, and the results of the parameter variations is examined. Finally, conclusions are presented in the last section.

II. IM Mathematical Model

The dynamic model of the three-phase IM can be expressed in the stationary reference frame α-β such as:

$$\begin{aligned} \mathbf{v}_s &= R_s\,\mathbf{i}_s + \tfrac{d\boldsymbol{\lambda}_s}{dt} \\ 0 &= R_r\,\mathbf{i}_r + \tfrac{d\boldsymbol{\lambda}_r}{dt} - j\omega_r\,\boldsymbol{\lambda}_r \\ \boldsymbol{\lambda}_s &= L_s\,\mathbf{i}_s + L_m\,\mathbf{i}_r \\ \boldsymbol{\lambda}_r &= L_m\,\mathbf{i}_s + L_r\,\mathbf{i}_r \end{aligned} \tag{1}$$

where R_s and R_r are the stator and rotor resistances, respectively, L_m is the magnetizing inductance, L_s and L_r are the stator and rotor inductances, $\mathbf{v}_s$, $\mathbf{i}_s$, $\mathbf{i}_r$, are the stator voltage vector, the stator current and the rotor current vectors, $\boldsymbol{\lambda}_s$ and $\boldsymbol{\lambda}_r$ are the stator and rotor flux vectors. All electrical variables mentioned in (1) are two-dimensional complex space vector where the real and imaginary part denotes the components in the α-β plane. A general block diagram is represented in Fig. 1.

The electromagnetic torque can be expressed by:

$$T_e = \frac{3}{2}\,p_p\,\frac{L_m}{L_r}\,\mathrm{Im}\left\{\overline{\boldsymbol{\lambda}}_r\,\mathbf{i}_s\right\} \tag{2}$$

where p_p is the number of pole pairs and $\overline{\lambda}_r$ is the complex conjugate of the rotor flux vector. In order to describe the behavior of the mechanical speed ω_m and the electric rotor speed ω_r according to the electromagnetic torque T_e and load torque T_l, the mechanical equation is given by:

$$J\,\frac{d\omega_m}{dt} + B\,\omega_m = T_e - T_l \tag{3}$$

where J is the inertia of the mechanical shaft and B the friction coefficient. The mechanical speed in terms of electrical rotor speed is defined as:

$$\omega_m = \frac{\omega_r}{p_p}. \tag{4}$$

The continuous model (1)-(4) can be represented using the state-space representation as follows:

$$\begin{aligned} \dot{\mathbf{x}}(t) &= \mathbf{A}\mathbf{x}(t) + \mathbf{B}\mathbf{u}(t) \\ \mathbf{y}(t) &= \mathbf{C}\,\mathbf{x}(t) \end{aligned} \tag{5}$$

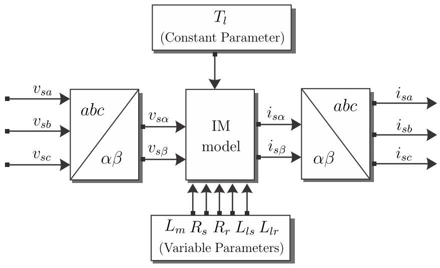

Fig. 1. Block diagram of the IM model.

where: $\mathbf{x}(t) = [i_{s\alpha},\ i_{s\beta},\ \lambda_{r\alpha},\ \lambda_{r\beta}]^T$ represent the state vector considering the stator current and the rotor flux variables, $\mathbf{u}(t) = [v_{s\alpha},\ v_{s\beta}]^T$ are the voltage input applied to the stator, and $\mathbf{y}(t)$ denotes the output vector. The superscript $(^T)$ is used to denote the transposed matrix and to define the dynamic of the electrical drive are used the matrices $\mathbf{A}$, $\mathbf{B}$ and $\mathbf{C}$. Then:

$$\mathbf{A} = \begin{bmatrix} c_1 & 0 & c_2 & c_3\omega_r \\ 0 & c_1 & -c_3\omega_r & c_2 \\ c_5 & 0 & c_6 & -\omega_r \\ 0 & c_5 & \omega_r & c_6 \end{bmatrix} \tag{6}$$

$$\mathbf{B} = \begin{bmatrix} c_4 & 0 \\ 0 & c_4 \\ 0 & 0 \\ 0 & 0 \end{bmatrix} \tag{7}$$

$$\mathbf{C} = \begin{bmatrix} 1 & 0 & 0 & 0 \\ 0 & 1 & 0 & 0 \\ 0 & 0 & 0 & 0 \\ 0 & 0 & 0 & 0 \end{bmatrix} \tag{8}$$

where:

$$c_1 = -\left(\tfrac{R_s}{\sigma\,L_s} + \tfrac{L_m^2}{\sigma\,L_s\,L_r\,\tau_r}\right) \quad c_2 = \tfrac{L_m}{\sigma\,L_s\,L_r\,\tau_r} \quad c_3 = \tfrac{L_m}{\sigma\,L_s\,L_r}$$
$$c_4 = \tfrac{1}{\sigma\,L_s} \quad c_5 = \tfrac{L_m}{\tau_r} \quad c_6 = -\tfrac{1}{\tau_r}$$
$$\sigma = 1 - \tfrac{L_m^2}{L_s\,L_r} \quad \tau_r = \tfrac{L_r}{R_r}.$$

III. Discrete-Time IM Model

The first order Euler approximation is applied in order to predict the state variables in the next sampling time and to keep computing cost low. The derived approximation is given by:

$$\dot{x} \simeq \frac{x(k+1) - x(k)}{T_s} \tag{9}$$

where x is the state variable, T_s is the sampling time and k represent the current sample.

Using (9) and (5), can be rewritten as:

$$x(k+1) = (I + A\,T_s)\,x(k) + B\,T_s\,u(k) \tag{10}$$

where $x(k) = [i_{s\alpha}(k)\ i_{s\beta}(k)\ \lambda_{r\alpha}(k)\ \lambda_{r\beta}(k)]^T$, I is the identity matrix and $u(k) = [v_{s\alpha}(k)\ v_{s\beta}(k)]^T$.

IV. Types of Three-phase Induction Motor Power Supplies

In this section, two types of three-phase IM power supplies are described. These are considered in the analysis of impact of parameter variations.

A. Pure Sinusoidal Waveforms

This method consists of the direct connection of the stator windings to three-phase voltages sinusoidal, which have a 120 degree phase shift between each other, with the amplitude and frequency adjusted to the IM nominal voltage values.

B. Three-phase voltage source inverter

One of the most used configurations of power electronic converters consists of an uncontrolled rectifier connected to a voltage source inverter (VSI) through a DC-Link. Fig. 2 shows the three-phase inverter which has three legs, each consisting of two electronic switches. The output of the VSI corresponds to each midpoint between these switches. A three-phase VSI with pulse width modulation (PWM) allows the control of the three-phase output voltages in amplitude and frequency through three sinusoidal reference voltages of controlled amplitude. In the PWM technique, each reference voltage is compared to a triangular waveform, the comparator's output defines the switching states used to drive the inverter switches.

The triangular waveform has a switching frequency that sets the frequency at which the switches will operate. On the other hand, the sinusoidal reference signal has the desired fundamental frequency of the inverter voltage output.

The output voltages of the inverter v_{zN} with respect to the negative bus of the DC-link N, are defined by the switching states S_z in each leg as follow:

$$v_{zN} = V_{dc} S_z \tag{11}$$

where the phases are represented by $z = [a, b, c]$.

Considering balanced operating conditions, the relationship between the phase voltages of the VSI output v_{zN} with the phase voltages v_{zn} and the negative DC-link bus voltages v_{nN} is expressed by:

$$\begin{aligned} v_{zn} &= v_{zN} - v_{nN} \\ &= V_{dc} S_z - \frac{1}{3}\left(v_{aN} + v_{bN} + v_{cN}\right) \end{aligned} \tag{12}$$

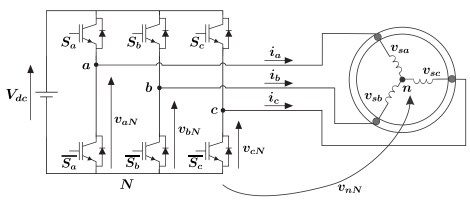

Fig. 2. VSI scheme connected to a 3-phase IM.

TABLE I
Mechanical and electrical parameters of IM

Parameter	Value	Parameter	Value
R_s	0.7384 Ω	p_p	2
R_r	0.7402 Ω	B	0.000503 kg.m^2/s
L_{ls}*	3.045 mH	J	0.0343 kg.m^2
L_{lr}*	3.045 mH	Nominal speed	1440 rpm
L_s	127.1 mH	Nominal power	7.5 kW
L_r	127.1 mH	Voltage (line-line)	400 V
L_m	124.1 mH	Nominal frequency	50 Hz

*Are the leakage inductances. $L_s = L_{ls} + L_m$ and $L_r = L_{lr} + L_m$

where v_{zn} are the voltages on IM stator windings with star connection, v_{sa}, v_{sb} and v_{sc}.

The output voltages provided by the VSI are not purely sinusoidal, since it provides discrete output voltages which contain components of higher frequencies multiples of the fundamental frequency [22], [23].

V. Analysis Method and Simulations

The simulations of the three-phase IM in open loop, for both mentioned models, are implemented using MATLAB/Simulink software. Table I presents the mechanical and electrical parameters of the IM under study. In all cases, constant load conditions of 25% of the nominal value is applied. Sampling time of 10 μs is considered.

Initially, a balanced set of three-phase, fundamental harmonic voltages, adjusted at the nominal voltage of the machine, are applied to the IM continuous model and the output currents in steady-state are obtained, disregarding the magnetic saturation effect, and by considering L_m, R_s, R_r, L_{ls}, and L_{lr}, constant in their nominal values.

The same power supply is applied to the discrete model and a single parameter is varied, measured and compared at once. The variation of the electrical parameters values are realized taking 13 points in a range of $\pm 30\%$ of their nominal values. Obtained results for the stator currents $i_{s\alpha}$ in steady-state applied to the IM discrete model, are shown in Fig. 3 and Fig. 4.

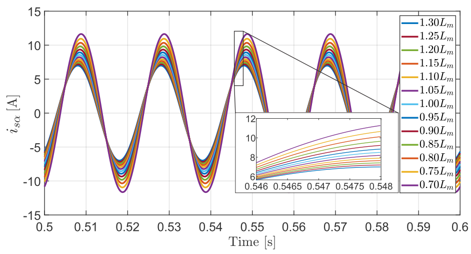

Fig. 3. Results of the current $i_{s\alpha}$ in steady-state, varying L_m parameter value and by applying three-phase sinusoidal waveforms at the IM discrete model.

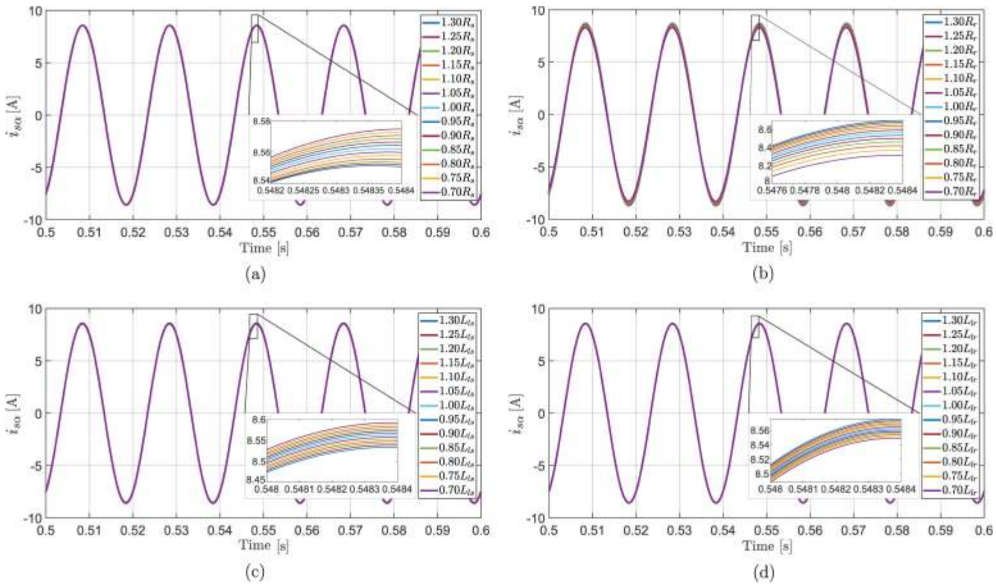

Fig. 4. Results of the current $i_{s\alpha}$ in steady-state, varying the parameter values: (a) R_s; (b) R_r; (c) L_{ls}; (d) L_{lr}, and by applying three-phase sinusoidal waveforms at the IM discrete model.

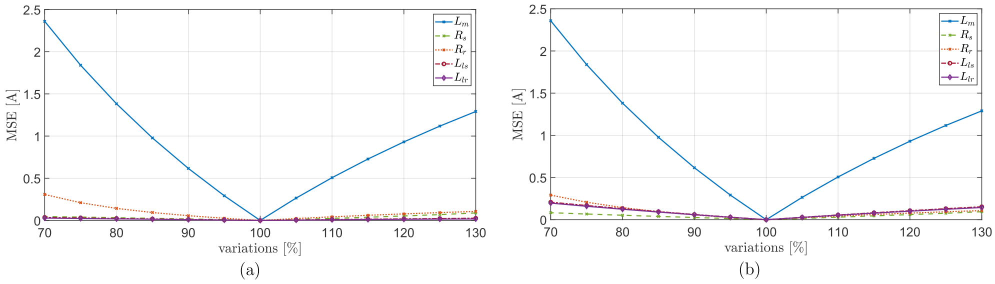

Fig. 5. MSE by considering the parameters variations in an IM model: (a) applying pure sinusoidal waveforms; (b) applying three-phase VSI.

The quantitative indicator, used to represent differences between the discrete model and the continuous model, is obtained by analyzing the results of the currents in steady-state of both models and by calculating the MSE between the stator currents obtained in continuous model $i_s^*(k)$ with electrical parameters fixed at the nominal values and the stator currents obtained in discrete model $i_s(k)$ considering the range of parameter variations above mentioned. MSE is given by:

$$\mathrm{MSE} = \sqrt{\frac{1}{n}\sum_{k=m+1}^{m+n}\left(i_s^*(k) - i_s(k)\right)^2} \qquad (13)$$

where n is the total number of samples taken in an interval, and m is the number taken as a starting point in steady-state. Both are represented by integer numbers.

By calculating the MSE for the stator currents $i_{s\alpha}$ and comparing, taking into account 13 variation points of each parameter, the results can be seen in Fig. 5(a). The curve that corresponds to the variation of the magnetization inductance represents the variable with the most significant impact on the MSE of the stator currents between the discrete model and continuous model, being L_m present in practically all the equations of the three-phase IM mathematical model. Table II

TABLE II
STEADY STATE ANALYSIS OF MSE OF THE STATOR CURRENTS IN α-β PLANE AT DIFFERENT VALUES OF THE ELECTRICAL PARAMETERS BY APPLYING THREE PURE SINUSOIDAL VOLTAGE

%	L_m [H]	MSE [A]	R_s [Ω]	MSE [A]	R_r [Ω]	MSE [A]	L_{ls} [H]	MSE [A]	L_{lr} [H]	MSE [A]
70	0.0869	2.3600	0.5169	0.0470	0.5181	0.3075	0.0021	0.0355	0.0021	0.0277
75	0.0931	1.8398	0.5538	0.0397	0.5552	0.2103	0.0023	0.0291	0.0023	0.0228
80	0.0993	1.3826	0.5907	0.0323	0.5922	0.1428	0.0024	0.0233	0.0024	0.0184
85	0.1055	0.9777	0.6276	0.0250	0.6292	0.0938	0.0026	0.0176	0.0026	0.0140
90	0.1117	0.6166	0.6646	0.0176	0.6662	0.0562	0.0027	0.0116	0.0027	0.0094
95	0.1179	0.2925	0.7015	0.0094	0.7032	0.0258	0.0029	0.0057	0.0029	0.0046
100	0.1241	0.0000	0.7384	0.0000	0.7402	0.0000	0.0030	0.0000	0.0030	0.0000
105	0.1303	0.2653	0.7753	0.0112	0.7772	0.0226	0.0032	0.0053	0.0032	0.0043
110	0.1365	0.5069	0.8122	0.0243	0.8142	0.0428	0.0033	0.0102	0.0033	0.0080
115	0.1427	0.7281	0.8492	0.0384	0.8512	0.0610	0.0035	0.0146	0.0035	0.0110
120	0.1489	0.9311	0.8861	0.0532	0.8882	0.0777	0.0037	0.0187	0.0037	0.0135
125	0.1551	1.1182	0.9230	0.0693	0.9253	0.0930	0.0038	0.0224	0.0038	0.0155
130	0.1631	1.2913	0.9599	0.0890	0.9623	0.1072	0.0040	0.0260	0.0040	0.0171

TABLE III
COMPARATIVE OF MSE OF THE STATOR CURRENTS IN α-β PLANE BY APPLYING THREE PURE SINUSOIDAL VOLTAGE RESPECT TO MSE USING THREE-PHASE VSI ON THE IM AT DIFFERENT VALUES OF THE L_m AND R_r

%	L_m [H]	MSE [A]	VSI-MSE [A]	R_r [Ω]	MSE [A]	VSI-MSE [A]
70	0.0869	2.3600	2.3578	0.5181	0.3075	0.2915
75	0.0931	1.8398	1.8381	0.5552	0.2103	0.2070
80	0.0993	1.3826	1.3814	0.5922	0.1428	0.1436
85	0.1055	0.9777	0.9768	0.6292	0.0938	0.0950
90	0.1117	0.6166	0.6160	0.6662	0.0562	0.0570
95	0.1179	0.2925	0.2922	0.7032	0.0258	0.0261
100	0.1241	0.0000	0.0000	0.7402	0.0000	0.0000
105	0.1303	0.2653	0.2650	0.7772	0.0226	0.0228
110	0.1365	0.5069	0.5065	0.8142	0.0428	0.0431
115	0.1427	0.7281	0.7274	0.8512	0.0610	0.0615
120	0.1489	0.9311	0.9303	0.8882	0.0777	0.0784
125	0.1551	1.1182	1.1172	0.9253	0.0930	0.0939
130	0.1631	1.2913	1.2901	0.9623	0.1072	0.1083

exposes the values of the MSE for each parameter variation under study. As can be seen, L_m reaches the highest MSE in magnetic saturation condition (low L_m). The next parameter that has a significant effect is R_r which shows a higher effect on stator currents MSE at low values. Still the MSE effect is approximately of 13% of L_m effect. The other parameters show an impact of approximately between 1% to 2% of L_m effect, being considered insignificant compared to L_m and R_r variations.

The same procedures described for evaluating the effect of parameter variations by applying three-phase pure sinusoidal voltage are performed using the three-phase VSI with carrier-based sinusoidal PWM, on both models. In Fig. 5(b), it can be noticed the magnetization inductance continues to have a greater impact than the other parameters on the stator current error. However, the impact of the rotor resistance represents approximately 12.3%, stator resistance 3.5% and the leakage inductances about 8.8%, at low values, with respect to the L_m effect.

Table III shows the comparison between the two types of IM power supplies in terms of the MSE of the stator current in steady-state and the variations of the L_m and R_r values.

VI. CONCLUSION

In this paper, a discrete model of an IM with electrical parameter variations is compared with a continuous model where the electrical parameters are fixed in nominal values. In order to determine the effects on the stator current in a steady-state, the variations of the paramenters are made in a range of 70% to 130% of nominal values and the errors are represented in terms of the MSE. The results of the analysis of the MSE of stator currents, in steady-state, with the variations of the parameters such as magnetization inductance, stator resistance, rotor resistance, leakage inductance of the stator and rotor, show that variations of the leakage inductances and stator resistance have an insignificant impact on the current. However, the variation of the rotor resistance is more notorious and the magnetization inductance has a the greatest impact in the IM powered by three-phase sinusoidal sources and with a three-phase VSI. Taking these conclusions into account, an analysis of the effects of variations of the electrical parameters on a closed-loop system by implementing a model-based control will be presented in future work.

ACKNOWLEDGMENT

The authors would like to thank the financial support from the Paraguayan Science and Technology National Council (CONACYT) through Grant Number POSG17-69.

REFERENCES

[1] M. Matsushita, F. Ishibashi, and S. Mizuno, "Calculation of magnetizing inductance and magnetizing current of squirrel cage induction motor," in *19th International Conference on Electrical Machines and Systems (ICEMS)*, November 2016, pp. 1–5.

[2] F. Wang, S. Li, X. Mei, W. Xie, J. Rodriguez, and R. M. Kennel, "Model-based predictive direct control strategies for electrical drives: An experimental evaluation of PTC and PCC methods," *IEEE Transactions on Industrial Informatics*, vol. 11, no. 3, pp. 671–681, June 2015.

[3] A. Favato, P. G. Carlet, F. Toso, and S. Bolognani, "A novel formulation of continuous control set mpc for induction motor drives," in *IEEE International Electric Machines Drives Conference (IEMDC)*, May 2019, pp. 2196–2202.

[4] M. Ayala, J. Doval-Gandoy, J. Rodas, O. Gonzalez, and R. Gregor, "Current control designed with model based predictive control for six-phase motor drives," *ISA Transactions*, 2019.

[5] O. Gonzalez, M. Ayala, J. Rodas, R. Gregor, G. Rivas, and J. Doval-Gandoy, "Variable-speed control of a six-phase induction machine using predictive-fixed switching frequency current control techniques," in *9th IEEE International Symposium on Power Electronics for Distributed Generation Systems (PEDG)*, June 2018, pp. 1–6.

[6] E. Levi, "Impact of iron loss on behavior of vector controlled induction machines," *IEEE Transactions on Industry Applications*, vol. 31, no. 6, pp. 1287–1296, 1995.

[7] M. Kral and R. Gono, "Dynamic model of asynchronous machine," in *18th International Scientific Conference on Electric Power Engineering (EPE)*, May 2017, pp. 1–4.

[8] S. A. A. Maksoud and T. V. Chestyunina, "Simulation and experimental increased temperature effect on induction motor parameters," in *XIV International Scientific-Technical Conference on Actual Problems of Electronics Instrument Engineering (APEIE)*, October 2018, pp. 258–263.

[9] Y. Kali, J. Rodas, M. Saad, J. Doval-Gandoy, and R. Gregor, "Nonlinear backstepping with time delay estimation for six-phase induction machine," in *IEEE International Electric Machines Drives Conference (IEMDC)*, May 2019, pp. 1798–1804.

[10] Y. Kali, M. Saad, J. Doval-Gandoy, J. Rodas, and K. Benjelloun, "Discrete sliding mode control based on exponential reaching law and time delay estimation for an asymmetrical six-phase induction machine drive," *IET Electric Power Applications*, vol. 13, no. 11, pp. 1660–1671, 2019.

[11] Y. Kali, J. Rodas, M. Saad, R. Gregor, K. Benjielloun, J. Doval-Gandoy, and G. Goodwin, "Speed control of a five-phase induction motor drive using modified super-twisting algorithm," in *International Symposium on Power Electronics, Electrical Drives, Automation and Motion (SPEEDAM)*, June 2018, pp. 938–943.

[12] J. Rodriguez and P. Cortes, *Predictive control of power converters and electrical drives*. John Wiley & Sons, 2012, vol. 40.

[13] A. Taheri and M. Mohammadbeigi, "Speed sensor-less estimation and predictive control of six-phase induction motor using extended Kalman filter," in *The 5th Annual International Power Electronics, Drive Systems and Technologies Conference (PEDSTC)*, February 2014, pp. 13–18.

[14] M. Ayala, O. Gonzalez, J. Rodas, R. Gregor, and J. Doval-Gandoy, "A speed-sensorless predictive current control of multiphase induction machines using a Kalman filter for rotor current estimator," in *International Conference on Electrical Systems for Aircraft, Railway, Ship Propulsion and Road Vehicles International Transportation Electrification Conference (ESARS-ITEC)*, November 2016, pp. 1–6.

[15] E. Zerdali and M. Barut, "The comparisons of optimized extended kalman filters for speed-sensorless control of induction motors," *IEEE Transactions on Industrial Electronics*, vol. 64, no. 6, pp. 4340–4351, June 2017.

[16] H. A. Toliyat, E. Levi, and M. Raina, "A review of RFO induction motor parameter estimation techniques," *IEEE Transactions on Energy Conversion*, vol. 18, no. 2, pp. 271–283, June 2003.

[17] M. S. Zaky, M. M. Khater, H. Yasin, and S. S. Shokralla, "Magnetizing inductance identification algorithm for operation of speed-sensorless induction motor drives in the field weakening region," in *12th International Middle-East Power System Conference (MEPCON)*, March 2008, pp. 103–108.

[18] L. Liu, Y. Guo, and J. Wang, "Online identification of mutual inductance of induction motor without magnetizing curve," in *Annual American Control Conference (ACC)*, June 2018, pp. 3293–3297.

[19] B. M. Chandra and S. T. Kalyani, "Online estimation of stator resistance in vector control of induction motor drive," in *IEEE Fifth India International Conference on Power Electronics (IICPE)*, December 2012, pp. 1–5.

[20] O. Kiselychnyk, M. Bodson, and J. Wang, "Comparison of two magnetic saturation models of induction machines and experimental validation," *IEEE Transactions on Industrial Electronics*, vol. 64, no. 1, pp. 81–90, January 2017.

[21] B. Karanayil, M. F. Rahman, and C. Grantham, "On-line rotor resistance identification for induction motor drive with artificial neural networks supported by a simple pi stator resistance estimator," in *The Fifth International Conference on Power Electronics and Drive Systems (PEDS)*, vol. 1, November 2003, pp. 433–438 Vol.1.

[22] N. Mohan, T. M. Undeland, and W. P. Robbins, *Power electronics: converters, applications, and design*. John Wiley & Sons, 2003.

[23] Keliang Zhou and Danwei Wang, "Relationship between space-vector modulation and three-phase carrier-based PWM: a comprehensive analysis [three-phase inverters]," *IEEE Transactions on Industrial Electronics*, vol. 49, no. 1, pp. 186–196, February 2002.